

Investigations into the Behavior, Detection, and Mitigation of Oil in a Sea Ice Environment

by

Durell Sterling Desmond

A Thesis submitted to the Faculty of Graduate Studies of

The University of Manitoba

in partial fulfillment of the requirements of the degree of

Doctor of Philosophy

Department of Environment and Geography

University of Manitoba

Winnipeg, Manitoba, Canada

Copyright © 2024 by Durell Sterling Desmond

Abstract

The Arctic is warming at a rate of three times the global average, and projections warn that the average surface Arctic Ocean temperature may increase by 3 °C by 2100. Due to this Arctic warming, there have been steady decreases in sea ice extent and thickness. In particular, the Arctic has lost much of its multi-year ice (MYI) (i.e., ice that survives multiple summers) and is dominated by first-year ice (FYI) (i.e., ice that grows in the winter but melts in the summer). FYI is more saline than MYI and therefore has a lower albedo, thereby increasing the input of solar radiation into the ice-ocean system by 50%. Further Arctic amplification is caused by the thinning and reduction of snow cover and the occurrence of a longer open water season. A direct consequence of this Arctic warming is an increased interest in oil exploration, extraction, and transport, owing to the greater feasibility, which increases the likelihood of a potential oil spill in the marine environment. Notably, spillage by either an oil tanker or an underwater pipeline poses the biggest threat to the Arctic environment and its inhabitants.

In order to combat this threat, the establishment of viable oil detection and mitigation techniques suitable for Arctic environments are currently in development. This urgency has led to the conduction of several oil-in-ice experiments to study various aspects of oil spill preparedness. The research herein aims to build on past work with a focus on oil behavior (i.e., migration tendencies, encapsulation potential, partitioning within sea ice, evaporation, dissolution, photooxidation, biodegradation), detection (i.e., radar), and mitigation (i.e., bioremediation) in sea-ice environments. This research consists of data collected from two artificial oil-in-ice mesocosm experiments in which microbial analyses (community composition), physical analyses (X-ray, temperature, salinity, brine volume), chemical analyses (oil dielectrics, infrared spectroscopy, gas chromatography–mass spectrometry), and modeling/simulations (computational chemistry, sea ice dielectrics, and normalized radar cross-section) were undergone. This study helps to discern how oil influences the physical properties of sea ice and how, in turn, sea ice influences the chemical (and, therefore, the physical) properties of oil.

Acknowledgement

I thank the Creator for my many blessings, including the privilege to learn and grow in understanding.

I thank my family and friends for their loving patience throughout this journey.

I also thank my advisors Drs. Gary Stern and Dustin Isleifson for their support and guidance throughout this endeavor. Likewise, I thank Drs. Georg Schreckenbach, Eric Collins, and Baiyu (Helen) Zhang for their role in helping to evaluate and improve this work as part of my Ph.D. examination committee. I give a special thanks to the late Dr. David Barber who opened a path for me and gave me an opportunity to shine, inspiring me to do my best. I also give a special thanks to Drs. Diana Saltymakova and Odile Crabeck (former colleagues) who helped and supported me throughout my degree. I owe much of my success to these two titans who lifted me up to new heights.

As well, I would like to thank Jake Ritchie, Debbie Armstrong, and Emmelia Stainton for their assistance in acquiring the necessary supplies used for the experiments; Dr. Marcos Lemes and Dave Binne for their kind help in conducting these experiments at the Centre for Earth Observation Science (CEOS) and Sea-ice Environmental Research Facility (SERF), respectively; Drs. James Xidos, Gregory Bridges, and Horace Luong, for their assistance with experiment measurements; Dr. Glen Hostetler for his support and friendship.

Finally, I would like to thank the Canada Research Chair (CRC) programs, Natural Sciences and Engineering Research Council (NSERC) of Canada, Canada Foundation for Innovation (CFI), Microbial Genomics for Oil Spill Preparedness in Canada's Arctic Marine Environment (GENICE), ArcticNet Networks of Centres of Excellence, Arctic Science Partnership (ASP), and the University of Manitoba (UofM) for their financial support, as well as Tundra Oil&Gas Ltd. for donating the crude oil used for this research. This work was made possible by the facilities of the Shared Hierarchical Academic Research Computing Network (SHARCNET: www.sharcnet.ca) and Compute/Calcul Canada as well as Software for Chemistry & Materials (SCM).

“What you believe, you can achieve.”

-Mary Kay Ash

Contributions of Authors

This thesis contains four manuscripts that have been published in either Marine Pollution Bulletin or the Journal of Physical Chemistry, comprising Chapters 2 to 5 herein. The papers have several authors, but Desmond, D.S. is the first author. The following describes the contribution of each author for the respective papers.

Saltymakova, D.¹, Desmond, D.S.¹, Isleifson, D., Firoozy, N., Neusitzer, T.D., Xu, Z., Lemes, M., Barber, D.G., and Stern, G.A., 2020. “Effect of dissolution, evaporation, and photooxidation on crude oil chemical composition, dielectric properties and its radar signature in the Arctic environment.” *Marine Pollution Bulletin* 151: 110629, <https://doi.org/10.1016/j.marpolbul.2019.110629>.

¹equal authors contribution

- Saltymakova, D.: Samples collection and preparation. Operation, identification, and analysis of GCxGC-HR-TOF-MS and QqQ-MS, statistical analyses, ATR-IR data analysis, compiled data analyses, and manuscript preparation.
- Desmond, D.S.: Experiment lead and organizer, experiment setup, samples collection and preparation, helped with operation and data interpretation of GCxGC-HR-TOF-MS and μ -CT, sea ice physics data collection, ATR-IR data collection and analysis, computational chemistry, optical measurements, and thermal and electromagnetic properties modeling and measurements. Helped with manuscript preparation entailing the majority of the writing and editing.
- Isleifson, D.: Remote sensing guidance and manuscript editing.
- Firoozy, N.: Experiment setup, NRCS sensitivity analysis.
- Neusitzer, T.D.: Experiment setup, sampling, modeling of complex permittivity.
- Xu Z.: Supervision of optical measurements, calibration, and processing of optical measurements.

- Lemes, M.: Sample measurement and processing by compact micro-computed tomography, the guidance of results interpretation.
- Barber, D.G.: Sea ice thermodynamic guidance and funding.
- Stern, G.A.: Program lead, analytical chemistry, and statistical analysis guidance, funding.

Reprinted (adapted) with permission from **Desmond, D.S., D. Saltymakova, O. Crabeck, G. Schreckenbach, J.D. Xidos, D.G. Barber, D. Isleifson, and G.A. Stern, “Methods for Interpreting the Partitioning and Fate of Petroleum Hydrocarbons in a Sea Ice Environment.” *J. Phys. Chem. A* 126 (5): 772-786, 2022, <https://doi.org/10.1021/acs.jpca.1c08357>. Copyright 2022 American Chemical Society."**

- Desmond, D.S.: Chemical modeling, processing of the physical properties of sea ice, data analysis and interpretation, manuscript preparation (including writing and figure/table creation).
- Saltymakova, D.: Chemical analysis by GCxGC-HR-TOF-MS and QqQ-MS.
- Crabeck, O.: Manuscript editing, data interpretation, and figure creation.
- Schreckenbach, G.: Guidance and manuscript editing.
- Xidos, J.D.: Guidance and manuscript editing.
- Barber, D.G.: Funding.
- Isleifson, D.: Funding and manuscript review.
- Stern, G.A.: Funding and manuscript review.

Desmond, D.S., Saltymakova, D., Smith, A., Wolfe, T., Snyder, N., Polcwiartek, Bautista, M., Lemes, M., Hubert, C.R.J., Barber, D.G., Isleifson, D., and Stern, G.A., 2021. “Photooxidation and biodegradation potential of a light crude oil in first-year sea ice.” *Marine Pollution Bulletin* 165: 112154, <https://doi.org/10.1016/j.marpolbul.2021.112154>.

- Desmond, D.S.: Conceptualization, investigation, methodology, formal analysis, visualization, writing – original draft, writing – review & editing.

- Saltymakova, D.: Supervision, conceptualization, investigation, formal analysis, methodology, visualization, writing – review & editing preparation.
- Smith, A.: Conceptualization, investigation, methodology, visualization, writing – original draft.
- Wolfe, T.: Investigation, writing – original draft.
- Snyder, N.: Investigation, writing – review & editing.
- Polcwiartek, K.: Investigation, visualization.
- Bautista, M.: Investigation, visualization.
- Lemes, M.: Investigation, writing – review & editing.
- Hubert, C.R.J.: Project administration, funding acquisition, writing – review & editing.
- Barber, D.G.: Funding acquisition.
- Isleifson, D.: Writing – review and editing.
- Stern, G.A.: Project administration, funding acquisition, writing – review & editing.

Desmond, D.S., Crabeck, O., Lemes, M., Harasyn, M.L., Mansoori, A., Saltymakova, D., Fuller, M.C., Rysgaard, S., Barber, D.G., Isleifson, D., Stern, G.A., 2021. "Investigation into the geometry and distribution of oil inclusions in sea ice using non-destructive X-ray microtomography and its implications for remote sensing and mitigation potential." *Marine Pollution Bulletin* 173: 112996, <https://doi.org/10.1016/j.marpolbul.2021.112996>.

- Desmond, D.S.: Conceptualization, investigation, methodology, formal analysis, visualization, writing – original draft, writing – review & editing.
- Crabeck, O.: Formal analysis, methodology, visualization, writing – review & editing.
- Lemes, M.: Investigation, methodology, writing – review & editing.
- Harasyn, M.L.: Formal analysis, writing – original draft, writing – review & editing.

- Mansoori, A.: Formal analysis, writing – review & editing.
- Saltymakova, D.: Visualization, writing – review & editing.
- Fuller, M.C.: Writing – review & editing.
- Rysgaard, S.: Funding acquisition, writing – review & editing.
- Barber, D.G.: Funding acquisition.
- Isleifson, D.: Writing – review & editing.
- Stern, G.A.: Project administration, funding acquisition, writing – review & editing.

Table of Contents

Abstract	iii
Acknowledgement.....	iv
Contributions of Authors.....	v
Table of Contents	ix
List of Tables.....	xiii
List of Figures	xiv
List of Acronyms.....	xix
1 Introduction.....	1
1.1 Climate Change and its Impact on Sea Ice.....	1
1.1.1 Climate Change	1
1.1.2 Background: Sea Ice.....	3
1.1.3 Reduction of Sea Ice Extent and Thickness	4
1.2 Marine Transportation and the Potential for Oil and Fuel Pollution.....	5
1.3 Petroleum Oil and its Threat to the Arctic and its Inhabitants	6
1.4 Oil Spill Preparedness and Response in the Arctic	11
1.4.1 Oil Behavior and Fate	12
1.4.2 Oil Spill Detection and Monitoring.....	18
1.4.3 Mitigation Methods	20
1.5 Proposed Research Goals / Research Aims and Objectives	25
1.5.1 Project 1 (Chapter 2): “Effect of dissolution, evaporation, and photooxidation on crude oil chemical composition, dielectric properties and its radar signature in the Arctic environment.”	26
1.5.2 Project 2 (Chapter 3): “Methods for Predicting Partitioning and Fate of Petroleum Hydrocarbons in a Sea Ice Environment”	28
1.5.3 Project 3 (Chapter 4): “Photooxidation and biodegradation potential of a light crude oil in first-year sea ice”	30
1.5.4 Project 4 (Chapter 5): “Investigation into the geometry and distribution of oil inclusions in sea ice using non-destructive X-ray microtomography and its implications for remote sensing and mitigation potential”	32
1.6 References	33

2	Effect of Dissolution, Evaporation, and Photooxidation on Crude Oil Chemical Composition, Dielectric Properties and its Radar Signature in the Arctic environment	41
2.1	Abstract	41
2.2	Introduction	41
2.3	Methods	44
2.3.1	Experiment Overview	44
2.3.2	Sample Preparation (Ice Core and Water Samples)	47
2.3.3	Analytical Instrumentation	48
2.3.4	Statistical Analysis	51
2.3.5	Computational Chemistry	51
2.3.6	Optical Measurements	56
2.3.7	Thermal and Electromagnetic Properties	56
2.4	Results and Discussion	60
2.4.1	Crude Oil Distribution and Sea Ice Thermodynamic Properties	60
2.4.2	Effect of Dissolution on Crude Oil Partitioning	64
2.4.3	Evaporation	70
2.4.4	Photooxidation	72
2.4.5	Remote Sensing Detection of Oil Spills in a Sea-Ice Environment	74
2.5	Conclusion	77
2.6	Acknowledgements	79
2.7	References	80
3	Methods for Interpreting Partitioning and Fate of Petroleum Hydrocarbons in a Sea Ice Environment	88
3.1	Abstract	88
3.2	Introduction	89
3.3	Experimental and Theoretical Methods	94
3.3.1	Oil-in-ice Mesocosm Experiment Overview	94
3.3.2	Physical Properties of Sea Ice	96
3.3.3	Chemical Analysis	98
3.3.4	Computational Details	100
3.4	Results and Discussion	104
3.4.1	Brine Volumes, Salinities, and Oil Migration	104
3.4.2	Application of Modeling to the Experimental Data Analysis	108

3.5	Conclusions	127
3.6	Acknowledgements	130
3.7	References	130
4	Photooxidation and Biodegradation Potential of a Light Crude Oil in First-Year Sea Ice	140
4.1	Abstract	140
4.2	Introduction	140
4.3	Methods	142
4.3.1	Experiment Overview	142
4.3.2	Sample Preparation	146
4.3.3	Analytical Instrumentation	147
4.3.4	Microbial Analysis	154
4.4	Results and Discussion	156
4.4.1	Sea Ice Geophysics and Oil Distribution	156
4.4.2	Microbial Populations Capable of Biodegradation	158
4.4.3	Extent of Oil Transformation	161
4.5	Conclusion	173
4.6	Acknowledgements	174
4.7	References	175
5	Investigation into the Geometry and Distribution of Oil Inclusions in Sea Ice using non-destructive X-ray Microtomography and its Implications for Remote Sensing and Mitigation Potential	181
5.1	Abstract	181
5.2	Introduction	182
5.3	Materials and Methods	186
5.3.1	Source of X-ray Samples	186
5.3.2	Preparation of the X-ray Samples Before Scanning	188
5.3.3	Experimentally Determined Volume Fractions	191
5.3.4	Analysis by Micro-Computed Tomography (μ -CT) X-ray	192
5.3.5	Proximity of Oil and Brine Inclusions Analysis	200
5.3.6	Individual Object Analysis of Sea Ice Inclusions	201
5.3.7	Remote Sensing Modeling: Application of Inclusion Geometry Analysis	202
5.4	Results and Discussion	206
5.4.1	Qualitative Analysis	206

5.4.2	Quantitative Analysis	210
5.5	Conclusion.....	214
5.6	Acknowledgements	215
5.7	References	216
6	Conclusion.....	224
6.1	Summary of Findings	224
6.2	Limitations and Future Work	225
6.3	Proposed Arctic Oil Spill Strategy based on Conducted Research and Suggested Future Work	229
6.4	References	231
7	Appendix	233
7.1	Supplementary Tables and Figures	233
7.2	Additional Contributions to the Literature	259
7.3	Sea Ice and Sea Ice Dielectrics.....	262
7.4	Sea Ice and Oil Interactions	267
7.4.1	References	271
7.5	Sea Ice and Oil Weathering.....	272
7.5.1	References	275
7.6	Radar	277
7.6.1	References	281
7.7	Instrumentation for Oil Analysis.....	282
7.7.1	Gas Chromatography.....	283
7.7.2	Mass Spectrometry	284
7.7.3	Infrared Spectroscopy	286
7.7.4	X-ray Microtomography	288
7.7.5	Dielectrics.....	288
7.7.6	References	289
7.8	Optical Measurements (Supplementary Information of Chapter 2)	291
7.9	Dielectric Measurement: Resonance Perturbation Method (Quality Assurance/Control) (Supplementary Information of Chapter 2)	292
7.10	NRCS Modeling (Supplementary Information of Chapter 2)	293

List of Tables

Table 1.1 Examples of Chemical Groups contained within Petroleum Crude Oils	9
Table 2.1 Physical properties of low molecular weight (MW) and high MW chemical compounds	44
Table 2.2 Modeled physical properties of compounds found in crude oil using ADF2017 COSMO-RS.....	53
Table 2.3 Evolution of crude oil in sea ice: Changes in physical, chemical, and optical properties	72
Table 2.4 The sensitivity analysis of NRCS (dB) versus permittivity for VV polarization at 40 degrees with a root-mean-square surface roughness of 5 millimeters	76
Table 3.1 Calculated Physical Properties of Compounds Found in Crude Oil Using COSMO-RS	102
Table 4.1 Oil Dielectric Measurements of Ice Samples at Frequencies TE_{101} (1.8 GHz), TE_{104} (2.9 GHz), and ATR-IR Calculated Indices	150
Table 4.2 Modeled Physical Properties of Compounds found in Crude Oil using ADF2017/2018 COSMO-RS. Adapted from Saltymakova et al., 2020a and Desmond et al., 2019b.	162
Table 5.1 In Situ μ -CT Sea Ice Characteristics pertaining to a subset of the X-ray Samples	190
Table 5.2 Results of blind test assessing accuracy of method used to experimentally measure the oil volumes of the X-ray samples. Note ‘true volume’ pertains to known amounts of crude oil placed inside polypropylene tubes.....	191
Table 5.3 Averaged (STDEV) 3D Individual Object Analysis of Sphericity and Structure Model Index (SMI) for a Subset of 2015-2018 X-ray Samples	198
Table 5.4 Comparison of CT-derived and experimentally determined volumes for the media of brine, pure ice, and crude oil for sea ice sample “Feb. 7/18 Middle S3C1” (see Table 5.1 and Fig. 5.5)	200
Table 5.5 Comparisons between modeled and experimental NRCS (dB) for various sampling times (Desmond et al., 2019a; Neusitzer et al., 2018).	205
Table 5.6 Calculated NRCS penetration depths (cm) of the circular disk dielectric mixture model of sea ice for various sampling times (Desmond et al., 2019a; Neusitzer et al., 2018a)	205
Table 5.7 Calculated effective permittivities “seen” by the I ² EM NRCS model of the circular disk dielectric mixture model of sea ice for various sampling times (Desmond et al., 2019a; Neusitzer et al., 2018a).....	205
Table 5.8 RMS heights and correlation lengths (L) of relatively smooth and rough ice obtained using LiDAR	205
Table S2.1 Average Surrogate Recoveries	233
Table S2.2 Table of identified compounds in the crude oil composition, their quantifiers, and recovery standards.....	234
Table S2.3 Multiple reaction monitoring mass spectrometry method for steranes and tepanes.....	237
Table S3.1 Table of identified compounds in the crude oil composition, their quantifiers, and recovery standards.....	238
Table S3.2 Multiple reaction monitoring mass spectrometry method for steranes and terpanes ..	240
Table S4.1 Indices and Formulae used in Calculating Indices	241
Table S4.2 Measured Ice Thicknesses (cm) of Sampled Ice Cores.....	241

List of Figures

Fig. 1.1 Depiction showcasing the connectivity between the concepts of oil behavior, oil detection and monitoring, and oil mitigation.	26
Fig. 2.1 Temporal profile of the recorded temperatures for a vertical cross section of the test tank pertaining to the water column, sea ice, and air above from January 31 to March 14, 2017. The break in the temperature profile from February 15 to March 8 pertains to the transition period between phases one and two. Coring dates are in bold.	46
Fig. 2.2 Sea ice thermodynamic properties and crude oil content averaged (std. dev.) over the vertical cross sections of sampled ice cores. Note that (Cox and Weeks, 1983; Leppäranta and Manninen, 1988) were used for calculating the brine salinities and volumes.	60
Fig. 2.3 A, B, C -Plots of crude oil volume fraction (air neglected) in the top 2.5 cm (phase 1 ice core samples), corresponding bulk salinity, modeled NRCS signal (VV polarization at 40 degrees with a root-mean-square surface roughness of 5 millimeters) and modeled sea ice permittivity (5.5 GHz). D - Modeled sea ice permittivity (5.5 GHz) vs bulk salinity. B, C, D graph constructed based on samples collected on February 10/2017.	64
Fig. 2.4 Principal component analysis of the samples using PC2 and PC3 components. n-alk – straight chain alkanes; i-alk – isoprenoid and methyl substituted alkanes; ACP – alkylcyclopentanes; ACH – alkylcyclohexanes; MACH – methylalkylcyclohexanes; Str. – steranes; Terp. – terpanes; AB – alkylbenzenes; MAB – methylalkylbenzenes; TMAB – trimethylalkylbenzenes with isoprenoid chain; Nap – naphthalene; Ph. – phenanthrene; DBT – dibenzothiophene; DBF – dibenzofuran; C0, C1, C2, C3, C4, C5 – correspond to the number of methyl substitutions.	65
Fig. 2.5 Partitioning of steranes and terpanes within the vertical cross-section of the low contaminated and high contaminated ice cores. We calculated the relative percent of an individual compound per slice as a concentration of the individual compound in the slice divided by the total of its concentration in the ice core.	67
Fig. 2.6 Strength of the relationships between bulk salinity with crude oil volume fraction and analyzed compound concentrations in low and high contaminated ice cores evaluated using Spearman's rank correlation coefficient (mg/mL*- mg of crude oil per 1 mL of melted ice core sample).	68
Fig. 2.7 Distribution Tetramethylnaphthalenes/Methylphenanthranes ratio in the sea ice cross section.	70
Fig. 2.8 Modeled complex permittivity of the sea ice cross section of ice cores 4 (red), 11 (green), and an average of 13 and 14 (blue), which correspond to the three respective sampling dates.	75
Fig. 3.1 (Upper panel) Temporal evolution of the seawater, sea ice surface, air temperature, and the averaged ice thickness during the cycle of growth 1 and 2. (Bottom panel) Evolution of the ice surface and the position of the different cores sampled on February 10 and 15 and March 14.	96
Fig. 3.2 Vertical profiles of (a) sea ice temperature, (b) average bulk ice salinity, (c) average brine volume fraction, (d) brine salinity, and (e) whisker box plot of oil volume and (f) oil volume per sampling dates. The horizontal dotted line shows the ice thickness reached at the oil injection during	

growth cycle 1. The vertical green dotted line in panel (c) shows the 5 % brine volume fraction permeability threshold according to Golden et al. (2007). The errors bars in panels (b) and (c) show the standard deviation of the averaged parameters.	107
Fig. 3.3 (a) Relationship between molecular volume (\AA^3), aqueous solubility at $-2.4\text{ }^\circ\text{C}$ and salinity of 35 g/kg, and log K_{OW} for the different groups of oil compounds provided in Table 3.1. The y axis is a logarithmic scale, and the size of the data points are proportional to their respective log K_{OW} value. (b) Impact of NaCl salt concentration (ppt) on the aqueous solubility of naphthalene and C30 tricyclic terpane (terpane C-30).....	109
Fig. 3.4 The relative abundance of trimethyl naphthalene (TMN), dodecane, and C30 tricyclic terpane (terpane C-30) retrieved in the ice (whisker box plot). The abundance of TMN, dodecane, and terpane C-30 in the initial oil mixture is showed by the dotted, light gray, and light purple lines, respectively. Relative abundance was calculated as the amount in ng of each species divided by the sum of the three species in ng multiplied by 100 (e.g., $\text{TMN} / (\text{TMN} + \text{dodecane} + \text{terpane C-30})$).	111
Fig. 3.5 (a) Amount in nanograms of trimethyl naphthalene (TMN), dodecane, and C30 tricyclic terpane (terpane C-30) measured in sea ice during growth cycle 1 and 2. (b) The vertical distribution of dodecane and Terpane C-30 at the end of cycle 2.	113
Fig. 3.6 GC-MS/MS chromatograms of the distribution of steranes and terpanes in the composition of top and bottom sections of the ice and water column of growth cycle 1. Core #6 was procured during the February 10 sampling date of the experiment, and the water sample was collected on February 15. Note that multiple reaction monitoring transitions are provided at the figure top. For instance, for transition $217 \rightarrow 121$, 217 is the parent (precursor) ion and 121 is the daughter (product) ion. More details on the multiple reaction monitoring mass spectrometry method for steranes and terpanes is provided in Table S3.2. Upward/downward arrows indicate increases/decreases in concentration in relation to the top ice core section.	115
Fig. 3.7 Partitioning of naphthalenes based on GCxGC-TOF. Sample core #10 was collected on the February 15 sampling date of the experiment. Note that (1) C_{1-4} indicate the number of methyl substitutions, and (2) sections 0–2.5 cm and 16–27 cm indicate the top and bottom sections of the ice core. In the figure, the two-dimensional chromatogram is provided at the front, and the one-dimensional chromatogram of the 1 st retention time axis is provided in the back. Upward/downward arrows indicate increases/decreases in proportion relative to each ice core section.	116
Fig. 3.8 (a) Tricyclic Terpane C_{23}/C_{30} ratio through the ice depth for various sampled ice cores from the February 10 and 15 (growth cycle 1) and March 14 (growth cycle 2) sampling dates. The blue dotted line and the black dashed line indicate the ratio in the seawater and technical oil mixture, respectively. (b) Linear correlation between the Tricyclic Terpane C_{23}/C_{30} ratio and oil volume (mL) for the top 2.5 cm of ice for ice cores sampled throughout the experiment.	118
Fig. 3.9 Sea ice profile of n-alkanes ratio (C_{11-14}/C_{15-18}) for representative ice cores sampled on February 10 and 15 and March 14. The blue dotted line and the black dashed line indicate the ratio in the seawater and technical oil mixture, respectively.	122
Fig. 3.10 (a) Ts/TM ratio and (b) 2-MN/1-MN ratio in the seawater and in the ice top and bottom layers. The dashed line shows the ratio of the original oil mixture.....	124
Fig. 3.11 Structures of Ts ($18\alpha(\text{H})$ -22,29,30-trisnorneohopane) and Tm ($17\alpha(\text{H})$ -22,29,30-trisnorhopane) isomers.	124

Fig. 3.12 Concentrations (ng/mL) of dissolved naphthalenes in the water column taken on the February 15/17 sampling date. N – naphthalene (parent); MN, methyl naphthalenes; DMN, dimethyl naphthalenes; TMN, trimethyl naphthalenes; TeMN, tetramethyl naphthalenes.....	127
Fig. 3.13 Graphical abstract providing an overview of Chapter 3.	139
Fig. 4.1 Augmented tank (left), Native tank (middle), and an example of an ice core taken during the experiment (right). Photos were taken Feb. 26/18.	143
Fig. 4.2 Experimental setup of the cavity allowing sample collection at three sites representing different crude oil contents – Site 1: Low Concentration, Site 2: Moderate Concentration, and Site 3: High Concentration.	145
Fig. 4.3 Ambient daily (24-hr) temperature (solid) and incident sunlight (dotted) profiles.	146
Fig. 4.4 Measured temperatures of top, middle, and bottom sectioned ice cores using a temperature probe for Native (A) and Augmented (B) tanks. Calculated brine volume fractions of top, middle, and bottom sectioned ice cores for Native (C) and Augmented (D) tanks using the measured temperatures and bulk salinities following (Frankenstein and Garner, 1967). Measured oil volume fractions (V_{OIL}/V_{ICE}) of top, middle, and bottom sectioned ice cores for Native (E) and Augmented (F) tanks following (Desmond et al., 2019a).....	157
Fig. 4.5 Relative sequence abundance of bacterial lineages at the class level (A), and within the Gammaproteobacteria lineage at the genus level (B). The bars reflect the mean community composition across all ice samples collected on a given sampling date. Classes that never comprised >1% of the microbial community are not shown in (A). MMG3: Marine methylotrophic group 3.	159
Fig. 4.6 Relative sequence abundance of bacterial lineages at the genus level for the melt pond samples on April 10. The bars reflect the mean community composition across all samples collected on that sampling date. Genera that never comprised >1% of the microbial community are not shown. MMG3: Marine methylotrophic group 3.	160
Fig. 4.7 A) PAR transmittance for Native tank and Augmented tank. Daily Average Sunlight Peak Hours (10 am to 3 pm); B) Average snow thickness accumulated on both Native and Augmented pools.	164
Fig. 4.8 The average dielectric constant of extracted oil taken from sampled sea ice core sections (i.e., top ice sections, middle and bottom ice sections) of Native (A) and Augmented (B) pools. All measurements were made at 1.8 GHz and 22.5 °C. Averaged ATR-IR absorbance of the C-O (1250 cm^{-1}) ether band associated with ester transformation products for Native (C) and Augmented (D) pools.	166
Fig. 4.9 ATR-IR Absorbance Spectrum of the technical mixture versus the extracted oil samples “Feb. 7 Augmented Site 3 Core 1 Middle Section” and “Feb. 26 Augmented Middle Section” (see Table 4.1).	167
Fig. 4.10 Temporal concentrations of heterocyclic aromatics found in the water column by GC–MS.	168
Fig. 4.11 C17/Pr ratio measured per ice core (A) and depth water column (B). Error bars show standard deviation.	169
Fig. 4.12 μ -CT Tomographic grayscale images of coronal (X-Z) view vertical slices of three oil-contaminated samples showcasing the oil, and brine inclusion distribution. In these images, air is shown in black, brine is shown in white, ice is shown in light grey, and oil is shown in dark grey.	

Box plots showing the percentage of oil and brine interface connection for the two μ -CT oil-contaminated sea ice samples.....	172
Fig. 5.1 Example photos of thick sections and a thin section of sea ice from an oil-in-ice mesocosm depicting alternating granular and columnar layers (Desmond et al., 2021).....	188
Fig. 5.2 Example of how X-ray samples were placed on a metal plate and encased in styrofoam prior to placement inside the μ -CT chamber for scanning.....	189
Fig. 5.3 Sub-sectioned X-ray sample placed inside a polypropylene Falcon tube and subsequently mounted on a rotating sample stage within the μ -CT chamber with installed thermocouples.....	193
Fig. 5.4 Panel A shows a raw transversal in the XZ direction of a test sample contained in a polypropylene tube in which crude oil was injected. Panel B shows a second test sample contained in a polypropylene tube in which both crude and corn oil was injected. The density contrast of the different medium (ice, crude oil, corn oil and polypropylene tube) are shown in the color bar. Panel C shows a transversal slice of the test sample in panel A. Panel D shows a CT histogram of the medium highlighted in panel C. The histogram combined the data over a stack of 147 slices.....	195
Fig. 5.5 Panel (A) shows a raw transversal slice of an oil-contaminated ice sample (Feb. 7/18 Middle S3C1) contained in a polypropylene tube. In this image, brine appears in white and very light grey, air bubbles appear in black, and oil inclusions appear in dark grey. Panel (B) shows histograms delineating the light blue and dark blue lines shown in the panel A image. Panel (C) shows the ice matrix in green, and the oil and polypropylene tube pixels in red, selected using the Ct-value of oil from the panel B histogram.....	197
Fig. 5.6 The 3D decomposition of top sections of sea ice cores from SERF 2018 in which oil, air, and brine are represented in red, blue, and white respectively.....	207
Fig. 5.7 Percentage of oil and brine boundary overlap (interface connection) for a subset of X-ray samples presented as box plots.....	208
Fig. 5.8 The panel (a) shows IQR box plot for the distribution of CT-derived major diameter of all oil, brine and air inclusions analyzed. The panel (b) shows IQR box plot for the distribution of CT-derived major diameter of oil inclusions for various samples from the different experiment (2016, 2017, 2018). The box is defined by the first and third quartiles of the distribution, the line in the box is the median. The panel (c) shows the histogram of the orientation angles (theta) for all the oil, brine and air inclusions analyzed.	211
Fig. S2.1 Reconstructed images of core 9 0-2.5 cm (left), core 9 2.5-5 cm (middle), and core 16 0-4 cm (right) showing sliced ensembles in a 3D view. In these images, the air is shown in black, brine is shown in light blue/white, ice is shown in blue, and oil is shown in red. The polypropylene tubes are visible in each image in red, bounding the sample within.....	242
Fig. S2.2 A - Average bulk Salinity Profiles for all the ice cores (Tot.), Phases 1 (Feb. 10 + 15) and Phase 2 (Mar. 14); B - Average bulk Salinity Profiles for the three sampling dates on the right... 242	242
Fig. S2.3 Bulk salinity and n-alkanes concentration distribution profiles for cores #7 and 8. The n-alkanes constitute the majority of the relative oil composition based on GC-MS (Desmond et al., 2019a).....	243
Fig. S2.4 Infrared spectra of a representative set of crude oil samples derived from top sections of sampled ice from the Feb. 10, Feb. 15, and Mar. 14/17 sampling dates.	243
Fig. S4.1 Relative sequence abundance of bacterial lineages at the genus level for the depth water samples throughout the experiment duration. The bars reflect the mean community composition across all samples collected on that sampling date. Genera that never comprised >1% of the	

microbial community are not shown. MMG3: Marine methylotrophic group 3. In this figure, “Control” corresponds to the Native tank and “Test” corresponds to the Augmented tank.	245
Fig. S4.2 Correlation of the C-H aromatic ring and C-O ether ATR-IR Absorbance bands showing loss of aromaticity due to inclusions of oxygen from photo-oxidation transformation.	246
Fig. S4.3 Association between the measured oil dielectric constants (Fig. 4.8) and ATR-IR absorbance of the C-O (1250 cm^{-1}) ether band (Fig. 4.9) for Augmented (left), Native (middle), and combined (right) pools.	246
Fig. S5.1 Example photo of a vertical slab of sea ice from an oil-in-ice mesocosm depicting alternating granular and columnar layers (Desmond et al., 2021).	247
Fig. S5.2 Sub-sectioned X-ray samples placed inside polypropylene Falcon tubes.	248
Fig. S5.3 Tomographic grayscale images of horizontal slices (XY-Plane) of a subset of sea ice samples showcasing the oil, air, and brine inclusion distribution. In these images, air is shown in black, brine is shown in white, ice is shown in light grey, and oil is shown in dark grey. The polypropylene tubes (~3 cm OD) are visible in each image in dark grey, bounding the sample within.	249
Fig. S5.4 The 3D decomposition of top and middle sections of sea ice cores from SERF 2016-2018 in which oil, air, and brine are represented in red, blue, and white respectively.	254

List of Acronyms

2D – Two Dimensional

3D – Three Dimensional

ACs – Analyzed Compounds

ADF – Amsterdam Density Functional

ADF-GUI – Amsterdam Density Functional – Graphical User Interface

ASP – Arctic Science Partnership

ATR-IR – Attenuated Total Reflection Infrared Spectroscopy

AVG – Average

B – Bioaccumulative

BPT – Boundary Perturbation Model

CBM - Community-Based Monitoring

CBR - Community-Based Response

CEOS – Centre for Earth Observation Science

CFI – Canada Foundation for Innovation

COSMO-RS – COnductor like Screening MOdel for Realistic Solvents

COSMO-SAC – COnductor like Screening MOdel for Segmented Activity Coefficients

CRC – Canada Research Chair

DMN - Dimethylnaphthalene

EI – Electron impact

FTIR – Fourier Transform Infrared

FY – First-Year

FYI – First-Year Ice

GC – Gas-liquid Chromatography

GCxGC-HR-TOF-MS – Multidimensional Gas Chromatography High Resolution Time Of Flight Mass Spectrometry

GC-HR-TOF-MS – Gas Chromatography-High Resolution Time Of Flight Mass Spectrometry

GC-MS – Gas Chromatography–Mass Spectrometry

GPR – Ground Penetrating Radar

GUI – Graphical User Interface

H – Horizontal

HCs – Hydrocarbons

HMW – Higher Molecular Weight

I²EM – Integral Equation Model

IOA - Individual Object Analyses

IR – Infrared

K_{ow} – Octanol–Water partition coefficient

LiDAR – Light Detection and Ranging

LMW – Lower Molecular Weight

MMG3 – Marine Methylotrophic Group 3

MN – Methylnaphthalene

MW – Microwave

MW – Molecular Weight

MY – Multiyear

MYI – Multi-Year Ice

NRCS – Normalized Radar Cross-Section

NSERC – Natural Sciences and Engineering Research Council

NSO – Nitrogen, Sulfur, or Oxygen

OTUs – Operational Taxonomic Units

PAHs – Polycyclic Aromatic Hydrocarbons

P – Persistent

PAR – Photosynthetically Active Radiation

PCA – Principal Component Analysis

PCR – Polymerase Chain Reaction

PPT – Parts Per Thousand

Pr – Pristane

PVS – Polder-van Santen/de Loo

QqQ-MS – Triple Quadrupole-Mass Spectrometry

S – Salinity

SAR – Synthetic Aperture Radar

SCM – Software for Chemistry & Materials

SERF – Sea-Ice Environmental Research Facility

SMI – Structure Model Index

S/N – Signal-to-Noise ratio

STDEV – Standard Deviation

T – Temperature

TMN - Trimethylnaphthalene

TeMN - Tetramethylnaphthalene

TOF – Time of Flight

TVB – Tinga-Voss-Blossey

UAV – Unmanned Aerial Vehicle

UNIFAC - UNIQUAC Functional-group Activity Coefficients

UofM – University of Manitoba

μ -CT – Micro-Computed Tomography

1 Introduction

1.1 Climate Change and its Impact on Sea Ice

1.1.1 Climate Change

Climate change is defined as a change in the normal climate which can last over generations. Annual occurrences of extremely dry or wet conditions are not necessarily considered climate change but may be variations in climate if they are within the expected statistical deviations of a normal climate. Global climate change is defined as a change in climate over the entire planet, typically in one direction. The Little Ice Age during 1500 to 1850 A.D. is an example of global climate change. This event cooled the whole planet, allowing sea ice growth in both the northern and southern hemispheres. Anthropogenic climate change is defined as the change in climate arising from human activities in addition to the natural fluctuations and long-term evolution of the atmosphere arising from normal climate change. The effects of Anthropogenic climate change to alter the global climate were first noted during the 19th-century industrialization. Through extensive agricultural development and coal-burning, stored carbon was released from the rocks and soil that originally contained this element for thousands of years. The released elemental carbon then formed atmospheric carbon dioxide, thus altering the atmosphere's composition (MacDonald, 1988).

The greenhouse effect arises from the occurrence of carbon dioxide and other greenhouse gases (e.g., methane, tropospheric ozone, freon, chlorofluorocarbons, nitrogen

oxides) in the earth's atmosphere, which act to trap heat near earth's surface. The majority of the radiation emitted by the high-temperature sun is in the visible-wavelength region, which is weakly absorbed by earth's atmospheric gases. Conversely, the cooler earth emits radiation within the infrared regime of the electromagnetic spectrum. These longer infrared wavelengths are highly absorbed by greenhouse gases such as carbon dioxide, which warms the surface by downward radiation of infrared energy. Increasing the concentration of such greenhouse gases will have an increased warming effect in the lowest part of the atmosphere. Unfortunately, carbon dioxide levels have grown exponentially, increasing by ~25% since 1850. This exponential growth in carbon dioxide correlates well with carbon releases from fossil fuel combustion and land use (e.g., deforestation). Overall, carbon dioxide has functioned as a positive feedback mechanism for global warming (MacDonald, 1988; Schneider, 1989)

The rate of global warming observed since the industrial revolution is unparalleled. The world is currently 1.1 °C warmer compared to pre-industrial levels and is headed towards +1.5 °C (Fritz and Ramirez, 2021; IPCC, 2021). An increase in the global average surface temperature of 1.1 °C may not seem substantial. However, the Ice Age extreme 18,000 years ago had a global temperature that was only 5 °C colder compared to today. Therefore, a warming of 1.1 °C can have a substantial impact on the world (Schneider, 1989). For instance, global warming has caused greater climate variability, thereby increasing the frequency of extreme weather events such as floods, droughts, wildfires, hurricanes, and tornadoes (MacDonald, 1988; Schneider, 1989). Global warming does not discriminate and affects every country. However, northern countries may experience a faster rate of change

compared to the tropics (Schneider, 1989). In particular, the Arctic has experienced an amplified warming at twice the global average over the last 50 years (Pithan and Mauritsen, 2014; Brown et al., 2017) and is currently warming at a rate of 3X the global average (AMAP, 2021). Notably, the disappearance of sea ice has been considered a vital indicator of climate change in the Arctic (Walsh et al., 2005).

1.1.2 Background: Sea Ice

Sea ice is a heterogeneous mixture comprising a solid pure ice background with liquid brine inclusions and air pockets. As sea ice has a lower density than seawater, it thus floats. A sponge on seawater would be a simple, yet appropriate, analogy to describe sea ice under warm conditions ($\geq -5^{\circ}\text{C}$), allowing for the uptake and movement of fluids through interconnected brine veins. However, according to the “rules of fives” (Golden et al., 2007), when the ice temperature is $< -5^{\circ}\text{C}$, the bulk salinity is < 5 , and the brine volume (porosity) is $< 5\%$, sea ice may not be permeable disallowing fluid movement through its disconnected brine veins. The formation of sea ice types is described below (and is provided with additional detail in Section 7.3 of the Appendix).

When the ocean surface reaches its salinity-specific freezing point, loose crystals known as frazil ice form due to a slight supercooling of the water. Depending on the temperature, wind speed, and wave effects, the agitation of frazil crystals may start to subside and fuse to create a thin ice cover known as nilas. Additional thickening of ice will then occur through the freezing of the seawater below, creating what is called congelation growth or columnar ice (Eicken, 2003; Thomas and Dieckmann, 2010). On the other hand, under turbulent conditions of the ocean surface, frazil crystals will agglomerate into small clumps

as the nilas sheet formation becomes inhibited by ocean swells. As these little clumps of frazil continue freezing, they are battered by waves and connect with other clusters forming small, rounded pans known as ‘pancake ice’. As the wave energy dampens, the pancakes will begin to amalgamate and form a consolidated sheet. Further thickening will then ensue via congelation growth from the underside of the ice (Thomas and Dieckmann, 2010).

As sea ice grows, the brine layers pinch off into pockets of dense brine and form a series of vertical channels that allow the brine to be expelled into the seawater during freezing (Thomas and Dieckmann, 2010). The brine content, and the salts therein, is initially higher near the top of the sea ice and are driven downward by their density, forming the characteristic ‘c-curve’ salinity profile of new sea ice types (Backstrom and Eicken, 2006). Throughout a winter season, a continuously formed ice sheet may grow to be 1 to 2 m thick by the span of a year, termed first-year (FY) ice. FY ice that survives the summer melt then becomes what is known as multiyear (MY) ice, which is generally thicker. MY ice, unlike FY ice, is not very saline.

1.1.3 Reduction of Sea Ice Extent and Thickness

There has been an apparent reduction of sea-ice thickness and extent over the past several decades owing to the effects of global warming. Arctic sea ice has become younger due to thinning of MY ice and the increasing dominance of FY ice. Sea ice with an age older than three years currently comprises a slight portion of the Arctic sea ice cover and can only be found close to the coasts of Arctic Canada and Greenland (Barber et al., 2017). The albedo of FY ice is lower than MY ice and can accelerate melting through positive feedback. This positive feedback is most pronounced during early and late summer (Barber et al., 2017).

Throughout the Arctic, trends of prolonged periods of open water have also been observed, owing to an earlier ice melt and a later ice formation. More open water has been observed beyond the expected fall freeze, with the average melt season extending by five days/decade. Trends of decreasing snow cover have also been observed in the Arctic. In particular, thinning of Spring snow cover has been observed in the western Arctic, with Chukchi and Beaufort seas experiencing the most significant thinning (Barber et al., 2017). Both a reduction of snow and ice cover contribute to a lowered albedo, thus reducing the amount of solar radiation reflected back into space (MacDonald, 1988). This feedback causes an intensified warming of the ocean, hastening the rate of ice loss. For instance, passive microwave imagery measurements between the period of 1972 to 2002 indicate a $0.30 \pm 0.03 \times 10^6 \text{ km}^2/10 \text{ yr}$ decrease in Arctic sea-ice extent. Moreover, between 1979 and 2002, a $0.36 \pm 0.05 \times 10^6 \text{ km}^2/10 \text{ yr}$ decrease is observed indicating an accelerated loss of sea-ice extent by 20% (Walsh et al., 2005; Cavalieri et al., 2003). More recently, Ivanova et al. (2015) reported a $-56,000 \text{ km}^2/\text{yr}$ decrease in the Arctic sea-ice extent between 1979 and 2012. When compared to Cavalieri and Parkinson (2012), who for the period of 1979-2010 reported a $-49,600 \text{ km}^2/\text{yr}$ decrease, it indicates a 12% acceleration in the reduction of sea-ice extent (Barber et al., 2017). According to NSIDC (<http://nsidc.org/arcticseaicenews/>), the cumulative August ice loss in the Arctic since 1979 is $3.15 \times 10^6 \text{ km}^2$, which is equal to approximately double the size of the state of Alaska (NSIDC, 2021).

1.2 Marine Transportation and the Potential for Oil and Fuel Pollution

With the continued effects of global warming, declining sea ice conditions have contributed to increased marine transportation activity in Arctic waters (Pizzolato, 2014;

Dawson et al., 2018; Andrews et al., 2017). Significant decreases in MYI and FYI have resulted in a lengthened shipping season. The loss of MYI has especially been beneficial for shipping activities, as older ice is most hazardous for vessel traffic (Pizzolato, 2014). Oil exploration, extraction, and transport activities in the Arctic have become of particular interest due to greater feasibility and increasing demand for oil and gas worldwide (AMAP, 2010). The Arctic is known to contain some of the largest untapped natural resource reserves globally, which are becoming increasingly available for exploitation (Dawson et al., 2018; AMAP, 2010). However, with increased shipping activity and resource development in the Arctic, there exists a higher potential for oil spillage in the marine environment. In addition to natural oil seeps, oil discharges at sea may arise from shipping accidents, offshore oil production, pipeline ruptures, and chronic releases from oil tankers and other vessels. While most oil spills are small in nature, pipeline and tanker accidents provide the means for a larger oil spill (AMAP, 2010). The occurrence of a large oil spill would have major consequences on the Arctic marine environment and its local inhabitants.

1.3 Petroleum Oil and its Threat to the Arctic and its Inhabitants

Petroleum oils are complex mixtures containing 1000s of compounds consisting of both hydrocarbons and nonhydrocarbons (Stout and Wang, 2016; Wang et al., 2016; AMAP, 2010). Hydrocarbons (HCs) are compounds that exclusively contain the elements of hydrogen and carbon. While the chemical composition of an oil comprises mostly HCs, the elements of nitrogen, sulphur, and oxygen (NSOs) may also be present in the form of heterocyclic compounds. Inorganic metals such as uranium, copper, calcium, sodium, aluminum, iron, nickel, and vanadium may also exist in a petroleum mixture. Major

compound groups of an oil include alkanes, cycloalkanes, aromatics and polycyclic aromatic hydrocarbons (PAHs), as well as heterocyclic compounds (AMAP, 2010). Example structures of these compound groups are provided in Table 1.1. These compound groups can be further categorized into four major fractions (SARA): Saturates (encompassing alkanes and cycloalkanes), Aromatics (including PAHs), Resins, and Asphaltenes (both of which encompass NSOs) (Lee et al., 2015). The classification of oil type is inherently linked to the concentration of these compound groups. Generally speaking, paraffinic oils contain high concentrations of normal and iso-alkanes, moderate concentrations of cycloalkanes, and low concentrations of aromatic HCs and NSOs. Naphthenic oils contain high concentrations of cycloalkanes, low concentrations of normal and iso-alkanes, and low concentrations of aromatic HCs and NSOs. Aromatic oils contain high concentrations of aromatic HCs and NSOs, moderate concentrations of normal and iso-alkanes, and low concentrations of cycloalkanes. Heavy oils contain very high concentrations of aromatic HCs and NSOs, low concentrations of normal and iso-alkanes, and low concentrations of cycloalkanes. Finally, mixed oils contain moderate amounts of each compound group (Stout and Wang, 2016). Similar to oil type, the oil's physical properties (e.g., density) are related to the oil composition. Heavier oils have higher densities, whereas lighter oils (e.g., paraffinic) encompass lower densities (Stout and Wang, 2016). For instance, a light crude oil has a density less than 870 kg/m^3 , medium and heavy crude oils have densities between 870 to 920 and 920 to 1000 kg/m^3 , respectively, and an extra-heavy crude oil has a density higher than 1000 kg/m^3 (Viscopedia). The relative toxicity of oil types is also composition dependent (Anderson, 1974). Oils which contain higher concentrations of aromatic HCs (especially

PAHs) and NSOs are of particular concern (Anderson, 1974; Fritt-Rasmussen et al., 2015). Aromatic HCs and NSOs are more water soluble than alkanes of similar molecular weight and are expected to exist in higher concentrations in water soluble fractions relative to the parent oil (Anderson, 1974). In particular, PAHs are amongst the most persistent organic pollutants in Arctic areas (AMAP, 2004) due to their relatively high bioaccumulation and moderate degradability (Fritt-Rasmussen et al., 2015; Neff, 1979; Varanasi, 1989; Southworth et al., 1978). Larger PAHs have the potential for greater bioaccumulation (Fritt-Rasmussen et al., 2015; Arnot, 2006) and may also be carcinogenic and mutagenic (e.g., benzo[a]pyrene) (Safety Data Sheet). In the case of an Arctic oil spill, PAHs are likely to find their way into the water column and sediment where they are available for uptake by aquatic organisms either through direct ingestion or diet. These PAHs are likely to bioaccumulate not only in biota, but also humans. Arctic indigenous communities rely on traditional food (e.g., seal, whale, caribou, and fish) for their livelihood as well as their economic, psychological, social, and cultural well-being (AMAP, 2009). Dietary exposure to persistent pollutants is, therefore, of concern to northern indigenous populations owing to their consumption of tissue from marine top predators (AMAP, 2009). It is important to note that while PAHs can accumulate in all living organisms (Meador et al., 1995; Mlyczyńska et al., 2023), bioaccumulation/biomagnification through higher trophic levels in the food chain is generally minimal as larger organisms can metabolize these compounds (Liu et al., 2023).

Table 1.1 Examples of Chemical Groups contained within Petroleum Crude Oils


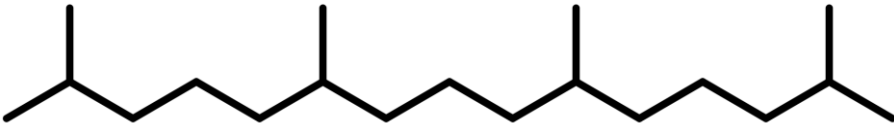
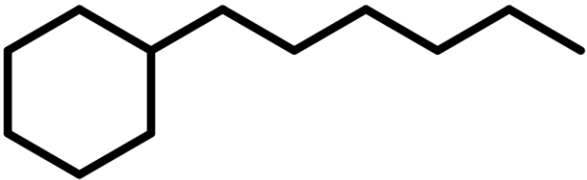
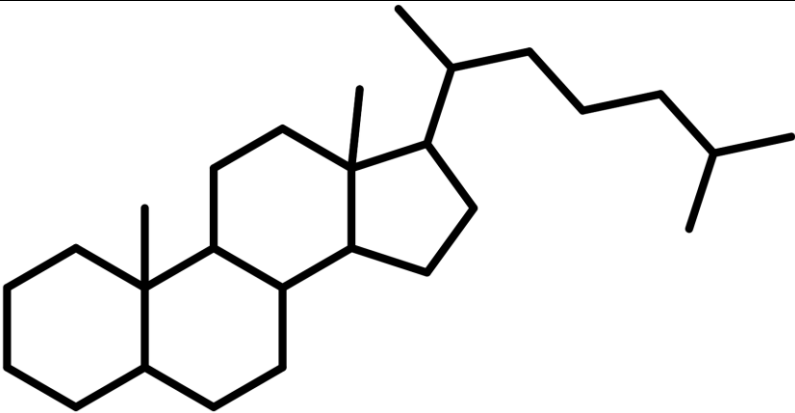
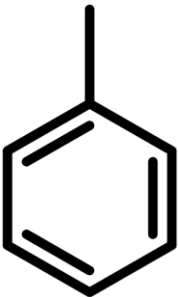
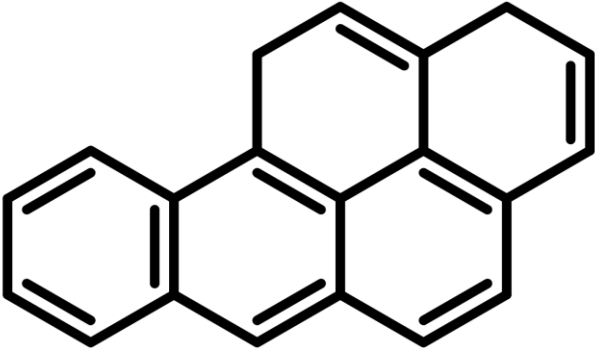
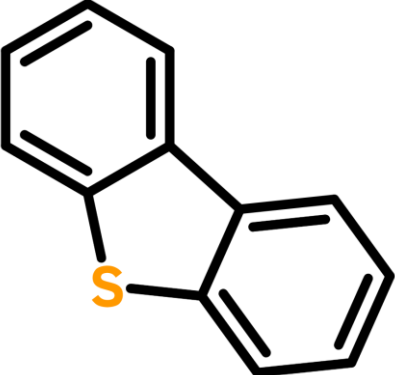
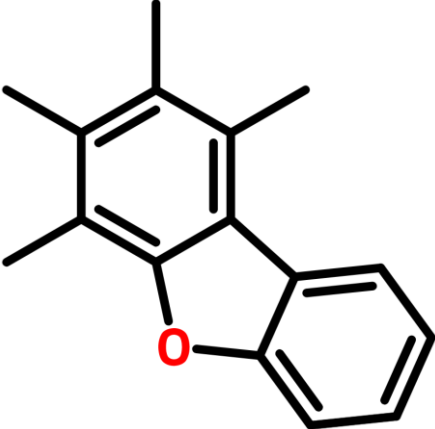
Alkanes	
 (n-tetradecane)	Normal Alkane – Straight alkane chain without any hydrocarbon branches
 Acyclic Isoprenoid (pristane)	Branched Alkane – Alkane with one or more branched hydrocarbon alkyl group
Cycloalkanes	
 (Hexylcyclohexane)	Alkylated Monocyclic Alkane – 1 cyclic alkane ring with one or more branched hydrocarbon alkyl group
 Steranes (Cholestane)	Alkylated Polycyclic Alkane – 2 or more cyclic alkane rings with one or more branched hydrocarbon alkyl group
Aromatics	
 (Toluene)	Alkylated Monocyclic Aromatic – 1 aromatic hydrocarbon ring with one or more branched hydrocarbon alkyl group

Table 1.1 Continued	
 <p data-bbox="597 657 799 688">(benzo[a]pyrene)</p>	<p data-bbox="1182 306 1382 541">Polycyclic Aromatic Hydrocarbon – 2 or more aromatic hydrocarbon rings</p>
Heterocyclics	
 <p data-bbox="581 1113 812 1144">(Dibenzothiophene)</p>	<p data-bbox="1182 730 1333 856">Heterocyclic compound containing sulfur</p>
 <p data-bbox="500 1581 893 1610">(1,2,3,4-tetramethyldibenzofuran)</p>	<p data-bbox="1182 1150 1328 1318">Alkylated heterocyclic compound containing oxygen</p>

1.4 Oil Spill Preparedness and Response in the Arctic

In order to combat the increasing potential of a large oil spill in Arctic waters, efforts to develop oil spill preparedness and response technologies suitable for Arctic conditions have been an ongoing endeavour by each Arctic country (e.g., AMAP, 2010; Reports – Arctic Response Technology). Each Arctic country's (i.e., United States (Alaska), Canada, Greenland, Iceland, Faroe Islands, Norway, Russian Federation) preparedness and response programs vary widely as they are based on governmental policy and regulations adopted under national legislation. However, each respective response program takes steps to track, control, and clean-up spilled oil in the case of an accidental release. Small spills require preparedness at the local level, whereas larger spills from a pipeline or tanker vessel entail preparedness at the state or national level (AMAP, 2010).

The Arctic encompasses a plethora of challenges concerning oil response and contingency. The presence of ice (drifting and static), heavy winds, low temperatures, remoteness, poor infrastructure, and darkness during winter months impose severe limitations to response efforts that would otherwise be applicable to an open water setting (Wilkinson et al., 2017; AMAP, 2010). These challenges must be fully recognized in order to determine appropriate strategies for responding to various oil spill scenarios. Varying ice conditions and seasons (e.g., freeze-up, winter, and break-up) result in a vast number of differing ice environments and oil-in-ice situations (Wang et al., 2017; Wilkinson et al., 2017). To better respond to the vast complexities of an oil-in-ice environment, reliance on a combination of viable responses may prove more efficient and effective rather than over-reliance on a single oil spill response mechanism (AMAP, 2010). Currently, a breadth of

knowledge exists concerning oil spill behavior and fate, oil spill detection and monitoring, and oil spill mitigation and clean-up methods concerning Arctic waters.

1.4.1 Oil Behavior and Fate

Understanding the behavior and fate of oil is important when deliberating appropriate tactics to respond to an oil spill. Knowledge of not only the bulk oil movement, but also the oil's weathering processes, is necessary for both the development of oil spill response modeling and the improvement of oil spill preparedness in Arctic waters (AMAP, 2010; Lee et al., 2015). The following outlines some of the existing knowledge concerning the behavior and fate of oil following an Arctic oil spill.

1.4.1.1 Oil Spill Behavior in a Sea Ice Environment

A basic summary of oil behavior in an Arctic environment is provided below. More information on spill behavior in a sea ice environment can be found within Section 7.4 of the Appendix.

The variety of oil spill scenarios in the Arctic Ocean are numerous and will depend on the season and type of oil spill event (e.g., shipping accident, pipeline rupture, oil well blowout), amongst other factors. During the summer, spilled oil will typically adhere to the surface of ice floes. Depending on the strength of winds and currents, the floes may come together, squeezing the oil between them, or drift apart, allowing the oil to spread out over a larger distance (Dickins and Buist, 1999; Venkatesh et al., 1990). If a spill were to be released from below ice cover during the winter, the oil will disperse into tiny droplets and rise through the water column, given that the density of the oil is lower than the surrounding seawater (Wilkinson et al., 2013; 2017). Depending on the type of ice and its temperature, a

variety of scenarios may unfold once the oil reaches the underside of the ice. 1) If the surface of the ice is unconsolidated (i.e., frazil or pancake ice without further congelation), the oil will be able to rapidly migrate through the ice layer followed by a lateral spreading along the ice-air interface (Wilkinson et al., 2014). 2) If the ice surface is fully consolidated (nilas) and cold (i.e., $<-5^{\circ}\text{C}$), the oil will coalesce to form an oil slick at the ice-water interface (Wilkinson et al., 2014; Golden et al., 1998). As the oil layer thickens, lateral spreading of the slick will occur and will tend to pool at regions of thinner ice (Wilkinson et al., 2013; 2017). 3) Pooled oil under columnar ice will have the potential for uptake and entrainment within the porous bottom of the sea ice (Petrich et al., 2013; Oggier et al., 2020). If the ice is warm (i.e., $\geq -5^{\circ}\text{C}$) (e.g., spring-summer transition), the oil will subsequently migrate towards the ice surface. If the ice is cold (e.g., winter), the oil may remain at the sea ice subsurface (Oggier et al., 2020; Golden et al., 2007). During the ice growth season, the pooled oil can become encapsulated, restricting any further horizontal spreading. The ability of growing sea ice to encapsulate stationary oil will depend on the insulating properties of the oil and the amount of heat from the ocean/atmosphere to the ice-oil-ocean interface. Once the oil layer has become encapsulated, a new secondary frazil-columnar ice growth will ensue below the ice-oil sandwich (Martin, 1979). Finally, it is worth pointing out that MY ice is much thicker than FY ice and contains little to no brine channels. Upward oil migration through MY ice is, therefore, much slower than FY ice and may be limited to cracks within the ice (AMAP, 2010).

1.4.1.2 Oil Weathering and Transformation Processes

In addition to the bulk movement of oil within a sea ice environment, the chemical composition of the oil may be altered through weathering and transformation processes. As the oil's chemical composition changes, so too do its physical properties (e.g., density and viscosity) (Desmond et al., 2019a, 2019b; Fingas, 2011). Thus, the oil's chemical composition and physical behavior are interconnected and dynamic (Stout and Wang, 2016). Evaporation, photooxidation, dissolution, and biodegradation are some of the processes relevant to an Arctic oil spill. The following will provide a brief review of these processes in Arctic waters. Additional information on sea ice and oil weathering is provided in Section 7.5 of the Appendix.

1.4.1.2.1 Evaporation

Evaporation potential is primarily governed by 1) the amount of volatile compounds contained in the oil and 2) the spill-specific conditions such as ambient temperature and the location of the spilled oil (i.e., surfaced oil versus oil that is encapsulated or below sea ice) (AMAP, 2010; Stout and Wang, 2016). Paraffinic oils contain a high degree of compounds encompassing low boiling points and high vapor pressures, and therefore possess a greater evaporation potential than aromatic oils (AMAP, 2010; Stout and Wang, 2016; Lee et al., 2015). There is reduced potential for evaporation in an Arctic setting compared to open waters (Faksness et al., 2011). Depending on the ice conditions, oil spreading may be restricted, and evaporative loss reduced due to increased oil thickness. Furthermore, at cold ambient temperatures, vapor pressures will be lower, resulting in reduced evaporation rates.

For instance, oil constituent vapor pressures at 0 °C are approximately 10x lower than at 25 °C (AMAP, 2010).

1.4.1.2.2 Photooxidation

Spilled oil exposed to the presence of light and oxygen leads to a variety of oxygen-containing compounds, including carbonyls, ketones, aldehydes, alcohols, peroxides, sulfoxides, epoxides, and fatty acids (AMAP, 2010; Stout and Wang, 2016; Albaig S. et al., 2016; Larson et al., 1977; Nicodem et al., 1997). The photooxidation rate is related to the intensity of ultraviolet radiation from sunlight and the location of the spilled oil (Stout and Wang, 2016). For instance, if oil were to be encapsulated in sea ice, photooxidation would be more prominent closer to the surface where sunlight is less attenuated. Photooxidation is known to preferentially affect alkyl-substituted PAHs, in which higher branched PAHs have greater susceptibility (Bobinger and Andersson, 2009; Garrett et al., 1998; Prince et al., 2003). Therefore, an aromatic-based oil would be more prone to photooxidation than a paraffinic oil.

Although photodegradation does not significantly impact the mass balance of a spilled oil, photooxidation can affect other weathering/transformation processes such as dissolution and biodegradation. The creation of oxidized transformation products results in compounds which are more polar and readily soluble, hastening dissolution (Lee et al., 2015). These polar products can also be more biologically toxic than the original photooxidized compound (Larson et al., 1977; Nicodem et al., 1997; Maki et al., 2001). While photooxidation favors the degradation of alkyl substituted aromatic compounds, microorganisms preferentially degrade unsubstituted aromatics and alkanes (Bacosa et al.,

2015; Garrett et al., 1998). However, the success of microbial degradation relies on the presence of molecular oxygen and reactive oxygen species, which inadvertently is facilitated by the effects of photooxidation (Maki et al., 2001).

1.4.1.2.3 Dissolution

Dissolution of water-soluble oil components is of particular interest as this process increases bioavailability and potential uptake of dissolved hydrocarbons by marine biota (AMAP, 2010; Stout and Wang, 2016). The rate and extent of dissolution depends primarily on the water-soluble fraction of oil and its surface area relative to seawater or brine (AMAP, 2010). Low molecular weight compounds are both volatile and water-soluble and are prone to both evaporation and dissolution processes. Although both processes compete, dissolution is less significant than evaporation (Stout and Wang, 2016; Lee et al., 2015). Aromatic HCs and NSOs are especially water-soluble (Nicodem et al., 1997). Consequently, an aromatic-based oil would be more susceptible to dissolution than a paraffinic oil. In a sea ice environment, dissolution may either be hastened or reduced depending on the spill scenario. The cold temperature inherent to an Arctic setting will act to reduce the rate of dissolution. For instance, oil constituent solubilities at 0 °C are approximately 4x lower than at 25 °C (AMAP, 2010). However, the presence of ice cover may facilitate increased dissolution through reduced evaporation (Faksness et al., 2011) and greater exposure to brine (Faksness and Brandvik, 2008), where water-soluble components can be flushed down into the water column (Payne et al., 1991; AMAP, 2010). Finally, in the case of spilled oil below sea ice or on open water between ice floes, dissolution efficiency will increase as the oil spreads and becomes more fully exposed to seawater (AMAP, 2010).

1.4.1.2.4 Biodegradation

Biodegradation of petroleum HCs is a vital process that has the potential to eliminate considerable fractions of spilled oil (AMAP, 2010). As such, this process is regarded as a potential remediation method for oil-infested waters (AMAP, 2010). The mass-loss rate caused by biodegradation is slower than other weathering processes such as evaporation and dissolution (Stout and Wang, 2016). Biodegradation is also slower in the cold Arctic compared to temperate regions (AMAP, 2010; Vergeynst et al., 2018). There are many types of bacteria capable of degrading petroleum hydrocarbons (AMAP, 2010; Prince et al., 2010). However, the efficiency of microbial degradation is likely to be improved by the presence of indigenous bacteria acclimated to the presence of oil (e.g., by natural oil seeps) (Stout and Wang, 2016). Biodegradation is known to preferentially degrade n-alkanes, followed by branched alkanes, olefins, monoaromatics, PAHs, and lastly, highly condensed cycloalkanes, resins, and asphaltenes (Stout and Wang, 2016; Prince and Walters, 2016). Therefore, a paraffinic oil would be most susceptible to biodegradation, whereas a heavy oil containing little, or no n-alkanes would undergo minimal degradation. Biodegraded compounds are typically converted into oxidized products (Vergeynst et al., 2019; Prince and Walters, 2016; AMAP, 2010), which can then be dissolved, further degraded, or retained within the oil (Stout and Wang, 2016). In the Arctic, biodegradation is more likely to occur within seawater, as it is known to possess a larger active microbial population than sea ice (Vergeynst et al., 2019).

1.4.2 Oil Spill Detection and Monitoring

Given the increasing potential for oil spills in the Arctic, oil spill detection techniques suitable for usage in the presence of various sea ice conditions are required. Detecting a probable spill would allow for a more efficient mitigation response. Similar to oil spill response measures in open water conditions, the goal of oil spill detection in ice-covered waters is to minimize the ecological and socioeconomic damage. However, traditional remote sensing methods suitable for the open ocean are challenged by the complexity of sea ice and are therefore less effective and practical for usage (Wang and Stout, 2007; AMAP, 2010). Over the past decades, research into testing and developing remote sensing capabilities suitable for ice-covered waters have made significant advances (e.g., Pegau et al. 2017; Wang and Stout, 2007; Fingas and Brown, 2000). Several above-ice sensors (i.e., microwave scatterometers, ground penetrating radars, visible and thermal infrared cameras, and laser fluorescence polarization) and below-ice sensors (i.e., spectral radiance and irradiance, laser fluorescence polarization, optical cameras, broadband acoustics, narrowband acoustics, and multibeam acoustics) have shown potential for remote detection. However, the presence and extent of ice and snow cover, the location of the spilled oil (i.e., above, encapsulated, below), and other environmental conditions (e.g., dark, cloudy, turbulent) have proven to limit the practicability and success of the various oil spill detection and monitoring techniques available. For instance, certain airborne techniques may suffer in their ability to ‘see’ through or penetrate the sea ice and potential snow cover to infer the presence of oil. Furthermore, remote sensing methods applied on the ice surface may be impractical for deployment on young or deformed ice.

1.4.2.1 Performance Limitations of Remote Sensors

There have been several papers which have assessed the suitability of various sensors for oil spill detection under Arctic settings (e.g., Praks et al., 2004; Wang and Stout, 2007; Fingas and Brown, 2000; Wilkinson et al., 2017; Firoozy et al., 2018; Pegau et al. 2017). Through these works, it has been demonstrated that each potential sensor suitable for oil-ice detection has their own disadvantages and advantages which dictate under which arctic oil spill condition they will be effective (i.e., under snow cover, above ice, encapsulated by ice, under ice, and season). For instance, under water acoustic sensors have demonstrated to be effective within 6 cm of ice encapsulation from below, although detection would be most prominent for oil situated directly under ice. Similarly, optical sensors and fluorescence polarization (from below) have proven to be capable of detecting oil under or within 6 cm of encapsulation. However, the presence of turbidity would impact the effectiveness of these sensors. Unlike optical and thermal sensors, radar is capable of detection under dark conditions and is suitable for most Arctic ambient weather. Full polarimetric synthetic aperture radar (SAR) has shown potential for detecting oil under snow, on ice, and within the upper ice layer (depending on the ice's salinity) with the use of near-surface scatterometer instruments (e.g., Brekke et al. 2014; Firoozy et al., 2018), in which their usage has demonstrated the possibility of space-borne SAR response. (Additional information on radar remote sensing is provided in Section 7.6 of the Appendix.) In a real-world oil spill scenario in the Arctic, a combination of sensors should be utilized to balance their disadvantages and optimize the success and accuracy of detection.

1.4.2.2 *Logistics of a Real-World Oil Spill Scenario*

Logistically speaking, available optical spectrometers and microwave radar satellites (e.g., Landsat ETM and RADARSAT) should be used to assess the actuality of a random oil spill in the Arctic with high resolution (Wilkinson et al., 2017; Praks et al., 2004). In the case of a probable detection, airborne vehicles such as an aircraft (i.e., unmanned and manned), carrying a suite of suitable airborne sensors (Pegau et al. 2017) or a helicopter, carrying an airborne ground penetrating radar (GPR), could be used on a closer scale. Similarly, a marine vessel carrying a near-surface scatterometer and remote system for unmanned underwater vehicles capable of carrying a suite of suitable above-looking waterborne sensors (e.g., acoustics) (Pegau et al. 2017) could also be used on a closer scale depending on feasibility and conditions. If capable of going on-site, GPR could be used on-ice. Lastly, atypical measures using sniffer dogs on ice (winter condition) or buoys carrying oil-detection sensors (summer) may also show promise for detection (Wilkinson et al., 2017).

1.4.3 Mitigation Methods

Oil spill clean-up methods used in the Arctic consist of mechanical containment and recovery, dispersants, in situ burning, and bioremediation. Mechanical containment and recovery of oil from the surface is the primary method used in all Arctic countries. The use of pre-approved dispersants is a secondary method used in all Arctic countries except Greenland. In situ burning is a secondary method used in the United States and Canada and is a tertiary method (used occasionally or in specific circumstances) for the Russian Federation. Bioremediation is a tertiary method used only in the United States and Canada (AMAP, 2010). Each response technology has inherent limitations and capabilities that make

it deemed either suitable or unreliable depending on the specific oil spill scenario. The behavior of spilled oil is controlled by the presence and concentration of ice (e.g., no ice, broken ice, and solid ice). Therefore, each season (i.e., summer open water, fall freeze-up, mid-winter, spring thaw) will dictate the movement of oil and the feasibility of using a particular response method (Wilkinson et al., 2017). The following will provide a brief review of the viable Arctic response methods and their applicability.

1.4.3.1 Mechanical Containment and Recovery

The objectives of mechanical containment and recovery are to limit the spread of spilled oil using booms and recover the contained oil onto vessels for disposal (e.g., through skimmers). This method relies on the oil being on the sea surface. Therefore, this recovery method does not apply to total ice coverage or when oil is encapsulated within the ice. The presence of partial ice cover (greater than 60%) can function as naturally occurring booms, helping to minimize the spread of oil (Dickins and Buist, 1999). When ice concentrations are lower than 10%, floating ice pieces can hinder placed booms, tearing floatation chambers or breaking the cables within (Wilkinson et al., 2017). Other challenges include the icing of equipment, increased oil viscosity, reduced flow of oil to the skimmer, and separation of oil from water and ice (AMAP, 2010; SINTEF, 2006). The many apparent mechanical containment and recovery challenges stem from this method originally being developed for open-water conditions. Hence, there is limited potential for success in ice-infested waters, despite being regarded as the primary oil spill clean-up method used in the Arctic (AMAP, 2010).

1.4.3.2 Dispersants

The main objective of using dispersants is to facilitate the transport of spilled oil from the sea surface into the water column. Dispersants on surfaced oil lower the interfacial tension between the oil and seawater, thus allowing turbulence of waves to transform the majority of the oil into tiny droplets capable of rapid dilution into the water column (Wilkinson et al., 2017). Incorporating small oil droplets into the water column stimulates the natural process of microbial degradation, potentially leading to the substantial reduction of oil (Wilkinson et al., 2017; Prince et al., 2013; Lee et al., 2015). However, concerns have been voiced regarding the increased exposure and availability of dispersed oil to marine biota and the potential adverse effects that could ensue (Wilkinson et al., 2017).

Dispersants in the Arctic are postulated to have limited success due to the cold temperatures and ice. The presence of ice dampens the mixing energy required to disperse the oil, and the increased viscosity of the oil at low temperatures may also impede the dispersion process (AMAP, 2010). Therefore, the use of dispersants is expected to work most optimally in open water conditions and amongst broken ice. Brandvik et al. (2006) reported dispersants as an appropriate oil spill response method for Arctic waters of up to 50% ice cover (Wilkinson et al., 2017).

1.4.3.3 In Situ Burning

In situ burning is one of the response techniques with the greatest potential for Arctic oil spill clean-up (AMAP, 2010). In situ burning, like that of any fire, requires oxygen, an ignition source, and fuel. In the context of an oil spill, the fuel source is provided by the vaporization of oil. A particular oil's ignitability and potential to perform a steady-state burn

will depend on the prior composition of oil (i.e., lighter and more volatile or heavier), as well as its slick thickness and specific oil spill scenario. An oil thickness of ~1 mm has been found to be sufficient to ignite a fresh crude oil, whereas an aged, unemulsified crude oil or diesel fuel requires a minimum thickness between 2-5 cm. The minimum ignitable thickness of a residual oil such as Bunker C requires a thickness of ~10 mm (Wilkinson et al., 2017; Potter and Buist, 2008). The effectiveness of in situ burning in Arctic waters is primarily governed by the extent of ice coverage. Ice coverage exceeding 70% allows for burning to be accomplished without the use of any mechanical containment systems, as the ice serves as a natural barrier to confine the oil's movement on the water surface. In contrast, ice cover below 30% functions similar to burning in open water, requiring the use of a fire-resistant boom. Ice cover between 30 and 70% is considered to be the most challenging for in situ burning as ice concentrations are too low to function as a natural containment system, but is also too high for the effective use of mechanical containment (Potter and Buist, 2008; Brandvik et al. 2006; Evers et al., 2006). In situ burning is considered to be most optimal for oil spills in broken ice, which are the most hazardous for clean-up personnel. Burning in pack ice during break-up is likely more feasible than freeze-up (given the same ice concentration). The presence of slush ice during fall freeze-up can greatly hinder the containment and thickening of slicks for burning (Wilkinson et al., 2017; Potter and Buist, 2008). In situ burning is also considered optimal for spills on ice and snow-covered surfaces, in which 70% snow by weight of oiled snow can successfully burn. In situ burning of oil released through brine channels into melt ponds during spring thaw is also deemed achievable (Wilkinson et al., 2017).

With any human intervention technique such as burning, concerns will follow regarding the resultant impact on the Arctic environment and ecosystem. Studies have shown that oil-burning leads to an increased concentration of total and high molecular weight PAHs in seawater (e.g., Gulec and Holdway, 1999). However, the resulting toxicity has been deemed less significant compared to dispersed oil from the use of chemical dispersants (Fritt-Rasmussen et al., 2015; Gulec and Holdway, 1999). Notably, the precipitated smoke resulting from burning has shown more severe effects than the burn residues (Fritt-Rasmussen et al., 2015; Sheppard et al., 1983).

1.4.3.4 Bioremediation

One approach to mitigate an Arctic oil spill is through biodegradation (as outlined in Section 1.4.1.2.4). Bioremediation has seen very limited application in the Arctic and is currently considered a last response option by the United States and Canada (AMAP, 2010). This approach is, however, highly sought after as it is considered more environmentally friendly compared to burning which generates the adverse effect of smoke (Sheppard et al., 1983). Bioremediation is also seen to be a favourable alternative to other mitigation clean-up methods which require the presence of on-site personnel (Fritt-Rasmussen et al., 2015). Due to the inherent remoteness of the Arctic, the prospect of degrading oil by naturally occurring microbial communities is highly attractive. While bioremediation is a viable response option in more southerly latitudes, the extent and success of its use in an Arctic marine setting requires further study (Gaden, A., 2019). Few studies on the biodegradation potential of oil in a sea ice environment have been conducted (e.g., Vergeynst et al., 2018; Boccadoro et al., 2018). Results indicate that biodegradation is most prominent towards the sea ice base layer

and within brine and seawater. Given that brine and seawater are the media in which microorganisms proliferate, biodegradation of oil within sea ice has not found success owing to a low oil-brine contact. Given the nature of these findings, bioremediation is expected to show the most promise during summer open water conditions, underneath grown sea ice (such as during the winter months), and in the presence of a spring melt pond, when oil can be in direct contact with potential oil-degrading bacteria.

1.5 Proposed Research Goals / Research Aims and Objectives

My research seeks to add to the body of knowledge concerning oil spill behavior, detection, and mitigation in Arctic waters (see Section 1.4) to aid in developing oil spill detection algorithms and behavior models necessary for advancing policy and oil spill mitigation procedures. It is essential to research all aspects of oil behavior, detection, and mitigation due to their connectedness and reliance on one another (e.g., Fig. 1.1). For instance, without understanding the behavior of oil, it would not be possible to formulate proper mitigation procedures nor assess the feasibility of remote sensing technologies given a particular oil spill scenario. Furthermore, the ability to dispatch an appropriate mitigation response depends on the success of firstly detecting an oil spill. In order to achieve my overarching research goal, four projects (which comprise the body of my thesis) were pursued to study certain aspects of oil behavior (i.e., migration tendencies, encapsulation potential, partitioning within sea ice, evaporation, dissolution, photooxidation, biodegradation), detection (i.e., radar), and mitigation (i.e., bioremediation) in sea-ice environments. The fundamentals (including objectives and hypotheses) of each project are

outlined below. An overarching hypothesis for the four projects is that *oil will influence the physical properties of sea ice and will be chemically and physically affected by the sea ice.*

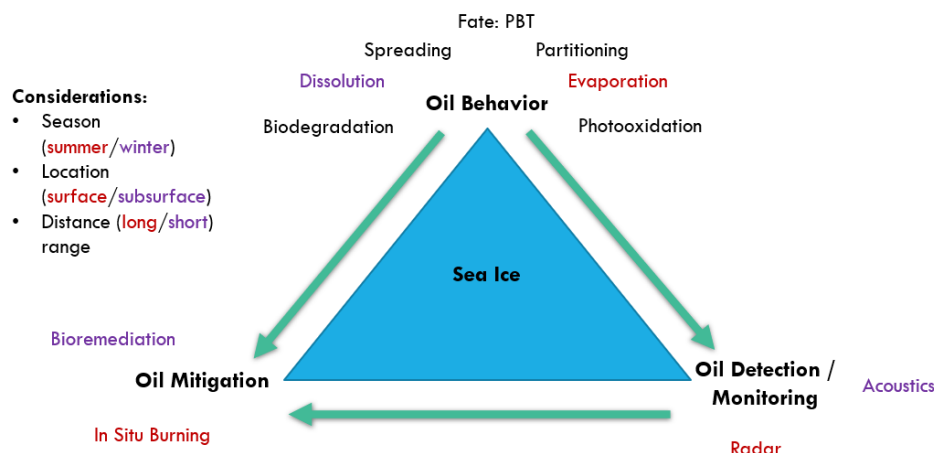


Fig. 1.1 Depiction showcasing the connectivity between the concepts of oil behavior, oil detection and monitoring, and oil mitigation.

1.5.1 Project 1 (Chapter 2): “Effect of dissolution, evaporation, and photooxidation on crude oil chemical composition, dielectric properties and its radar signature in the Arctic environment.”

The objectives of this project were to:

1. Investigate the bulk movement, evaporation, dissolution, photooxidation, and partitioning of crude oil in FY sea ice.
2. Assess how the oil’s physical properties (i.e., dielectrics and thermal conductivity) change with the oil’s movement and weathering.
3. Examine the effect of oil on the dielectrics and radar signature of sea ice.

To accomplish these objectives, an oil-in-ice mesocosm experiment was conducted during the winter of 2017 using an insulated fibreglass above-ground pool with a 3 m

diameter and a 1 m depth. The experiment was conducted at the Sea-ice Environmental Research Facility (SERF), where artificial sea ice was grown from open water. Once the ice grew to a sufficient thickness, crude oil was injected from below the ice and interacted freely with the seawater and ice. After a set time, the ice was thawed, creating an open water scenario with surfaced oil. The ice was then refrozen, and the movement and effects of the oil were again observed. Throughout the experiment, temperature, bulk salinity, and oil volume profiles were measured using a combination of in-situ sensors and physical sampling of the ice. From the procured samples, the oil composition was analyzed using multidimensional gas chromatography-high resolution time of flight mass spectrometry (GCxGC-HR-TOF-MS), Triple Quadrupole GC-MS (QQ-MS), and Attenuated Total Reflection Infrared Spectroscopy (ATR-IR). Resonance perturbation, a cavity perturbation technique, was used to measure the dielectric constant of oil samples. (A description of the analytical instruments and techniques used for oil analysis is provided in Section 7.7 of the Appendix.) Lastly, the dielectrics and thermal conductivity of the sea ice were modeled using the measured geophysical parameters of the ice. The normalized radar cross-section of the ice was subsequently simulated using the modeled sea ice dielectrics. This experiment emulated:

1. An oil release from below warm sea ice (such as what may be observed during the spring-summer transition).
2. Oil surfaced on open water (like summer conditions).
3. The formation of ice from open water with surfaced oil (like fall-freeze up).

This project is essential as there is insufficient knowledge on oil weathering rates and how oil properties change under freezing temperatures and in a sea-ice environment. Much research has investigated the bulk movement of oil in sea ice, but little has provided a comprehensive study on how the oil's composition changes within sea ice. A more comprehensive understanding of how the oil's composition changes within sea ice is, therefore, needed to improve Arctic oil weathering models and plan proper mitigation responses. Finally, a better understanding of the oil's impact on sea ice geophysical parameters relevant to remote sensing is required to better establish potential detection technologies such as radar.

This project aimed to test the following hypotheses:

1. The dissolution of lighter crude oil fractions increases with decreases in oil concentration.
2. Compounds will partition inside brine channels by molecular weight.
3. Oil permittivity is affected by composition and intermolecular interactions.
4. The presence of oil in sea ice will cause a reduction of salinity, thereby reducing the dielectrics and radar signature of sea ice.
5. The effect of oil on salinity will increase with increasing oil concentration.

1.5.2 Project 2 (Chapter 3): “Methods for Predicting Partitioning and Fate of Petroleum Hydrocarbons in a Sea Ice Environment”

The objectives of this project were to:

1. Investigate the movements and interactions of crude oil constituents in a sea-ice environment.
2. Assess the potential for predicting the relative movements of oil constituents within sea ice based on comparisons between estimated molecular properties and experimentally derived chemical compositional data.
3. Provide a theoretical assessment of oil constituents' potential for persistence, bioaccumulation, and toxicity in an Arctic environment.
4. Raise awareness of the use of computational quantum chemistry to describe macroscopic situations such as oil-in-ice, which rely on calculations at sub-zero temperatures.

To accomplish these objectives, computational quantum chemistry was used to simulate the effects of evaporation, dissolution, and compound partitioning within sea ice by calculating physical properties (i.e., vapor pressures, solubilities, octanol-water partition coefficients, molecular volumes, liquid density) at temperatures and salinities relevant to an Arctic environment. The potential of using these calculated physical properties for predicting the relative movements of oil constituents in a sea ice environment was assessed by comparison with experimental compositional data generated as part of the SERF 2017 oil-in-ice mesocosm study (1st project – Chapter 2).

This project brings two rather disparate fields – computational chemistry and environmental chemistry – together in a very unique manner, contributing to the knowledge of how the physical properties of oil constituents influence their movement and fate within a sea ice environment. This project is significant because modeling research that directly

addresses the partitioning of individual compounds in a sea-ice environment is non-existent. The use of quantum chemistry is especially advantageous as it allows for modeling properties at sub-zero temperatures relevant to an Arctic setting.

This project aimed to test the following hypotheses:

1. A difference in physical properties explains oil partitioning in sea ice.
2. Computational chemistry can predict or interpret the relative movements of oil constituents.
3. Lighter molecules have a greater tendency to be controlled by brine advection processes
4. Molecules which are more hydrophobic concentrate in areas of lower salt concentration

1.5.3 Project 3 (Chapter 4): “Photooxidation and biodegradation potential of a light crude oil in first-year sea ice”

The objectives of this project were to:

1. Better understand the fate of oil spilled in the Arctic marine environment.
2. Better understand the potential for natural attenuation of oil in sea ice.
3. Assess changes in crude oil composition and microbial communities over time.

To accomplish these objectives, an oil-in-ice mesocosm experiment was conducted at SERF during the winter of 2018. Unlike the 2017 study, this experiment involved the use of *two* outdoor above-ground pools (7m³ and 12m³). Both pools were filled with artificial seawater mixed with nutrients, while only the larger pool was inoculated with Arctic

indigenous bacteria. Crude oil was released beneath the ice of both pools once the ice was grown sufficiently. Ice cores and water samples were extracted periodically, achieving a spatial and temporal mapping of the oil's evolution. The composition of the oil derived from the extracted cores was assessed using resonance perturbation, ATR-IR, and GC-HR-TOF-MS (see Section 7.7 of the Appendix). Bacterial communities present in both the extracted cores and water samples were measured. Incident and transmitted light throughout the experiment was measured using photodiodes. This experiment emulated an oil spill beneath grown sea ice that was initially cold and impermeable to upward oil migration (such as what would occur during mid-winter). As the experiment progressed, the sea ice environment came to emulate warm sea ice with the occurrence of a melt pond (similar to what would occur during the spring-summer transition).

This project focuses on the potential for photo- and biodegradation of the bulk crude oil content encapsulated in the upper regions of the ice during freezing (e.g., winter) and thawing (spring-summer), with consideration on the fate of transformed products. This research is vital as a greater understanding of oil-ice interactions during freezing and thawing is necessary to provide further insight regarding the possible fate of crude oil in an Arctic marine setting, especially during polarized seasons. Notably, the fate of transformed products is crucial in the assessment of potential adverse effects.

This project aimed to test the following hypotheses:

1. Oil permittivity is affected by compositional changes.
2. Photooxidation will increase the oil permittivity.

3. Dissolution within sea ice will act to decrease the oil permittivity.
4. Surficial oil will remain separate from the brine.
5. Biodegradation extent on surficial oil-in-ice will be minimal, but apparent in water.

1.5.4 Project 4 (Chapter 5): “Investigation into the geometry and distribution of oil inclusions in sea ice using non-destructive X-ray microtomography and its implications for remote sensing and mitigation potential”

The objectives of this project were to:

1. Assess the qualitative and quantitative capabilities of X-ray microtomography for examining oil-contaminated sea ice.
2. Examine the microstructure of the surficial layers of sea ice exposed to oil.
3. Determine the geometry and distribution of sea ice inclusions.
4. Assess the implications for airborne remote sensing and bioremediation of the upper sea ice layers.

To accomplish these objectives, X-ray microtomography (μ -CT) was used to analyze sea ice samples taken from both the SERF 2017 (1st project – Chapter 2) and 2018 (3rd project – Chapter 4) oil-in-ice mesocosm studies (see Section 7.7 of the Appendix). A three-dimensional image of the spatial distribution of sea ice inclusions (oil, air, brine) was made, and the geometry, size, and orientation of inclusions were quantified. Implications of the generated results were discussed in the context of 1) airborne remote detection of oil-contaminated sea ice using radar, which depends on the orientation, distribution, volume, and shape of sea ice inclusions, and 2) bioremediation of oil-in-ice, which depends on the

proximity of the brine and oil. The findings of this study aid in the development of remote sensing algorithms required to detect oil within surficial sea ice and the planning and coordination of bioremediation efforts suitable for ice-infested waters. This study is significant, as prior research has indicated that it is nearly impossible to identify oil-in-ice using X-ray μ -CT owing to the similar absorption contrast between oil and ice. In this study, we offer a novel methodology for analyzing oil-contaminated sea ice with the use of polypropylene tubes.

This project aimed to test the following hypotheses:

1. The use of a polypropylene tube can enhance the capacity for imaging oil-in-ice.
2. Oil will become incorporated in the sea ice matrix and will appear dispersed.
3. Oil will remain separate from the brine.
4. Oil inclusions will resemble the geometry of an oblate spheroid.

1.6 References

Albaig S.J., Bayona, J.M., Radović, J.R., 2016. “Photochemical effects on oil spill fingerprinting”, in *Standard Handbook Oil Spill Environmental Forensics: Fingerprinting and Source Identification*, Chap. 20, S. Stout and Z. Wang (2nd ed.), Elsevier/Academic Press.

AMAP, 2004. AMAP Assessment 2002: Persistent Organic Pollutants in the Arctic. Arctic Monitoring and Assessment Programme (AMAP), Oslo, Norway. xvi +310 pp.

AMAP, 2009. AMAP Assessment 2009: Human Health in the Arctic. Arctic Monitoring and Assessment Programme (AMAP), Oslo, Norway. xiv+254 pp. Possible impact of climate change on Contaminants in the arctic.

AMAP, 2010. AMAP Assessment 2007: oil and gas activities in the arctic — effects and potential effects. *Arctic Monitoring & Assessment Programme*, Oslo, vols. 1 and 2.

AMAP, 2021. Arctic Climate Change Update 2021: Key Trends and Impacts. Summary for Policy-makers. Arctic Monitoring and Assessment Programme (AMAP), Tromsø, Norway. 16 pp

Anderson, J.W., Neff, J.M., Cox, B.A., Tatem, H.E., Hightower, G.M., 1974. “Characteristics of dispersions and water-soluble extracts of crude and refined oils and their toxicity to estuarine crustaceans and fish.” *Mar. Biol.* 27: 75–88.

Andrews, J., Babb, D., Barber, D.G., 2017. “Climate change and sea ice: Shipping accessibility on the marine transportation corridor through Hudson Bay and Hudson Strait (1980-2014).” *Elem Sci Anth* 5: 15. DOI: <https://doi.org/10.1525/elementa.130>

Annot, J.A., Gobas, F.A.P.C., 2006. “A review of bioconcentration factor (BCF) and bioaccumulation factor (BAF) assessments for organic chemicals in aquatic organisms.” *Environmental Reviews* 14: 257–297.

Backstrom, L.G.E., Eicken, H., 2006. “Capacitance probe measurements of brine volume and bulk salinity in first-year sea ice.” *Cold Reg. Sci. Technol.* 46: 167–180.

Bacosa, H.P., Erdner, D.L., Liu, Z., 2015. “Differentiating the roles of photooxidation and biodegradation in the weathering of Light Louisiana Sweet crude oil in surface water from the Deepwater Horizon site.” *Marine Pollution Bulletin* 95: 265-272.

Barber, D.G., Meier, W.N., Gerland, S., Mundy, C.J., Holland, M., Kern, S., Li, Z., Michel, C., Perovich, D.K., Tamura, T., 2017. Arctic sea ice. In: Snow, Water, Ice and Permafrost in the Arctic (SWIPA). Arctic Monitoring and Assessment Programme (AMAP), Oslo, Norway, pp. 119–127.

Bobinger, S., Andersson, J.T., 2009. “Photooxidation products of polycyclic aromatic compounds containing sulfur.” *Environ. Sci. Technol.* 43: 8119–8125.

Boccadoro, C., Krolicka, A., Receveur, J., Aeppli, C., Le Floch, S., 2018. “Microbial community response and migration of petroleum compounds during a sea-ice oil spill experiment in Svalbard” *Marine Environmental Research* 142: 214-233.

Brandvik, P.J., Sørheim, K.R., Singaas, I., Reed, M., 2006. Short state-of-the-art report on oil spills in ice-infested waters—Final: SINTEF Materials and Chemistry, Oil in Ice—JIP Report No. 1, 63 pp.

Brekke, C., Holt, B., Jones, C., Skrunes, S., 2014. “Discrimination of oil spills from newly formed sea ice by synthetic aperture radar.” *Remote Sens. Environ.* 145: 1–14.

Brown, R., Schuler, D.V., Bulygina, O., Derksen, C., Luojus, K., Mudryk, L., Wang, L., Yang, D., 2017. Arctic terrestrial snow cover. In: Snow, Water, Ice and Permafrost in the Arctic (SWIPA). Arctic Monitoring and Assessment Programme (AMAP), Oslo, Norway, pp. 25–64.

Cavalieri, D.J., Parkinson, C.L., 2012. “Arctic sea ice variability and trends, 1979–2010.” *The Cryosphere* 6: 881–889.

“Crude Oil.” *Viscopedia: A free encyclopedia for viscosity*, <https://wiki.anton-paar.com/en/crude-oil/>.

Dawson, J., Pizzolato, L., Howell, S.E.L., Copland, L., Johnston, M.E., 2018. “Temporal and Spatial Patterns of Ship Traffic in the Canadian Arctic from 1990 to 2015.” *Arctic* 71(1): 15–26.

Desmond, D.S., Neusitzer, T.D., Lemes, M., Isleifson, D., Saltymakova, D., Mansoori, A., Barber, D.G., Stern, G.A., 2019a. “Examining the Physical Interactions of Corn Oil (Medium Crude Oil Surrogate) in Sea Ice and its Potential for Chemical Partitioning within an Arctic Environment.” Proceedings of the Forty-second AMOP Technical Seminar, Environment and Climate Change Canada, Ottawa, ON, Canada, pp. 66–95.

Desmond, D.S., Saltymakova, D., Neusitzer, T.D., Firoozy, N., Isleifson, D., Barber, D.G., Stern, G.A., 2019b. “Oil Behavior in Sea Ice: Changes in Chemical Composition and Resultant Effect on Sea Ice Dielectrics.” *Marine Pollution Bulletin* 142: 216–233.

Dickins, D.F., Buist, I., 1999. “Countermeasures for ice-covered waters.” *Journal of Pure and Applied Chemistry* 71: 173–191.

Eicken, H., 2003. “From the microscopic to the macroscopic to the regional scale: Growth, microstructure and properties of sea ice.” Contribution to Thomas D. & G. S. Dieckmann (eds.): *SEA ICE - AN INTRODUCTION TO ITS PHYSICS, BIOLOGY, CHEMISTRY AND GEOLOGY*, Blackwell Science, London, 2003, pp. 22–81

Evers K.-U., Singsaas, I., Sørheim, K.R., 2006. “Oil Spill Contingency Planning in the Arctic-Recommendations”, Work package 4 Environmental Protection and Management System for the Arctic, GROWTH Project GRD2-2000-30112 “ARCOP”, available as ARCOP WP 4 Report 4.2.2.4, 2006, <http://www.arcop.fi>

Faksness, L.-G., Brandvik, P.J., 2008. “Distribution of water soluble components from Arctic marine oil spills — a combined laboratory and field study.” *Cold Reg. Sci. Technol.* 54: 97–105. <https://doi.org/10.1016/J.COLDREGIONS.2008.03.005>.

Faksness, L.G., Brandvik, P.J., Daae, R.L., Leirvik, F., Børseth, J.F., 2011. “Large-scale oil-in-ice experiment in the Barents Sea: monitoring of oil in water and MetOcean interactions.” *Mar. Pollut. Bull.* 62: 976–984. <https://doi.org/10.1016/J.MARPOLBUL.2011.02.039>.

Fingas, M., 2011. Introduction to Spill Modeling. In: Fingas, M. (Ed.), *Oil Spill Science and Technology*. Elsevier, New York, pp. 187-200.

Fingas, M., Brown, C., 2000. "A Review of the Status of Advanced Technologies for the Detection of Oil in and with Ice". *Spill Science & Technology Bulletin* 6(5/6): 295-302.

Firoozy, N., Neusitzer, T., Chirkova, D., Desmond, D.S., Lemes, M.J.L., Landy, J., Mojabi, P., Rysgaard, S., Stern, G., Barber, D.G., 2018. "A controlled experiment on oil release beneath thin sea ice and its electromagnetic detection." *IEEE Trans. Geosci. Remote Sens.* 56: 4406–4419.

Fritt-Rasmussen, J., Wegeberg, S., Gustavson, K., 2015. "Review on Burn Residues from In Situ Burning of Oil Spills in Relation to Arctic Waters." *Water, Air, & Soil Pollution* 226: 329

Fritz, A., Ramirez, R. (2021, August 9). *Earth is warming faster than previously thought, scientists say, and the window is closing to avoid catastrophic outcomes*. CNN. <https://www.cnn.com/2021/08/09/world/global-climate-change-report-un-ipcc/index.html>.

Gaden, A. (2019), GENICE-Microbial Genomics for Oil Spill Preparedness in Canada's Arctic Marine Environment. Retrieved from <http://umanitoba.ca/faculties/environment/departments/ceos/research/GENICE.html>.

Garrett, R.M., Pickering, I.J., Haith, C.E., Prince, R.C., 1998. "Photooxidation of crude oils." *Environ. Sci. Technol.* 32: 3719–3723.

Golden, K.M., Ackley, S.F., Lytle, V.I., 1998. "The percolation phase transition in sea ice." *Science* 282: 2238–2241.

Golden, K.M., Eicken, H., Heaton, A.L., Miner, J., Pringle, D.J., Zhu, J., 2007. "Thermal Evolution of Permeability and Microstructure in Sea Ice." *Geophys. Res. Lett.* 34: 1-13. DOI: 10.1029/2007GL030447

Gulec, I., Holdway, D.A., 1999. "The toxicity of laboratory burned oil to the amphipod *Allorchestes compressa* and the snail *Polinices conicus*." *Spill Science & Technology Bulletin* 5(2): 135–139.

Intergovernmental Panel on Climate Change (IPCC), 2021. Climate Change 2021: The Physical Science Basis. *IPCC Sixth Assessment Report*. https://www.ipcc.ch/report/ar6/wg1/downloads/report/IPCC_AR6_WGI_Full_Report.pdf

Ivanova, N., Pedersen, L.T., Tonboe, R.T., Kern, S., Heygster, G., Lavergne, T., Sørensen, A., Saldo, R., Dybkjær, G., Brucker, L., Shokr, M., 2015. "Inter-comparison and

evaluation of sea ice algorithms: towards further identification of challenges and optimal approach using passive microwave observations.” *The Cryosphere* 9: 1797-1817.

Larson, R.A., Hunt, L.L., Blankenship, D.W., 1977. “Formation of toxic products from a #2 fuel oil by photooxidation.” *Environ. Sci. Technol.* 11: 492-496.

Lee, K. (chair), Boufadel, M., Chen, B., Foght, J., Hodson, P., Swanson, S., Venosa, A., 2015. Expert Panel Report on the Behaviour and Environmental Impacts of Crude Oil Released into Aqueous Environments. Royal Society of Canada, Ottawa, ON. ISBN: 978-1-928140-02-3

Liu, B., Gao, L., Ding, L., Lv, L., Yu, Y., 2023. “Trophodynamics and bioaccumulation of polycyclic aromatic hydrocarbons (PAHs) in marine food web from Laizhou Bay, China.” *Marine Pollution Bulletin* 194 (Part B): 115307.

Macdonald, G.J., 1988. "Scientific Basis for the Greenhouse Effect." *Journal of Policy Analysis and Management* 7.3: 425.

Maki, H., Sasaki, T., Harayama, S., 2001. “Photo-oxidation of biodegraded crude oil and toxicity of the photo-oxidized products.” *Chemosphere* 44: 1145-1151.

Martin, S., 1979. “A Field Study of Brine Drainage and Oil Entrainment in First-Year Sea Ice.” *J. Glaciol.* 22(88): 473–502.

Meador, J.P., Stein, J.E., Reichert, W.L., Varanasi, U., 1995. “Bioaccumulation of polycyclic aromatic hydrocarbons by marine organisms.” *Rev Environ Contam Toxicol.* 143: 79-165.

Mlyczyńska, E., Bongrani, A., Rame, C., Węgiel, M., Maślanka, A., Major, P., Zarzycki, P., Ducluzeau, P.H., De Luca, A., Bourbao-Tournois, C., Froment, P., Rak, A., Dupont, J., 2023. “Concentration of Polycyclic Aromatic Hydrocarbons (PAHs) in Human Serum and Adipose Tissues and Stimulatory Effect of Naphthalene in Adipogenesis in 3T3-L1 Cells.” *Int J Mol Sci.* 24(2):1455.

National snow and Ice data center (NSIDC). NSIDC Arctic News and Analysis RSS. (2021, August 18). <http://nsidc.org/arcticseaicenews/>.

Neff, J.M., 1979. “Polycyclic aromatic hydrocarbons in the aquatic environment, sources, fates, and biological effects.” *Applied Science*, London, Great Britain, 262 pp.

Nicodem, D.E., Fernandes, M.C.X., Guedes, C.L.B., and Correa, R.J., 1997. “Photochemical processes and the environmental impact of petroleum spills.” *Biogeochem.* 39: 121-138.

Oggier, M., Eicken, H., Wilkinson, J., Petrich, C., O'Sadnick, M., 2020. "Crude oil migration in sea-ice: Laboratory studies of constraints on oil mobilization and seasonal evolution." *Cold Regions Science and Technology* 174: 102924.

Payne, J.R., Hachmeister, L.E., McNabb, G.D., Sharpe, H.E., Smith, G.S., Menen, C.A., 1991. "Brine-induced advection of dissolved aromatic hydrocarbons to Arctic bottom waters." *Environ. Sci. Technol.* 25: 940–951.

Pegau, W.S., Garron, J., Zabilansky, L., Bassett, C., Bello, J., Bradford, J., Carns, R., Courville, Z., Eicken, H., Elder, B., Eriksen, P., Lavery, A., Light, B., Maksym, T., Marshall, H.-P., Oggier, M., Perovich, D., Pacwiardowski, P., Singh, H., Tang, D., Wiggins, C., Wilkinson, J., 2017. "Detection of oil in and under ice". In the Proceedings of the International Oil Spill Conference, pp. 1-20.

Petrich, C., Karlsson, J., Eicken, H., 2013. "Porosity of Growing Sea Ice and Potential for Oil Entrainment." *Cold Reg. Sci. Technol.* 87: 27-32.

Pithan, F., Mauritsen, T., 2014. "Arctic amplification dominated by temperature feedbacks in contemporary climate models." *Nature Geoscience* 7:181-184.

Pizzolato, L., Stephen, E.L., Derksen, C., Dawson, J., Copland, L., 2014. "Changing sea ice conditions and marine transportation activity in Canadian Arctic waters between 1990 and 2012." *Climatic Change* 123: 161-173.

Potter, S., Buist, I., 2008. In situ burning for oil spills in Arctic waters—State-of-the-art and future research needs. In *Oil spill response—A global perspective*, eds. W.F. Davidson, K. Lee, and A. Cogswell, 23–39. Springer

Praks, J., Eskelinen, M., Pulliainen, J., Pyhälä, T., Hallikainen, M., 2004. "Detection of oil pollution on sea ice with airborne and spaceborne spectrometer". 0-7803-8742-2/04/\$20.00 (C) 2004 IEEE: 273-276.

Prince, R.C., Walters, C.C., 2016. "Biodegradation of oil hydrocarbons and its implications for source identification", in *Standard Handbook Oil Spill Environmental Forensics: Fingerprinting and Source Identification*, Chap. 19, S. Stout and Z. Wang (2nd ed.), Elsevier/Academic Press.

Prince, R.C., Gramain, A., McGenity, T.J., 2010. "Prokaryotic hydrocarbon degraders", in *Handbook of Hydrocarbon and Lipid Microbiology*, K.N. Timmis, ed. (Berlin, Heidelberg: Springer), pp. 1669–1692.

Prince, R.C., McFarlin, K.M., Butler, J.D., Febbo, E.J., Wang, F.C.Y., Nedwed, T.J., 2013. "The primary biodegradation of the dispersed crude oil in the sea." *Chemosphere* 90: 521–526. doi:10.1016/j.chemosphere.2012.08.020.

Reports. Arctic Response Technology | Oil Spill Preparedness. (n.d.). Retrieved September 16, 2021, from <http://www.arcticresponsetechnology.org/reports/>.

“Safety Data Sheet.” ThermoFisher SCIENTIFIC, [msds \(fishersci.com\)](https://www.fishersci.com/msds/).

Schneider, S.H., 1989. "The Greenhouse Effect: Science and Policy." *Science* 243.4892: 771-81.

Sheppard, E.P., Wells, R.A., Georghiou, P.E., 1983. “The mutagenicity of a Prudhoe Bay crude oil and its residues from an experimental in situ burn.” *Environmental Research* 30: 427–441.

SINTEF, 2006. JIP (Joint Industry Program): Oil spill contingency for Arctic and ice-infested waters.

Southworth, G.R., Beauchamp, J.J., Schmieder, P.K., 1978. “Bioaccumulation potential of polycyclic aromatic hydrocarbons in *Daphnia pulex*.” *Water Research* 12(11): 973-977.

Stout, S.A., Wang, Z., 2016. “Chemical fingerprinting methods and factors affecting petroleum fingerprints in the environment”, in *Standard Handbook Oil Spill Environmental Forensics: Fingerprinting and Source Identification*, Chap. 3, S. Stout and Z. Wang (2nd ed.), Elsevier/Academic Press.

Thomas and Dieckmann (2010). *Sea Ice: an Introduction to its Physics, Chemistry, Biology and Geology*, second edition Blackwell.

Varanasi, U., 1989. *Metabolism of polycyclic aromatic hydrocarbons in the aquatic environment*. Boca Raton: CRC Press.

Venkatesh S., El-Tahan, H., Comfort, G., Abdelnour, R., 1990. “Modelling the Behavior of Oil Spills in Ice- infested Water.” *Atmosphere-Ocean* 28(3): 303-329.

Vergeynst, L., Christensen, J.H., Kjeldsen, K.U., Meire, L., Boone, W., Malmquist, L.M.V., Rysgaard, S., 2019. “In situ biodegradation, photooxidation and dissolution of petroleum compounds in Arctic seawater and sea ice.” *Water Res.* 148: 459–468.

Vergeynst, L., Kjeldsen, K.U., Lassen, P., Rysgaard, S., 2018. “Bacterial community succession and degradation patterns of hydrocarbons in seawater at low temperature.” *Journal of Hazardous Materials* 353: 127-134.

Walsh, J.E., Anisimov, O., Hagen, J., Jakobsson, T., Oerlemans, J., Prowse, T.D., Romanovsky, V., Savelieva, N., Serreze, M., Shiklomanov, A., Shiklomanov, I., Solomon, S., 2005. "Chapter 6: Cryosphere and hydrology." *Arctic Climate Impact Assessment*.

Wang, F., Pućko, M., Stern, G., 2017. Transport and transformation of contaminants in sea ice. In: *Sea Ice*. 3rd ed. (D.N. Thomas, Ed). Wiley-Blackwell, Oxford. pp. 472–491.

Wang, Z., Stout, S.A., 2007. “Oil Spill Remote Sensing: A Forensics Approach.” *Oil Spill Environmental Forensics: Fingerprinting and Source Identification*, Elsevier/Academic Press.

Wang, Z., Yang, C., Yang, Z., Brown, C.E., Hollebone, B.P., Stout, S.A., 2016. “Petroleum biomarker fingerprinting for oil spill characterization and source identification”, in *Standard Handbook Oil Spill Environmental Forensics: Fingerprinting and Source Identification*, Chap. 4, S. Stout and Z. Wang (2nd ed.), Elsevier/Academic Press.

Wilkinson, J., Beegle-Krause, C.J., Evers, K.-U., Hughes, N., Lewis, A., Reed, M., Wadhams, P., 2017. “Oil spill response capabilities and technologies for ice-covered Arctic marine waters: A review of recent developments and established practices”. *Ambio* 46(Suppl. 3): S423–S441.

Wilkinson, J., Maksym, T., Bassett, C., Lavery, A., Singh, H., Chayes, D., Elosegui, P., Wadhams, P., Ulrich-Evers, K., Jochmann, P., 2014. “Experiments on the Detection and Movement of Oil Spilled Under Sea Ice”. In the Proceedings of the HYDRALAB IV Joint User Meeting, pp. 1-11.

Wilkinson, J., Maksym, T., Hole, W., 2013. “Capabilities for detection of oil spills under sea ice from autonomous underwater vehicles.” Arctic Response Technology Oil Spill Preparedness, Final Report 5.2.

2 Effect of Dissolution, Evaporation, and Photooxidation on Crude Oil Chemical Composition, Dielectric Properties and its Radar Signature in the Arctic environment

2.1 Abstract

Accidental release of petroleum in the Arctic is of growing concern owing to increases in ship traffic and possible future oil exploration. A crude oil-in-sea ice mesocosm experiment was conducted to identify oil-partitioning trends in sea ice and determine the effect of weathering on crude oil permittivity. The dissolution of the lighter fractions increased with decreasing bulk oil-concentration because of greater oil-brine interface area. Movement of the oil towards the ice surface predominated over dissolution process when oil concentrations exceeded 1 mg/mL. Evaporation decreased oil permittivity due to losses of low molecular weight alkanes and increased asphaltene-resin interactions. Photooxidation increased the permittivity of the crude oil due to the transformation of branched aromatics to esters and ketones. Overall, the weathering processes influenced crude oil permittivity by up to 15%, which may produce sufficient quantifiable differences in the measured normalized radar cross-section of the ice.

2.2 Introduction

The persistent decrease in Arctic sea-ice extent (Comiso et al., 2008) has led to a tripling in ship traffic in North Canadian waters since 1990 (Carter et al., 2018). The

increased activity brings a greater risk of accidental spills of fuel-oils and other transportation-related contaminants. Climate change has also focused attention on Arctic oil exploration (Gautier et al., 2009) since significant oil reserves are estimated to exist in the Arctic (Epov et al., 2010; Houseknecht and Bird, 1985; McGlade, 2012). While the current indefinite ban on offshore exploration in the Canadian Arctic is in place (Government Canada, 2018), it is prudent to take this time to identify reliable detection, suitable mitigation and working control policies for crude oil spills.

Early detection of oil spills in ice-rich marine waters will lead to a fast mitigation response thereby minimizing both the environmental and economic impacts should such a spill occur. While the presence of crude oil in first-year sea ice was detectable through normalized radar cross-section (NRCS) measurements (Firoozy et al., 2018, 2017; Neusitzer et al., 2018), future investigations must take into account initial crude oil composition as well as its alteration due to weathering processes (Wang and Fingas, 2003). Crude oil weathering may significantly impact dielectric properties as a result of close correlation between the density, thermal conductivity, and dielectric constant (i.e., the relative permittivity) of each compound found in crude oil (Table 2.1) (Aboul-Seoud and Moharam, 1999; Desmond et al., 2019c, 2019b; Panuganti et al., 2016).

A great number of studies have investigated crude oil weathering in open water (Gros et al., 2014; Tapan and Harayama, 2000); however, the processes may either be slowed or accelerated in the presence of sea ice. Crude oil evaporation is reduced at lower temperatures in the presence of sea ice (Atlas and Bartha, 1972; Faksness et al., 2011). Dissolution can increase in the ice-covered water due to the larger exposure of the crude oil to the liquid

phase in the brine channels (Faksness and Brandvik, 2008). Crude oil photooxidation in the ice is possible due to light penetration (Sydnes, 1991), but the rate and the light penetration depth is not well-established. Biodegradation can also occur in the sea ice (Ballesterio and Magdol, 2011; Brakstad et al., 2008), and depends on the microbial community composition as well as on the factors controlling microbial habitats such as different ice thermodynamic states and the presence or absence of snow cover.

In this study, we examined the influence of the chemical and physical properties of individual crude oil compounds on chemical partitioning, weathering susceptibility, and dielectric properties. The data presented in this study was obtained as part of a crude oil in sea ice mesocosm experiment conducted at the University of Manitoba Sea-ice Environmental Research Facility (SERF) and is the third in a series of oil-in-ice experiments (Desmond et al., 2019a, 2019b, 2019c; Firoozy et al., 2017; Neusitzer et al., 2018).

The current study differs from the previous research in several ways: 1) no snow cover allowing an increased potential for photo-oxidation; 2) migration of the oil through non-fractured ice, allowing for a further investigation into oil partitioning and comprehensive analysis of oil on brine displacement; 3) detailed analysis of the relationship between oil density, dielectric constant/thermal conductivity, and chemical composition.

Table 2.1 Physical properties of low molecular weight (MW) and high MW chemical compounds

Physical property	The lowest	Low	High	The Highest	References
Polarity	Saturates	Aromatics	Resins	Asphaltenes	(Likhatsky and Syunyaev, 2010; Panuganti et al., 2016; Van Dyck et al., 2017)
Density	Linear alkanes Low MW n-alkanes, alkyl cyclopentanes, and alkyl cyclohexanes	cycloalkanes High MW n-alkanes, alkyl cyclopentanes, and alkyl cyclohexanes	non-hetero aromatics Low MW aromatics High MW alkyl benzenes and alkyl naphthalenes	heterocyclic compounds High MW aromatics Low MW alkyl benzenes and alkyl naphthalenes	(“Dielectric Constants of common Liquids,” n.d.; Dymond and Malhotra, 1987; Panuganti et al., 2016)
Dielectric constant	Linear alkanes Low MW alkanes	cycloalkanes High MW alkanes	non-hetero aromatics Low MW aromatics Low MW alkenes/alkynes	heterocyclic compounds High MW aromatics High MW alkenes/alkynes	(Carey and Hayzen, n.d.; “Dielectric Constants of common Liquids,” n.d., “List of Dielectric Constants,” n.d.; Klamt et al., 1998; Panuganti et al., 2016; Sen et al., 1992; Van Dyck et al., 2017)
Thermal conductivity	Linear alkanes Small ring size/ low MW alkanes	cycloalkanes Large ring size/ high MW alkanes Alkyl cycloalkanes	non-hetero aromatics Low MW Aromatics	heterocyclic compounds High MW Aromatics	(“API Tech Data Book 10,” 2016; Elam et al., 1989; Jamieson et al., 1975; Jamieson and Cartwright, 1983; Lashkarbolooki et al., 2017; Lei et al., 1997)

2.3 Methods

2.3.1 Experiment Overview

An artificial oil-in-ice mesocosm experiment was conducted at the University of Manitoba Sea-ice Environmental Research Facility (SERF) from January 31 to March 14, 2017. Before the beginning of the experiment, a curtain was fixed inside the pool in order to control migration of oil through the ice rather than infiltration along the sides of the tank (see Firoozy et al., 2018 for more details). Furthermore, the tank was equipped with a heating

coil, a thermistor string, and a temperature data logger. A thermocouple string was used to measure the in-situ ice temperature profile at intervals of 2.5 cm, from top to bottom, every 15 minutes. The experiment was divided into two phases (Fig. 2.1). Phase 1 began on January 31 with the formation of ice from open artificial seawater (i.e., 33 g/L consisting of 54% Cl^- , 32% Na^+ , 8% SO_4^{2-} , 4% Mg^{2+} , 1% Ca^{2+} , and 1% K^+). After 2 days, on February 2, 20 L of a light sour crude oil (Tundra Oil and Gas Partnership) was injected under ~6 cm of ice towards one edge of the pool. This created a gradient of oil concentrations between opposite ends. Within a day after the injection, the oil was encapsulated within the ice due to the low ice temperatures (Fingas and Hollebone, 2003). By February 10, the ice had grown an additional 19 cm (for a total of 25 cm) and the first sampling set, consisting of 9 ice cores, was taken from different locations within the pool (Fig. 2.1). Another two 26 cm ice cores were sampled on February 15, after the thaw. Ice core sampling locations were selected based on the level of crude oil on the ice surface. As the crude oil was not homogeneously distributed under the ice, a representative subset of ice cores was sampled within the two extremes of crude oil being visually present/absent at the surface of the ice or at the oil introductory ice depth (5-7 cm).

At the end of phase 1 on February 15, the tank was heated until the ice was completely melted. During the transition period, an oil slick of ~3-4 cm thickness appeared on the surface of the water. Phase 2 then began on March 8th, with the commencement of the formation of pancake ice (Fig. 2.1). The average ambient temperature during the second phase was -15 °C, and by March 15, the ice grew to a thickness of 20 cm. At this time, a final series of 4 ice

cores were collected from the most visually clean and more highly contaminated sections of the pool.

In close proximity to the test tank, a set of 3 field blanks consisting of 450 mL of 1) n-hexanes (Fisher Chemical, Optima Grade) (see Section 2.3.2), 2) Milli-Q water (18.2 MΩ) and 3) artificial seawater (the same formulation noted above) in 500 mL glass jars were exposed to the surrounding atmosphere during each sampling period to control for the background contamination. Upon completion of the sampling, each glass jar was sealed and subsequently treated in the same manner as the melted ice cores and water samples during sample preparation.

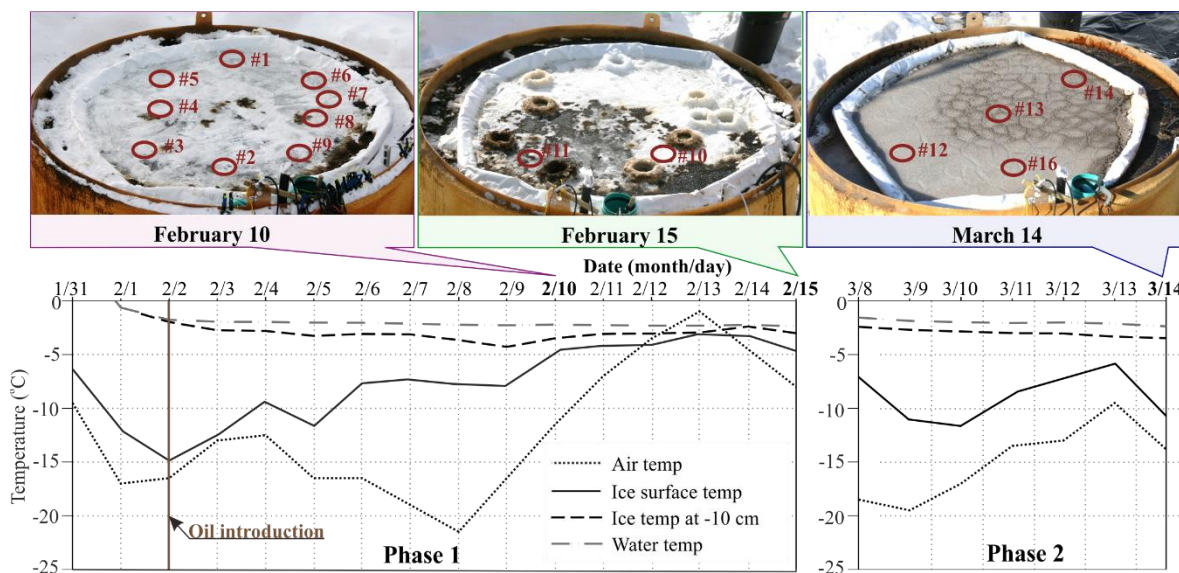


Fig. 2.1 Temporal profile of the recorded temperatures for a vertical cross section of the test tank pertaining to the water column, sea ice, and air above from January 31 to March 14, 2017. The break in the temperature profile from February 15 to March 8 pertains to the transition period between phases one and two. Coring dates are in bold.

2.3.2 Sample Preparation (Ice Core and Water Samples)

Immediately after sampling, the visually contaminated ice cores were sliced into 0-2.5, 2.5-5, 5-7 (oil introduction ice thickness) and 7-13 cm sections. The remainder of the ice core was sliced into two equal pieces. The lesser contaminated ice cores (i.e., ice cores without visually observable crude oil) were sliced into 0-2.5, 2.5-5, 5-15 and 15-25 cm sections. Sample preparation was carried out following a similar procedure as to what is described by (Desmond et al., 2019c). In brief, prior to extraction, all melted ice samples were spiked with deuterated n-alkane (D_{26} - D_{72} , Fisherbrand, 7 compound mix) and polycyclic aromatic hydrocarbons (PAHs) (D_8 , D_{10} , D_{12} , Wellington Laboratories, 8 compound mix) recovery standards. Liquid-liquid sample extractions were carried out using a 250 mL separatory funnel with a minimum of three consecutive 50 mL washes with hexane (Fisher Chemical, Optima Grade) followed by three washes with 50 mL of dichloromethane (Fisher Chemical, Optima Grade) or until the water was completely colorless. Sample extracts were first concentrated down to ~15 mL using a rotary evaporator and then to dryness using a nitrogen evaporator (50°C bath temperatures). Surrogate recoveries varied between 12.7 and 104.8% (Appendix Section 7.1, Table S2.1). Greater losses of the low molecular weight (MW) compounds were associated with the use of nitrogen evaporation and the long sample preparation process. These losses were, however, significantly minimized for the reconstituted samples with larger oil volumes (Desmond et al., 2019c). Each reconstituted oil sample (i.e., oil recovered from the ice and water collections), the technical oil mixture, and field blanks were diluted with hexane to a concentration of 1% volume/volume prior to analysis by gas chromatography.

2.3.3 Analytical Instrumentation

LECO Pegasus® gas chromatography-high resolution time of flight mass spectrometry (GCxGC-HR-TOF-MS) was used to measure the composition of aliphatic and aromatic hydrocarbons as well as dibenzothiophenes and dibenzofurans. The *GCxGC-HR-TOF-MS* system was equipped with an Agilent 7890A gas chromatograph and Agilent 7693 autosampler. The sample injection volume was set to 2 μ L. All samples were run using a two-dimensional column setup, for increased separation of crude oil compounds (Djokic et al., 2012), using helium as the carrier gas with a 1.40 mL/min flow rate. The system was equipped with a RESTEK Rxi-PAH capillary column (60 m length, 0.25 mm internal diameter, 0.10 μ m film thickness) for the first dimension and a DB-1HT column (10 cm length, 0.25 mm internal diameter, 0.10 μ m film thickness) for the second. The initial oven temperature was set to 40 °C, with an isotherm of one minute, followed by a temperature increase to 70 °C at 10 °C/min, and a further increase to 310 °C at 2.5 °C/min rate. The secondary oven temperature was set to +5°C relative to the primary GC oven temperature, and the modulator temperature was set to +15°C relative to the secondary oven temperature. The modulator cycle was 4 seconds with a 1-second duration of the hot pulse and cooling time between stages. The mass spectrometer conditions consisted of an electron ionization energy of 70 eV, an ion source temperature of 250 °C, a mass range between 50-520 m/z, and an operational TOF resolution of 25 000.

All 299 of the monitored compounds by GCxGC-HR-TOF-MS are listed in Table S2.2 (Appendix Section 7.1). The following set of standards was used for quantitative and semiquantitative analysis: n-alkanes (mix of three SPEX standards: C₁₁-C₁₈, odd C₁₅-C₃₅,

even C₁₆-C₃₆), alkylcycloalkane mixture #1 (Chiron, 9 compounds), alkylbenzene mixture (Chiron, 16 compounds), PAHs mixtures (CV calibration mix #5, Restek, 16 compounds), PAH dibenzothiophene (and alkylated homologues) mixture (Chiron, 20 compounds), and dibenzofuran (SPEX). The calibration curves were run in the range of 3.9-1000 ng/mL, with the exception of n-alkanes which were run within 4.9 - 5000 ng/mL. The calibration curves had 9 – 11 points and R² values higher than 0.95. A minimum signal-to-noise ratio was set to 6 for all of the compounds. The method detection limits varied from 3.9 to 105 ng/mL based on the lowest range of the calibration curve. 77 samples were analyzed in total, including field and lab blanks. Duplicates were run every 15 samples (5 in total). The difference between duplicates varied within 5% for all 299 compounds. The GCxGC-HR-TOF-MS system was tuned and validated before and after a sequence of standard/sample runs as well as between each set of 6-8 standards/samples. Corrections to the samples based on blanks were not made as none of the studied compounds were detected in the field and lab blanks, except for n-alkanes which were found to have concentrations varying between 0 – 69.4 ng/mL.

Agilent 7010B Triple Quadrupole GC-MS (QqQ-MS) was used for the analysis of steranes and terpanes due to its ability to resolve complex organic mixtures (Philp et al., 1988) and greater sensitivity relative to the LECO. The QqQ-MS system was equipped with a PAL RSI 85 autosampler, 7890B gas chromatograph, and a Rxi-PAH column (60m x 250 µm x 0.1 µm). The initial oven temperature was set to 60°C. After 1 minute, the temperature was increased to 200 °C at 20°C/min, then to 320 °C at 4 °C/min where it was then held for 12 min. The electron ionization energy was set to 70 eV, and the oven temperature to 250°C.

Helium was used as a carrier gas with a flow rate of 1.1 mL/min. Nitrogen was used as a collision gas with a flow rate of 1.5 mL/min and an ion gain of 5. The mass range was set to 50-520 m/z. The sample injection volume was set to 2 μ L.

The 56 compounds measured using the multiple reaction monitoring are listed with their parameters in Table S2.3 (Appendix Section 7.1). Hopanes and steranes (Chiron, 12 mix) were used as an external standard mixture for quantification over a concentration range of 15.625 - 500 ng/mL. The calibration curves had 8 points and R^2 values higher than 0.95. A minimum signal-to-noise ratio was set to 6 for all of the compounds. The instrument detection limit varied from 13.4 to 25.0 ng/mL. Since each sample was run at the same concentration used in GCxGC-HR-TOF-MS analysis, it was possible to use the closest perdeuterated n-alkane (tetracosane, octacosane or dotriacontane) as recovery standards.

Attenuated Total Reflection Infrared Spectroscopy (ATR-IR) was used to monitor the bulk crude oil composition including heavy compounds such as asphaltenes and heterocyclics, which are not suitable for GC-MS. A representative subset of oil samples (i.e., total of 30 samples which contained more than 100 μ L of crude oil and the technical oil mixture), with spatial and temporal variation, were placed on the ATR-IR (Alpha-P, Bruker) diamond cell and were analyzed with a 2 cm^{-1} resolution over a 4000-374 cm^{-1} range. An air background subtraction was performed on all measured spectra.

Compact Micro-Computed Tomography (μ -CT) X-ray (SKYSCAN 1174, Bruker) was used to observe the difference in the porosity of the oil-contaminated sea ice between the two phases of the experiment (Crabeck et al., 2016). Cylindrical sections, with 3 cm diameters and 3 cm heights, were cut from the top sections of oil-contaminated ice cores

taken from phases 1 and 2, respectively. The analysis was conducted by 3D imaging of the samples density contrast between its different components (i.e., brine, air, ice, and oil). Data processing included removal of ring-artifacts corrections, beam-hardening, post-alignment, and Gaussian smoothing.

2.3.4 Statistical Analysis

Prior to statistical analysis, empty data entries, which correspond to non-detected compound concentrations, were substituted with randomly generated values ranging between 17 and 50% of the minimum detected concentration.

For Principal Component Analysis (PCA) we prepared a 30 x 35 matrix, which consisted of compound groups concentrations from the top and bottom sections of the ice cores. The matrix was treated with a centered log-ratio to eliminate the variability between the samples (Yunker et al., 2005) caused by different contamination levels and to normalize the data. The calculations were performed in OriginLab software using a correlation matrix. The effect was similar to the one described in Faith, 2015.

The calculations of the Spearman correlation coefficient were performed in SigmaPlot Systat Software Inc. on the log-transformed matrix (low contaminated ice cores 37x19 and high-contaminated ice cores 37x52).

2.3.5 Computational Chemistry

A popular implicit solvation model, COnductor like Screening MOdel for Realistic Solvents (COSMO-RS) embedded within the Amsterdam Density Functional (ADF2017/2018) modeling suite (Klamt et al., 1998; Louwen, J.N., Pye, C., and Lenthe, 2008; Pye and Ziegler, 1999), was used to simulate the effects of evaporation and dissolution.

Using ADF-GUI (2017), molecules and ions of interest were first built in a low energy state conformation and were further minimized through molecular mechanics. Gas-phase geometry optimizations were then performed using the Becke Perdew exchange-correlation functional (GGA: BP), the scalar relativistic ZORA Hamiltonian, a TZP (triple Zeta, one polarization function) small core basis set, and an integration accuracy with adequate quality. Frequency calculations were also carried out to ensure the nature of the stationary points (i.e., no imaginary frequencies). The resulting COSMO kf files were input into COSMO-RS allowing for calculations of pure liquid solute vapor pressures and solubilities of compounds in saltwater (seawater and melted sea ice) (Table 2.2). The temperatures recorded during the sampling sets at the sea-ice surface were used for calculating vapor pressures while the average temperature measured at the sea-ice bottom was used for calculating $\log K_{ow}$ and S_{water} . Seawater salinity (35 g/kg) was simulated through the solubility of liquid solutes (compounds of interest) diluted in a 5-component solvent mixture (i.e., H₂O at 965 g/kg, Cl⁻ at 20 g/kg, Na⁺ at 11 g/kg, SO₄²⁻ at 3 g/kg, and Mg²⁺ at 1 g/kg) mimicking reference values of seawater composition. Liquid densities and Van der Waals volumes were calculated using the pure compound property prediction embedded within ADF2018 COSMO-RS. The static relative dielectric constant (ϵ) at zero hertz was calculated based on the computed liquid densities following Eq. (2.1) (Panuganti et al., 2016) where ρ = density (g/mL).

$$2.1 \quad \epsilon = \frac{2\rho+3}{3-\rho}$$

Table 2.2 Modeled physical properties of compounds found in crude oil using ADF2017 COSMO-RS

Compounds	Density, kg/L	Dielectric constant	Vapor pressure, μBar	Solubility – 2.4°C, ng/L	
	25°C	25°C	-12°C	Freshwater	35 g/g Salty water
Strait chain alkanes					
Undecane	0.733	1.970	101.01	19250.00	9940.00
Tridecane	0.746	1.993	5.50	981.60	456.06
Pentadecane	0.756	2.011	0.30	48.41	20.24
Heptadecane	0.764	2.025	0.02	2.44	0.92
Nonadecane	0.770	2.036	<10 ⁻²	0.14	0.05
Henicosane	0.775	2.045	<10 ⁻²	0.01	0.002
Tricosane	0.779	2.052	<10 ⁻²	0.0004	0.0001
Pentacosane	0.783	2.060	<10 ⁻²	0.00002	0.00001
Heptacosane	0.786	2.065	<10 ⁻²	0.000001	0.0000002
Nonacosane	0.789	2.071	<10 ⁻²	0.0000001	0.00000001
Cycloalkanes					
Cyclopentane	0.790	2.072	194683.49	262221040	190575390
n-Hexylcyclopentane	0.802	2.095	56.73	89430	48540
n-Octylcyclopentane	0.806	2.102	3.31	4930	2420
n-Decylcyclopentane	0.809	2.108	0.18	246.25	108.57
n-Tridecylcyclopentane	0.812	2.113	<10 ⁻²	3.12	1.18
n-Hexadecylcyclopentane	0.814	2.117	<10 ⁻²	0.04	0.01
cyclohexane	0.826	2.140	648.83	92444180	64548810
n-Butylcyclohexane	0.818	2.125	244.74	569010	329430
n-Pentylcyclohexane	0.819	2.127	648.83	136080	74870
n-Decylcyclohexane	0.822	2.132	0.05	95.56	40.69
n-Undecylcyclohexane	0.822	2.132	0.12	7.62	3.17
n-Tetradecylcyclohexane	0.823	2.134	<10 ⁻²	0.02	0.01

Table 2.2. Continued

Steranes					
5 α -pregnane, C ₂₁	0.903	2.292	1.25	513.70	226.11
5 α ,14 β ,17 β -ethylpregnane, C ₂₂	0.905	2.296	0.42	182.32	77.32
20S/R 13 β ,17 α -diacholestane, C ₂₇	0.894	2.274	<10 ⁻²	0.21	0.07
20S/R 5 α ,14 β ,17 β -Cholestane, C ₂₇	0.894	2.274	<10 ⁻²	0.66	0.23
20S/R 5 α ,14 α ,17 α -Cholestane, C ₂₇	0.894	2.274	<10 ⁻²	0.56	0.19
20S/R 24-ethyl-5 α ,14 β ,17 β -Cholestane, C ₂₉	0.893	2.271	<10 ⁻²	0.08	0.02
20S/R 24-ethyl-5 α ,14 α ,17 α -Cholestane, C ₂₉	0.893	2.271	<10 ⁻²	0.06	0.02
Terpanes					
18 α (H)-22,29,30-trisnorneohopane, C ₂₇ Ts	0.901	2.288	0.02	17.38	6.70
17 α (H)-22,29,30-trisnorhopane, C ₂₇ Tm	0.901	2.288	0.03	23.18	9.02
17 α (H), 21b(H)-hopane, C ₃₀	0.894	2.274	<10 ⁻²	1.55	0.55
Tricyclic terpane C ₂₃	0.861	2.208	0.10	56.84	23.07
Tricyclic terpane C ₂₉	0.854	2.194	<10 ⁻²	0.01	0.002
Tricyclic terpane C ₃₀	0.853	2.192	<10 ⁻²	0.002	0.0005
Alkylbenzenes					
1,2,3-Trimethylbenzene	0.881	2.247	676.18	70150280	48783840
1,2,4-Trimethylbenzene	0.881	2.247	552.59	48573540	33289220
n-Butylbenzene	0.871	2.227	146.28	9903320	6395610
n-Hexylbenzene	0.863	2.212	8.38	528500	306960
n-Octylbenzene	0.858	2.202	0.48	28550	14940
n-Decylbenzene	0.854	2.194	0.03	1940	924.73
n-Dodecylbenzene	0.851	2.188	<10 ⁻²	84.15	35.85
n-Tetradecylbenzene	0.849	2.184	<10 ⁻²	5.36	2.07
n-Hexadecylbenzene	0.847	2.180	<10 ⁻²	0.29	0.10
n-Octadecylbenzene	0.845	2.176	<10 ⁻²	0.01	0.004

Table 2.2 Continued

Polycyclic aromatic hydrocarbons					
Naphthalene	1.003	2.507	101.42	168905100	121161900
1-Methylnaphthalene	0.989	2.475	27.68	53814830	36889860
2-Methylnaphthalene	0.989	2.475	21.36	42793080	29145260
1-Ethylnaphthalene	0.978	2.451	8.06	14951260	9752920
1,8-Dimethylnaphthalene	0.977	2.449	661.27	31915480	21787150
1-Propylnaphthalene	0.963	2.418	2.45	4346740	2711350
1-Butylnaphthalene	0.951	2.392	0.63	1091650	647840
2,3,6,7-Tetramethylnaphthalene	0.959	2.410	29.05	1728520	1058550
1-Pentylnaphthalene	0.941	2.371	0.14	242750	136320
Phenanthrene	1.065	2.651	0.40	16660260	11046620
1-Methylphenanthrene	1.048	2.611	40.82	7819240	5075100
1-ethylphenanthrene	1.034	2.578	13.07	2393820	1484120
Acenaphthalene	0.845	2.176	7.18	66827460	46343770
Acenaphthene	0.972	2.438	7.41	35600040	23970720
Fluorene	0.944	2.377	1.40	27432670	18570380
Anthracene	1.065	2.651	0.37	14097490	9256560
Chrysene	1.103	2.744	<10 ⁻²	1513010	926110
Pyrene	1.043	2.599	0.06	6435150	4074990
Fluoranthene	1.067	2.656	0.04	6039190	3839590
Benzo-a-anthracene	1.103	2.744	2.62	2071760	1296360
Benzo-a-pyrene	1.081	2.690	1.16	1152880	702300
Dibenzo-a-h-anthracene	1.128	2.808	0.05	189450	110010
Heterocyclic and other aromatics					
Dibenzofuran	1.153	2.873	2.53	40771920	28085320
Dibenzothiophene	1.147	2.857	0.45	24607790	16555580
1-methoxy-8-methylnaphthalene-1-ketal *	1.005	2.511	8.55	791208230	541357520
1-methoxy-8-methylnaphthalene-1,4-diol *	1.159	2.889	<10 ⁻²	6059508380	3986412890

Table 2.2 Continued

*- Based on structures from (Sydnes et al., 1985)

2.3.6 Optical Measurements

A single optical channel spectrum instrument (ASD FieldSpec Handheld 2) was used to measure the incident sunlight $E_d(\lambda, 0)$, reflected irradiance from the surface of the sea ice $E_u(\lambda)$, and transmitted sunlight $E_d(\lambda, h)$. These measurements were used to assess the interaction and impedance of the light and oil in a sea-ice environment within the wavelength range of 390 to 700 nm. The surface albedo $\alpha(\lambda)$ and transmittance ratio $T(\lambda, h)$ of the oil and oil-contaminated sea ice were calculated using Eq. (2.2) and (2.3). Further information/details on how the light measurements were taken and processed can be found in Section 7.8 of the Appendix.

$$2.2 \quad \alpha(\lambda) = \frac{E_u(\lambda)}{E_d(\lambda, 0)}$$

$$2.3 \quad T(\lambda, h) = \frac{E_d(\lambda, h)}{E_d(\lambda, 0)}$$

2.3.7 Thermal and Electromagnetic Properties

Our *thermal conductivity model* accounted for thermal conductivities of crude oil Eq. (2.4) (Aboul-Seoud and Moharam, 1999) and pure sea ice Eq. (2.5) (Pringle et al., 2007). The model is based on the assumption that the thermal conductivity of a mixture is a function of the thermal conductivities of the components and their volume fractions Eq. (2.6) (Montaron, 2012). Changes in the thermal conductivity of the sea ice can result in a subsequent change in ice temperature through a positive/negative feedback loop. To gauge the extent of this subsequent temperature change (ΔT) due to the direct contribution of the

oil, we subtracted Eq. (2.5) from Eq. (2.6) and solved to estimate ΔT , keeping all other variables constant Eq. (2.7) and (2.8).

$$2.4 \quad k_{crude\ oil} = 2.540312\left(\frac{\gamma}{T}\right) 0.5 - 0.0144485$$

$$2.5 \quad k_{sea\ ice} = 2.11 - 0.011 T + 0.13 \left(\frac{S}{T}\right)$$

$$2.6 \quad k_{oil\ in\ ice} = k_{sea\ ice} \left(\frac{V_{sea\ ice}}{V_{total}}\right) + k_{crude\ oil} \left(\frac{V_{crude\ oil}}{V_{total}}\right)$$

$$2.7 \quad \Delta k = k_{sea\ ice} \left(\frac{V_{sea\ ice}}{V_{total}} - 1\right) + k_{crude\ oil} \left(\frac{V_{crude\ oil}}{V_{total}}\right)$$

$$2.8 \quad \Delta k = 2.11 - 0.011\Delta T + 0.13 \left(\frac{S}{\Delta T}\right)$$

where k is the thermal conductivity in (W/m·K); γ is the specific gravity of the crude oil, T is the temperature in K (2.4) and °C (2.5); S (ppt) – bulk salinity; V – volume.

Resonance Perturbation, a Cavity Perturbation Method presented in (Chen et al., 2004) was used to determine the relative dielectric constant of a subset of the extracted crude oil samples to examine the impact of weathering on the electromagnetic properties of crude oil (see Section 7.9 of the Appendix for additional details). Cavity perturbation is a relative permittivity measurement technique that makes use of an electromagnetic cavity resonator (custom design fabricated by Professor Gregory Bridges, Advanced RF Systems Lab). In this technique, the electromagnetic reflection coefficient ($|S_{11}|$) at the input to the cavity is measured using a vector network analyzer for a range of frequencies when the cavity is empty and when the cavity is perturbed by the sample of interest. The permittivity of the sample can be determined from the frequency shift in the local minima of $|S_{11}|$ and the change in the phase of $|S_{11}|$ between the empty and perturbed cases. The relative dielectric constants for the

weathered crude oil samples were calculated from their respective $|S_{11}|$ data using Eq. (2.9) and (2.10).

$$2.9 \quad \psi = [\sin(\frac{m\pi}{2})\sin((\frac{p\pi}{d}) * 100 \text{ mm})]^2$$

$$2.10 \quad \epsilon'_r = 1 - 2 \left[\frac{(f_s - f_0)}{f_0} \frac{V_C}{4 \psi V_S} \right]$$

where m and p – correspond to the resonant mode TE_{m0p} propagating within the cavity; V_S – oil sample volume; V_C – resonant cavity volume; f_s – frequency at which the local $|S_{11}|$ minimum occurs when perturbing the cavity with the oil sample in a glass tube; f_0 – frequency at which the local $|S_{11}|$ minimum occurs when perturbing the cavity with the empty glass tube (i.e., the “unperturbed” case). Eq. (2.9) provides ψ , a correction factor for the electric field strength of the TE_{m0p} modes at the perturbation location within the cavity, and Eq. (2.10) solves for ϵ'_r , the real component of relative complex permittivity.

Modeling Complex Permittivity. The relative complex permittivity of a medium affects the measured radar or radiometric signature of the profile interrogated by a remote sensing platform. As sea ice is a mixture of several media (pure ice, brine, air, precipitated salts), the effective complex permittivity of sea ice can be modeled as a function of the permittivities of its constituent components (Ulaby and Long, 2014). For this research, we used the three-phase Polder-van Santen/de Looer mixture model Eq. (2.11) to account for the crude oil encapsulated within sea ice (Neusitzer et al., 2018).

$$2.11 \quad \epsilon_{eff} = \epsilon_i + 3v_b \epsilon_{eff} \frac{\epsilon_b - \epsilon_i}{\epsilon_b + 2\epsilon_{eff}} + 3v_{oil} \epsilon_{eff} \frac{\epsilon_{oil} - \epsilon_i}{\epsilon_{oil} + 2\epsilon_{eff}}$$

Here ϵ denotes relative permittivity, v denotes volume fraction and the subscripts i and b denote ice and brine respectively. This model was applied to the ice samples collected

February 10, 15, and March 14 for a frequency of 5.5 GHz to coordinate with the center frequency of the polarimetric scatterometer system used during this experiment (Firoozy et al., 2018). Note that ϵ_{oil} was determined by the cavity perturbation method at 1.8 GHz. This was due to the upper limits of the possible frequency ranges applicable to the apparatus and method used. However, $\epsilon_{oil}[1.8 \text{ GHz}]$ is expected to have a reasonably similar value as to what it would have at 5.5 GHz as these frequencies are above the relaxation frequency of crude oil (Friisø et al., 1998). Above the relaxation frequency, the permittivity of a material tends to very gradually decrease with frequency; that is until ionic and electronic dispersion occurs at much higher frequencies ($\geq \text{THz}$).

Modeling Normalized Radar Cross-Section. The normalized radar cross-section (NRCS) (VV polarization) of the oil-contaminated sea ice was simulated using the PRISM-1 forward scattering model (Ulaby and Long, 2014). Other appropriate surface scattering models for sea ice which could have been used include the Integral Equation Model (I²EM) (Fung et al., 2002; Ulaby and Long, 2014) and Boundary Perturbation Model (BPT) (Firoozy et al., 2015; Imperatore et al., 2009). The surface roughness of the profile is assumed to be 5 millimeters, and the reference look angle is 40 degrees. The frequency of simulation is 5.4 GHz, like that of the RADARSAT Constellation Mission (RCM) or the European Sentinel-1. The equations pertaining to the NRCS simulation are provided in Section 7.10 of the Appendix. Simulations were conducted with these parameters fixed, as the intent of this model is to demonstrate the extent of the impact of oil in sea ice.

2.4 Results and Discussion

2.4.1 Crude Oil Distribution and Sea Ice Thermodynamic Properties

The maximum oil volume fraction found in the ice core samples taken on February 10 occurred in the ice core slice corresponding to the point of oil introduction (5-7 cm) (Fig. 2.2). As air temperatures warmed (≥ -5 °C) (Fig. 2.1) and brine volumes increased (Dickins and Buist, 1999; Golden et al., 1998; Martin, 1979a), oil migrated up towards the ice surface, doubling its volume by February 15th (Fig. 2.2). Due to the lower density of the technical oil mixture (816 kg/m^3) (85% paraffinic: 15% aromatic by GC-MS) and the weighted average of its constituents (Table 2.2) relative to that of seawater/brine ($>1020 \text{ kg/m}^3$), the components of oil naturally migrated up towards the ice-air interface, through brine channels, air pockets and/or fractures within the ice (Cartagena, 2002; Fingas and Hollebone, 2003), where the density is much lower ($<1.5 \text{ kg/m}^3$).

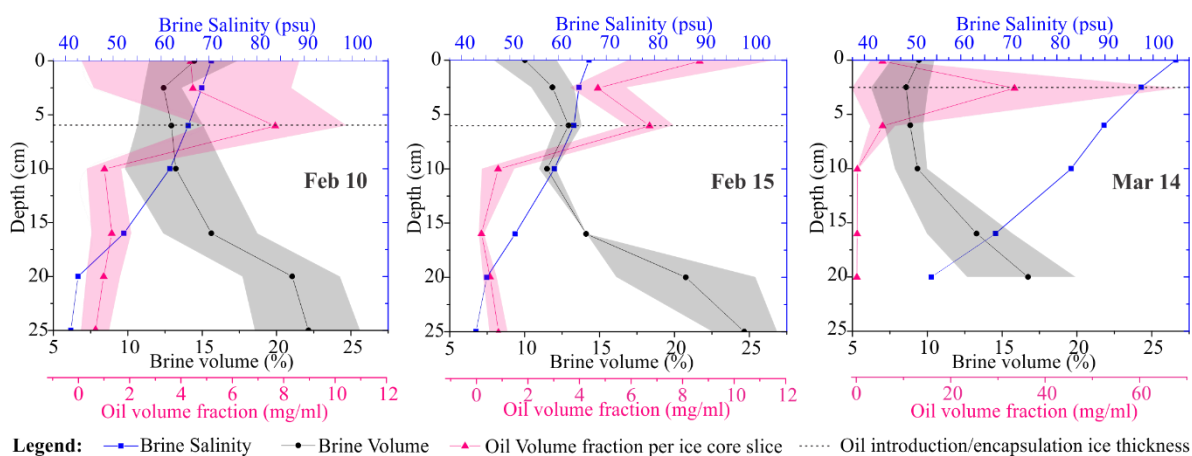


Fig. 2.2 Sea ice thermodynamic properties and crude oil content averaged (std. dev.) over the vertical cross sections of sampled ice cores. Note that (Cox and Weeks, 1983; Leppäranta and Manninen, 1988) were used for calculating the brine salinities and volumes.

On March 8th, at the beginning of phase 2 of the experiment, crude oil was present as a surface slick (3-4 cm thick) over the open water and was therefore further subjected to weathering processes such as evaporation, emulsification, dissolution, and photooxidation (Faksness et al., 2011). As wind strength increased, creating turbulence in the tank and consequent mixing of the surface crude oil with the underlying water, pancake ice began to form as the temperature dropped below -18°C (Fig. 2.1). Crude oil permeated the slush present between the ridged roundish ice surfaces. As the ice area increased, turbulence in the water decreased and the majority of the crude oil was encapsulated under the ice forming a series of liquid lenses approximately 2.5 cm below the ice surface (Fig. 2.2). Such behavior was observed before by Buist and Dickins, 1987.

Formation of the ice in the presence of strong wind leads to an increased porosity of the sea ice. To evaluate the difference in porosity between phase 1 and phase 2 of the experiment, the densities of cores 9 and 16 were experimentally determined. The air-inclusive densities found for these cores were 0.91 and 0.78 g/cm³, respectively. Furthermore, the μ -CT computed air volume fraction for samples 9 (0-2.5 cm), 9 (2.5-5 cm), and 16 (0-4 cm) was found to be 2.2, 1.4, and 4.6 %, respectively, in overall agreement with the experimentally determined densities. These results clearly show a significant increase in porosity for phase 2 of the experiment by a factor of ~2.5. Three-dimensional ensembles of the reconstructed X-ray samples can be seen in Fig. S2.1 (Appendix Section 7.1).

Air temperatures were lower during the second phase of the experiment giving rise to an increase in brine salinity and a decrease in brine volume fraction (Fig. 2.2). The averaged brine volume fraction and bulk salinity profiles seen for both phases of the experiment show

a normal c-shape (Fig. 2.2 and Fig. S2.2A – Appendix Section 7.1) (Martin, 1979b; Weeks, 1986) and the vertical ice temperature profile characteristically increased downwards the sea ice column (Fig. 2.1). These results clearly suggest that the sea-ice growth in the tank emulates natural sea ice (Notz and Worster, 2009; Weeks, 1986).

The influence of the oil on ice temperature was less pronounced in the 2017 experiment compared to the 2016 field season due to a minor crude oil impact on sea ice albedo. During the 2016 season, much of the crude oil migrated onto the ice surface through the sides of the tank allowing for a larger surficial oil magnitude in addition to a greater crude oil volume found in ice cores (i.e., 2 times higher on average). As crude oil absorbs light due to its low albedo, sea ice temperature increases, which provokes brine drainage and constrains the ice growth (Desmond et al., 2019c). However, this effect was only established when a substantial oil volume fraction occurred as seen in the 2016 experiment. For this reason, a strong correlation between oil volume fraction and ice thickness was observed only in the 2016 experiment ($R^2=0.75$).

The loss of salinity in the 2017 season is associated with brine displacement, which occurred during crude oil migration. For this reason, a stronger correlation between oil volume fraction and bulk salinity within the top section of the ice ($R^2=0.82$) was observed in this experiment (Fig. 2.3A) compared to the 2016 experiment ($R^2=0.46$) (Desmond et al., 2019c). This impact of oil on surface salinity is further demonstrated by the bulk salinity and brine volume profiles exhibited by the February 15 sampling set when a large oil volume reached the ice surface resulting in a salinity decrease for the top of the ice in comparison to

February 10 (Fig. 2.2 and Fig. S2.2B – Appendix Section 7.1). However, the warmer ambient condition preceding February 15 also had an impact on the change in the salinity profiles.

Based on the above evidence, we postulate that the primary cause of sea ice temperature increase for the 2016 experiment was caused by a lowering of albedo. Whereas for the 2017 experiment, the warming of the sea ice was presumably a direct result of salinity loss which acted to increase the thermal resistivity of the ice (Eq. (2.5)). Both of these processes act to influence the overall sea ice temperature; however, they differ fundamentally in their processes.

Migration of crude oil on the ice surface from February 10 to February 15 contributed to a decreased bulk salinity and therefore the modeled thermal conductivity (~ 0.5 W/mK) and resulted in an approximate 0.6 °C increase of the surface ice temperature. Similarly, a sharp dip in the thermal conductivity of contaminated sea ice (~ 1.5 W/mK) on March 14 occurred at the ice depth of 2.5 cm, due to the large oil fraction encapsulated at this depth, and resulted in an approximate 2.4 °C increase of the surface ice temperature. For comparison, a maximum temperature increase of ~ 4 °C was experimentally observed for the first 2.5 cm of ice in the former 2016 experiment due to the oil presence (Desmond et al., 2016c). This contrast is likely a result of the differences between the oil migration and oil magnitude seen for both experiments, as well as the ambient temperature and intensity of sunlight.

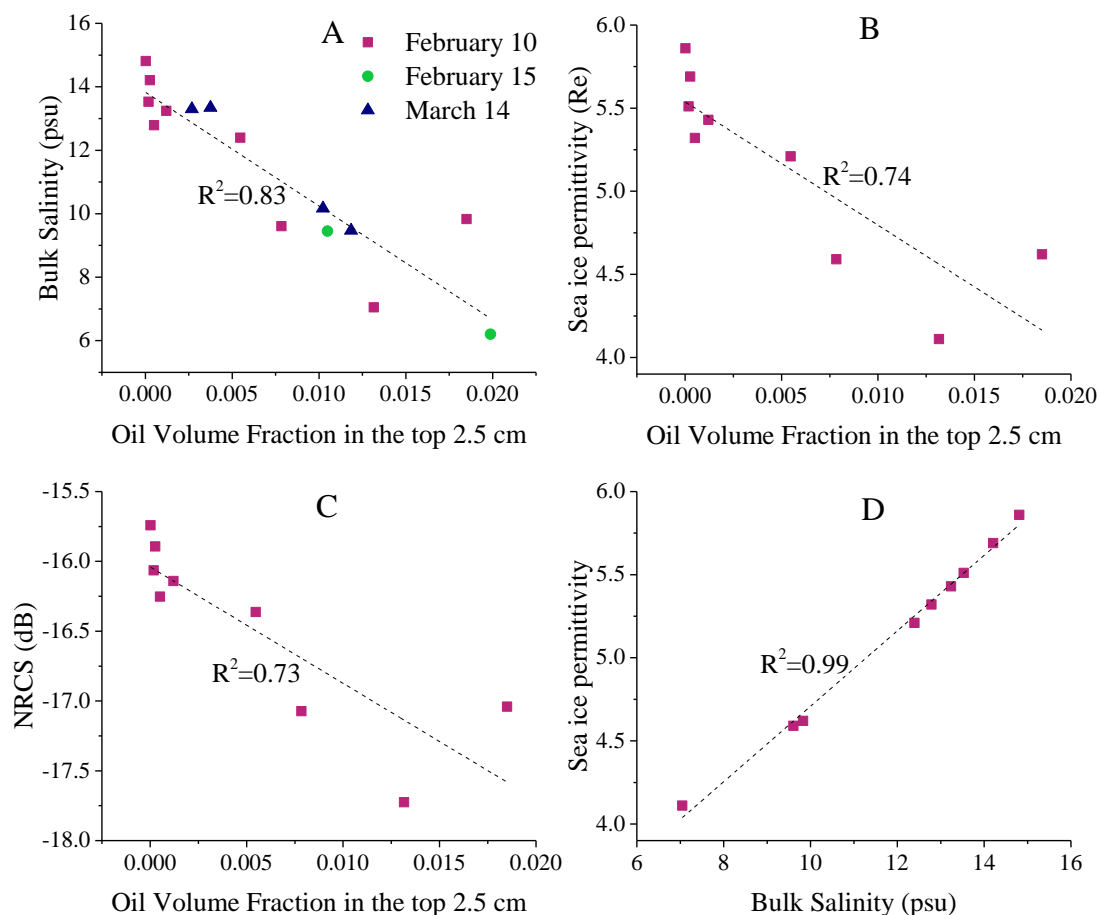


Fig. 2.3 A, B, C -Plots of crude oil volume fraction (air neglected) in the top 2.5 cm (phase 1 ice core samples), corresponding bulk salinity, modeled NRCS signal (VV polarization at 40 degrees with a root-mean-square surface roughness of 5 millimeters) and modeled sea ice permittivity (5.5 GHz). D - Modeled sea ice permittivity (5.5 GHz) vs bulk salinity. B, C, D graph constructed based on samples collected on February 10/2017.

2.4.2 Effect of Dissolution on Crude Oil Partitioning

In order to identify the migration trends in the ice cores, we conducted PCA on the concentration data of chemical compound groups (Fig. 2.4). Each ice core was separated into top and bottom sections. The top section includes the sum of all the analyzed compounds (Σ_{AC}) in the ice core slices from the ice surface down to the core slice at the crude oil

introduction ice thickness (5-7 cm). The bottom section, therefore, includes the Σ_{ACs} below 7 cm down to the ice-water interface. Each core was then chemically designated as being either low or more highly contaminated with oil depending on the ratio of $\Sigma_{AC\ top}/\Sigma_{AC\ bot.}$ More specifically, the more highly contaminated cores had $\Sigma_{AC\ top}/\Sigma_{AC\ bot} > 25$ and a concentration of more than 1 mg/mL (crude oil mass per melted sample volume) whereas the lower contaminated cores had $\Sigma_{AC\ top}/\Sigma_{AC\ bot} < 3$ with a concentration of less than 0.84 mg/mL.

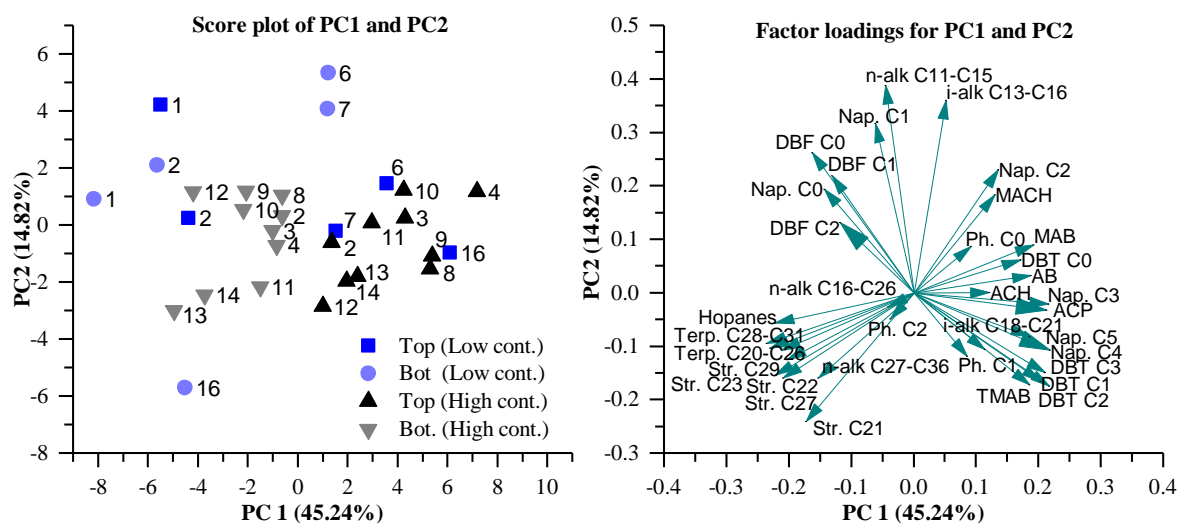


Fig. 2.4 Principal component analysis of the samples using PC2 and PC3 components. n-alk – straight chain alkanes; i-alk – isoprenoid and methyl substituted alkanes; ACP – alkylcyclopentanes; ACH – alkylcyclohexanes; MACH – methylalkylcyclohexanes; Str. – steranes; Terp. – terpanes; AB – alkylbenzenes; MAB – methylalkylbenzenes; TMAB – trimethylalkylbenzenes with isoprenoid chain; Nap – naphthalene; Ph. – phenanthrene; DBT – dibenzothiophene; DBF – dibenzofuran; C0, C1, C2, C3, C4, C5 – correspond to the number of methyl substitutions.

The score plot for PC1, which gives rise to 45% of the observed variability, shows that the data can be categorized into two clusters along this axis (Fig. 2.4). The component loading vectors for the cycloalkanes, alkylbenzenes, and PAH compounds generally align in

the more positive direction along PCA 1 being more predominate in the top more highly contaminated ice core sections. Conversely, the component loading vectors for the terpanes, steranes, and heavy MW n-alkanes tend to align in the more negative direction and are more predominate in the bottom core sections. The heavier and lighter compounds are separated along the PCA 2 axis contributing to ~14% of the total variability corresponding to some of the low contaminated slices.

Encapsulated crude oil in sea ice is present in the form of disks with different diameters (Desmond et al., 2018a). Once brine channels expand, crude oil has the potential to interact with brine. The degree of interaction is dependent on oil droplet size. Heavier crude oil droplets will experience higher buoyant force and will reach the surface faster than smaller droplets. Since the crude oil volumes in cores 1, 6 and 7 were low, the oil stayed at the same depth longer, allowing more water-soluble and volatile compound groups (Table 2.2) such as the shorter chain n- and i-alkanes, the C₀ and C₁ naphthalenes, C₀ and C₁ dibenzofurans to interact, dissolve, and follow the brine. Additionally, compounds present in smaller droplets dissolve more efficiently due to a higher surface area per molecule compared to larger droplets. This phenomenon is also observed in n-alkanes concentrations, which follow the salinity profiles in low contaminated ice cores (Fig. S2.3 – Appendix Section 7.1).

PC3 and PC 4 described an additional 3.3 and 2.1 % respectively. However, this data was not presented herein since the clustering of the samples, as well as directions of loading vectors, are similar to PC 1 and PC2.

The individual compound concentrations change in the sea ice cross-sections with the ice depth. The chemical composition at the oil introduction ice thickness best resembles the

technical oil mixture. The plots of MW vs. percent composition of steranes and terpanes in ice-cores 1 and 2 (low and high contaminated ice cores, respectively) is shown in Fig. 2.5. The results demonstrate that the low MW compounds tend to move up through the ice core whereas the higher MW compounds migrate down towards the ice-water interface. This relationship is more visible in low contaminated cores. The plot also shows a decrease of data dispersion (or an increase in data association) with a decrease in crude oil concentration. This phenomenon shows the partitioning of oil compounds by molecular weight after initial dissolution in brine where lower content of crude oil dissolves more efficiently and shows a clear connection between dissolution and partitioning.

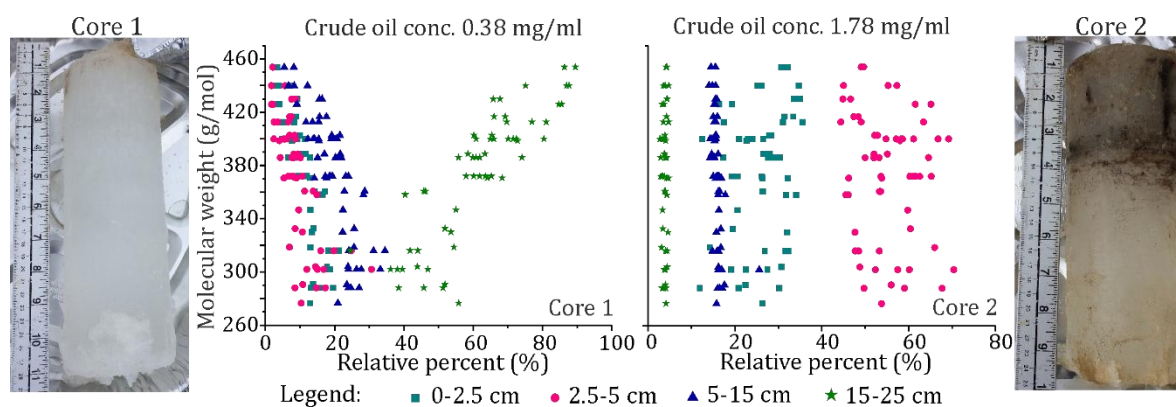


Fig. 2.5 Partitioning of steranes and terpanes within the vertical cross-section of the low contaminated and high contaminated ice cores. We calculated the relative percent of an individual compound per slice as a concentration of the individual compound in the slice divided by the total of its concentration in the ice core.

To provide further evidence on the connection between dissolution and oil magnitude, Spearman correlation coefficient was used to calculate the strength of the relationship between bulk salinity, the chemical composition of ACs and the crude oil volume fraction (Fig. 2.6). Low contaminated ice cores show higher values for almost every analyzed group of compounds in comparison to the more highly contaminated ice cores. This demonstrates

the tendency of oil to dissolve and follow the depth profile of brine within the more lightly contaminated ice cores (Fig. S2.3 – Appendix Section 7.1).

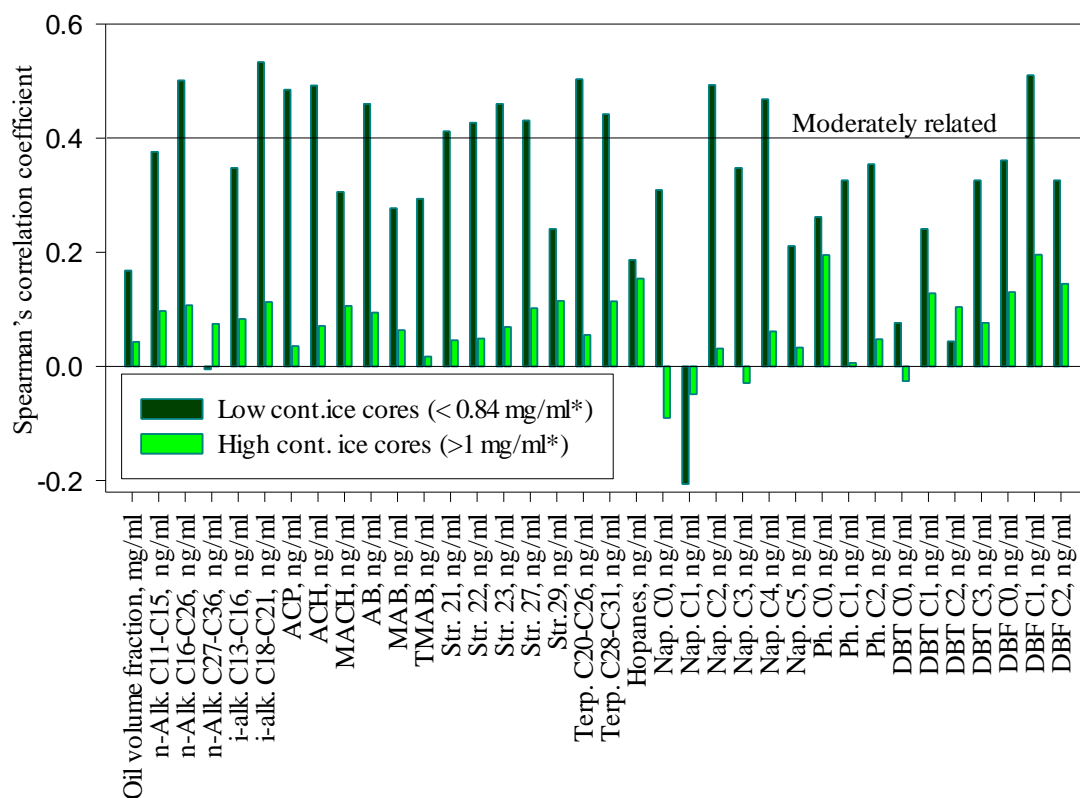


Fig. 2.6 Strength of the relationships between bulk salinity with crude oil volume fraction and analyzed compound concentrations in low and high contaminated ice cores evaluated using Spearman's rank correlation coefficient (mg/mL*- mg of crude oil per 1 mL of melted ice core sample).

Crude oil partitioning is ultimately explained by a difference in the physical properties (e.g., density, vapor pressure, solubility, molecular weight, and volume) of the oil constituents and their interactions with the sea ice environment. Therefore, COSMO-RS (Table 2.2) was used to help predict the behavior of compounds in sea ice. For example, the computed solubility, vapor pressure and liquid density of tetramethylnaphthalenes are

respectively 4.8, 1.4 and 1.1 times lower than methylphenanthrenes (based on calculated properties of representative compound isomers) despite their relatively close molecular weights (i.e., 184 and 192 g/mol respectively) and molecular volumes (197 and 185 Å³ respectively). Consequently, solubility is the most prominent property which differentiates these two molecules.

The profile of tetramethylnaphthalenes/methylphenanthrenes ratio (Fig. 2.7) resembles the bulk crude oil content distribution (Fig. 2.2). Tetramethylnaphthalene migrates more closely with the bulk crude oil due to its lower solubility than methylphenanthrene. Consequently, the averaged ratio is observed to be higher overall for the top sections of the ice relative to the bottom sections. A higher tetramethylnaphthalene concentration increased the averaged ratio at the oil introduction ice thickness from 2.1 (technical mixture) to 2.4 on February 10 and 15. Methylphenanthrene has the potential to follow the brine more closely because of its higher solubility. Consequently, dissolution and subsequent migration of methylphenanthrene towards the water-ice interface acted to decrease the ratio below the oil introduction ice thickness. The slight increase in the ratio from a depth of 16 cm to 25 cm is likely a result of the increased dissolution of methylphenanthrene into the water column owing to its higher solubility, similar to migration tendencies described in (Desmond et al., 2019c; Payne et al., 1991). The ratio shows the same pattern through the whole experiment.

Coupling the observed dissolution of the light fraction of crude oil in the brine with the presence of crude oil-degrading bacteria in sea ice (Brakstad et al., 2008; Delille et al., 1997) may result in effective bioremediation of crude oil in the Arctic. The light fraction of crude oil is toxic for marine animals (Anderson et al., 1974) and the success of its

bioremediation will be crucial. We predict that microbial biodegradation will effectively increase as the concentration of crude oil in the ice decreases due to the growth of the dissolution efficiency.

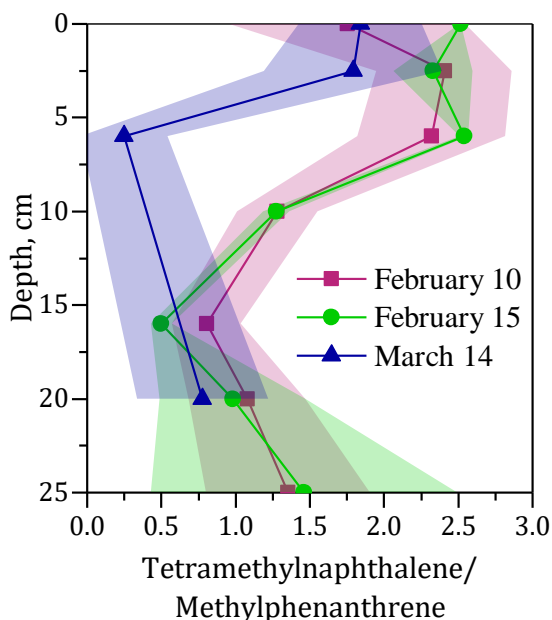


Fig. 2.7 Distribution Tetramethylnaphthalenes/Methylphenanthranes ratio in the sea ice cross section.

2.4.3 Evaporation

We investigated the physical properties (i.e., dielectric constant and thermal conductivity) of five highly contaminated crude oil samples (two intervals of core 4, 11, 13 and 14) derived from the first 5 cm of the ice to establish the effect of evaporation and photooxidation processes on the crude oil dielectric constant. We also analyzed 30 samples (including the five samples above) derived from the first 7.5 cm on ATR-IR for accurate comparison with physical properties, taking into account the polar, paraffin, and asphaltene fractions (Fresco-Rivera et al., 2007; Klein, 2012; Wang and Stout, 2016).

The first two sampling dates (February 10 and February 15) show an overall steady decrease of the relative oil permittivity (i.e., dielectric constant) in comparison to the technical mixture (Table 2.3). However, a marginal decrease in the aliphatic index, calculated as $(1450+1376)\text{cm}^{-1}/A_{\text{tot}}$, an increase in the long-chain index $(724\text{cm}^{-1}/(1450+1376)\text{cm}^{-1})$, as well as growth of aromatic condensation $(A(864+814+743)\text{cm}^{-1}/A_{\text{tot}})$ (Fernández-Varela et al., 2006) (Table 2.3) should act to increase the permittivity (Table 2.1, Table 2.2).

The decreases in relative permittivity seen for the February 10 and 15 oil samples can be explained by two facts. Firstly, an overall increase in lower molecular weight n-alkanes relative to higher can be seen in the surficial ice (top 2.5 cm) according to GC-MS data (Table 2.3), which would act to decrease the relative permittivity of the surficial oil (Table 2.1, Table 2.2). Secondly, crude oil is not only a mixture of compounds, but it is also a mixture of an enormous number of molecular interactions (Punase and Hascakir, 2017). Interactions of asphaltenes with saturate, aromatic and resin fractions play an essential role in total crude oil polarity, and we can measure the interactions by Colloidal Instability Index (CII) which decreases with an increase of stability of the mixture (Loeber et al., 1998) and decrease of mixture polarity (Likhatsky and Syunyaev, 2010):

$$2.12 \quad CII = \frac{\text{Asphaltenes} + \text{Saturates}}{\text{Aromatics} + \text{Resins}}$$

Based on the formula, the observed decrease in permittivity can be attributed to the faster loss of saturates (aliphatic index) in comparison to the total aromatic content including resins and asphaltenes (aromaticity index calculated as $1600/A_{\text{tot}} \text{ cm}^{-1}$) (Table 2.3), which leads to an increase in asphaltenes interaction with resin and decreases the polarity of the mixture. For the confirmation of this theory, the change in saturated, aromatic, resin and

asphaltene fractions as well corresponding dielectric constants should be measured in future research.

Table 2.3 Evolution of crude oil in sea ice: Changes in physical, chemical, and optical properties

	Technical oil mixture	February 10	February 15	March 14
<i>Physical properties (Averaged)</i>				
Dielectric constant	2.24	2.10	1.98	2.32
Thermal conductivity [mW/(m·K)]	127	120	103	126
Albedo in visible spectrum (390-700 nm)**	0.31*	0.69	0.43	0.33
Light transmittance ratio (390-700 nm)**	0.21*	0.41	0.35	0.25
<i>Chemical properties (Averaged)</i>				
<i>GC-MS</i>				
n-Alkanes C ₁₁ -C ₁₅ / C ₂₇ -C ₃₆ (top 2.5 ice cm)	13.24	27.66	32.49	2.87
n-Alkanes C ₁₆ -C ₂₆ / C ₂₇ -C ₃₆ (top 2.5 ice cm)	7.75	46.94	32.03	16.10
<i>ATR-IR Spectral Indexes</i>				
Aliphatic	0.80	0.77	0.77	0.71
Long chain index	0.04	0.05	0.05	0.06
Aromaticity index	0.003	0.004	0.004	0.004
Di- and monosubstituted aromatic rings	0.52	0.51	0.51	0.66
Three substituted aromatic rings	0.41	0.41	0.41	0.29
Aromatic condensation	0.15	0.16	0.17	0.22
Carbonyl (Ketones/Esters)	0.018	0.018	0.025	0.030
Ether (Ester)	0.001	0.001	0.001	0.021

*- crude oil presence in the open water during the transition time between phases

** - values for crude oil-contaminated sea ice

2.4.4 Photooxidation

Photooxidation polarizes the molecules and should increase the permittivity of the crude oil through its incorporation of heteroatoms. For confirmation, the physical properties of 1,8-dimethyl naphthalene and the products after its photooxidation - 1-methoxy-8-methylnaphthalene-1-ketal and 1-methoxy-8-methylnaphthalene-1,4-diol (Sydnes et al., 1985) were modeled (Table 2.2). To observe the extent of interaction and impedance of sunlight by the oil's presence, the albedo and transmission of photosynthetically active radiation (PAR) within the visible region (390-700 nm) were monitored. A steady decrease of sea ice albedo and transmittance was observed over the three sampling dates (Table 2.3)

owing to the systematically larger magnitudes of oil found towards the surface of the ice at these times (Fig. 2.2). Furthermore, despite the decrease in ice thickness measured on March 14 compared to the other two sampling dates, a reduced transmittance was observed in contrast to that which would have been seen in the absence of oil.

Solar radiation could still transmit through the oil-contaminated sea ice (Table 2.3) due to the dispersion of oil. Photochemical transformations were first observed on February 15 in an increase of IR absorbance bands of C=O (ketone and ester) at $1720 - 1690\text{ cm}^{-1}$, evaluated as a ratio $A(1717+1707+1700)\text{ cm}^{-1}/A_{\text{tot}}$, and almost doubled by March 14 relative to the start of the experiment.

During the transition between phases when the ice was melted and the crude oil was presented as a surface slick over open water, the oil exhibited massive sunlight absorption and its lowest observed albedo and transmittance (Table 2.3). The associated photooxidation resulted in an increase of the C-O (ester) absorbance band (Table 2.3; Fig. S2.4 – Appendix Section 7.1), evaluated as $A(1250\text{ cm}^{-1})/A_{\text{tot}}$, on March 14, indicating a growth in the transformations of aromatic ring structures to esters. Furthermore, a decrease of trisubstituted aromatics $A(814\text{ cm}^{-1})/A(864+814+743)\text{ cm}^{-1}$ and an increase of mono and disubstituted aromatic rings $A(743\text{ cm}^{-1})/(864+814+743)\text{ cm}^{-1}$ was observed, possibly due to the higher liability for photooxidation of higher branched compounds (Bobinger and Andersson, 2009; Garrett et al., 1998). The photooxidation of branched aromatics is also supported by GC-MS data. For example, the tetramethylnaphthalene/methylphenanthrene ratio detected on March 14 is lower in comparison to February 10 and 15 (Fig. 2.7). We link the observed increase of oil permittivity in the March 14 samples with the photooxidation of crude oil molecules.

2.4.5 Remote Sensing Detection of Oil Spills in a Sea-Ice Environment

Permittivity (i.e., dielectrics) is not directly measured with remote sensing technologies; it is a governing factor for active microwave measurements. Microwave scattering measured by satellite or surface-based radar systems is related to the incidence angle, surface roughness, volume fractions of all the components of sea ice (brine, air, crude oil), and permittivity profile including real and imaginary parts (Firoozy et al., 2014; Ulaby and Long, 2014). Herein, we consider a surface scattering approach.

The permittivity of crude oil-contaminated sea ice is a function of temperature, the volume fractions of brine and crude oil, where crude oil has the lowest permittivity and brine - the highest (Neusitzer et al., 2018).

As can be seen from Fig. 2.8, the reduction of the profile's complex permittivity (from 5 to 4.3 for the real and 0.4 to 0.16 for the imaginary part of the complex permittivity in the top layers) was observed from February 10 to February 15. This change can primarily be attributed to a reduction of the ice's salinity (Fig. S2.2B – Appendix Section 7.1). Considering other profile parameters to be unchanged, this property alone can decrease the radar signature (i.e., NRCS). The slight leftward shift in both components of the relative permittivity profile for the ice sample from March 14 can be attributed to the temperature profile of the sea ice being colder than those of the samples from February 10 and 15 (Fig. 2.1).

The formation of liquid crude lenses during the second phase of the experiment led to a drop in both components of the permittivity at encapsulation depth (2.5 cm), as a result of the large crude oil volume and low salinity (Fig. 2.2). Such a decrease is significant and

can be expected to further impact the NRCS (Firoozy et al., 2017). The oil spill is more likely to happen in early freeze-up with a heightened shipping or industrial activity than mid-winter. Therefore, the presence of oil in the top part of the sea ice profile where it can be detected by radar is a likely scenario. During the fall freeze-up period (alike Phase 2 herein), the backscattering signature shows a general increase with sea ice thickness increase (Isleifson et al., 2010). A local measured decrease in the NRCS of newly forming sea ice could be used as a metric for detection of oil spills. Further studies that quantify the decrease under a variety of surface conditions are required for these results to be useful in an operational scenario. The research results presented in this manuscript provide baseline information that is critical for developing appropriate bounds for this metric.

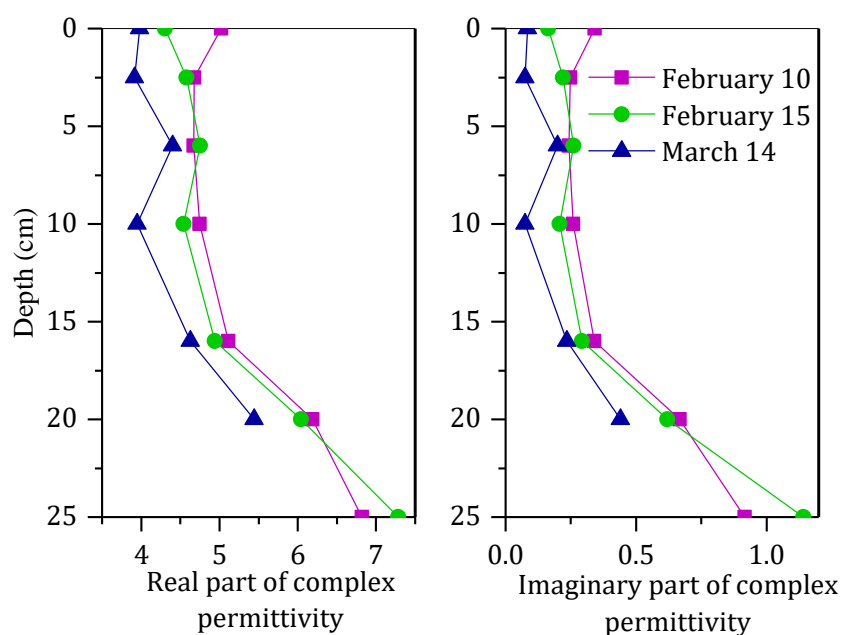


Fig. 2.8 Modeled complex permittivity of the sea ice cross section of ice cores 4 (red), 11 (green), and an average of 13 and 14 (blue), which correspond to the three respective sampling dates.

Table 2.4 provides a high-level look at the sensitivity of the normalized radar cross section values associated with a homogeneous oil-contaminated sea ice profile to changes in the relative permittivity of oil when all other factors are held constant. The HH polarization follows the trend of VV polarization very closely, and as such is not included here. As can be seen, the changes in both real and imaginary parts of the crude oil permittivity can result in distinguishable variations in simulated NRCS data.

Table 2.4 The sensitivity analysis of NRCS (dB) versus permittivity for VV polarization at 40 degrees with a root-mean-square surface roughness of 5 millimeters

	2	2.5	3	3.5	4	4.5
0	-23.46	-21.27	-19.83	-18.75	-17.90	-17.20
0.2	-23.32	-21.21	-19.79	-18.73	-17.89	-17.19
0.4	-22.92	-21.03	-19.70	-18.67	-17.85	-17.16
0.6	-22.35	-20.76	-19.54	-18.57	-17.78	-17.11
0.8	-21.70	-20.42	-19.33	-18.44	-17.68	-17.04
1	-21.02	-20.02	-19.09	-18.27	-17.57	-16.96

Note: The first column represents the imaginary, and the first row represents the real part of the effective permittivity of the oil-contaminated profile.

Our past experiments with a polarimetric C-band scatterometer system (Firoozy et al., 2017) have shown that a change of at least 2 dB would be necessary for detecting an oil spill event in this configuration. Analysis must take the signal to noise ratio into account, as well as limited radiometric samples that are used to calculate the NRCS. From Fig. 2.3, a significant decrease in the surficial sea ice dielectrics and NRCS can be seen for the first sampling date in which a lowering of 2 dB is observed for a 1% oil volume fraction (air neglected) when comparing sea ice sections with lowest to highest salinity. Moreover, a decrease of 5 dB (VV polarization), 5.5 dB (HH polarization), and 4.5 dB (VH polarization) were observed experimentally 4-hours after oil injection (Firoozy et al., 2018).

As was described in Sections 2.4.3 and 2.4.4, weathering processes affect the permittivity and thermal conductivity of crude oil (Table 2.3) owing to changes in oil composition. A close connection between oil density (Eq. (2.4)) and relative permittivity is observed between the oil mixture (Table 2.3) and its individual constituents (Table 2.2, Eq. (2.1)). These changes have the potential to be detected via remote sensing systems via an inversion algorithm e.g., Firoozy et al. (2018, 2017, 2015), allowing for the inferred state of oil composition (i.e., light, medium, heavy) remotely and thus a faster implication of an appropriate mitigation response (Desmond et al., 2018b). However, small changes in the ambient temperature impact brine volume which is the major contributor to microwave scattering from the sea ice. Therefore, further research under a variety of constant temperatures with the use of different types of fuel is required to determine a detection limit for the minimum crude oil volume fraction that would produce a noticeable change in the NRCS of the sea ice.

2.5 Conclusion

Dissolution, evaporation, and photooxidation altered the chemical composition of the crude oil within a sea ice environment. The dissolution percentage of the light oil fraction increased with decreases in oil concentration. In this experiment, samples with a crude oil concentration more than 1 mg/mL tended to move toward the ice surface perturbing brine, whereas the oil constituents of lightly contaminated cores tended to dissolve and follow the path of brine. We explain this effect by the limited interface area of the brine with crude oil, which is higher in the low contaminated ice cores, as well as higher buoyancy of larger droplets which drove them to the surface faster. Oil concentrated low MW compounds at the

ice surface, and high MW compounds at the ice-water interface after being dissolved in brine. The separation between compounds is governed by their physical properties such as density, molecular size and weight, solubility, and vapor pressure.

Evaporation affected low MW compounds which migrated on the ice surface. It acted to decrease the crude oil permittivity (in part) due to losses of low MW alkanes and higher volatilization of saturates in comparison to aromatics, which increased asphaltenes interaction with resin and decreased the polarity of the mixture. Photooxidation peaked when the ice was melted entirely and enlarged the permittivity of the crude oil due to transforming branched aromatics to esters and ketones. When crude oil was encapsulated, the light penetrated the sea ice surface and could provoke photooxidation inside the ice to a smaller extent.

The permittivity of the crude oil is a function of an individual compounds concentration as well as intermolecular interaction since different bounds and forces between molecules act to increase or decrease the relative permittivity. The weathering processes influence crude oil permittivity and the changes may produce sufficient quantifiable differences in the NRCS of the ice. However, we need to consider that the permittivity of crude oil contaminated sea ice can also be influenced by fluctuations in ambient temperature, salinity, air, and crude oil volume fraction, which may affect complex permittivity in greater extent. Consequently, directly inferring the composition of an oil (light, medium, heavy) may not be feasible through direct monitoring with radar but may be feasible through the use of an inversion algorithm facilitating the use of multiple technologies such as radar, lidar, and radiometry.

This study built upon the results of its predecessor (Desmond et al., 2019c; Firoozy et al., 2017; Neusitzer et al., 2018) allowing for a more complete understanding of oil behavior within sea ice and the potential for remote sensing detection and mitigation strategies. In particular, this study featured not only an oil spill from beneath sea ice but a study on the freeze-up of surfaced weathered oil in open water. Through this research, an examination of the photo-oxidation potential of oil-in-ice and above open water was conducted. A more thorough analysis was conducted on 1) oil's direct influence on brine, 2) the partitioning of oil constituents, and 3) a more comprehensive investigation as to the relationship between the density and dielectrics of oil, and the potential for not only detecting oil in sea ice, but also the possibility of inferring the oil type directly or through inversion.

2.6 Acknowledgements

This research was funded by GENICE, Genome Canada, Research Manitoba. The authors thank Canada Research Chair (CRC) programs, Natural Sciences and Engineering Research Council (NSERC) of Canada, the Canada Foundation for Innovation (CFI) and the University of Manitoba. We also thank Dave Binne (SERF Technician, CEOS), Jake Ritchie (Technician, CEOS), Gregory Bridges (Advanced RF Systems Lab, Dept. of Elec. & Comp. Eng.), Horace Luong (Dept. of Chem.), Lesa Cafferty (Cafferty's Scientific Glassblowing), as well as the Manitoba Chemical Analysis Laboratory (MCAL) and Manitoba Institute for Materials (MIM). This work was made possible by the facilities of the Shared Hierarchical Academic Research Computing Network (SHARCNET: www.sharcnet.ca) and Compute/Calcul Canada as well as Software for Chemistry & Materials (SCM).

2.7 References

- ADF2017, SCM, Theoretical Chemistry, Vrije Universiteit, Amsterdam, The Netherlands, <http://www.scm.com>
- ADF2018, SCM, Theoretical Chemistry, Vrije Universiteit, Amsterdam, The Netherlands, <http://www.scm.com>
- ADF-GUI 2017, SCM, Amsterdam, The Netherlands, <http://www.scm.com>
- Aboul-Seoud, A., Moharam, H.M., 1999. "A Simple Thermal Conductivity-Temperature Correlation for Undefined Petroleum and Coal Liquid Fractions." *Chem. Eng. Res. Des.* 77: 248–252. <https://doi.org/10.1205/026387699526043>
- Anderson, J.W., Neff, J.M., Cox, B.A., Tatem, H.E., Hightower, G.M., 1974. "Characteristics of dispersions and water-soluble extracts of crude and refined oils and their toxicity to estuarine crustaceans and fish." *Mar. Biol.* 27: 75–88. <https://doi.org/10.1007/BF00394763>
- API Tech Data Book 10, 2016.
- Atlas, R.M., Bartha, R., 1972. "Biodegradation of petroleum in seawater at low temperatures." *Can. J. Microbiol.* 18: 1851–1855. <https://doi.org/10.1139/m72-289>
- Ballesterio, H., Magdol, Z., 2011. "Biodegradation of Polycyclic Aromatic Hydrocarbons in Simulated Arctic Sea Ice Brine Channels and Protistan Predation." *Int. Oil Spill Conf. Proc.* 2011, abs272. <https://doi.org/10.7901/2169-3358-2011-1-272>
- Bobinger, S., Andersson, J.T., 2009. "Photooxidation Products of Polycyclic Aromatic Compounds Containing Sulfur." *Environ. Sci. Technol.* 43: 8119–8125. <https://doi.org/10.1021/es901859s>
- Brakstad, O.G., Nonstad, I., Faksness, L.-G., Brandvik, P.J., 2008. "Responses of Microbial Communities in Arctic Sea Ice After Contamination by Crude Petroleum Oil." *Microb. Ecol.* 55: 540–552. <https://doi.org/10.1007/s00248-007-9299-x>
- Buist, I.A., Dickins, D.F., 1987. "Experimental spills of crude oil in pack ice." *Int. Oil Spill Conf. Proc.* 1987: 373–381. <https://doi.org/10.7901/2169-3358-1987-1-373>
- Carey, A.A., Hayzen, A.J., n.d. The Dielectric Constant and Oil Analysis [WWW Document]. URL <https://www.machinerylubrication.com/Read/226/dielectric-constant-oil-analysis> (accessed 4.2.19).
- Cartagena, E., 2002. Density of Seawater - The Physics Factbook [WWW Document]. URL <https://hypertextbook.com/facts/2002/EdwardLaValley.shtml>
- Carter, N.A., Dawson, J., Joyce, J., Ogilvie, A., 2018. Arctic Corridors and Northern Voices: Governing marine transportation in the Canadian Arctic (Arviat, Nunavut community report).

Chen, L.F., Ong, C.K., Neo, C.P., Varadan, V. V., Varadan, V.K., 2004. Microwave electronics : measurement and materials characterization. Wiley.

Comiso, J.C., Parkinson, C.L., Gersten, R., Stock, L., 2008. "Accelerated decline in the Arctic sea ice cover." *Geophys. Res. Lett.* 35: L01703.
<https://doi.org/10.1029/2007GL031972>

Cox, G.F.N., Weeks, W.F., 1983. "Equations for Determining the Gas and Brine Volumes in Sea-Ice Samples." *J. Glaciol.* 29: 306–316.
<https://doi.org/10.3189/S0022143000008364>

Crabeck, O., Galley, R., Delille, B., Else, B., Geilfus, N.-X., Lemes, M., Des Roches, M., Francus, P., Tison, J.-L., Rysgaard, S., 2016. "Imaging air volume fraction in sea ice using non-destructive X-ray tomography." *Cryosph.* 10: 1125–1145.
<https://doi.org/10.5194/tc-10-1125-2016>

Delille, D., Bassères, A., Dessommes, A., 1997. "Seasonal Variation of Bacteria in Sea Ice Contaminated by Diesel Fuel and Dispersed Crude Oil." *Microb. Ecol.* 33: 97–105.
<https://doi.org/10.1007/s002489900012>

Desmond, D., Crabec, O., Lemes, M., Polcwiartek, K., Neusitzer, T., Saltymakova, D., Snyder, N., Rysgaard, S., Barber, D., Stern, G., 2018a. "Investigation into the geometry and distribution of oil inclusions in sea ice using non-destructive X-ray microtomography and its implications for remote sensing and mitigation potential." In: ArcticNet Annual Scientific Meeting. Ottawa.

Desmond, D., Neusitzer, T., Firoozy, N., Isleifson, D., Lemes, M., Barber, D.G., Stern, G.A., 2019a. "Examining the physical processes of corn oil (medium crude oil surrogate) in sea ice and its resultant effect on complex permittivity and normalized radar cross-section." *Mar. Pollut. Bull.* 142: 484–493.
<https://doi.org/10.1016/J.MARPOLBUL.2019.03.067>

Desmond, D., Neusitzer, T., Isleifson, D., Saltymakova, D., Wolfe, T., Polcwiartek, K., Snyder, N., Barber, D., Stern, G., 2018b. Remote sensing of oil spills in a sea ice environment: investigations on oil composition and mitigation potential, in: ArcticNet Annual Scientific Meeting. Ottawa.

Desmond, D., Neusitzer, T., Lemes, M., Isleifson, D., Saltymakova, D., Mansoori, A., Barber, D., Stern, G., 2019b. Examining the Physical Interactions of Corn Oil (Medium Crude Oil Surrogate) in Sea Ice and its Potential for Chemical Partitioning within an Arctic Environment, in: 42nd AMOP Technical Seminar on Environmental Contamination and Response. Halifax, Canada.

Desmond, D., Saltymakova, D., Neusitzer, T., Firoozy, N., Isleifson, D., Barber, D.G., Stern, G.A., 2019c. "Oil behavior in sea ice: Changes in chemical composition and resultant effect on sea ice dielectrics." *Mar. Pollut. Bull.* 142: 216–233.
<https://doi.org/10.1016/J.MARPOLBUL.2019.03.021>

Dickins, D., Buist, I., 1999. "Countermeasures for Ice Covered Waters." *Pure Appl. Chem.* 71: 173–191. <https://doi.org/10.1351/pac199971010173>

Dielectric Constants of common Liquids [WWW Document], n.d. URL https://www.engineeringtoolbox.com/liquid-dielectric-constants-d_1263.html

Djokic, M.R., Dijkmans, T., Yildiz, G., Prins, W., Geem, K.M.V., 2012. "Quantitative analysis of crude and stabilized bio-oils by comprehensive two-dimensional gas-chromatography." *J. Chromatogr. A* 1257: 131–140. <https://doi.org/10.1016/J.CHROMA.2012.07.035>

Dymond, J.H., Malhotra, R., 1987. "Densities of n-alkanes and their mixtures at elevated pressures." *Int. J. Thermophys.* 8: 541–555. <https://doi.org/10.1007/BF00503641>

Elam, S.K., Tokura, I., Saito, K., Altenkirch, R.A., 1989. "Thermal conductivity of crude oils." *Exp. Therm. Fluid Sci.* 2: 1–6. [https://doi.org/10.1016/0894-1777\(89\)90043-5](https://doi.org/10.1016/0894-1777(89)90043-5)

Epov, M.I., Burshtein, L.M., Kaminskii, V.D., Kurchikov, A.R., Malyshev, N.A., Prischepa, O.M., Safronov, A.F., Stupakova, A.V., Suprunenko, O.I., 2010. "Geology and hydrocarbon resources of the continental shelf in Russian Arctic seas and the prospects of their development." *Russ. Geol. Geophys.* 51: 3–11. <https://doi.org/10.1016/J.RGG.2009.12.003>

Faith, M., 2015. "Centered Log-Ratio (clr) Transformation and Robust Principal Component Analysis of Long-Term NDVI Data Reveal Vegetation Activity Linked to Climate Processes." *Climate* 3: 135–149. <https://doi.org/10.3390/cli3010135>

Faksness, L.-G., Brandvik, P.J., 2008. "Distribution of water soluble components from Arctic marine oil spills — A combined laboratory and field study." *Cold Reg. Sci. Technol.* 54: 97–105. <https://doi.org/10.1016/J.COLDREGIONS.2008.03.005>

Faksness, L.G., Brandvik, P.J., Daae, R.L., Leirvik, F., Børseth, J.F., 2011. "Large-scale oil-in-ice experiment in the Barents Sea: Monitoring of oil in water and MetOcean interactions." *Mar. Pollut. Bull.* 62: 976–984. <https://doi.org/10.1016/J.MARPOLBUL.2011.02.039>

Fernández-Varela, R., Gómez-Carracedo, M.P., Fresco-Rivera, P., Andrade, J.M., Muniategui, S., Prada, D., 2006. "Monitoring photooxidation of the Prestige's oil spill by attenuated total reflectance infrared spectroscopy." *Talanta* 69: 409–417. <https://doi.org/10.1016/J.TALANTA.2005.10.006>

Fingas, M.F., Hollebone, B.P., 2003. "Review of behaviour of oil in freezing environments." *Mar. Pollut. Bull.* 47: 333–340. [https://doi.org/10.1016/S0025-326X\(03\)00210-8](https://doi.org/10.1016/S0025-326X(03)00210-8)

Firoozy, N., Mojabi, P., Barber, D., 2014. Microwave remote sensing of multi-layered rough-surface snow-covered sea ice dielectric profile: Sensitivity analysis and

inversion, in: 2014 IEEE Geoscience and Remote Sensing Symposium. IEEE, pp. 4872–4875. <https://doi.org/10.1109/IGARSS.2014.6947586>

Firoozy, N., Mojabi, P., Barber, D.G., 2015. "Nonlinear Inversion of Microwave Scattering Data for Snow-Covered Sea-Ice Dielectric Profile Reconstruction." *IEEE Geosci. Remote Sens. Lett.* 12: 209–213. <https://doi.org/10.1109/LGRS.2014.2332534>

Firoozy, N., Neusitzer, T., Chirkova, D., Desmond, D.S., Lemes, M.J.L., Landy, J., Mojabi, P., Rysgaard, S., Stern, G., Barber, D.G., 2018. "A Controlled Experiment on Oil Release Beneath Thin Sea Ice and Its Electromagnetic Detection." *IEEE Trans. Geosci. Remote Sens.* 56: 4406–4419. <https://doi.org/10.1109/TGRS.2018.2818717>

Firoozy, N., Neusitzer, T., Desmond, D.S., Tiede, T., Lemes, M.J.L., Landy, J., Mojabi, P., Rysgaard, S., Stern, G., Barber, D.G., 2017. "An Electromagnetic Detection Case Study on Crude Oil Injection in a Young Sea Ice Environment." *IEEE Trans. Geosci. Remote Sens.* 55: 4465–4475. <https://doi.org/10.1109/TGRS.2017.2692734>

Fresco-Rivera, P., Fernández-Varela, R., Gómez-Carracedo, M.P., Ramírez-Villalobos, F., Prada, D., Muniategui, S., Andrade, J.M., 2007. "Development of a fast analytical tool to identify oil spillages employing infrared spectral indexes and pattern recognition techniques." *Talanta* 74: 163–175. <https://doi.org/10.1016/J.TALANTA.2007.05.047>

Friisø, T., Schildberg, Y., Rambeau, O., Tjomsland, T., Førde, H., Sjøblom, J., 1998. "Complex permittivity of crude oils and solutions of heavy crude oil fractions." *J. Dispers. Sci. Technol.* 19: 93–126. <https://doi.org/10.1080/01932699808913163>

Fung, A.K., Liu, W.Y., Chen, K.S., Tsay, M.K., 2002. "An Improved Iem Model for Bistatic Scattering From Rough Surfaces." *J. Electromagn. Waves Appl.* 16: 689–702. <https://doi.org/10.1163/156939302X01119>

Garrett, R.M., Pickering, I.J., Haith, C.E., Prince, R.C., 1998. "Photooxidation of Crude Oils." *Environ. Sci. Technol.* 32: 3719–3723. <https://doi.org/10.1021/ES980201R>

Gautier, D.L., Bird, K.J., Charpentier, R.R., Grantz, A., Houseknecht, D.W., Klett, T.R., Moore, T.E., Pitman, J.K., Schenk, C.J., Schuenemeyer, J.H., Sørensen, K., Tennyson, M.E., Valin, Z.C., Wandrey, C.J., 2009. "Assessment of undiscovered oil and gas in the Arctic." *Science* 324: 1175–9. <https://doi.org/10.1126/science.1169467>

Golden, K.M., Ackley, S.F., Lytle, V.I., 1998. "The Percolation Phase Transition in Sea Ice." *Science* (80-.). 282: 2238–2241. <https://doi.org/10.1126/science.282.5397.2238>

Government Canada, 2018. Arctic offshore oil and gas [WWW Document]. URL <https://www.rcaanc-cirnac.gc.ca/eng/1535571547022/1538586415269>

Gros, J., Nabi, D., Würz, B., Wick, L.Y., Brussaard, C.P.D., Huisman, J., van der Meer, J.R., Reddy, C.M., Arey, J.S., 2014. "First Day of an Oil Spill on the Open Sea:

Early Mass Transfers of Hydrocarbons to Air and Water." *Environ. Sci. Technol.* 48: 9400–9411. <https://doi.org/10.1021/es502437e>

Houseknecht, D.W., Bird, K.J., 1985. Oil and Gas Resources of the Arctic Alaska Petroleum Province.

Imperatore, P., Iodice, A., Riccio, D., 2009. "Electromagnetic Wave Scattering From Layered Structures With an Arbitrary Number of Rough Interfaces." *IEEE Trans. Geosci. Remote Sens.* 47: 1056–1072. <https://doi.org/10.1109/TGRS.2008.2007804>

Isleifson, D., Byongjun Hwang, Barber, D.G., Scharien, R.K., Shafai, L., 2010. "C-Band Polarimetric Backscattering Signatures of Newly Formed Sea Ice During Fall Freeze-Up." *IEEE Trans. Geosci. Remote Sens.* 48: 3256–3267. <https://doi.org/10.1109/TGRS.2010.2043954>

Jamieson, D.T., Cartwright, G., 1983. Thermal Conductivity of Cycloaliphatic Liquids, in: Thermal Conductivity 16. Springer US, Boston, MA, pp. 435–438. https://doi.org/10.1007/978-1-4684-4265-6_38

Jamieson, D.T., Irving, J.B., Tudhope, J.S., 1975. "Prediction of the thermal conductivity of petroleum products." *Wear* 33: 75–83. [https://doi.org/10.1016/0043-1648\(75\)90225-2](https://doi.org/10.1016/0043-1648(75)90225-2)

Klamt, A., Jonas, V., Bürger, T., Lohrenz, J.C.W., 1998. "Refinement and Parametrization of COSMO-RS." *J. Phys. Chem. A*. <https://doi.org/10.1021/JP980017S>

Klein, D., 2012. Infrared spectroscopy and mass spectrometry, in: Organic Chemistry. John Wiley & Sons, Inc., Danvers, Massachusetts.

Lashkarbolooki, M., Hezave, A.Z., Bayat, M., 2017. "Correlating thermal conductivity of pure hydrocarbons and aromatics via perceptron artificial neural network (PANN) method." *Chinese J. Chem. Eng.* 25: 547–554. <https://doi.org/10.1016/J.CJCHE.2016.08.025>

Lei, Q., Hou, Y.-C., Lin, R., 1997. "A new correlation for thermal conductivity of liquids." *Chem. Eng. Sci.* 52: 1243–1251. [https://doi.org/10.1016/S0009-2509\(96\)00481-2](https://doi.org/10.1016/S0009-2509(96)00481-2)

Leppäranta, M., Manninen, T., 1988. The brine and gas content of sea ice with attention to low salinities and high temperatures.

Likhatsky, V. V., Syunyaev, R.Z., 2010. "New Colloidal Stability Index for Crude Oils Based on Polarity of Crude Oil Components." *Energy & Fuels* 24: 6483–6488. <https://doi.org/10.1021/ef101033p>

List of Dielectric Constants [WWW Document], n.d. URL http://www.appliedmc.com/content/images/Dielectric_Constants.pdf

- Loeber, L., Muller, G., Morel, J., Sutton, O., 1998. "Bitumen in colloid science: a chemical, structural and rheological approach." *Fuel* 77: 1443–1450. [https://doi.org/10.1016/S0016-2361\(98\)00054-4](https://doi.org/10.1016/S0016-2361(98)00054-4)
- Louwen, J.N., Pye, C., and Lenthe, E.V., 2008. ADF2008. 01 COSMO-RS, SCM, Theoretical Chemistry [WWW Document]. Vrije Univ. Amsterdam, Netherlands. URL <https://www.scm.com/>
- Martin, S., 1979a. "A Field Study of Brine Drainage and Oil Entrainment in First-Year Sea Ice." *J. Glaciol.* 22: 473–502. <https://doi.org/10.3189/S0022143000014477>
- Martin, S., 1979b. "A Field Study of Brine Drainage and Oil Entrainment in First-Year Sea Ice." *J. Glaciol.* 22: 473–502. <https://doi.org/10.3189/S0022143000014477>
- McGlade, C.E., 2012. "A review of the uncertainties in estimates of global oil resources." *Energy* 47: 262–270. <https://doi.org/10.1016/J.ENERGY.2012.07.048>
- Montaron, B., 2012. Scale-independent mixing laws.
- Neusitzer, T.D., Firoozy, N., Tiede, T.M., Desmond, D.S., Lemes, M.J.L., Stern, G.A., Rysgaard, S., Mojabi, P., Barber, D.G., 2018. "Examining the Impact of a Crude Oil Spill on the Permittivity Profile and Normalized Radar Cross Section of Young Sea Ice." *IEEE Trans. Geosci. Remote Sens.* 56: 921–936. <https://doi.org/10.1109/TGRS.2017.2756843>
- Notz, D., Worster, M.G., 2009. "Desalination processes of sea ice revisited." *J. Geophys. Res.* 114: 5006. <https://doi.org/10.1029/2008JC004885>
- Panuganti, S.R., Wang, F., Chapman, W.G., Vargas, F.M., 2016. "A Simple Method for Estimation of Dielectric Constants and Polarizabilities of Nonpolar and Slightly Polar Hydrocarbons." *Int. J. Thermophys.* 37: 75. <https://doi.org/10.1007/s10765-016-2075-8>
- Payne, J.R., Hachmeister, L.E., McNabb, G.D., Sharpe, H.E., Smith, G.S., Menen, C.A., 1991. "Brine-induced advection of dissolved aromatic hydrocarbons to Arctic bottom waters." *Environ. Sci. Technol.* 25: 940–951. <https://doi.org/10.1021/es00017a018>
- Philp, R.P., Oung, J., Lewis, C.A., 1988. "Biomarker determinations in crude oils using a triple-stage quadrupole mass spectrometer." *J. Chromatogr. A* 446: 3–16. [https://doi.org/10.1016/S0021-9673\(00\)94412-1](https://doi.org/10.1016/S0021-9673(00)94412-1)
- Pringle, D.J., Eicken, H., Trodahl, H.J., Backstrom, L.G.E., 2007. "Thermal conductivity of landfast Antarctic and Arctic sea ice." *J. Geophys. Res.* 112: C04017. <https://doi.org/10.1029/2006JC003641>
- Punase, A., Hascakir, B., 2017. "Stability Determination of Asphaltenes through Dielectric Constant Measurements of Polar Oil Fractions." *Energy & Fuels* 31: 65–72. <https://doi.org/10.1021/acs.energyfuels.6b01045>

Pye, C.C., Ziegler, T., 1999. "An implementation of the conductor-like screening model of solvation within the Amsterdam density functional package." *Theor. Chem. Accounts Theory, Comput. Model. (Theoretica Chim. Acta)* 101: 396–408. <https://doi.org/10.1007/s002140050457>

Sen, A.D., Anicich, V.G., Arakelian, T., 1992. "Dielectric constant of liquid alkanes and hydrocarbon mixtures." *J. Phys. D. Appl. Phys.* 25: 516–521. <https://doi.org/10.1088/0022-3727/25/3/027>

Sydnese, L.K., 1991. "Oil, water, ice and light." *Polar Res.* 10: 609–618. <https://doi.org/10.1111/j.1751-8369.1991.tb00679.x>

Sydnese, L.K., Hansen, S.H., Burkow, I.C., 1985. "Factors affecting photooxidation of oil constituents in the marine environment. I. Photochemical transformations of dimethylnaphthalenes in an aqueous environment in the presence and absence of oil." *Chemosphere* 14: 1043–1055. [https://doi.org/10.1016/0045-6535\(85\)90025-6](https://doi.org/10.1016/0045-6535(85)90025-6)

Tapar, K.D., Harayama, S., 2000. "Fate of Crude Oil by the Combination of Photooxidation and Biodegradation." *Environ. Sci. Technol.* 34: 1500–1505. <https://doi.org/10.1021/ES991063O>

Ulaby, F.T., Long, D.G., 2014. *Microwave Radar and Radiometric Remote Sensing*. Univ. Michigan Press, Ann Arbor, MI, USA.

Van Dyck, C., Marks, T.J., Ratner, M.A., 2017. "Chain Length Dependence of the Dielectric Constant and Polarizability in Conjugated Organic Thin Films." *ACS Nano* 11: 5970–5981. <https://doi.org/10.1021/acsnano.7b01807>

Wang, Z., Fingas, F.M., 2003. "Development of oil hydrocarbon fingerprinting and identification techniques." *Mar. Pollut. Bull.* 47: 423–452. [https://doi.org/10.1016/S0025-326X\(03\)00215-7](https://doi.org/10.1016/S0025-326X(03)00215-7)

Wang, Z., Stout, S.A., 2016. Photochemical effects on oil spill fingerprinting, in: *Standard Handbook Oil Spill Environmental Forensics*. Academic Press, pp. 917–959. <https://doi.org/10.1016/B978-0-12-803832-1.00020-9>

Weeks, W., 1986. The Growth, Structure, and Properties of Sea Ice, in: *The Geophysics of Sea Ice*. Springer US, Boston, MA, pp. 9–164. https://doi.org/10.1007/978-1-4899-5352-0_2

Yunker, M.B., Belicka, L.L., Harvey, H.R., Macdonald, R.W., 2005. "Tracing the inputs and fate of marine and terrigenous organic matter in Arctic Ocean sediments: A multivariate analysis of lipid biomarkers." *Deep. Res. II* 52: 3478–3508. <https://doi.org/10.1016/j.dsr2.2005.09.008>

Chapter 2 featured an oil-in-ice mesocosm experiment which investigated aspects of oil behavior (i.e., migration tendencies, encapsulation potential, partitioning within sea ice, evaporation, dissolution, photooxidation) and remote sensing detection (i.e., radar). Specifically, this chapter aimed to test the following hypotheses:

1. The dissolution of lighter crude oil fractions increases with decreases in oil concentration.
2. Compounds will partition inside brine channels by molecular weight.
3. Oil permittivity is affected by composition and intermolecular interactions.
4. The presence of oil in sea ice will cause a reduction of salinity, thereby reducing the dielectrics and radar signature of sea ice.
5. The effect of oil on salinity will increase with increasing oil concentration.

Each of these assumptions was found to be true based on the data presented in Chapter 2. However, the fundamental basis for the second hypothesis still required investigation as the rationale for why compounds inside brine channels partition by molecular weight still required examination. To this end, Chapter 3 sought to provide enlightenment on this shortcoming by further studying oil behavior in sea ice (i.e., migration tendencies, partitioning within sea ice, evaporation, dissolution).

3 Methods for Interpreting Partitioning and Fate of Petroleum Hydrocarbons in a Sea Ice Environment

3.1 Abstract

Decreases in Arctic Sea ice extent and thickness have led to more open ice conditions, encouraging both shipping traffic and oil exploration within the northern Arctic. As a result, the increased potential for accidental releases of crude oil or fuel into the Arctic environment threatens the pristine marine environment, its ecosystem, and local inhabitants. Thus, there is a need to develop a better understanding of oil behavior in a sea ice environment on a microscopic level.

Computational quantum chemistry was used to simulate the effects of evaporation, dissolution, and partitioning within sea ice. Vapor pressures, solubilities, octanol-water partition coefficients, and molecular volumes were calculated using quantum chemistry and thermodynamics for pure liquid solutes (oil constituents) of interest. These calculations incorporated experimentally measured temperatures and salinities taken throughout an oil-in-ice mesocosm experiment conducted at the University of Manitoba, during 2017. Their potential for interpreting the relative movements of oil constituents was assessed. Our results suggest that the relative movement of oil constituents are influenced by differences in physical properties. Lighter molecules showed a greater tendency to be controlled by brine advection processes due to their greater solubility. Molecules which are more hydrophobic were found to concentrate in areas of lower salt concentration.

3.2 Introduction

Within the Canadian Arctic, a persistent decrease in sea-ice extent (AMAP, 2017; Arctic Sea Ice News and Analysis) has led to a tripling in ship traffic in North Canadian waters since 1990 (Andrews et al., 2017; Carter et al., 2018; Dawson et al., 2018), with most shipping activity occurring in Nunavut waters (Dawson et al., 2018). Increased shipping can potentially benefit local Arctic communities through the facilitation of new economic developments (e.g., marine tourism, food security, community accessibility, production of supplies, and reduced living expenses) (Johnston et al., 2019; Johnston et al., 2017; Kelley and Ljubicic, 2012; Carter et al., 2019; Olsen et al., 2019). However, with this increasing activity comes a higher risk of accidental spills of fuel-oils (AMAP, 2010; AMAP, 2009) and the expansion of oil resource development (Gautier et al., 2009), all of which would have adverse outcomes for local communities who coexist with their natural environment (Kelley and Ljubicic, 2012; Ford et al., 2014). The protection of water is not only vital to ensuring the sustainability of clean community drinking water but also the local ecosystem health and function. Traditional country food (e.g., caribou, fish, walrus, seals, whales, and polar bears) is a critical component to indigenous communities as they are an essential resource all year round and are vital to Inuit culture (Berkes, 2017; Ljubicic et al., 2018). Consequently, there is a need to understand the fate of petroleum contamination in an Arctic environment, so that the quality of Arctic waters and local wildlife can be better monitored and maintained.

Sea ice is a heterogeneous porous medium consisting of a pure ice matrix with embedded air pockets and liquid brine inclusions (i.e., high salinity water) (Thomas and Dieckmann, 2010). During sea ice growth, solutes from seawater as dissolved salts are

expelled from the growing ice matrix and concentrated at the ice crystal limits and interstices, forming liquid salty inclusions called brine (Thomas and Dieckmann, 2010). The top of the sea ice is in contact with the cold atmosphere, causing brine inclusions to freeze and shrink, leading to an increase in brine salinity (concentration-effect). As the sea ice temperature increases toward the bottom, brine inclusions enlarge, and their salinity decreases (dilution effect). In cold ice ($<-5\text{ }^{\circ}\text{C}$), brine channels are typically disconnected, disallowing fluid movement. However, in warmer ice (typically $\geq -5\text{ }^{\circ}\text{C}$), brine channels expand and interconnect allowing for the movement of brine and entrained oil (Golden et al., 1998; Desmond et al., 2019a; Saltymakova et al., 2020; Oggier et al., 2020). According to Golden et al. (2007), once the brine volume represents more than 5 % of the sea ice volume, the sea ice is permeable and able to exchange fluid with the underlying seawater. The most active transport process responsible for exchanging solutes is brine drainage; that is, the natural convection that replaces salty, dense brine by less dense underlying brine or seawater (Hunke et al., 2011). Ultimately, this leads to an export of solutes (i.e., salts) down and out of the ice into the underlying seawater.

As sea ice is a porous medium, there lies the potential for uptake of oil in brine channels and the exchange of oil solute compounds during brine convection (Oggier et al., 2020; Maus et al., 2015; Petrich et al., 2013). Partitioning of oil through sea ice toward the surface (air-ice interface), or alternatively the subsurface (water-ice interface), is dependent upon the physiochemical properties of the oil and the porosity of the ice, the composition of the subsurface water, air temperature, and the properties of the individual compounds found in oil (Berkowitz et al., 2008a, 2008b). Of the sea ice pollution experiments conducted, little

research has been done to investigate the behavior of oil constituents (Desmond et al., 2019a, 2019b; Payne et al., 1991; Saltymakova et al., 2020) or organic contaminants (Garnett et al., 2019, 2021; Pućko et al., 2012, 2015, 2017) within sea ice. Of the work conducted, it has been established that polar compounds have a greater tendency to dissolve in brine and are transported within sea ice through brine convection processes similarly to dissolved salts (Payne et al., 1991; Garnett et al., 2019, 2021; Pućko et al., 2012, 2015, 2017). Consequently, polar compounds tend to distribute themselves in the ice similar to salts, concentrating in the upper and lower ice layers, forming the characteristic c-curve profile (Desmond et al., 2019b; Garnett et al., 2019, 2021). It has also been postulated that compounds which are more hydrophobic tend to adhere to the surfaces of brine channels, whereby increasing hydrophobicity relates to a stronger retention within ice interstices (Garnett et al., 2019, 2021). Lastly, a tendency for lower molecular weight (LMW) compounds to concentrate in the upper ice layers, and conversely higher molecular weight (HMW) compounds in the lower layers, has also been observed (Desmond et al., 2019a, 2019b; Saltymakova et al., 2020). Given the observed differences in partitioning between molecules of different size and polarity, we hypothesize that movement of oil constituents is not entirely governed by the same transport mechanisms as brine but is also influenced by the physical properties (e.g., octanol–water partition coefficient, aqueous solubility, vapor pressure, and density) of individual compounds. Expanding on the research conducted by Pućko et al. (2012, 2015, 2017), and Garnett et al. (2019, 2021), who focused on the partitioning of polar contaminants within sea ice, we seek to investigate the microscopic behaviors of non-polar hydrocarbons in a sea ice environment. Furthermore, to better understand the influence of physical

properties on oil constituent partitioning, we make use of computational quantum chemistry to calculate the physical properties of hydrocarbons in order to better interpret their differences in chemical partitioning.

The knowledge of physical properties of chemicals is crucial to understanding and predicting their fate in any environment as well as for biochemical transport. Currently, experimental data exists for various physical properties such as partitioning coefficients (e.g., oil–water and octanol–water), aqueous solubilities, Henry’s Law constants, Setschenow (salting out) constants, enthalpies, diffusion coefficients, activity coefficients, and vapor pressures (PubChem, EPI Suite, DDBST, Letinski et al., 2016; Finizio and Guardo, 2001; Bowman and Sans, 1983; Bradley et al., 1973; Goldfarb and Külaots, 2010; Reza et al., 2002; Miller and Wasik, 1985; Banerjee et al., 1980; Shiu et al., 1997; Polak and Lu, 1973). There are also various methods to interpolate/extrapolate properties utilizing correlations or UNIFAC (UNIQUAC Functional-group Activity Coefficients) (Fredenslund et al., 1975) structure relationships based on experimental data and/or theory (Molinspiration cheminformatics; EPI Suite; Finizio and Guardo, 2001; COSMO-RS property prediction; Bowman and Sans, 1983; Mackay and Wesenbeeck, 2014; Koenhen and Smolders, 1975; Ni and Yalkowsky, 2003; Yu and Yu, 2013; Miller and Wasik, 1985; Banerjee, 1996; Banerjee et al., 1980; Arey et al., 2005). However, there are very few experimentally determined values or correlations for a range of temperatures other than for standard conditions (Reza et al., 2002; Bradley et al., 1973; Finizio and Guardo, 2001; Polak and Lu, 1973; Shiu et al., 1997; Banerjee, 1996). This severely limits the applicability of correlations for estimating molecular properties (e.g., in cold Arctic marine waters) as they are dependent on the

molecule subsets and temperature(s) under which the experimental data was acquired. However, quantum mechanical methods have the potential to estimate molecular properties relevant to fate and transport in non-standard conditions. The use of quantum mechanics may be preferable to traditional modeling methods which are based solely on experimental correlations, due to (1) the lack of experimental literature for numerous molecules, (2) large uncertainties and inaccuracies in experimental data, (3) inconsistent experimental conditions (e.g., temperature and pressure), and (4) the fact that traditional property estimation methods such as EPI Suite calculate only at standard conditions. Standard temperature results may not be suitable at sub-zero temperatures as the ratios of property values between molecules change with temperature.

Currently, there is a dearth of modeling research dealing with oil behavior in a sea ice environment (Afenyo et al., 2016a, 2016b). Furthermore, the current models and methods pertain to bulk oil movement and do not directly address partitioning of individual compounds in a sea-ice environment. To this end, an artificial oil-in-ice mesocosm experiment was conducted at the University of Manitoba Sea-ice Environmental Research Facility (SERF) in 2017 as part of Microbial Genomics for Oil Spill Preparedness in the Canadian Arctic (GENICE). This experiment emulated both an oil release from below warm sea ice (denoted growth cycle 1) and the formation of ice from open water with surfaced oil (denoted growth cycle 2). From this experiment, crude oil-contaminated ice cores were sampled and analyzed using analytical instrumentation to achieve a greater understanding of oil constituent partitioning in sea ice. A popular computational quantum chemistry model was used to provide an assessment of the potential for predicting the relative movements and

fate of oil constituents within sea ice based on comparisons between estimated molecular properties and experimentally derived chemical compositional data.

3.3 Experimental and Theoretical Methods

3.3.1 Oil-in-ice Mesocosm Experiment Overview

An artificial oil-in-ice mesocosm experiment was conducted at the University of Manitoba Sea-ice Environmental Research Facility (SERF) during the Winter of 2017 (as detailed in Saltymakova et al., 2020) (Fig. 3.1). An insulated fibreglass tank with a 7 m³ capacity, a diameter of 3 m, and a 1 m depth was located outdoors and experienced ambient winter conditions similar to what would naturally occur in the Arctic. Artificial seawater was prepared from groundwater mixed with sea salts (54% Cl⁻, 32% Na⁺, 8% SO₄²⁻, 4% Mg²⁺, 1% Ca²⁺, and 1% K⁺ – mass percent) to a salinity of 33 parts per thousand (ppt), emulating a natural seawater composition (Millero, 2005; Hare and others, 2013). The tank was equipped with a thermocouple string and a temperature data logger. The thermocouple string was constructed with sensors at 2.5 cm intervals, and the logger was configured to collect readings at 15-minute intervals. The thermocouple string was positioned vertically in the tub, giving a time-series temperature profile of the air, ice, and water column. A heating cable and mixers were positioned at the tanks bottom, allowing for a controlled thaw of the sea ice when required. The tank was also fitted with a poly(vinyl chloride) pipe which served as a premise for oil injection beneath the ice sheet. Lastly, a curtain was fixed inside the tank to ensure oil migration through sea ice brine channels, avoiding penetration along the tank edges (Fig. 3.1).

The experiment consisted of two growth cycles (Fig. 3.1). Growth cycle 1 began on Jan. 31 with the formation of ice from open water. Two days later (on February 2), after the ice cover reached a thickness of 8 cm (Fig. 3.1), 20 L of a light sour crude oil (Tundra Oil & Gas) with a density of 0.82 g/mL was injected into the seawater below the sea ice. The oil was injected via a Masterflex tubing placed through the poly(vinyl chloride) pipe fitted at the edge of the tank creating a gradient of oil concentrations towards the tank's opposite end (Fig. 3.1). The amount of oil injected was based on a previous experiment which showed that 20 L was a sufficient volume to detect oil-in-ice using radar (Firoozy et al., 2017). By February 10 (day 11 of the first growth cycle), the ice had grown to a thickness of 24 ± 1 cm (Fig. 3.1), and nine ice cores were extracted using a 9 cm diameter core barrel (Kovacs Enterprise Mark II coring system) from locations of low to high oil contamination (Fig. 3.1). On February 15 (day 16 of the first growth cycle), the ice had grown an additional 2 cm, and two more ice cores were collected (Fig. 3.1). Following the collection of the two cores on February 15, 5 L of underlying seawater samples was immediately collected from ~15 cm below the ice surface and at the tank's bottom through a cored hole using Masterflex tubing and a pump. At the end of growth cycle 1 (on February 15), the tank was entirely melted with the use of a heating cable, and the oil surfaced creating an open water scenario. Once the ambient temperature cooled below -10 °C (Fig. 3.1), the heating cable was turned off, and the second growth cycle commenced on March 8 with the formation of newly grown sea ice in the presence of the surfaced oil. Seven days later, on March 14, the ice had grown to a thickness of 20 ± 1 cm and 4 ice cores were collected from areas of low to high oil contamination (Fig. 3.1). From the collected cores, the salinity of the ice and the chemical

composition of the oil were determined spatially and temporally throughout the oil-in-ice mesocosm experiment. The following sections describe these methods.

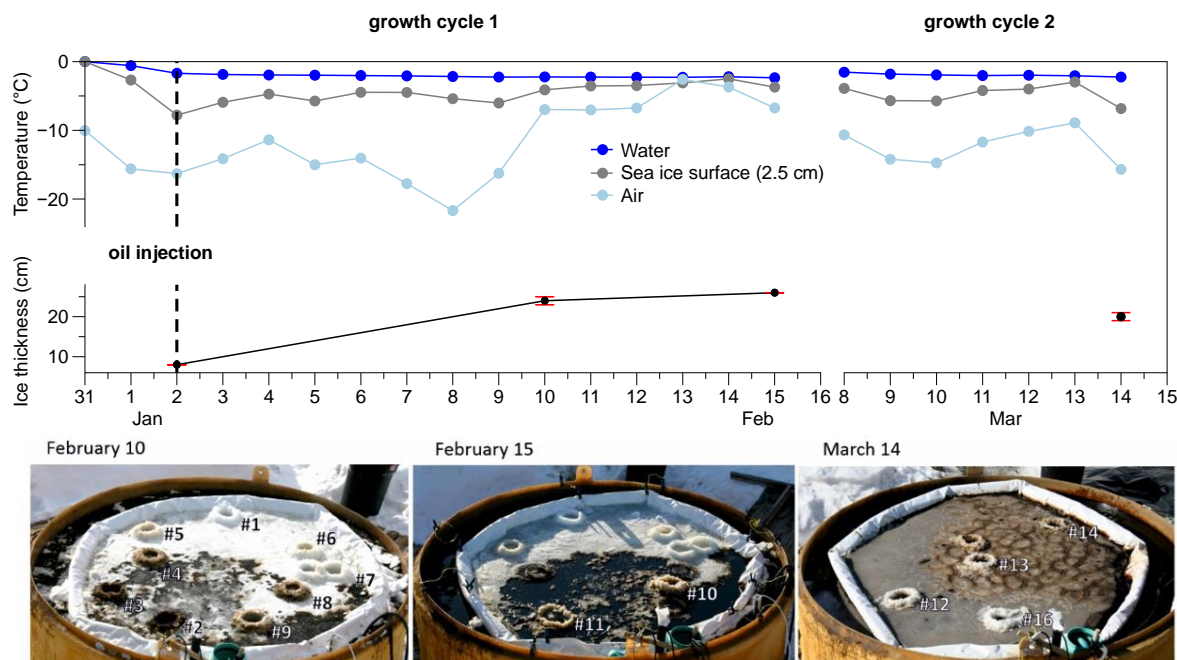


Fig. 3.1 (Upper panel) Temporal evolution of the seawater, sea ice surface, air temperature, and the averaged ice thickness during the cycle of growth 1 and 2. (Bottom panel) Evolution of the ice surface and the position of the different cores sampled on February 10 and 15 and March 14.

3.3.2 Physical Properties of Sea Ice

The ice core samples collected on February 10, February 15, and March 14 were horizontally sectioned at specific intervals. Ice cores with visually observed oil were sliced at 0–2.5, 2.5–5, 5–7.5, and 7.5–13 cm intervals, while the remainder of each core was sliced into two equal pieces (here, 0 cm indicates the top of the ice and larger numbers imply greater depth towards the ice/water interface). Ice cores with no visually observed oil were sectioned into 0–2.5, 2.5–5, 5–15, and 15–25 cm intervals. Each ice core section was then melted at room temperature in glass jars which were previously sterilized with solvents (e.g., hexanes)

and baked at 550 °C. The final volumes of each melted ice core section and of seawater samples were determined with graduated cylinders (accurate to ≤ 0.5 ml). The oil was separated from the seawater and from bulk melted sea ice using hexane and dichloromethane (Fisher Chemical, Optima Grade) via liquid-liquid extractions in 250 mL separatory funnels. Separation consisted of using at least three consecutive 50 mL washes with hexane (Fisher Chemical, Optima Grade) and subsequently three 50 mL washes with dichloromethane (Fisher Chemical, Optima Grade). Sample extracts were concentrated down to ~15 mL in falcon tubes by rotary evaporation and then to dryness with nitrogen evaporation equipped with a 50 °C bath. The collected oil fractions were measured for their respective oil volumes by placing an empty falcon tube beside the oil-filled tube and filling it with known quantities of water, using 10–100 μ L pipettes, until both volumes were level with one another. This method of measuring extracted oil volumes was found to be accurate to ± 10 μ L (Desmond et al., 2021a). The sea ice bulk salinity and seawater salinity were measured (accuracy of 0.5% of reading ± 1 digit) after the oil extraction with a conductivity meter (Orion Star A212 – Thermo Scientific).

Brine volume is the amount of liquid salted water present in sea ice, and it is calculated according to Cox and Weeks (1983) for ice temperatures < -2 °C and Leppäranta and Manninen (1988) for ice temperatures ≥ -2 °C; (Eqs. 3.1 – 3.5). Brine salinity (S_B) was calculated from the measured sea-ice temperatures (via in situ thermocouples) and the freezing point of seawater (Eq. 3.6) (Cox and Weeks, 1983; Leppäranta and Manninen, 1988; UNESCO, 1978).

$$3.1 \quad D_i = 917 - 0.1403 * T$$

$$3.2 \quad F_1 = -4.732 - 22.4 * T - 0.6397 * T^2 - 0.01074 * T^3$$

$$3.3 \quad F_2 = 0.08903 - 0.01763 * T - 5.33 * 10^{-4} * T^2 - 8.801 * 10^{-6} * T^3$$

$$3.4 \quad V_B/V = [(D_i/1000) * S]/[F_1(T) - (D_i/1000) * S * F_2(T)]$$

$$3.5 \quad \% V_B = (V_B/V) * 100$$

$$3.6 \quad S_B = \frac{1}{1 - \left(\frac{54.11}{T}\right)} * 1000$$

where D_i is the density of pure ice (kg/m^3), F_1 and F_2 are auxiliary functions; V_B/V is the brine volume fraction; $\% V_B$ is the brine volume fraction in percent (%); S is the bulk ice salinity (psu), T ($^{\circ}\text{C}$) is the sea ice temperature, and S_B is the brine salinity.

3.3.3 Chemical Analysis

Each reconstituted oil sample (derived from the sea ice and seawater samples) was diluted with hexane to a concentration of 1% vol/vol. The chemical composition of the oil was then analyzed on a LECO Pegasus multidimensional gas chromatography-high resolution time of flight mass spectrometer (GCxGC-HR-TOF-MS) and an Agilent 7010B Triple Quadrupole GC-MS (QQQ-MS) (as detailed in Saltymakova et al., 2020). Investigated compounds consisted of the following chemical groups: n-alkanes, naphthalenes (unsubstituted and methyl-substituted), steranes, and terpanes. All monitored compounds by GCxGC-HR-TOF-MS and QQQ-MS are listed in Table S3.1 (Appendix Section 7.1).

The *GCxGC-HR-TOF-MS* system was comprised of an Agilent 7693 autosampler and an Agilent 7890A gas chromatograph. Each sample was injected into the instrument with a 2 μL volume and was carried by helium with a flow rate of 1.40 mL/min. The instrument was run using a two-dimensional column setup with a RESTEK Rxi-PAH capillary column

(60 m length, 0.25 mm internal diameter, and 0.10 μm film thickness) for the first dimension and a DB-1HT column (10 cm length, 0.25 mm internal diameter, and 0.10 μm film thickness) for the second. The oven temperature was initially set to 40 $^{\circ}\text{C}$ for 1 min, with an increase to 70 $^{\circ}\text{C}$ at 10 $^{\circ}\text{C}/\text{min}$ and then a further increase to 310 $^{\circ}\text{C}$ at 2.5 $^{\circ}\text{C}/\text{min}$. The secondary oven temperature and the modulator temperature were set to +5 and +20 $^{\circ}\text{C}$ relative to the primary oven temperature, respectively. The modulator cycle was set to 4 s and consisted of a 1 s duration of the hot pulse and cooling time between stages. The mass spectrometer settings consisted of an ion source temperature of 250 $^{\circ}\text{C}$, an electron ionization energy of 70 eV, a mass range between 50 and 520 m/z , and an operational TOF resolution of 25 000. External standards were used to quantify n-alkanes and naphthalenes. Calibration curves were created using n-alkanes (mix of three SPEX standards: C11–C18, odd C15–C35, even C16–C36) and PAHs mixtures (CV calibration mix #5, Restek, 16 compounds) standards. The calibration curves ranged from 3.9 to 1000.0 ng/mL for naphthalenes and from 4.9 to 5000.0 ng/mL for n-alkanes.

The QQQ-MS system consisted of a PAL RSI 85 autosampler, a 7890B gas chromatograph, and a Rxi-PAH column (60m \times 250 μm \times 0.1 μm). Each sample was injected with a 2 μL volume and carried using helium with a flow rate of 1.5 mL/min. The oven temperature was initially set to 60 $^{\circ}\text{C}$ for 1 min, followed by an increase to 200 $^{\circ}\text{C}$ at 20 $^{\circ}\text{C}/\text{min}$, and then a further increase to 320 $^{\circ}\text{C}$ at 4 $^{\circ}\text{C}/\text{min}$, where it was held for 12 min. The mass spectrometer settings were as follows: the electron ionization energy was set to 70 eV; nitrogen was used as a collision gas with a flow rate of 1.5 mL/min and an ion gain of 5; and the mass range was set to 50–520 m/z . Steranes and terpanes were measured using multiple

reaction monitoring with their parameters listed in Table S3.2 (Appendix Section 7.1). Quantification was carried out using hopanes and steranes (Chiron, 12 mix) external standard mixture over a concentration range of 15.6–500.0 ng/mL.

3.3.3.1 *Quality Assurance/Control*

Preceding oil extraction from sea ice and seawater samples (Section 3.3.2), each sample was spiked with deuterated n-alkane ($D_{26} - D_{72}$, Fisherbrand, seven compound mix) and polycyclic aromatic hydrocarbons (PAHs) (D_8 , D_{10} , and D_{12} , Wellington Laboratories, eight compound mix) recovery standards. Surrogate recoveries ranged from 12.7 to 104.8% with low molecular weight compounds suffering greater losses. These losses were found to be attributed primarily to the use of nitrogen evaporation. However, losses were notably reduced for reconstituted samples with larger oil volumes (Desmond et al., 2019a).

All calibration curves consisted of at least eight points and had R^2 values greater than 0.95. A minimum signal-to-noise ratio of 6 was achieved for all compounds. GCxGC-HR-TOF-MS and QQQ-MS detection limits varied from 3.9 to 105.0 ng/mL and 13.4 to 25.0 ng/mL, respectively. Duplicates were run every 15 samples and reproducibility was found to be within 5%.

3.3.4 Computational Details

A computational model was employed to simulate the effects of partitioning, evaporation, and dissolution of oil-in-ice through the calculation of octanol–water partition coefficients, vapor pressures, molecular volumes, liquid densities, and solubilities in salty water (seawater) for a subset of compounds found in crude oil (Table 3.1). In order to perform these calculations, we used the Amsterdam Density Functional (ADF) modeling suite (te

Velde et al., 2001; ADF 2020; ADF-GUI 2020). First, molecules and ions of interest were constructed in the graphical user interface (GUI) in a low energy state conformation, based on simple concepts such as conformations that reduce steric as much as possible. Their energies were further minimized through molecular mechanics using the GUI. Subsequent gas-phase geometry optimizations followed by COSMO single points (Klamt et al., 1998; Pye et al., 1999) were completed using the pre-set COSMO-RS computational settings (i.e., Becke Perdew exchange-correlation functional (GGA:BP86) (Becke, 1988; Perdew, 1986), the scalar relativistic ZORA Hamiltonian (van Lenthe et al., 1993; van Lenthe et al., 1994; van Lenthe et al., 1999), a TZP small core basis set (van Lenthe and Baerends, 2003), and an integration accuracy with “good” quality). Frequency calculations were also performed for complex molecules such as steranes and terpanes to confirm the existence of a true local minimum on the potential energy surface (no imaginary frequencies).

Next the numerical output from the ADF calculations (COSMO kf files) was used as input for the CONductor like Screening MOdel for Realistic Solvents (COSMO-RS) module (Klamt et al., 1998; Louwen et al. 2008; Pye and Ziegler, 1999), embedded within the ADF modeling suite. All compounds of interest were modeled as liquid solutes, as all compounds in an oil are dissolved in one another. Therefore, we treated compounds which would naturally be solid at the given temperatures as a liquid. Vapor pressure was calculated at both standard condition (i.e., 25°C and 1 atm.) and at -12 °C to simulate evaporation at the sea ice–air interface. Saltwater solubility was calculated at -2.4 °C (a seawater temperature observed during the experiment) to simulate dissolution at the water-ice interface. Seawater salinity (35 g/kg) was simulated through the solubility of liquid solutes diluted in a 5-

component solvent mixture (i.e., Mg^{2+} at 1 g/kg, SO_4^{2-} at 3 g/kg, Na^+ at 11 g/kg, Cl^- at 20 g/kg, H_2O at 965 g/kg) (Han et al., 2018) mimicking natural seawater composition (Hare et al., 2013). Equation 3.6 was used to calculate the salinity of brine within the ice based on sea ice temperature, which served as an input for calculating oil constituent solubilities within the sea ice. We used the octanol–water pre-set to calculate octanol–water partition coefficients ($\log K_{ow}$) at -2.4°C . Liquid density and molecular volume (Van der Waals volume) were calculated at standard conditions using the pure compound property prediction (https://www.scm.com/doc/COSMO-RS/Property_Prediction.html?highlight=pure+compound+properties).

Table 3.1 Calculated Physical Properties of Compounds Found in Crude Oil Using COSMO-RS

Compounds	Density, kg/L	Molecular Volume, \AA^3	$\log K_{ow}$	Vapor pressure, μbar	Vapor pressure, μbar	Aqueous Solubility in 35 g/kg saltwater, ng/L
	25°C	25°C	-2.4°C	25°C	-12°C	-2.4°C
n-Alkanes						
Dodecane, C_{12}	0.740	214.8	7.63	278.6	24.48	2030
Tetradecane, C_{14}	0.751	248.6	8.92	19.47	1.18	77.52
Hexadecane, C_{16}	0.760	282.5	10.13	1.63	0.07	3.70
Octadecane, C_{18}	0.767	316.3	11.28	0.15	$<10^{-2}$	0.20
Steranes						
5 α -pregnane, C_{21}	0.903	321.3	8.70	20.48	1.25	201.0
5 α ,14 β ,17 β -ethylarenes, C_{22}	0.905	338.3	9.13	7.93	0.42	68.37
20S/R 13 β ,17 α -diacholestane, C_{27}	0.894	422.9	11.89	0.02	$<10^{-2}$	0.06
20S/R 5 α ,14 β ,17 β -Cholestane, C_{27}	0.894	422.9	11.50	0.05	$<10^{-2}$	0.17
20S/R 24-ethyl-5 α ,14 β ,17 β - Cholestane, C_{29}	0.893	456.8	12.33	0.01	$<10^{-2}$	0.02

Table 3.1 Continued

Steranes						
18 α (H)-22,29,30-trisnorneohopane, C ₂₇ Ts	0.901	418.2	10.15	0.64	0.02	5.85
17 α (H)-22,29,30-trisnorhopane, C ₂₇ Tm	0.901	418.2	10.04	0.73	0.03	7.88
17 α (H), 21b(H)-hopane, C ₃₀	0.894	471.3	11.16	0.06	<10 ⁻²	0.47
Tricyclic terpane C ₂₃	0.861	370.3	9.62	2.24	0.10	20.27
Tricyclic terpane C ₂₉	0.854	471.9	13.23	<10 ⁻²	<10 ⁻²	0.002
Tricyclic terpane C ₃₀	0.853	488.8	13.83	<10 ⁻²	<10 ⁻²	0.0004
Aromatics						
Naphthalene, C ₁₀	1.003	123.5	3.41	1081	101.4	1.153E+08
1-Methylnaphthalene, C ₁₁	0.989	141.9	3.78	344.2	27.68	3.487E+07
2-Methylnaphthalene, C ₁₁	0.989	141.9	3.83	274.4	21.36	2.752E+07
1,8-Dimethylnaphthalene, C ₁₂	0.977	160.3	4.41	5694	661.3	2.260E+07
1,3,6-Trimethylnaphthalene, C ₁₃	0.967	178.8	4.81	1336	129.4	3.033E+06
2,3,6,7-Tetramethylnaphthalene, C ₁₄	0.959	197.2	5.49	362.1	29.05	1.099E+06

3.3.4.1 Quality Assurance/Control

The COSMO-RS theory and accuracy is given in (Pye et al., 2009; <https://www.scm.com/doc/COSMO-RS/General.html#ref10>; <https://www.3ds.com/products-services/biovia/products/molecular-modeling-simulation/solvation-chemistry/cosmotherm>; https://www.scm.com/doc/COSMO-RS/Property_Prediction.html?highlight=pure+compound+properties). COSMO-RS is known to be superior in its overall accuracy compared to other methods such as UNIFAC (UNIQUAC Functional-group Activity Coefficients) (Fredenslund et al., 1975) and COSMO-SAC (Segment Activity Coefficient) (Xiong et al., 2014; Hsieh et al., 2010; Chen

et al., 2016). Overall, the accuracy of COSMO-RS is roughly equivalent to 0.4 kcal/mol for the test set (mostly at room temperature). The typical error of the liquid density and molecular volume calculations (based on pure compound property prediction) are 0.005 L/mol and 3 Å³, respectively (https://www.scm.com/doc/COSMO-RS/Property_Prediction.html?highlight=pure+compound+properties). Unlike many other available methods, COSMO-RS applies thermodynamically consistent equations capable of predicting properties as a function of temperature. Although most of the training data for the COSMO-RS parameters come from systems at standard temperature, the temperature-dependent interaction energy terms in COSMO-RS capture the effect of temperature increases and decreases. These temperature adjustments are optimal if the system is within 50 K of standard temperature. Since our work herein deals with sub-zero temperatures warmer than -13 °C, the methodology is expected to be applicable. Moreover, the relative accuracy is expected to be superior due to some cancellation of errors. As our work herein focuses on observing trends and ratios, relative accuracy is most important.

3.4 Results and Discussion

3.4.1 Brine Volumes, Salinities, and Oil Migration

During both growth cycles 1 and 2, the sea ice temperature displayed a linear gradient; that is, the bottom of the ice had a temperature close to the seawater freezing point, and the temperature decreased toward the air-ice interface (Fig. 3.2a). Sea ice was warmer during the cycle of growth 1 and on Feb 15 due to the warmer atmospheric temperature during that cycle. Bulk ice salinity (Fig. 3.2b) displayed a c-shaped profile similar to what would be observed for growing first year sea ice in the Arctic. The brine volume fraction profile displayed a

similar c-shape, with larger brine volumes (Fig. 3.2c) at the top and the bottom than in the interior ice layers. However, the volume of brine toward the bottom of the ice was notably larger than that toward the top. The brine salinity was the highest in the cold ice surface layer and decreased toward the bottom (Fig. 3.2d). The brine volume fraction was always higher than 5 %, indicating that the ice was permeable to fluid movement through brine convection. The bulk ice salinity c-shaped profile and the decrease in bulk ice salinity between February 10 and 15 in the interior ice layers confirmed that the desalinization process through brine convection was active and that dissolved salt in brine was transported out of the ice. This is further supported by the increase in seawater salinity which was originally 32.62 ppt on February 2 and increased to 37.94 ppt on February 15.

During both cycles 1 and 2, the oil concentrated in the top layers of the sea ice cover with oil volumes always lower than 1 mL below the 7.5 cm depth (Fig. 3.2e). Notably, more oil was observed towards the surface of the ice (top 2.5 cm) on the February 15 sampling date when the ice temperature was warmest (Fig. 3.2a) owing to the warm air temperatures preceding this date (Fig. 3.1). These observations for the first growth cycle show that oil localized below a growing sea ice cover tends to move upward into the sea ice and concentrate in the top surface layers rather than being incorporated in new layers of forming ice. The crude oil used in the oil-in-ice experiment is predominantly composed of alkanes (~75%) (Desmond et al., 2019a) which have densities lower than 0.8 g/mL (Table 3.1; Engineering ToolBox, 2017), resulting in a lower oil mixture density (0.82 g/mL) (by weighted average) when compared to seawater/brine (>1.020 g/mL) (Cartagena, 2002). This natural buoyancy allows for the upward migration of the bulk oil in sea ice when brine

channels connect (i.e., permeable sea ice, brine volume >5%). The oil distribution of the second growth cycle (Fig. 3.2e) shows that sea ice formed from oil-contaminated surface water incorporates oil during the formation of its top ice layers. According to Fig. 3.2F, larger oil volumes were incorporated into the sea ice matrix during the cycle of growth 2, suggesting that growing ice from oil contaminated water takes up more oil. While most of the oil was concentrated in the upper ice layers, some residual amounts were found in the interior layers suggesting that brine drainage might transport oil downward. During the oil's migration, its composition did not remain the same throughout the ice and water column but was altered due to differences in physical properties. In what follows, we demonstrate a few examples of how oil constituents partitioned in the sea ice and how COSMO-RS derived physical properties aided in data interpretation. Further examples of the use of COSMO-RS to explain and justify oil-partitioning trends can be seen in (Desmond et al., 2019a, 2019b, 2021b; Saltymakova et al., 2020).

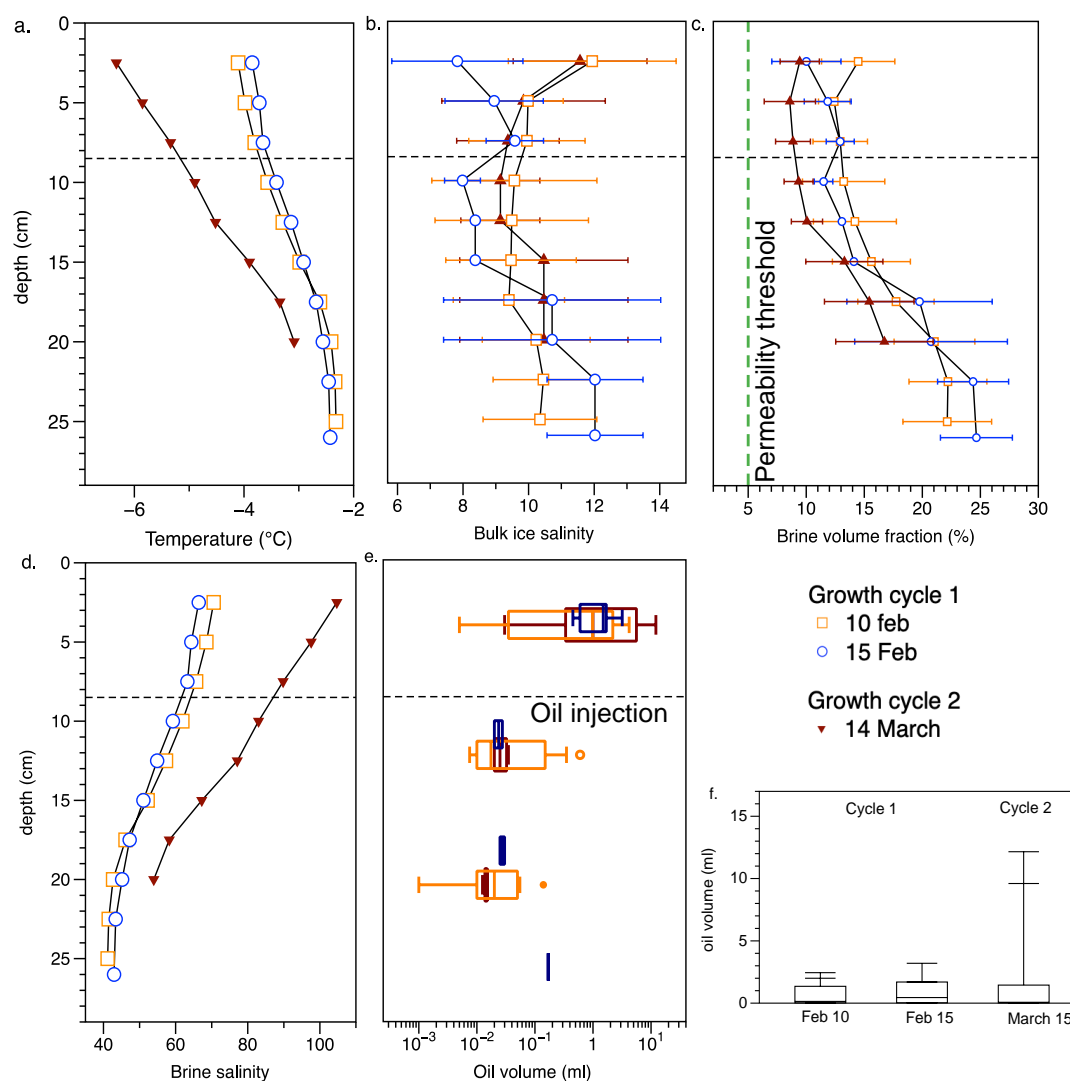


Fig. 3.2 Vertical profiles of (a) sea ice temperature, (b) average bulk ice salinity, (c) average brine volume fraction, (d) brine salinity, and (e) whisker box plot of oil volume and (f) oil volume per sampling dates. The horizontal dotted line shows the ice thickness reached at the oil injection during growth cycle 1. The vertical green dotted line in panel (c) shows the 5 % brine volume fraction permeability threshold according to Golden et al. (2007). The errors bars in panels (b) and (c) show the standard deviation of the averaged parameters.

3.4.2 Application of Modeling to the Experimental Data Analysis

Results of COSMO-RS property calculations for a subset of compounds (i.e., naphthalenes, n-alkanes, steranes, and terpanes) found in the crude oil used in the above-mentioned experiment (Section 3.3.1) are provided in Table 3.1. The investigated compounds differ in their size (i.e., molecular volume), ranging from $\sim 100 \text{ \AA}^3$ to $\sim 500 \text{ \AA}^3$. Observation shows that as the size of the molecule changes, so do its other physical properties. Fig. 3.3a plots the relationship between molecular volume, aqueous solubility, and log K_{OW} for all the compounds listed in Table 3.1. For the respective compound groups, we observe an increase in log K_{OW} , and conversely a decrease in aqueous solubility, with increases in molecular volume. Log K_{OW} is a measure of hydrophobicity, whereby larger values indicate a decreasing tendency to interact with the aqueous phase. The effect of hydrophobicity on aqueous solubility as a function of salt concentration is shown in Fig. 3.3b. Compounds which are less soluble and more hydrophobic (e.g., C_{30} tricyclic terpane) are more greatly impacted by the salting-out effect (Berkowitz et al., 2008a) relative to more soluble and less hydrophobic compounds (e.g., Naphthalene). In Fig. 3.3b, C_{30} tricyclic terpane (log $K_{OW} = 13.83$) is shown to be more sensitive to increasing salt content than naphthalene (log $K_{OW} = 3.41$).

Given the difference in physical properties between and within the different compound groups (Table 3.1; Fig. 3.3a), we hypothesize that they will partition differently in the ice. In the following, the use of calculated molecular volume, octanol–water partition coefficient, aqueous solubility, vapor pressure, and liquid density will be discussed in the interpretation of chemical data to assess: (1) partitioning between different chemical groups,

(2) partitioning based on molecular size, (3) partitioning of alkanes (n-C11 – n-C18), and (4) partitioning between isomers. Calculated octanol–water partition coefficients are then used to assess the environmental fate of compounds dissolved into the water column.

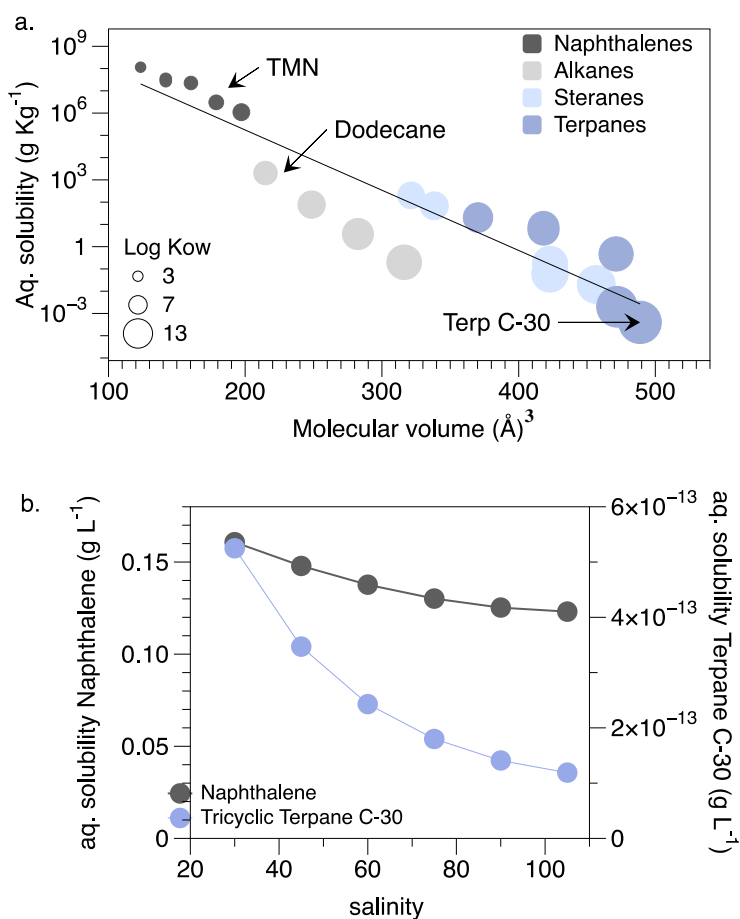


Fig. 3.3 (a) Relationship between molecular volume (\AA^3), aqueous solubility at -2.4°C and salinity of 35 g/kg, and $\log K_{OW}$ for the different groups of oil compounds provided in Table 3.1. The y axis is a logarithmic scale, and the size of the data points are proportional to their respective $\log K_{OW}$ value. (b) Impact of NaCl salt concentration (ppt) on the aqueous solubility of naphthalene and C30 tricyclic terpene (terpane C-30).

3.4.2.1 *Partitioning between Aromatics, Alkanes, and Terpanes*

In order to showcase the influence of differing physical properties on the partitioning between aromatics, alkanes, and terpanes in the ice, we plotted the relative abundance of trimethyl naphthalene (TMN), dodecane, and C30 tricyclic terpane in the ice (both growth cycles combined) in comparison to their relative amounts in the initial technical oil mixture (Fig. 3.4). Here, TMN represents the behaviors of aromatics, dodecane represents the behaviors of n-alkanes, and C30 tricyclic terpane represents the behavior of terpanes. From Figure 3.4, the initial oil mixture was composed of 16 % TMN, 83 % dodecane, and around 0.33 % C30 tricyclic terpane. The relative abundance of these compounds in the ice are different than in the initial oil mixture indicating that oil compounds partition during their incorporation and transport in the ice. The ice was enriched in aromatic TMN and depleted in the n-alkane dodecane (compared to the original oil mixture). The relative abundance of C30 tricyclic terpane in the ice was close to the value of the initial oil mixture suggesting that terpanes have a lower ability to partition compared to the aromatics and alkanes. The greater propensity for enrichment/depletion of TMN and dodecane relative to C30 tricyclic terpane is likely linked to their differences in physical properties. The aqueous solubility of TMN and dodecane were calculated to be 10^9 and 10^6 higher, respectively, than the solubility of C30 tricyclic terpane (Fig. 3.3a). Their log K_{ow} values are also several magnitudes lower, whereby TMN and dodecane have a log K_{ow} of 4.81 and 7.63, respectively, compared to C30 tricyclic terpane (log K_{ow} =13.83) (Fig. 3.3a). Similarly, the vapor pressures of TMN and dodecane are magnitudes higher than that of C30 tricyclic terpane (Table 3.1). Given the greater solubility, hydrophilicity, and volatility of TMN and dodecane relative to those of

C30 tricyclic terpane, there is greater potential for these compounds to (1) dissolve within brine channels and be subsequently transported as dissolved solutes, and (2) evaporate into the atmosphere. It is important to note that we would expect TMN to be depleted in the ice relative to dodecane, given the greater solubility and volatility of TMN as given by Table 3.1. This discrepancy is a result of modeling all compounds (and particularly aromatics) as pure liquid solutes. TMN as a pure substance (i.e., not dissolved in oil) is a solid while dodecane is a liquid. If we were to treat TMN as a solid, its solubility would still remain higher than dodecane, but its vapor pressure would be lower (as according to EPI Suite). A greater volatility (i.e., evaporative potential) for dodecane would explain its depletion in the ice relative to TMN (Fig. 3.4).

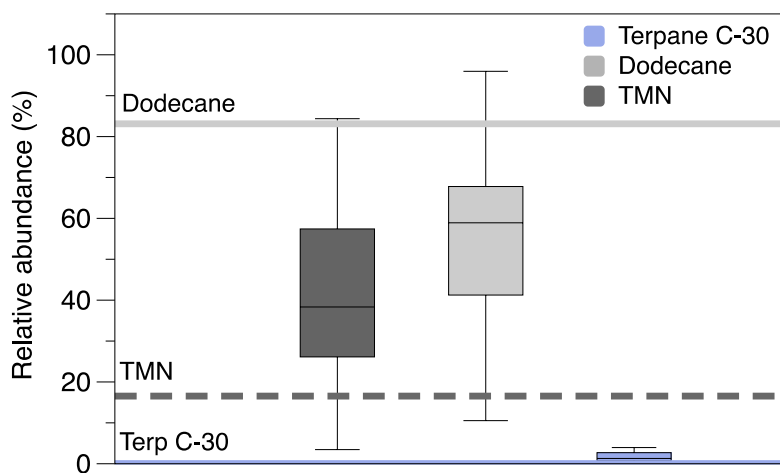


Fig. 3.4 The relative abundance of trimethyl naphthalene (TMN), dodecane, and C30 tricyclic terpane (terpane C-30) retrieved in the ice (whisker box plot). The abundance of TMN, dodecane, and terpane C-30 in the initial oil mixture is showed by the dotted, light gray, and light purple lines, respectively. Relative abundance was calculated as the amount in ng of each species divided by the sum of the three species in ng multiplied by 100 (e.g., $\text{TMN} / (\text{TMN} + \text{dodecane} + \text{terpane C-30})$).

To further illustrate the greater ability for TMN and dodecane to partition within and from the ice relative to C30 tricyclic terpane, we plotted the measured masses of these three compounds within the ice for both growth cycles 1 and 2 (Fig. 3.5a). We observe that the more soluble, more volatile, and less hydrophobic species (i.e., TMN and Dodecane) are found in higher quantities for the first growth cycle (oil spilled beneath grown ice) than the second growth cycle (ice grown from oil-contaminated water). This observation is likely due to a combination of factors. For growth cycle 2, in which the ice grew from open water with surfaced oil, TMN and dodecane were initially in direct contact with the atmosphere and likely evaporated to a larger degree compared to C30 tricyclic terpane. Second, the more soluble TMN and dodecane likely would have migrated downward during the salt rejection process by brine drainage, during the initial sea ice growth, where they could have been subsequently flushed into the water column. This concept of brine drainage for soluble species is illustrated by Fig. 3.5b. Fig. 3.5b shows the vertical distribution of dodecane and C30 tricyclic terpane at the end of growth cycle 2 (March 14). From Fig. 3.5b, we observe that the less soluble tricyclic terpane does not partition efficiently and stays accumulated in the upper ice layer, while the more soluble dodecane displays a pronounced c-shaped profile, indicative of the bulk salinity profile (Fig. 3.2b). In contrast to C30 tricyclic terpane, dodecane exhibits a greater ability to partition and dissolve in brine and be transported by drainage toward the sea water. Finally, it is worth pointing out that the more hydrophobic C30 tricyclic terpane may have been better retained in the upper ice regions during growth cycle 2 (Fig. 3.5b) due to a greater retention to the ice interstices, as indicated by Garnet et al. (2019, 2021).

Within this section, we depicted how a difference in physical properties between different chemical groups can impact how these chemical groups partition with respect to one another. In the following sections, we turn our attention to the partitioning exhibited between compounds within the same chemical group.

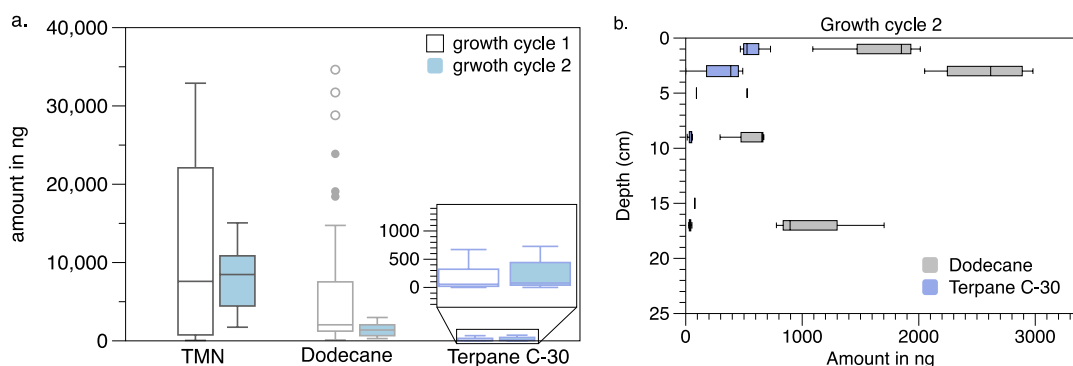


Fig. 3.5 (a) Amount in nanograms of trimethyl naphthalene (TMN), dodecane, and C30 tricyclic terpane (terpane C-30) measured in sea ice during growth cycle 1 and 2. (b) The vertical distribution of dodecane and Terpane C-30 at the end of cycle 2.

3.4.2.2 Partitioning in Brine Channels based on Size

It has been reported that chemical compounds partition inside brine channels based on molecular size, whereby smaller molecules have been observed to penetrate the narrower channels toward the top of the ice, and larger molecules move down toward where the brine channels are wider (Desmond et al., 2019a, 2019b; Saltymakova et al., 2020). Herein, this effect can be seen in the partitioning of steranes and terpanes as the concentration of low molecular weight (LMW) homologs increases toward the ice surface and decreases toward the subsurface (Fig. 3.6). In particular, C₂₁₋₂₂ steranes are observed to be concentrated in the top 0-2.5 cm section of the ice and are notably lower in the bottom 16-27 cm ice section and water column. Conversely, an apparent growth of C₂₇₋₂₉ steranes is observed in the water

column. Similarly, a growth of the relative abundance of pentacyclic terpanes (HMW) relative to tricyclic terpanes (LMW) toward the water column is observed (Fig. 3.6). This partitioning mirrors the molecular volumes (and weights) of the compounds which increase with an increase in the carbon number (Table 3.1). Despite the very low solubilities of steranes and terpanes (Table 3.1), HMW steranes and terpanes were identified in the water column in significantly higher amounts compared to the technical oil mixture and the top section of the ice during growth cycle 1. Aromatic compounds, for example, naphthalenes, demonstrate a similar partitioning pattern in which smaller molecules migrate up to the ice surface and larger, heavier molecules, migrate toward the water column. This can be seen in the naphthalenes' composition presented on ToF 2D chromatograms (Fig. 3.7). The concentration of methylnaphthalenes is higher in the top ice section compared to the bottom where the influence of tetramethylnaphthalenes grows.

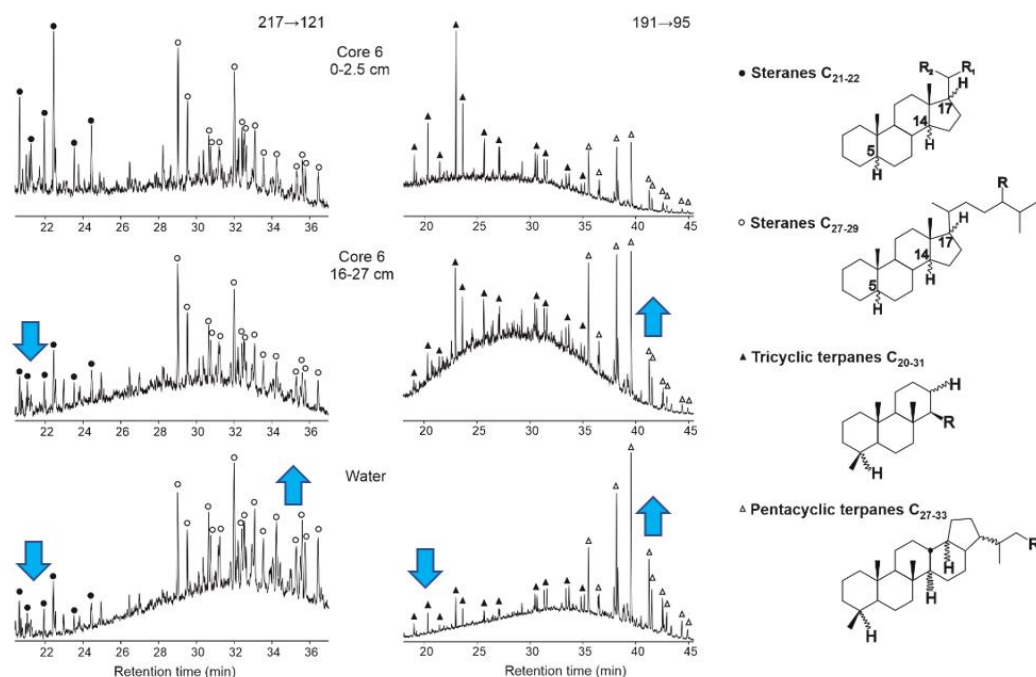


Fig. 3.6 GC-MS/MS chromatograms of the distribution of steranes and terpanes in the composition of top and bottom sections of the ice and water column of growth cycle 1. Core #6 was procured during the February 10 sampling date of the experiment, and the water sample was collected on February 15. Note that multiple reaction monitoring transitions are provided at the figure top. For instance, for transition 217→121, 217 is the parent (precursor) ion and 121 is the daughter (product) ion. More details on the multiple reaction monitoring mass spectrometry method for steranes and terpanes is provided in Table S3.2. Upward/downward arrows indicate increases/decreases in concentration in relation to the top ice core section.

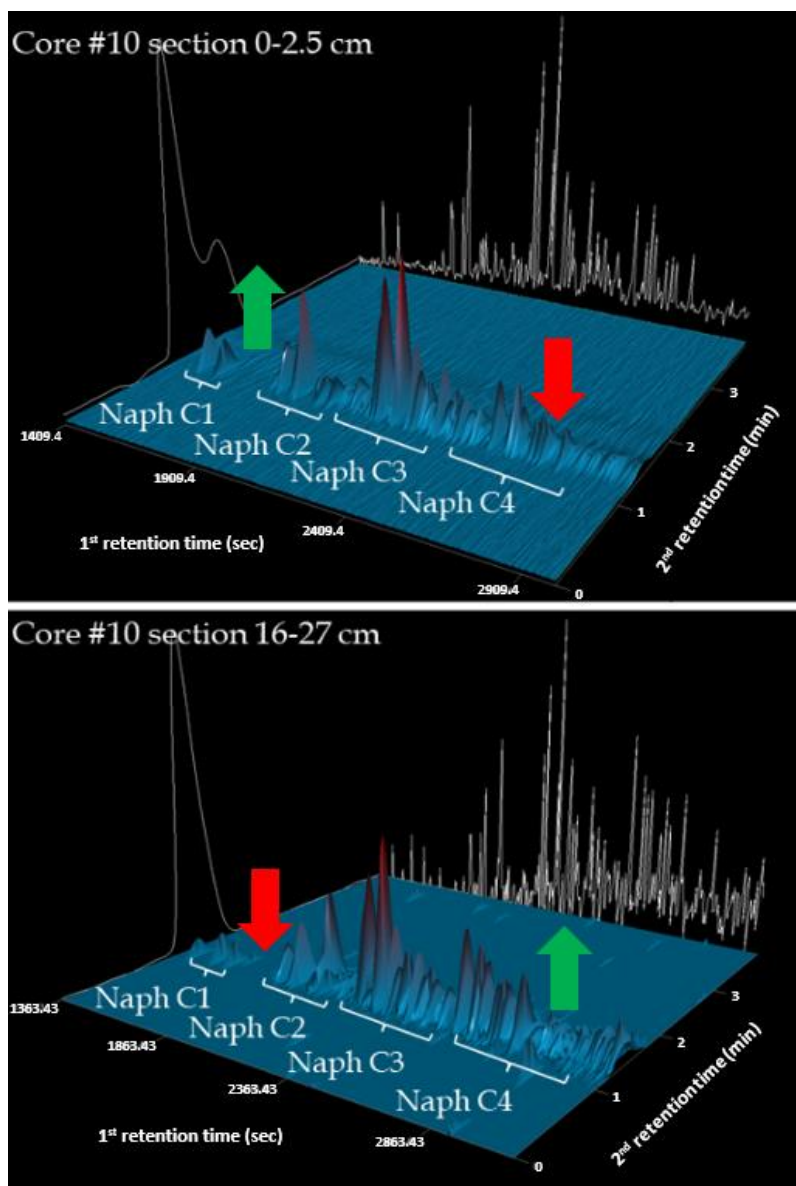


Fig. 3.7 Partitioning of naphthalenes based on GCxGC-TOF. Sample core #10 was collected on the February 15 sampling date of the experiment. Note that (1) C₁₋₄ indicate the number of methyl substitutions, and (2) sections 0–2.5 cm and 16–27 cm indicate the top and bottom sections of the ice core. In the figure, the two-dimensional chromatogram is provided at the front, and the one-dimensional chromatogram of the 1st retention time axis is provided in the back. Upward/downward arrows indicate increases/decreases in proportion relative to each ice core section.

To further analyze this trend, we plotted the ratio of C_{23}/C_{30} tricyclic terpane through the ice depth for various sampled cores (Fig. 3.8a). For all cores, this ratio was largest toward the ice surface and was lower towards the subsurface. Furthermore, this trend was observed for all sampling dates (both cycle 1 and 2). Notably, the ratio of C_{23}/C_{30} tricyclic terpane was observed to be 1.25 in the water column on February 15, lower than what was found in the ice (Fig. 3.8a), indicating a growth of HMW tricyclic terpanes in the water. Further observation of Fig. 3.8a shows the most variance in the C_{23}/C_{30} ratio between different cores at the top of the ice. In Fig. 3.8b, we observe a positive linear correlation between oil volume and the C_{23}/C_{30} tricyclic terpane ratio for the first 2.5 cm of surface ice. Consequently, the observed variance in Fig. 3.8a is believed to be due to a difference in oil concentration between the sampled cores. The concentration of C_{23} tricyclic terpane is 7X higher than C_{30} tricyclic terpane in the technical mixture. Therefore, as the bulk oil concentration increases in the surface ice sections, so does the concentration of C_{23} tricyclic terpane relative to C_{30} tricyclic terpane. Lastly, it is worth pointing out the slight c-curve shape trend depicted by the C_{23}/C_{30} tricyclic terpane ratio. While there is a more prominent increase in this ratio toward the ice surface, there is also a less pronounced increase at the subsurface for various cores (Fig. 3.8a). This c-shape trend resembles the bulk ice salinity profile (Fig. 3.2b), which may suggest the prominence of the less hydrophobic C_{23} tricyclic terpane to be transported similarly to solute salts by brine convection. Both Pućko et al. (2012, 2015, 2017) and Garnett et al. (2019, 2021) have reported the tendency of polar compounds to dissolve in brine and be subjected by the same convection processes. While C_{23} tricyclic terpane is not polar, its $\log K_{OW}$ is 1.4X lower than C_{30} tricyclic terpane (i.e., more hydrophilic) (Table 3.1), and may

interact more effectively with the brine owing to its greater aqueous solubility (10^4 X higher) (Table 3.1).

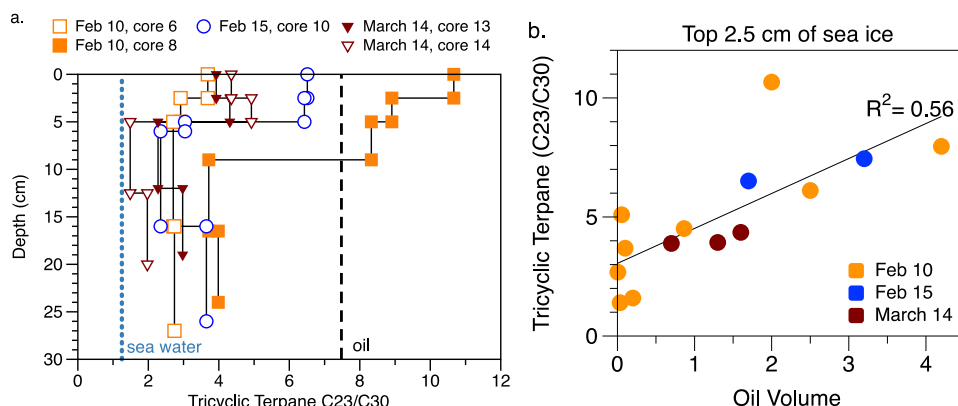


Fig. 3.8 (a) Tricyclic Terpane C_{23}/C_{30} ratio through the ice depth for various sampled ice cores from the February 10 and 15 (growth cycle 1) and March 14 (growth cycle 2) sampling dates. The blue dotted line and the black dashed line indicate the ratio in the seawater and technical oil mixture, respectively. (b) Linear correlation between the Tricyclic Terpane C_{23}/C_{30} ratio and oil volume (mL) for the top 2.5 cm of ice for ice cores sampled throughout the experiment.

Overall, we observe a trend in which molecules of smaller size concentrate toward the ice surface and molecules of larger size concentrate toward the subsurface (Figs. 3.6-3.8). However, given that the size of brine channels is on the order of micrometers (Light et al., 2003; Lieblappen et al., 2018), while molecules are on the order of angstroms, this partitioning may not be directly linked to the size of the molecule, but may be influenced by a combination of related physical properties (e.g., Fig. 3.3a). Based on Table 3.1, we see that the density of naphthalenes, steranes, and terpanes have an inverse relationship with carbon number increases (i.e., a smaller size equates to a denser molecule), suggesting that differences in density are not responsible for the trends observed in Figs. 3.6-3.8. A strong positive correlation ($R^2=0.99$) is observed between molecular volume and $\log K_{OW}$ (measure

of hydrophobicity) for all compound groups (Table 3.1; Fig. 3.3a). Garnet et al. (2019, 2021) report that compounds with greater hydrophobicity are more strongly retained by brine channel surfaces. Therefore, a plausible explanation may be that larger and more hydrophobic molecules have a greater tendency to adhere to ice interstices and do not move through the ice as easily as less hydrophobic molecules. However, this argument is flawed as we observe HMW steranes and terpanes concentrating in the water column on February 15 (which were clearly not retained by the ice) (Figs. 3.6 and 3.8a). Furthermore, during the second growth cycle (in which the oil was originally surfaced), we observe an abundance of the C_{23}/C_{30} tricyclic terpane ratio toward the ice surface (Fig. 3.8a), which indicates that the more hydrophobic C_{30} tricyclic terpane was not retained during its downward movement in the ice relative to the C_{23} tricyclic terpane. We, therefore, speculate that hydrophobicity ($\log K_{OW}$) may also relate to a lower affinity for concentrated brine owing to the salting-out effect (Fig. 3.3b) (Berkowitz et al., 2008a), whereby compounds which are less soluble partition away from areas of higher salt content (i.e., fractionation). From Fig. 3.3a, we observe a strong correlation between molecular volume and aqueous solubility, in which smaller molecules are more soluble. Larger molecules have lower solubilities and may not partition into upper layers of ice, which has higher brine salinity (i.e., more concentrated in salts) (Fig. 3.2d) owing to the salting-out-effect (Berkowitz et al., 2008a). Notably, the salinity of the seawater on February 15 was measured to be 37.94 ppt, which is lower than the concentration of salts within the sea ice (Fig. 3.2d), which may explain why we observed an abundance of HMW steranes and terpanes concentrating in the water column (Figs. 3.6 and 3.8a).

3.4.2.3 *Partitioning of n-Alkanes within the Ice*

Fig. 3.9 shows the C_{11-14}/C_{15-18} n-alkanes ratio for three representative cores pertaining to the sampling dates of February 10, February 15, and March 14, respectively. Similar to the c-shape trend observed for the tricyclic terpane C_{23}/C_{30} ratio (Fig. 3.8a), we also observe a c-shape trend for the February 10 (core 2) and February 15 (core 11) sampling dates; albeit more pronounced. This more apparent c-shape exhibited by these sampling dates may be related to the greater aqueous solubility of LMW n-alkanes such as dodecane (2030 ng/mL) compared to C_{23} tricyclic terpane (20.27 ng/mL) (Table 3.1), suggesting a greater prominence for dissolution and potential to be transported as dissolved solutes through brine convection (Fig. 3.2b). For the February 10 sampling date (core 2), we observe LMW n-alkanes concentrating toward both the surface and subsurface of the ice. We postulate that LMW n-alkanes concentrate toward the surface of the ice relative to high molecular weight (HMW) compounds due to their smaller size and greater hydrophilicity (Table 3.1) (see Section 3.4.2 for rationale). The greater solubility of LMW n-alkanes compared to HMW (Table 3.1) also allow for dissolution in brine channels and subsequent downward migration towards the bottom of the ice (i.e., brine convection) (Payne et al., 1991), thus concentrating LMW n-alkanes toward the ice's subsurface. Notably, there are fewer LMW n-alkanes at the surface compared to the subsurface for core 2, likely due to evaporation of the LMW's owing to their greater volatility (Table 3.1). For the February 15 sampling date (core 11), we also observe a c-shape profile similar to February 10 (core 2); however, there is a greater concentration of LMW n-alkanes at the surface compared to the subsurface. This difference can be explained by the influence of ambient conditions. Preceding February 15, warmer

ambient conditions (Fig. 3.1) allowed for a greater oil volume to penetrate the sea ice surface (Figs. 3.1 and 3.2e). LMW n-alkanes are naturally higher in concentration in the technical oil mixture and will concentrate as the bulk oil concentration increases at the surface ice, similar to what was observed for the C_{23}/C_{30} tricyclic terpane ratio (Fig. 3.8b). Additionally, warmer sea ice resulting from the warmer air temperature likely led to a loss of LMW n-alkanes from the sea ice base due to drainage into the water column. In contrast to February 10 and 15 (growth cycle 1), the n-alkane ratio shown by core 12 of the March 14 sampling date (growth cycle 2) does not depict a c-shape profile but is lowest at the ice surface and becomes progressively higher towards the sea ice base. This unique trend was observed for all phase 2 cores and is believed to have been driven (in part) by brine induced advection processes (Payne et al., 1991). We speculate that for core 12 (growth cycle 2), LMW n-alkanes were driven downward similar to the brine (i.e., gravity drainage) as sea ice grew from open water. The greater volatility for LMW alkanes (Table 3.1) may have also played a role in the deficiency of the $n\text{-}C_{11-14}/n\text{-}C_{15-18}$ ratio at the sea ice surface on March 14 (core 12), given that the oil was initially on the surface for phase 2 of the experiment.

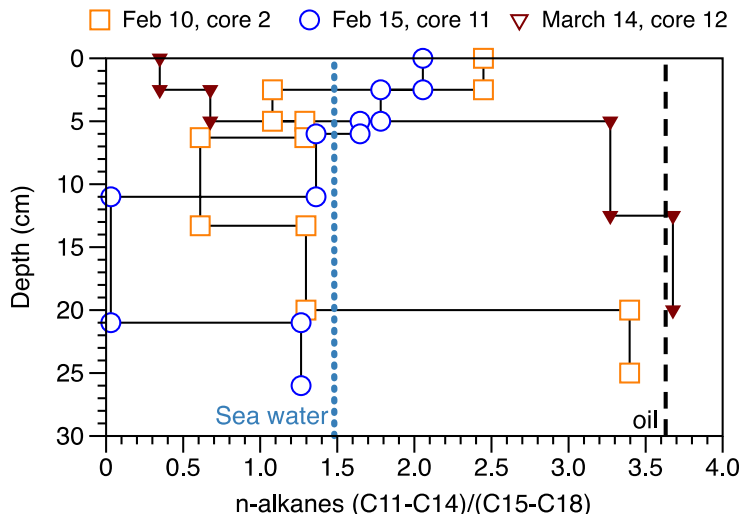


Fig. 3.9 Sea ice profile of n-alkanes ratio (C11-14/C15-18) for representative ice cores sampled on February 10 and 15 and March 14. The blue dotted line and the black dashed line indicate the ratio in the seawater and technical oil mixture, respectively.

3.4.2.4 Partitioning between Isomers in Brine Channels

Fig. 3.10 shows partitioning trends between two sets of isomers in the top (0-10 cm) and bottom (10-25 cm) ice core sections and the water column. Ratios of compound concentrations were averaged per respective sampling date for all sampled ice cores which contained each isomer pair. Note the relatively large standard deviations are due to the heterogeneity of oil-in-ice (Figs. 3.1 and 3.2e) which caused differences in partitioning tendencies as the oil-seawater interactions change with heavy to light oil concentrations (Saltymakova et al., 2020). The compound isomers in the following examples have the same molecular weights, volumes, and densities (Table 3.1). For our first example, we demonstrate the chemical migration tendency of Ts (18 α (H)-22,29,30-trisnorneohopane) relative to Tm (17 α (H)-22,29,30-trisnorhopane) (Fig. 3.11). Both Ts and Tm are relatively volatile with vapor pressures of 0.02 and 0.03 μ bar, respectively, at -12°C (Table 3.1). In contrast, both

Ts and Tm have relatively low aqueous solubilities (calculated values 5.85 and 7.88 ng/mL, Table 3.1) which are relatively negligible compared to their vapor pressures and may not have influenced the partitioning of these two isomers significantly. Additionally, Ts and Tm have log K_{OW} values of 10.15 and 10.04, respectively (Table 3.1). Log K_{OW} is a measure of hydrophobicity and a higher log K_{OW} may relate to a lower affinity for concentrated brine owing to the salting-out effect (Fig. 3.3b) (Berkowitz et al., 2008a). From Fig. 3.10 we see a greater tendency of Tm to migrate toward the surface than Ts for each sampling date. We speculate this may be partly due to the greater volatility of Tm relative to Ts (1.5X more volatile). Another explanation for this trend may be that Ts has a higher log K_{OW} (and lower solubility) than Tm and is slightly more hydrophobic. The salinity of the water column on February 15 was measured to be 38.67 ppt which is lower than the brine salinity observed for the ice (increasing toward the surface) (Fig. 3.2d). Therefore, Ts may partition into areas of lower salinity relative to Tm due to its greater hydrophobicity. Our second example demonstrates the chemical migration tendency of 2-methylnaphthalene relative to 1-methylnaphthalene (MN). Both isomers are relatively soluble, in contrast to their relatively low volatility. 1-MN was calculated to be 1.3X more soluble than 2-MN (Table 3.1). Additionally, the log K_{OW} of 2-MN was calculated to be 3.83, which is higher than the value calculated for 1-MN (3.78) (Table 1). From Table 3.1, we observe a greater tendency of 1-MN to dissolve and migrate towards the water column for all sampling dates. We speculate that 1-MN was driven downward by brine convection processes (Payne et al., 1991) due to its greater aqueous solubility relative to 2-MN. Another explanation for this observed trend may be related to the greater hydrophobicity of 2-MN relative to 1-MN. Compounds which

are more hydrophobic have a greater tendency to adhere to the surfaces of brine channels (Garnet et al., 2019, 2021), which may be why 2-MN was found to be more concentrated in the ice.

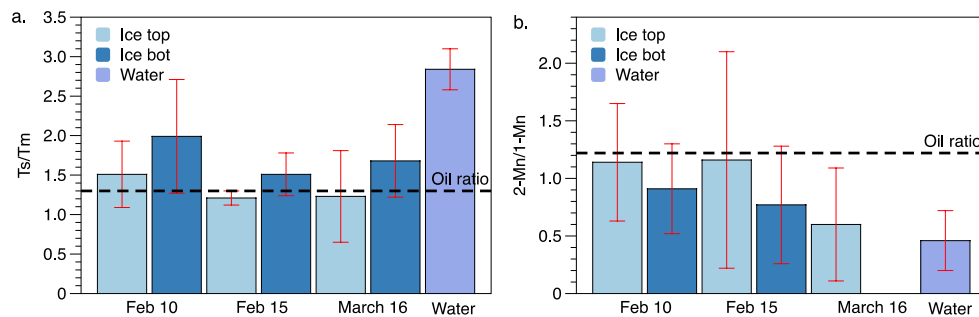


Fig. 3.10 (a) Ts/Tm ratio and (b) 2-MN/1-MN ratio in the seawater and in the ice top and bottom layers. The dashed line shows the ratio of the original oil mixture.

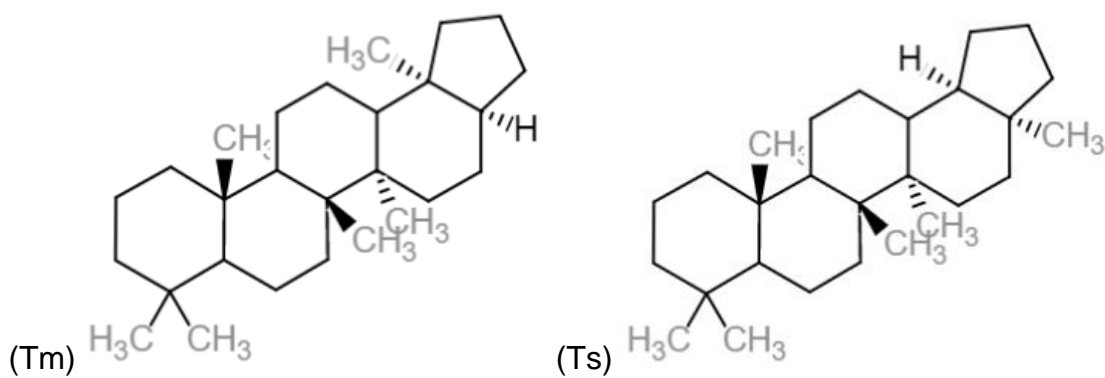


Fig. 3.11 Structures of Ts (18 α (H)-22,29,30-trisnorhopane) and Tm (17 α (H)-22,29,30-trisnorhopane) isomers.

3.4.2.5 Environmental Fate Assessment

Brine-induced advection of water-soluble compounds into the water column is a likely scenario (Payne et al., 1991), especially in ice-covered water where there is greater exposure to the liquid phase in brine channels (Faksness and Brandvik, 2008) and reduced potential for evaporation compared to open waters (Faksness et al., 2011). Fig. 3.12 shows the concentration of naphthalenes (naphthalene, methylnaphthalene – MN, dimethylnaphthalene – DMN, trimethylnaphthalene – TMN, tetramethylnaphthalene – TeMN) in the water column on the February 15th sampling date. In total, we observed 0.20 ng/mL of naphthalenes in the water column. Naphthalene was observed in the water at a concentration of 0.01 ng/mL, which is below the Canadian marine water quality guideline value of 1.4 ng/mL (Canadian Council of Ministers of the Environment, 1999). Higher concentrations of DMN, TMN, and TeMN were observed in the water (0.05 – 0.08 ng/mL) than both naphthalene and MN, due to their higher content in the technical oil mixture, larger size (see Section 3.4.2.2), lower volatility, and yet still relatively high solubility (Table 3.1; Fig. 3.7).

Although, the concentrations of naphthalenes were observed to be relatively low in the water, even small quantities of water dissolvable compounds found in oil can have severe consequences as they may be able to persist and bioaccumulate in marine organisms. Computational chemistry has been a valuable tool in performing preliminary screening and risk assessments of suspected compounds of interest (Louwen and Stedeford, 2011; EPI Suite; Molinspiration Property Calculation Service (www.molinspiration.com); Virtual Computational Chemistry Laboratory (<http://vcclab.org/>). The European Chemicals Agency

(ECHA) recommends the use of molecular properties such as the maximum molecular length, average maximum diameter, cross-sectional diameter, molecular weight, and octanol–water partition coefficient to provide insight as to the potential for bioaccumulation and toxicity (Louwen and Stedeford, 2011). For the purpose of this study, only the property of octanol–water partition coefficient ($\log K_{ow}$) will be considered to establish a general conclusion regarding the potential for bioaccumulation and persistence. Based on the considerations of ECHA, molecules with a $\log K_{ow} > 4.5$ are considered persistent (P) and bioaccumulative (B) (Louwen and Stedeford, 2011). TMN and TeMN have a $\log K_{ow}$ of 4.81 and 5.49 (Table 3.1), respectively, and therefore meet the general PB criteria. Lastly, the measured concentrations of steranes and terpanes (Table S3.1 – Appendix Section 7.1) in the water column on February 15 are 0.39 and 0.86 ng/mL, respectively. The steranes and terpanes identified in the water column (Fig. 3.6) have $\log K_{ow}$ values in the range of 9–14 (Table 3.1). These molecules are expected to persist due to their high resistance to microbial degradation (Prince and Walters, 2016).

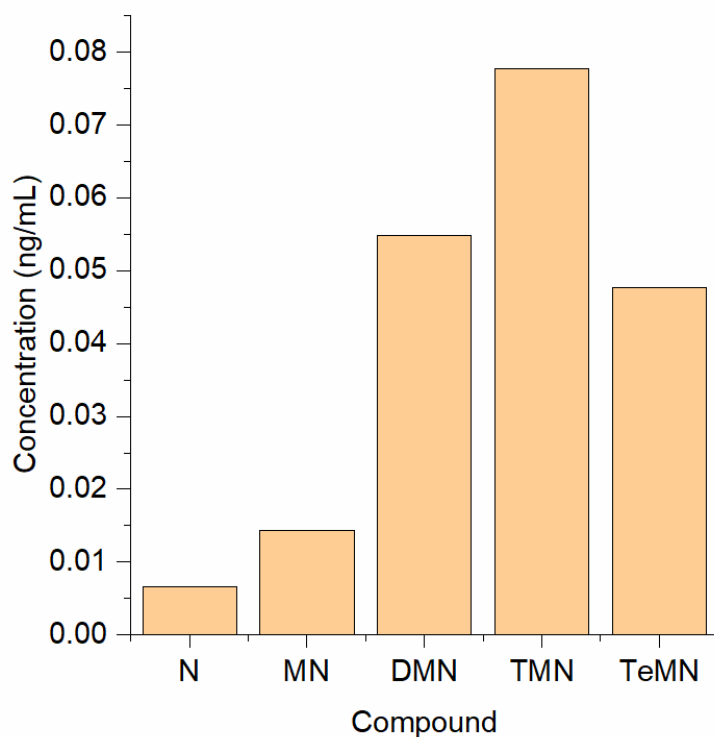


Fig. 3.12 Concentrations (ng/mL) of dissolved naphthalenes in the water column taken on the February 15/17 sampling date. N – naphthalene (parent); MN, methyl naphthalenes; DMN, dimethyl naphthalenes; TMN, trimethyl naphthalenes; TeMN, tetramethyl naphthalenes.

3.5 Conclusions

Herein, we have demonstrated that a combination of factors drives the movement of oil and its constituents: ambient temperature impacting sea ice porosity, brine convection processes governed by ambient temperature and growing sea ice, and differences in the physical properties between oil constituents. Permeable sea ice allowed for the migration of the bulk oil and its constituents throughout the vertical sea ice profile. The use of COSMO-RS derived physical properties in conjunction with thermodynamic state equations was found

to be useful in interpreting and explaining the partitioning behavior between lighter and heavier molecules of various hydrocarbon groups (i.e., naphthalenes, steranes, terpanes, and n-alkanes) as well as between isomers. We observed a trend in which smaller molecules concentrated toward the top of the ice and larger molecules at the bottom. We speculate that this result may be due to a combination of factors relating to hydrophobicity and aqueous solubility. Higher brine salinity found for higher regions of sea ice may influence the migration of more hydrophobic and less soluble compounds owing to the salting-out effect, causing molecules which are more hydrophobic to concentrate in areas of lower salt content. We also noticed a trend in which lighter and more soluble molecules tend to behave as solute salts relative to heavier and less soluble molecules. In particular, a c-shape trend was observed resembling the bulk salinity profile of the sea ice. Other factors such as the evaporation of more volatile components at the sea ice surface and the dissolution of more soluble components at the sea ice base into the water column are believed to have also influenced the partitioning of lighter molecules relative to heavier ones. Lastly, compounds which have dissolved in the water column are available for uptake in marine mammals and may prove persistent, bioaccumulative, and toxic to aquatic life. The ability of microbial bacteria to degrade dissolved hydrocarbons in Arctic waters will be crucial for limiting the threat made to biota and local inhabitants.

Overall, this manuscript has provided a general overview of how COSMO-RS predicted properties could be used to help predict the behavior of compounds within a sea ice environment and their subsequent ecotoxicological potential. The use of COSMO-RS provided a consistent method that allowed for relative comparisons relying on relative

accuracy. We hope that this study brings awareness to (1) computational quantum chemistry for describing macroscopic situations such as oil-in-ice, which rely on calculations at sub-zero temperatures, and (2) the scarcity of experimental literature at cold temperatures. In order to improve the absolute accuracy of COSMO-RS at lower temperatures, more experimental datasets are required.

Although the methods presented in this chapter provide a first step for predicting the partitioning and fate of petroleum hydrocarbons in a sea ice environment, the authors acknowledge many limitations in the conducted study. Namely, we recognize the complexity of sea ice and the frequently changing ambient conditions. Limited sampling of sea ice cores (and especially water samples) temporally disallowed a comprehensive analysis on the effect of changing temperature on the migration of oil constituents. Another limitation of this study is that we did not conduct a comprehensive investigation of different compound groups, as molecules, which differ in their properties, may partition differently in sea ice. Also, a thorough investigation into the effect of differing oil concentrations on chemical partitioning was not conducted. We speculate that lighter oil concentrations will allow for greater dissolution of molecules (due to greater surface area interaction with brine), thereby permitting a greater propensity for following brine movements. In contrast, higher oil concentrations may not readily permit molecules to be controlled by brine convection processes. Lastly, one limitation pertaining to our modeling method is that we treat all compounds as liquid solutes, including those that would normally be a solid (if not dissolved in oil). We acknowledge that this simplification in our modeling may not perfectly represent

aromatics but is likely a valid approximation. Future work should further develop the methods presented in this chapter, bearing in mind our experimental shortcomings.

3.6 Acknowledgements

This work was supported by the Canada Research Chairs (CRC) programs (Barber), Natural Sciences and Engineering Research Council (NSERC) of Canada (Stern, Schreckenbach, Desmond), the Canada Foundation for Innovation (CFI) (Barber), ArcticNet – Networks of Centres of Excellence (NCE) of Canada (Stern), and GENICE (Genome Canada LSARP (Grant No. 10203) and Research Manitoba) (Stern). This work was made possible by the facilities of the Shared Hierarchical Academic Research Computing Network (SHARCNET: www.sharcnet.ca) and Compute/CalculCanada as well as Software for Chemistry & Materials (SCM).

3.7 References

- ADF-GUI 2017, SCM, Amsterdam, The Netherlands, <http://www.scm.com>
- ADF2020, SCM, Theoretical Chemistry, Vrije Universiteit, Amsterdam, The Netherlands, <http://www.scm.com>
- ADF-GUI 2020, SCM, Amsterdam, The Netherlands, <http://www.scm.com>
- Afenyo, M., Khan, F., Veitch, B., Yang, M., 2016a. “Modeling oil weathering and transport in sea ice.” *Marine Pollution Bulletin* 107: 206–215.
- Afenyo, M., Veitch, B., Khan, F., 2016b. “A state-of-the-art review of fate and transport of oil spills in open and ice-covered water.” *Ocean Engineering* 119: 233–248.
- AMAP, 2009. AMAP Assessment 2009: Human Health in the Arctic. Arctic Monitoring and Assessment Programme (AMAP), Oslo, Norway. xiv+254 pp. Possible impact of climate change on Contaminants in the arctic. Pg. 11-1.
- AMAP, 2010. AMAP Assessment 2007: oil and gas activities in the arctic — effects and potential effects. *Arctic Monitoring & Assessment Programme*, Oslo, vols. 1 and 2.

AMAP, 2017. Snow, Water, Ice and Permafrost in the Arctic (SWIPA) 2017. Arctic Monitoring and Assessment Programme (AMAP), Oslo, Norway. xiv + 269 pp.

Andrews, J., Babb, D., and Barber, D.G., 2017. "Climate change and sea ice: Shipping accessibility on the marine transportation corridor through Hudson Bay and Hudson Strait (1980–2014)". *Elem Sci Anth.* 5:15. DOI: <http://doi.org/10.1525/elementa.130>.

"Arctic Sea Ice News and Analysis." National Snow & Ice Data Center, NASA, 2019, nsidc.org/arcticseaicenews/.

Arey, J.S., Nelson, R.K., Xu, L. Reddy, C.M., 2005. "Using Comprehensive Two-Dimensional Gas Chromatography Retention Indices To Estimate Environmental Partitioning Properties for a Complete Set of Diesel Fuel Hydrocarbons." *Anal. Chem.* 77: 7172-7182.

Banerjee, S., 1996. "Estimating Water Solubilities of Organics as a Function of Temperature." *Wat. Res.* 30(9): 2222-2225.

Banerjee, S., Yalkowsky, S.H., and Valvani, S.C., 1980. "Water Solubility and Octanol/Water Partition Coefficients of Organics. Limitations of the Solubility-Partition Coefficient Correlation." *American Chemical Society* 14(10): 1227- 1229.

Becke, A.D., 1988. "Density Functional Exchange Energy Approximation with Correct Asymptotic Behavior." *Physical Reviews A* 38: 3098-3100.

Berkes, F., 2017. "Arctic Fish, Northern Cultures, and Traditional Ecological Knowledge." *Marine Fishes of Arctic Canada*, University of Toronto Press, pp. 57–60.

Berkowitz, B., Dror, I., and Yaron, B., 2008a. "Contaminant Partitioning in the Aqueous Phase." *Contaminant Geochemistry: Interactions and Transport in the Subsurface Environment*, Springer.

Berkowitz, B., Dror, I., and Yaron, B., 2008b. "Partitioning of Volatile Compounds." *Contaminant Geochemistry: Interactions and Transport in the Subsurface Environment*, Springer.

Bowman, B.T., Sans, W.W., 1983. "Determination of Octanol-Water Partitioning Coefficients (K_{ow}) of 61 Organophosphorus and Carbamate Insecticides and their Relationship to Respective Water Solubility(s) Values." *J. Environ. Sci. Health B*18(6): 667-683.

Bradley, R.S., Dew, M.J., Munro, D.C., 1973. "The solubility of benzene and toluene in water and aqueous salt solutions under pressure." *High Temperatures - High Pressures* 5: 169-176.

Canadian Council of Ministers of the Environment, "Canadian water quality guidelines for the protection of aquatic life: Polycyclic aromatic hydrocarbons (PAHs)", in

Canadian environmental quality guidelines, 1999, Canadian Council of Ministers of the Environment, Winnipeg.

Cartagena, E., 2002. Density of Seawater - The Physics Factbook [WWW Document]. URL <https://hypertextbook.com/facts/2002/EdwardLaValley.shtml>

Carter, N.A., Dawson, J., Joyce, J., Ogilvie, A., 2018. Arctic Corridors and Northern Voices: Governing marine transportation in the Canadian Arctic (Arviat, Nunavut community report).

Carter, N.A., Dawson, J., Weber, M., 2019. Arctic Corridors and Northern Voices: governing marine transportation in the Canadian Arctic (Coral Harbour, Nunavut community report). Ottawa: University of Ottawa. <http://hdl.handle.net/10393/38505> DOI: 10.20381/RUOR38505.

Chen, W.L., Hsieh, C.M., Yang, L., Hsu, C.C., Lin, S.T., 2016. “A Critical Evaluation on the Performance of COSMO-SAC Models for Vapor-Liquid and Liquid-Liquid Equilibrium Predictions Based on Different Quantum Chemical Calculations.” *Ind. Eng. Chem. Res.* 55: 9312.

Cosmo-Rs, COSMOtherm, Biovia - Dassault Systèmes®. COSMO-RS, COSMOtherm, BIOVIA - Dassault Systèmes®. (n.d.). <https://www.3ds.com/products-services/biovia/products/molecular-modeling-simulation/solvation-chemistry/cosmotherm/> (accessed 2021).

Cox, G., Weeks, W., 1983. “Equations for determining the gas and brine volumes in sea-ice samples.” *J. Glaciol.* 29(102): 306–316.

Dawson, J., Pizzolato, L., Howell, S.E.L., Copland, L., Johnston, M., 2018. “Temporal and spatial patterns of ship traffic in the Canadian Arctic from 1990 to 2015.” *Arctic* 71(1), 15–26. doi:10.14430/arctic4698.

DDBST. (n.d.). <http://www.ddbst.com/> (accessed 2021).

Desmond, D.S., Crabeck, O., Lemes, M., Harasyn, M.L., Mansoori, A., Saltymakova, D., Fuller, M.C., Rysgaard, S., Barber, D.G., Isleifson, D., Stern, G.A., 2021a. “Investigation into the Geometry and Distribution of Oil Inclusions in Sea Ice using non-destructive X-ray Microtomography and its Implications for Remote Sensing and Mitigation Potential.” *Mar. Pollut. Bull.* 173: 112996. DOI: <https://doi.org/10.1016/j.marpolbul.2021.112996>

Desmond, D.S., Neusitzer, T.D., Lemes, M., D., Barber, D.G., and Stern, G.A., 2019b. “Examining the Physical Interactions of Corn Oil (Medium Crude Oil Surrogate) in Sea Ice and its Potential for Chemical Partitioning within an Arctic Environment.” Proceedings of the Forty-second AMOP Technical Seminar, Environment and Climate Change Canada, Ottawa, ON, Canada, pp. 66-95.

Desmond, D.S., Saltymakova, D., Neusitzer, T.D., Firoozy, N., Isleifson, D., Barber, D.G., and Stern, G.A., 2019a. "Oil Behavior in Sea Ice: Changes in Chemical Composition and Resultant Effect on Sea Ice Dielectrics." *Marine Pollution Bulletin* 142: 216-233.

Desmond, D.S., Saltymakova, D., Smith, A., Wolfe, T., Snyder, N., Polcwiartek, Bautista, M., Lemes, M., Hubert, C.R.J., Barber, D.G., Isleifson, D., and Stern, G.A., 2021b. "Photooxidation and biodegradation potential of a light crude oil in first-year sea ice" *Marine Pollution Bulletin* 165: 112154.

Engineering ToolBox, 2017. Hydrocarbons, linear alcohols and acids - densities. [online] Available at: https://www.engineeringtoolbox.com/density-alkane-alkene-benzene-carbon-number-alcohol-acid-alkyl-alkyne-d_1939.html

Faksness, L.-G., Brandvik, P.J., 2008. "Distribution of water soluble components from Arctic marine oil spills — a combined laboratory and field study." *Cold Reg. Sci. Technol.* 54: 97–105. <https://doi.org/10.1016/J.COLDREGIONS.2008.03.005>.

Faksness, L.G., Brandvik, P.J., Daae, R.L., Leirvik, F., Børseth, J.F., 2011. Large-scale oil-in-ice experiment in the Barents Sea: monitoring of oil in water and MetOcean interactions. *Mar. Pollut. Bull.* 62: 976–984. <https://doi.org/10.1016/J.MARPOLBUL.2011.02.039>.

Finizio, A., Guardo, A.D., 2001. "Estimating temperature dependence of solubility and octanol-water partition coefficient for organic compounds using RP-HPLC." *Chemosphere* 45: 1063-1070.

Firoozy, N., Neusitzer, T., Desmond, D.S., Tiede, T., Lemes, M., Landy, J., Mojabi, P., Rysgaard, S., Stern, G., Barber, D.G., 2017. "An Electromagnetic Detection Case Study on Crude Oil Injection in a Young Sea Ice Environment." *IEEE Trans. Geosci. Remote Sens.* 55(8): 4465-4475.

Ford, J., Willox, A.C., Chatwood, S., Furgal, C., Harper, S., Mauro, I., and Pearce, T., 2014. "Adapting to the Effects of Climate Change on Inuit Health." *American Journal of Public Health* 3(104): 9-17.

Fredenslund, A., Jones, R.L., and Prausnitz, J.M., 1975. "Group-contribution estimation of activity coefficients in nonideal liquid mixtures." *AIChE Journal* 21: 1086.

Garnett, J., Halsall, C., Thomas, M., Crabeck, O., France, J., Joerss, H., Ebinghaus, R., Kaiser, J., Leeson, A., Wynn, P.M., 2021. "Investigating the Uptake and Fate of Poly- and Perfluoroalkylated Substances (PFAS) in Sea Ice Using an Experimental Sea Ice Chamber." *Environ. Sci. Technol.* 55(14): 9601-9608. DOI: 10.1021/acs.est.1c01645

Garnett, J., Halsall, C., Thomas, M., France, J., Kaiser, J., Graf, C., Leeson, A., Wynn, P., 2019. "Mechanistic Insight into the Uptake and Fate of Persistent Organic Pollutants in Sea Ice." *Environ. Sci. Technol.* 53: 6757-6764.

Gautier, D.L., Bird, K.J., Charpentier, R.R., Grantz, A., Houseknecht, D.W., Klett, T.R., Moore, T.E., Pitman, J.K., Schenk, C.J., Schuenemeyer, J.H., Sørensen, K., Tennyson, M.E., Valin, Z.C., and Wandrey, C.J., 2009. "Assessment of undiscovered oil and gas in the Arctic." *Science* 324: 1175–9. <https://doi.org/10.1126/science.1169467>

General. Software for Chemistry & Materials. (n.d.).
<https://www.scm.com/doc/COSMO-RS/General.html#ref10> (accessed 2021).

Golden, K.M., Ackley, S.F., and Lytle, V.I., 1998. "The Percolation Phase Transition in Sea Ice." *Science* 282: 2238–2241.

Golden, K.M., Eicken, H., Heaton, A.L., Miner, J., Pringle, D.J., Zhu, J., 2007. "Thermal Evolution of Permeability and Microstructure in Sea Ice." *Geophys. Res. Lett.* 34: 1–13. DOI: 10.1029/2007GL030447

Goldfarb, J.L., Külaots, I., 2010. "Melting points and enthalpies of fusion of anthracene and its heteroatomic counterparts." *J Therm Anal Calorim* 102: 1063–1070. DOI 10.1007/s10973-010-0779-8.

Han, J., Dai, C., Yu, G., Lei, Z., 2018. "Parameterization of COSMO-RS model for ionic liquids." *Green Energy & Environment* 3: 247–265.

Hare, A.A., Wang, F., Barber, D., Geilfus, N.-X., Galley, R.J., Rysgaard, S., 2013. "pH evolution in sea ice grown at an outdoor experimental facility." *Mar. Chem.* 154: 46–54 (doi:10.1016/J.MARCHEM.2013.04.007)

Hunke, E.C., Notz, D., Turner, A.K., Vancoppenolle, M., 2011. "The Multiphase Physics of Sea Ice: A Review for Model Developers." *Cryosphere* 5, 989–1009. DOI: 10.5194/tc-5-989-2011

Hsieh, C.M., Sandler, S.I., Lin, S.T., 2010. "Improvements of COSMO-SAC for vapor-liquid and liquid-liquid equilibrium predictions." *Fluid Phase Equilib.* 297: 90.

Johnston, M., Dawson, J., Stewart, E., 2019. Marine Tourism in Nunavut: Issues and Opportunities for Economic Development in Arctic Canada. In: Koster R., Carson D. (eds) *Perspectives on Rural Tourism Geographies*. Geographies of Tourism and Global Change. Springer, Cham., 2019. DOI: https://doi.org/10.1007/978-3-030-11950-8_7

Johnston, M.E., Dawson, J., and Maher, P.T., 2017. "Strategic development challenges in marine tourism in Nunavut." *Resources* 6. <https://doi.org/10.3390/resources6030025>

Kelley, K.E., Ljubicic, G.J., 2012. "Policies and practicalities of shipping in arctic waters: Inuit perspectives from Cape Dorset, Nunavut." *Polar Geography* 35(1): 19–49. DOI:10.1080/1088937X.2012.666768

Klamt, A., Jonas, V., Bürger, T., Lohrenz, J.C.W., 1998. "Refinement and Parametrization of COSMO-RS." *J. Phys. Chem. A*. <https://doi.org/10.1021/JP980017S>

- Koenhen, D.M., Smolders, C.A., 1975. "The Determination of Solubility Parameters of Solvents and Polymers by Means of Correlations with Other Physical Quantities." *Journal of Applied Polymer Science* 19: 1163-1179.
- Leppäranta, M., Manninen, T., 1988. The Brine and Gas Content of Sea Ice With Attention to Low Salinities and High Temperatures.
- Letinski, D.J., Parkerton, T.F., Redman, A.D., Connelly, M.J., Peterson, B., 2016. "Water solubility of selected C9-C18 alkanes using a slow-stir technique: Comparison to structure - property models." *Chemosphere* 150: 416-423.
- Lieblappen, R.M., Kumar, D.D., Pauls, S.D., Obbard, R.W., 2018. "A Network Model for Characterizing Brine Channels in Sea Ice." *The Cryosphere* 12: 1013–1026. DOI: <https://doi.org/10.5194/tc-12-1013-2018>
- Light, B., Maykut, G.A., Grenfell, T.C., 2003. "Effects of Temperature on the Microstructure of First-Year Arctic Sea Ice." *Journal of Geophysical Research-Oceans* 108: 3051. DOI: 10.1029/2001jc000887.
- Ljubicic, G., Okpakok, S., Robertson, S., Mearns, R., 2018. Uqsuqtuurmiut inuita tuktimi qaujimaningit (Inuit knowledge of caribou from Gjoa Haven, Nunavut): Collaborative research contributions to co-management efforts. *Polar Record* 54: 213–233. <https://doi.org/10.1017/S0032247418000372>
- Louwen, J.N., Pye, C., Lenthe, E.V., 2008. ADF2008. 01 COSMO-RS, SCM, Theoretical Chemistry [WWW Document]. Vrije Univ. Amsterdam, Netherlands. URL <https://www.scm.com/>
- Louwen, J.N., Stedeford, T., 2011. "Computational assesement of the environmental fate, bioaccumulation, and oil toxicity potential of brominated benzylnopolystyrene." *Toxicology Mechanisms and Methods* 21(3): 183-192.
- Mackay, D., van Wesenbeeck, I., 2014. "Correlation of Chemical Evaporation Rate with Vapor Pressure." *Environ. Sci. Technol.* 48: 10259–10263. dx.doi.org/10.1021/es5029074
- Maus, S., Becker, J., Schneebei, M., Wiegmann, A., 2015. Oil Saturation of the Sea Ice Pore Space, Proceedings of the 23rd International Conference on Port and Ocean Engineering under Arctic Conditions, 2015.
- Miller, M.M., Wasik, S.P., 1985. "Relationships between Octanol-Water Partition Coefficient and Aqueous Solubility." *Environ. Sci. Technol* 19(6): 1985.
- Millero, F.J., 2005. Chemical Oceanography, 3rd Edition, Table 2.2, Page 62. CRC Press.
- Molinspiration cheminformatics. Molinspiration Cheminformatics. (n.d.). <https://www.molinspiration.com/> (accessed 2021).

Ni, N., Yalkowsky, S.H., 2003. "Prediction of Setschenow constants." *International Journal of Pharmaceutics* 254: 167–172.

Oggier, M., Eicken, H., Wilkinson, J., Petrich, C., O'Sadnick, M., 2020. "Crude oil migration in sea-ice: Laboratory studies of constraints on oil mobilization and seasonal evolution." *Cold Regions Science and Technology* 174: 102924.

Olsen, J., Carter, N.A., and Dawson, J., 2019. "Community perspectives on the environmental impacts of Arctic shipping: Case studies from Russia, Norway and Canada." *Cogent Social Sciences* 5(1): 1-20. <https://doi.org/10.1080/23311886.2019.1609189>

Payne, J.R., Hachmeister, L.E., McNabb, G.D., Sharpe, H.E., Smith, G.S., Menen, C.A., 1991. "Brine-induced advection of dissolved aromatic hydrocarbons to Arctic bottom waters." *Environ. Sci. Technol.* 25: 940–951.

Perdew, J.P., 1986. "Density Functional Approximation for the Correlation Energy of the Inhomogeneous Electron Gas." *Phys. Rev. B: Condens. Matter* 33: 8822-8824.

Petrich, C., Karlsson, J., Eicken, H., 2013. "Porosity of Growing Sea Ice and Potential for Oil Entrainment." *Cold Reg. Sci. Technol.* 87: 27-32.

Polak, J., Lu, B.C.-Y., 1973. "Mutual Solubilities of Hydrocarbons and Water at 0 and 25 °C." *Can. J. Chem.* 51: 4018-4023.

Prince, R.C., Walters, C.C., 2016. Biodegradation of oil hydrocarbons and its implications for source identification, in *Standard Handbook Oil Spill Environmental Forensics: Fingerprinting and Source Identification*, Chap. 19, S. Stout and Z. Wang (2nd ed.), Elsevier/Academic Press.

Pučko, M., Stern, G.A., Barber, D.G., Macdonald, R.W., Warner, K.-A., Fuchs, C., 2012. "Mechanisms and Implications of α -HCH Enrichment in Melt Pond Water on Arctic Sea Ice." *Environ. Sci. Technol.* 46: 1862–1869.

Pučko, M., Stern, G.A., Burt, A.E., Jantunen, L.M., Bidleman, T.F., Macdonald, R.W., Barber, D.G., Geilfus, N.-X., Rysgaard, S., 2017. "Current Use Pesticide and Legacy Organochlorine Pesticide Dynamics at the Ocean-Sea Ice-Atmosphere Interface in Resolute Passage, Canadian Arctic, During Winter-Summer Transition." *Sci. Total Environ.* 580: 1460-1469.

Pučko, M., Stern, G.A., Macdonald, R.W., Jantunen, L.M., Bidleman, T.F., Wong, F., Barber, D.G., Rysgaard, S., 2015. "The Delivery of Organic Contaminants to the Arctic Food Web: Why Sea Ice Matters." *Sci. Total Environ.* 506-507: 444-452.

Pure compound property prediction. Software for Chemistry & Materials. (n.d.). https://www.scm.com/doc/COSMO-RS/Property_Prediction.html?highlight=pure%2Bcompound%2Bproperties.

Pye, C.C., Ziegler, T., 1999. "An implementation of the conductor-like screening model of solvation within the Amsterdam density functional package." *Theor. Chem.*

Accounts Theory, Comput. Model. (Theoretica Chim. Acta) 101: 396–408.
<https://doi.org/10.1007/s002140050457>

Pye, C.C., Ziegler, T., van Lenthe, E., 2009. “An Implementation of the Conductor-Like Screening Model of Solvation within the Amsterdam Density Functional Package--Part II. COSMO for real solvents.” *Can. J. Chem.* 87(7): 790-797.
<https://link.gale.com/apps/doc/A204320231/CPI?u=winn62981&sid=bookmark-CPI&xid=95710c94>

Reza, J., Trejo, A., Vera-Ávila, L.E., 2002. “Determination of the temperature dependence of water solubilities of polycyclic aromatic hydrocarbons by a generator column-on-line solid-phase extraction-liquid chromatographic method.” *Chemosphere* 47: 933–945.

Saltymakova, D., Desmond, D.S., Isleifson, D., Firoozy, N., Neusitzer, T.D., Xu, Z., Lemes, M., Barber, D.G., and Stern, G.A., 2020. “Effect of dissolution, evaporation, and photooxidation on crude oil chemical composition, dielectric properties and its radar signature in the Arctic environment.” *Marine Pollution Bulletin* 151: 110629.

Shiu, W.-Y., Wania, F., Hung, H., Mackay, D., 1997. “Temperature Dependence of Aqueous Solubility of Selected Chlorobenzenes, Polychlorinated Biphenyls, and Dibenzofuran.” *J. Chem. Eng. Data* 42: 293-297.

te Velde, G., Bickelhaupt, F.M., Baerends, E.J., Fonseca Guerra, C., van Gisbergen, S.J.A., Snijders, J.G., Ziegler, T., 2001. “Chemistry with ADF.” *J. Comput. Chem.* 22, 931-967.

Thomas and Dieckmann (2010). *Sea Ice: an Introduction to its Physics, Chemistry, Biology and Geology*, second edition Blackwell.

UNESCO: Eighth report of the joint panel on oceanographic tables and standards, Technical papers in Marine Science, Division of Marine Sciences, Paris, France, 28, 1978.

US EPA. [2012]. Estimation Programs Interface Suite™ for Microsoft® Windows, v 4.11. United States Environmental Protection Agency, Washington, DC, USA.

U.S. National Library of Medicine. (n.d.). *PubChem*. National Center for Biotechnology Information. PubChem Compound Database.
<https://pubchem.ncbi.nlm.nih.gov/> (accessed 2021).

van Lenthe, E., Baerends, E.J., 2003. “Optimized Slater-type basis sets for the elements 1-118.” *Journal of Computational Chemistry* 24: 1142.

van Lenthe, E., Baerends, E.J., Snijders, J.G., 1993. “Relativistic regular two-component Hamiltonians.” *Journal of Chemical Physics* 99: 4597.

van Lenthe, E., Baerends, E.J., Snijders, J.G., 1994. “Relativistic total energy using regular approximations.” *Journal of Chemical Physics* 101:9783.

van Lenthe, E., Ehlers, A.E., Baerends, E.J., 1999. “Geometry optimization in the Zero Order Regular Approximation for relativistic effects.” *Journal of Chemical Physics* 110: 8943.

Virtual Computational Chemistry Laboratory. (n.d.). <http://vcclab.org/> (accessed 2021)

Xiong, R., Sandler, S.I., Burnett, R.I., 2014. “An improvement to COSMO-SAC for predicting thermodynamic properties.” *Ind. Eng. Chem. Res.* 53: 8265.

Yu, X., Yu, R., 2013. “Setschenow Constant Prediction Based on the IEF-PCM Calculations.” *Ind. Eng. Chem. Res.* 52: 11182–11188. dx.doi.org/10.1021/ie400001u

Chapter 3 investigated aspects of oil behavior (i.e., migration tendencies, partitioning within sea ice, evaporation, dissolution) by comparing computationally and experimentally derived data (Fig. 3.13). Specifically, this chapter aimed to test the following hypotheses:

1. A difference in physical properties explains oil partitioning in sea ice.
2. Computational chemistry can predict or interpret the relative movements of oil constituents.
3. Lighter molecules have a greater tendency to be controlled by brine advection processes.
4. Molecules which are more hydrophobic concentrate in areas of lower salt concentration.

Each of these assumptions was found to be true based on the data presented in Chapter 3. However, it may be premature to state that computational chemistry can predict the relative movements of oil constituents in sea ice under all oil-in-ice scenarios, as the model utilized does not consider the complexity and heterogeneous nature of sea ice and the frequently changing ambient conditions. Further research is required to study the fate and behavior of

oil under various circumstances. Furthermore, Chapter 3 fails to account for biodegradation and photooxidation weathering processes. To this end, Chapter 4 features an oil-in-ice mesocosm experiment which assesses the potential for photo- and biodegradation of the bulk crude oil content encapsulated in the upper regions of the ice during freezing (e.g., winter) and thawing (spring-summer), with consideration on the fate of transformed products.

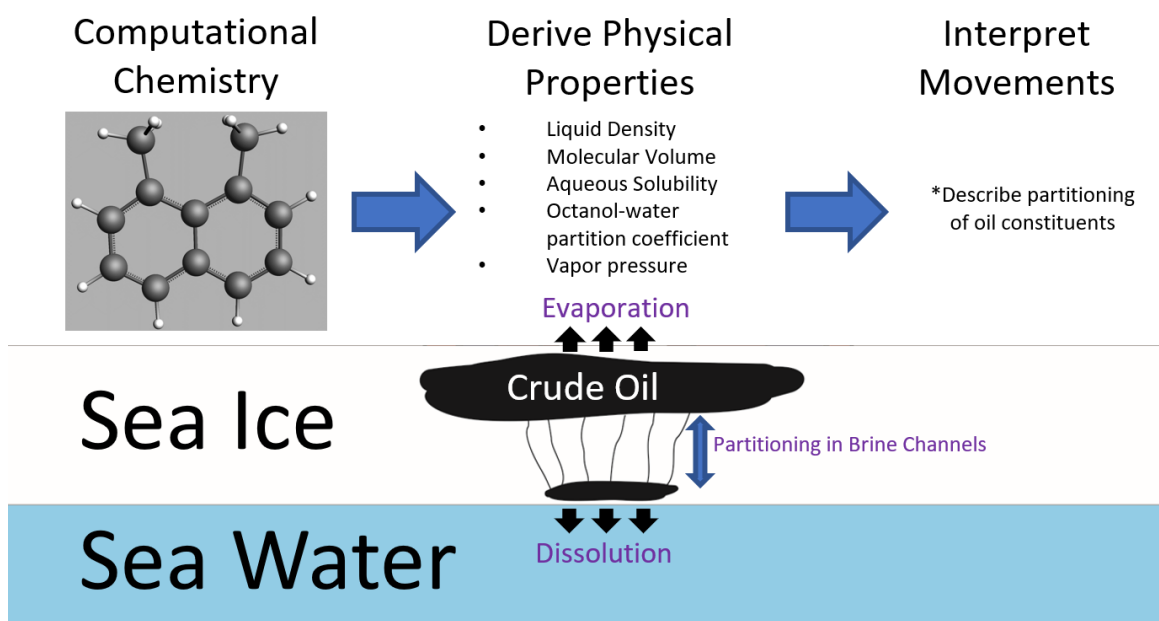


Fig. 3.13 Graphical abstract providing an overview of Chapter 3.

4 Photooxidation and Biodegradation Potential of a Light Crude Oil in First-Year Sea Ice

4.1 Abstract

Disappearing sea ice in the Arctic region results in a pressing need to develop oil spill mitigation techniques suitable for ice-covered waters. The uncertainty around the nature of an oil spill in the Arctic arises from the ice-covered waters and sub-zero temperatures, and how they may influence natural attenuation efficiency.

The Sea-ice Environmental Research Facility (SERF) was used to create a simulated Arctic marine setting. This chapter focuses on the potential for biodegradation of the bulk crude oil content (encapsulated in the upper regions of the ice), to provide insight regarding the possible fate of crude oil in an Arctic marine setting. Cheap and fast methods of chemical composition analysis were applied to the samples to assess for weathering and transformation effects. Results suggest that brine volume in ice may not be sufficient at low temperatures to encompass biodegradation and that seawater is more suitable for biodegradation.

4.2 Introduction

Decreasing Arctic ice cover has resulted in increased access for marine traffic (Dawson et al., 2018) and increased feasibility for oil and gas development within this region (AMAP, 2010), thus increasing the likelihood of petroleum products being spilled in the Arctic marine environment. In 2009, the U.S. Geological Survey estimated that the Arctic

might hold 30% of the world's undiscovered natural gas reserves and 13% of its undiscovered oil, mostly offshore under less than 500 m of water (Lewis & Prince, 2018). These resources will become increasingly accessible as ice cover continues to decline, leading to an urgency to develop oil spill response measures. Recently, significant oil extraction operations have transpired in the Siberian Shelf in Russia. On May 29/20, 20 000 tonnes of diesel oil leaked into the Ambarnaya river within the Arctic Circle, drifting 12 km from the site of accident (BBC News, 2020). Oil spilled in these waters has the potential to make its way into the Arctic Ocean, where it could become significantly weathered and travel within the ice to be released at a later time and place. Naturally occurring microbial communities catalysing bioremediation *via* natural attenuation, with potential stimulation by nutrients, is one approach towards oil spill remediation. The effectiveness of bioremediation in the icy Arctic marine settings remains poorly understood (Gaden, A., 2019). The uncertainty around the nature of an oil spill in the Arctic arises from the ice-covered waters and sub-zero temperatures, which could impact the efficiency of natural attenuation.

Sea-ice oil biodegradation studies have noted larger active microbial populations towards the sea ice base layer and within brine or sea water, and that sea water or brine is where microorganisms proliferate with access to nutrients required for effective biodegradation (Vergeynst et al., 2019; Boetius et al., 2015; Boccadoro et al., 2018; Prince and Walters, 2016). However, oil spilled in sea ice concentrates towards the sea ice surface layer by migrating through porous brine channels and interstices within the ice (Oggier et al., 2019; Desmond et al., 2019a; Saltymakova et al., 2020a). It is therefore important to investigate the potential of biodegradation in the upper regions of sea ice and the fate of

transformed oil constituents. In the Canadian Arctic, an oil spill is more likely to take place in early freeze-up with a heightened shipping or industrial activity than mid-winter (Martin, 1979; Oggier et al., 2019; BBC News, 2020), making the presence of oil in the sea ice surface layers a realistic scenario.

In order to better understand the potential for natural attenuation of oil in sea ice, an artificial oil-in-ice mesocosm experiment was conducted at the Sea-ice Environmental Research Facility (SERF) located at the University of Manitoba. Crude oil compositional changes were assessed based on measured oil dielectrics by cavity perturbation, absorption by infrared spectroscopy (IR), and compound concentrations by gas chromatography–mass spectrometry (GC–MS). Incident and transmitted light measurements by photodiodes, bacterial community analyses, physical properties derived from computational chemistry, and Compact Micro-Computed Tomography X-ray (μ -CT) analysis of oil-contaminated sea ice were also conducted to support and complement our compositional investigation of the oil. This chapter focuses on the potential for photo- and biodegradation of the bulk crude oil content (encapsulated in the upper regions of the ice) during the oil-in-ice mesocosm experiment, with the purpose of providing insight regarding the possible fate of crude oil in an Arctic marine setting. This research will aid in the development of an informed oil-spill response plan.

4.3 Methods

4.3.1 Experiment Overview

During the winter of 2018, the Sea-ice Environmental Research Facility (SERF) located at the University of Manitoba was used for experiments, in which we investigated

growing sea ice in the presence of bacteria and crude oil. Two round fibreglass tanks filled with artificial sea water (NaCl , MgCl_2 , MgSO_4 , and CaCl_2 to a salinity of ~ 33 psu) were utilized in this experiment (Fig. 4.1). The Augmented tank (1 m height, 4 m diameter) was inoculated with the addition of authentic/indigenous Arctic bacteria collected from Cambridge Bay. Enrichment cultures were grown at 4°C in the dark in a minimal medium of artificial seawater with 0.1% crude oil and diesel as their sole carbon and energy source. After four months of growth, when the bacteria culture reached a volume of 12 L, it was concentrated in four 50 ml tubes using centrifugation for transportation to the experimental site. The Native tank (1 m height, 3 m diameter) was not inoculated but contained the bacteria present from the local source groundwater used in the fabrication of the artificial seawater. A mixture of nutrient salts (6 mM NH_4NO_3 and 0.6 mM KH_2PO_4) was added to both tanks to support biodegradation of crude oil. The calculations of the concentration were based on the crude oil volume and were similar to that observed in Arctic marine waters during the summer season (Barber et al., 2017).



Fig. 4.1 Augmented tank (left), Native tank (middle), and an example of an ice core taken during the experiment (right). Photos were taken Feb. 26/18.

Two weeks later (on January 22), once the ice grew to a thickness of 29 cm (Augmented tank) and 25 cm (Native tank), ice cores were taken from both tanks to characterize background bacterial communities and determine baseline hydrocarbon concentrations. Twenty-four hours later, during the afternoon of Jan. 23, 6.6 L of a light Crude oil (Petroleum Crude Oil (Sour) from Tundra Oil & Gas Partnership) was injected underneath the ice from the bottom-centre of the tanks.

To concentrate the crude oil at the centre of each tank, an artificial cavity was created at the bottom of the ice. The cavity was made using insulation which was placed at the center of the pool covering 60% of the ice surface. Since the ice formation is governed by the low ambient temperature, the insulation at the ice-air interface prevents heat from escaping from the ice surface and slows down the ice growth (Weeks, 1986). The cavity allowed triplicate sampling in each of three areas of the tanks representing different crude oil levels of exposure – heavily, moderately, and lightly (visually clean) contaminated areas (Fig. 4.2). Oil contaminated ice cores and water samples were collected on February 7, February 26, March 16, April 10, and April 27 from both tanks. For each batch of samples, 9 cores were taken from each tank, with the exception of April 10 and 27. On April 10, only 6 cores were taken (as there were no moderately contaminated sites at this time), and on April 27, only water samples were taken due to the full melt of ice come late April. Each triplicate ice core set was collected for 1) microbial analyses (community composition), 2) physical analyses (X-ray, temperature, salinity, brine volume), and 3) chemical analyses (oil dielectrics, IR spectroscopy, GC–MS), respectively.

Each ice core was sliced into 3 sections with a sterilized saw to separate the coldest ice section, midsection including the oil introduction ice layer, and brine-rich bottom. For each core, the top section constituted 20% of the total length. The remaining ice core was divided at its mid-depth to yield the middle and bottom sections. This slicing scheme was chosen to optimize both the microbial and chemical analyses. Prior to being sliced, the temperature of each ice core section was measured with an ultra-accurate digital temperature probe (Traceable).

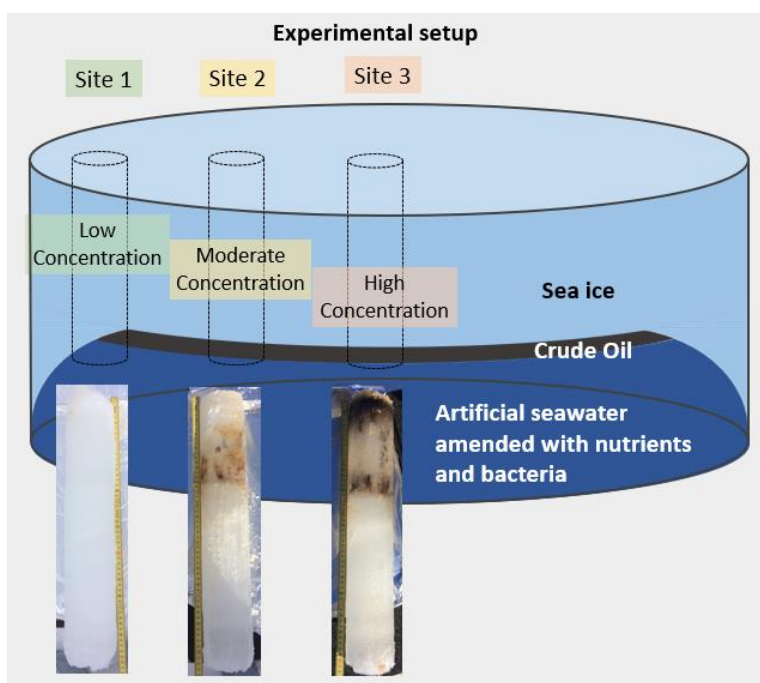


Fig. 4.2 Experimental setup of the cavity allowing sample collection at three sites representing different crude oil contents – Site 1: Low Concentration, Site 2: Moderate Concentration, and Site 3: High Concentration.

In addition to ice core sampling, water samples were collected on each sampling date from the bottom of each tank, stored in amber glass bottles and used for both microbial (1 L

water per DNA replicate) and chemical analysis (3 L of water). Hexane and saltwater field blanks were also taken on each sampling date.

Meteorological temperature data was obtained from the Winnipeg International Airport Station (Fig. 4.3).

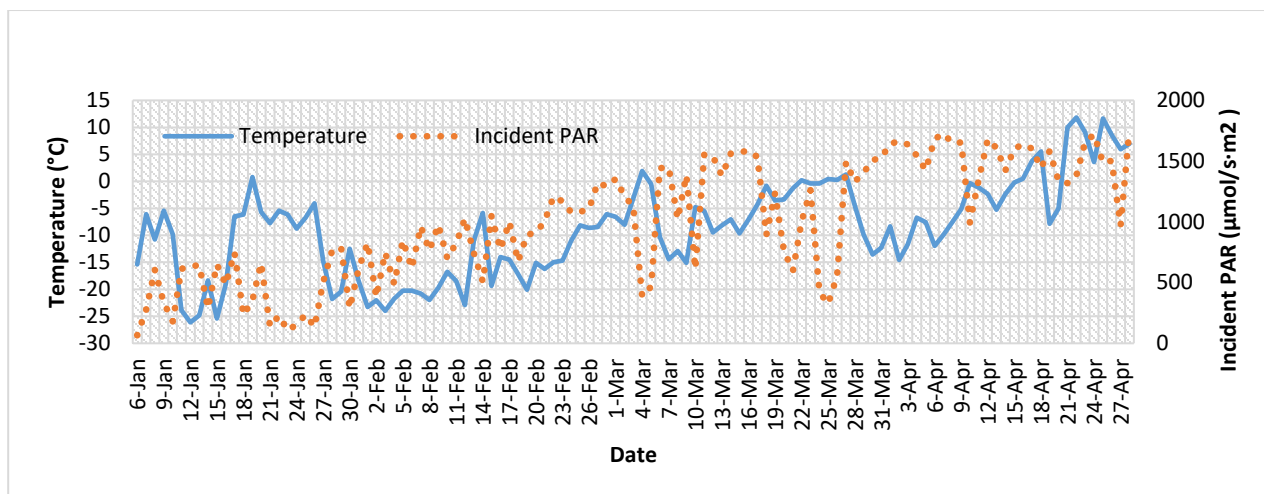


Fig. 4.3 Ambient daily (24-hr) temperature (solid) and incident sunlight (dotted) profiles.

4.3.2 Sample Preparation

Ice core samples reserved for chemical analyses were melted at room temperature and spiked with deuterated compounds (deuterated n-alkane D_{26-72} , Fisherbrand, and polycyclic aromatic hydrocarbons (PAHs) D_8 , D_{10} , D_{12} , Wellington Laboratories). The added deuterated compounds were used as surrogates to access the recovery. The added amounts were based on the level of sample contamination to achieve a close concentration to their non-deuterated counterparts. Water samples were spiked using the same process. The volume of each spiked sample was measured using a graduated cylinder before it was poured into a 1 L separatory funnel for extraction using hexane to extract the non-polar fraction of

hydrocarbons, followed by dichloromethane to extract more polar compounds. Samples were extracted with 20% aliquots of each solvent, relative to the total sample volume, consecutively until the remaining water was completely colorless (minimum of 3). Approximately 40 mL of the remaining sample water was collected into a vortex tube for bulk salinity analysis after the last solvent wash.

A rotary evaporator was used to remove the hexane and dichloromethane until 1–2 mL of the solvent-crude oil solution was remaining. After evaporation, any residual water was removed from the solution using ~1 g of sodium sulphate. The remaining solution was transferred into a pre-weighed glass vial and left open under a closed fume-hood. Once the solvent was fully evaporated the crude oil weight was measured. The crude oil was then diluted to approximately 1% m/v with iso-octane and transferred to a 2 mL GC vial. Using this procedure, PAH (parent and alkyl) recoveries ranged from 90 to 102% with a mean of $95 \pm 4\%$, and n-alkane recoveries ranged from 81 to 122% with a mean of $102 \pm 13\%$. Both the field blanks and laboratory blanks (i.e., hexane and Milli-Q water) were processed identically to the samples.

4.3.3 Analytical Instrumentation

4.3.3.1 *GC-HR-TOF-MS*

LECO Pegasus® gas chromatography-high resolution time of flight mass spectrometry (GC-HR-TOF-MS) was used to measure the composition of alkane and heterocyclic aromatic compounds. The instrument was equipped with a Restek Rxi-PAH column (60m x .025m x 0.1 μ m). Helium was used as a carrier gas with a constant flow rate of 1.4 mL/min. The auto-sampler performed 2 μ L injections at 300°C in splitless mode.

The oven starting temperature was held at 80°C for 1.5 minutes and then raised to 120°C at a rate of 20°C/minute, to 250°C at a rate of 3°C/minute, and finally to 300°C at a rate of 2°C/minute, where it was held at 300°C for 21.5 minutes. The GC transfer line was held at 320°C, and the ion source was held at 300°C. The mass spectrometer was run at a resolution of 25 000 and an acquisition rate of 40 to 550 m/z at 4 spectra/second. Calibration curves were created for dibenzofuran (SPEX), PAH dibenzothiophene (and alkylated homologs) mixture (Chiron, 20 compounds), and n-alkanes (mix of three SPEX standards: C_{C11-18}, odd C_{C15-35}, even C_{C16-36}).

Quality Assurance/Control. The linear range of the calibration curves was 4.9 - 5000 ng/mL for n-alkanes and 3.9-1000 ng/mL for all other compounds. Each consisted of 9 – 11 points with R² values greater than 0.95. The signal-to-noise ratio was set to 6. Based on the lowest range of the calibration curve, the method detection limits varied from 3.9 ng/ml for low MW range compounds and decreased to 620 ng/mL for heavy molecules. We ran one sample duplicate every 10 – 15 samples with the duplicate variability within 5%. The GC-HR-TOF-MS was tuned before and after a sequence of sample runs (every 10 – 12 samples) as well as between each set of samples. Before analysis, all samples were spiked with 25 µL of 4 µg/mL internal standard - 2-fluorobiphenyl (RESTEK) - to correct for the change in ion intensity. Each sample batch contained a sample duplicate and instrument blank. Further details on quality assurance/control can be found in (Saltymakova et al., 2020b).

4.3.3.2 ATR-IR

Attenuated Total Reflection Infrared Spectroscopy (ATR-IR) was used for characterizing the bulk oil composition including heteroatoms, resins and asphaltenes. ATR-

IR has previously been used as a simple and cheap alternative to GC–MS, capable of providing a general compositional analysis and degree of oil weathering and photo-/biodegradation (Fresco-Rivera, et al. 2007; Abdulkadir et al., 2016; Albaigés et al., 2016; Saltymakova et al., 2020a). A total of 42 samples which contained more than 100 μL of crude oil, representing spatial and temporal variation for both tanks, as well as the original technical oil mixture were placed on the ATR-IR (Alpha-P, Bruker) diamond cell and were analyzed with a 2 cm^{-1} resolution over a $4000\text{--}400\text{ cm}^{-1}$ range. An air background subtraction was performed on all measured spectra. All quantified peaks had a signal-to-noise (S/N) ≥ 3 . Various indices were calculated using ratios generated from peak areas. Table S4.1 (Appendix Section 7.1) provides some of the indices calculated and the formulae used, while Table 4.1 provides the calculated indices for a subset of the measured samples.

Quality Assurance/Control. Roughly 30 μL of each oil sample was placed on the ATR-IR diamond cell with the use of a micropipette to alleviate variance of the oil's thin films. Variation in the overall intensity of the IR spectrum due to unequal volumes placed on the ATR cell was found to be less than a factor of 0.2 compared to the measured intensities of 34 individual samples. Consequently, variation in the IR signal intensity from sample to sample was found to be relatively negligible.

4.3.3.3 $\mu\text{-CT}$

Compact Micro-Computed Tomography ($\mu\text{-CT}$) X-ray (SKYSCAN 1174, Bruker) was used to observe the distribution and local proximity of oil and brine inclusions within the oil-contaminated sea ice. Cylindrical sections, with 3 cm diameters and 3 cm heights, were cut from the top and middle sections of oil-contaminated ice cores. The analysis was

conducted following the methods presented in (Desmond et al., 2018) based on prior methods established by (Crabeck et al., 2016; Salomon et al., 2017; Firoozy et al., 2018).

Table 4.1 Oil Dielectric Measurements of Ice Samples at Frequencies TE_{101} (1.8 GHz), TE_{104} (2.9 GHz), and ATR-IR Calculated Indices

Sample	$Re(\epsilon_{r, oil})$, 2.9 GHz	$Re(\epsilon_{r, oil})$, 1.8 GHz	$Im(\epsilon_{r, oil})$, 1.8 GHz	Esters Index	1 or 2 Substituted Rings Index	3 Substituted Rings Index
2018 Crude Oil Tech Mix	2.13	2.26	0.0001	0.0006	0.514	0.247
Feb. 7 Augmented site 3-1 Top	2.35	2.39	0.0091	0.0104	0.831	0.077
Feb. 7 Augmented Site 3-1 Mid	2.78	2.79	0.0446	0.0133	0.871	0.078
Feb. 26 Augmented Site 2-1 Top	2.38	2.49	0.0118	0.0051	0.686	0.149
Feb. 26 Augmented Site 3-2 Top	2.29	2.33	0.0027	0.0016	0.496	0.236
Feb. 26 Augmented Site 2-1 Mid	2.26	2.35	0.0039	0.0010	0.447	0.221
Feb. 26 Augmented Site 3-2 Mid	2.25	2.29	0.0039	0.0016	0.512	0.244
Feb. 26 Augmented Site 3-2 Bot	2.25	2.37	0.0014	0.0013	0.443	0.262
Mar. 16 Augmented Site 3-2 Top	2.37	2.40	0.0077	0.0019	0.448	0.284
Mar. 16 Augmented Site 3-2 Mid	2.30	2.37	0.0198	0.0006	0.379	0.263
Apr. 10 Augmented Site 2-2 Top	2.24	2.35	0.0038	0.0019	0.519	0.268
Apr. 10 Augmented Site 2-2 Mid	2.34	2.43	0.0040	0.0031	0.576	0.197
Apr. 10 Augmented Site 2-2 Bot	2.27	2.33	0.0062	0.0036	0.627	0.177
Feb. 7 Native Site 3-2 Top	2.33	2.48	0.0155	0.0024	0.635	0.183
Feb. 7 Native Site 2-3 Top	2.42	2.46	0.0105	0.0041	0.646	0.199
Feb. 7 Native Site 2-1 Mid	2.40	2.54	0.0103	0.0015	0.543	0.199
Feb. 7 Native Site 2-3 Mid	3.06	3.26	0.0293	0.0142	0.887	0.064
Feb. 26 Site 3-1 Native Top	2.25	2.36	0.0026	0.0011	0.487	0.275
Feb. 26 Site 3-1 Native Mid	2.21	2.33	0.0027	0.0010	0.487	0.216
Mar. 16 Site 3-3 Native Top	2.24	2.29	0.0080	0.0020	0.456	0.250
Mar. 16 Native Site 2-2 Top	2.30	2.37	0.0038	0.0021	0.411	0.268
Mar. 16 Native Site 3-3 Mid	2.29	2.36	0.0089	0.0038	0.599	0.209
Mar. 16 Native Site 2-2 Mid	2.31	2.44	0.0039	0.0019	0.510	0.235
Apr. 10 Native Site 2 Core 3 Mid	2.36	2.42	0.0113	0.0009	0.406	0.267
R^2 (Linear) – $Re(\epsilon_{r, oil})$, 2.9 vs. 1.8 GHz	0.95					
R^2 (Linear) – Re vs. $Im(\epsilon_{r, oil})$, 1.8 GHz	0.57					
R^2 (Linear) – Esters vs. 1, 2 sub. Index	0.86					
R^2 (Linear) – Esters vs. 3 sub. Index	0.83					

4.3.3.4 Optical Measurements

Photosynthetically active radiation (PAR) sensors (MDS MK-L) were used to measure the incident sunlight $E_d(\lambda, 0)$ and transmitted sunlight $E_d(\lambda, h)$ intensities of both tanks; defined as # photons in the 400-700 nm interval arriving per unit time on a unit area of a flat receiver. These measurements were used to assess the potential interaction of the

light and oil in a sea-ice environment within the wavelength range of 400 to 700 nm. The transmittance $T(\lambda, h)$ of the oil-contaminated sea ice was calculated using Eq. (4.1), where λ is the wavelength (in meters) and h is the height (70 cm) from the sea ice surface to the bottom of the tank.

$$4.1 \quad T(\lambda, h) = \frac{E_d(\lambda, h)}{E_d(\lambda, 0)}$$

4.3.3.5 *Dielectric Measurement: Resonance Perturbation Method*

This technique was used to measure the dielectrics for a subset of the extracted crude oil samples from the oil-in-ice mesocosms (i.e., 24 samples containing ≥ 2 mL volume) to examine the impact of biodegradation/photo-oxidation on the electromagnetic properties of crude oil. Recent publications have shown that microwave measurements can be correlated to the density and chemical composition of crude oil (e.g., Alvarez et al., 2021; Saltyrnakova et al., 2020a; Desmond et al., 2019a, 2019b). Cavity perturbation is a relative dielectric measurement technique that makes use of an electromagnetic cavity resonator (custom built by Dr. Gregory Bridges, Advanced RF Systems Lab). The dimensions of the samples and custom cavity used in the setup are (O/D = 3 mm, I/D = 1.53-1.61 mm, H = 43 mm) and (W = 86 mm, H = 43 mm, L = 262 mm) respectively. All measurements were conducted at 22.5 °C.

Plots of the $|S_{11}|$ data for the resonant peak corresponding to the frequencies 1.8 (TE₁₀₁) and 2.9 (TE₁₀₄) GHz within the cavity were constructed. Subsequently, the dielectrics for crude oil samples were calculated from the $|S_{11}|$ data using Eqs. (4.2)–(4.7) (Chen et al., 2005), in which Eqs. (4.2)–(4.4) pertain to variables related to the cavity perturbation theory,

Eq. (4.5) provides ψ , a correction factor for TE_{m0p}, and finally Eqs. (4.6) and (4.7) solve for ϵ_r' and ϵ_r'' , the real and imaginary parts respectively, of the sample's relative dielectrics. The real part of an oil's relative dielectrics is related to its density and chemical alteration due to weathering and transformation processes (Alvarez et al., 2021; Saltymakova et al., 2020a; Desmond et al., 2019a, 2019b), while the imaginary component correlates to the asphaltene, metal, and aromatic content (Alvarez et al., 2021). The relative dielectric calculations are provided in Table 4.1.

$$4.2 \quad Q_L = f_0 / \Delta f_{\text{xdB}}$$

$$4.3 \quad \xi = \{(1 - |S_{11}|_{f_0}, \text{overcoupled}), 1 + |S_{11}|_{f_0}, \text{undercoupled}\}$$

$$4.4 \quad Q_U = Q_L \{(2/\xi)(|S_{11}|_{\text{xdB}}^2 - |S_{11}|_{f_0}^2)/(1 - |S_{11}|_{\text{xdB}}^2)\}^{1/2}$$

$$4.5 \quad \psi = [\sin(\frac{m\pi}{2})\sin((\frac{p\pi}{d}) * 100 \text{ mm})]^2$$

$$4.6 \quad \epsilon_r' = 1 - 2 \left[\frac{(f_s - f_0)}{f_0} \frac{V_C}{4 \psi V_S} \right]$$

$$4.7 \quad \epsilon_r'' = [V_C/4 \psi V_S][(1/Q_S) - (1/Q_0)]$$

where m and p – correspond to the resonant mode TE_{m0p} propagating within the cavity; d – 262 mm; Q – quality factor; V_S – oil sample volume; V_C – resonant cavity volume; f_s – frequency at which the local $|S_{11}|$ minimum occurs when perturbing the cavity with the oil sample in a glass tube; f_0 – frequency at which the local $|S_{11}|$ minimum occurs when perturbing the cavity with the empty glass tube (i.e., the “unperturbed” case); ψ – correction factor for the electric field strength of the TE_{m0p} modes at the perturbation location within the cavity; $|S_{11}|$ – the electromagnetic reflection coefficient at the input to the cavity; Δf_{xdB} –

the x dB bandwidth of the resonant peak where $|S_{11}| = x$ dB; $|S_{11}|_{x\text{dB}}$ – the value of $|S_{11}| = x$ dB in linear units.

Quality Assurance/Control. Precise measurements of the cavity and sample volume is required to calculate accurate dielectric values based on Eqs. (4.6) and (4.7). Soda Lime glass tubing was used for oil sample containment inside the resonant cavity. As manufactured tubing, drawn from molten glass, is not precise and varies in wall thickness, its inner and outer diameters can fluctuate over a 1-meter span. Furthermore, minute changes in the glass wall thickness (e.g., 0.1 mm) can affect the degree of losses associated with measurement in the resonant cavity. To avoid inaccuracy in results due to inconsistency in glassware dimensions, each glass tube was measured twice, with and without its oil sample, assuring an exact response from the resonant cavity. Furthermore, manual measurements of the inner diameters of the glass tubes were also taken with an inverted light microscope (OLYMPUS) equipped with an ocular ruler with 0.03 mm spacing. The measured inner diameters of the glass tubes ranged from 1.53 to 1.61 mm with an average \pm standard deviation of 1.56 ± 0.02 . An assigned uncertainty of 0.02 mm in the ability to read the ocular ruler results in an uncertainty in the hundredths place of calculated dielectric constants ($\Delta\epsilon'_r \leq 0.04$).

Further quality assurance is demonstrated by the reproducibility of results. Table 4.1 shows that the dielectric constant [1.8 GHz] of the 2018 technical mixture (2.26) is very close to the values obtained for 2017 (2.24) and 2016 (2.25) technical mixtures (Saltymakova et al., 2020a; Desmond et al., 2019a). Furthermore, the permittivity of the oil samples was observed to have a moderate decrease with frequency (Table 4.1). This is expected as these frequencies are above the relaxation frequency of crude oil (Friisø et al., 1998). Above the

relaxation frequency, the permittivity of crude oil decreases gradually until ionic and electronic dispersion occurs at much higher frequencies (\geq THz).

4.3.4 Microbial Analysis

Microbial cells were collected on 0.2 μ m polyethersulfone filters (Pall) using a vacuum pump and Pall Sentino manifold. The entire volume of thawed ice cores was filtered by decanting into 250 mL Pall Sentino disposable plastic filter cups. For heavily oil-contaminated sections, the liquid was first poured into a separatory funnel and allowed to settle before collecting the lower aqueous phase, which was then filtered as above. Melted ice was filtered until the flow rate began to slow appreciably, which was typically after around 900 mL had been filtered. Filters were then immediately transferred into 15 mL centrifuge tubes using sterile forceps and placed in a -80 °C freezer prior to DNA extraction.

DNA was extracted from the filters using the Qiagen PowerWater DNA extraction kit according to the manufacturer's instructions (QIAGEN, 2020) with minor modifications as described below. Bead beating was carried out using an Omni BeadRuptor instrument for 5 minutes at 2.4 m/s. After extraction, DNA was eluted into 35 μ L of nuclease-free ultrapure water and the concentration of DNA measured using a Qubit fluorometer.

Amplicon libraries were prepared using the most recent (as of November 2019) Earth Microbiome Project 16S rRNA gene primers: 515F (Parada) [GTGYCAGCMGCCGCGGTAA] and 806R (Apprill) [GGACTACNVGGGTWTCTAAT]. Polymerase chain reaction (PCR) was performed in triplicate for each sample using 5 nmol of DNA extract and 2x Kapa HiFi Hot Start Ready Mix in 25 μ L reaction volume. Thermocycler settings for the PCR reactions were to ramp up

to an initial melting temperature of 94 °C which was followed by 35 cycles of PCR with denaturing at 94 °C for 45 seconds, annealing at 50 °C for 60 seconds and elongation at 72 °C for 90 seconds, with a final 10 minutes elongation step at the end. Reactions were checked by running the products on an agarose gel and checking for a product of approximately 390 base pairs. Triplicate reactions were pooled and clean-up performed using Macherey-Nagel NucleoMag NGS Clean-Up and Size-Select beads.

Sequencing was carried out using an in-house Illumina Miseq sequencer with a dual indexing strategy that generated paired-end reads approximately 250 base pairs in length. Demultiplexed forward and reverse sequences were combined and quality filtered using the MetaAmp pipeline (Dong et al., 2017). MetaAmp was configured to remove sequences for which there was less than 50 base pairs of overlap between forward and reverse reads or more than 1 mismatch within the overlap region. Merged sequences with more than 1 expected error over the length of the sequence, calculated using Phred quality scores, were also removed, as were any sequences exhibiting mismatches in the primer region. Merged sequences were truncated to 248 base pairs and clustered into 97% identity operational taxonomic units (OTUs). Representative sequences from each OTU were used to assign a taxonomic classification to the OTU using the Silva v132 reference database.

All data analysis was carried out within the R version 3.5.2 statistical software environment (R Core Team, 2019) and plots produced using the R graphics package ggplot2. Initial filtering of the sequence data was carried out to remove OTUs assigned to chloroplasts or to Eukaryotes, which resulted in the removal of 10 out of 625 initially retrieved OTUs. Stacked bar plots were generated for OTUs grouped at the Class or, for Gammaproteobacteria

only, Genus taxonomic level. To avoid overly cluttered plots, any classes not constituting at least 1% of total sequences in at least one sample were not plotted. For Gammaproteobacterial genera this threshold was increased to 5% relative abundance. Sequences that could not be taxonomically classified at the class or genus level, as appropriate, were also omitted. These manipulations were carried out using the phyloseq R package (McMurdie and Holmes, 2013).

4.4 Results and Discussion

4.4.1 Sea Ice Geophysics and Oil Distribution

On January 8th, air temperature below 0 °C facilitated ice growth in both the Native and Augmented tanks (Fig. 4.3). Moderate differences in growth rates were observed spatially and temporally between mesocosms (Table S4.2 – Appendix Section 7.1). These differences in ice growth rates are likely attributed to 1) the different pool diameters and 2) insulation installed in the walls of the Native tank slowing initial heat loss. Over the course of the experiment, the ice temperature of both tanks increased with warmer ambient conditions (Figs. 4.3, 4.4). Due to the warmer ice temperatures and interactions with oil (Saltymakova et al., 2020a; Saltymakova et al., 2020b), changes in sea ice brine volume varied over time; however, the brine volume fraction was consistently higher at lower ice depths (Fig. 4.4C and D). Despite the differences in ice thickness, the observed temperature and brine volume fraction trends of both tanks were found to be relatively similar. However, their vertical oil distributions varied significantly over time (Fig. 4.4E and F). Notably, on Feb. 7, the largest oil fraction was observed in the top and middle ice section of the Native and Augmented tank, respectively. This result is likely due to the moderately warmer ice

temperatures seen for the Native tank on Feb. 7 allowing for greater oil entrainment and infiltration through the ice (Petrich et al., 2013; Maus et al., 2015; Oggier et al., 2019; Eicken, 2003; Petrich and Eicken, 2010).

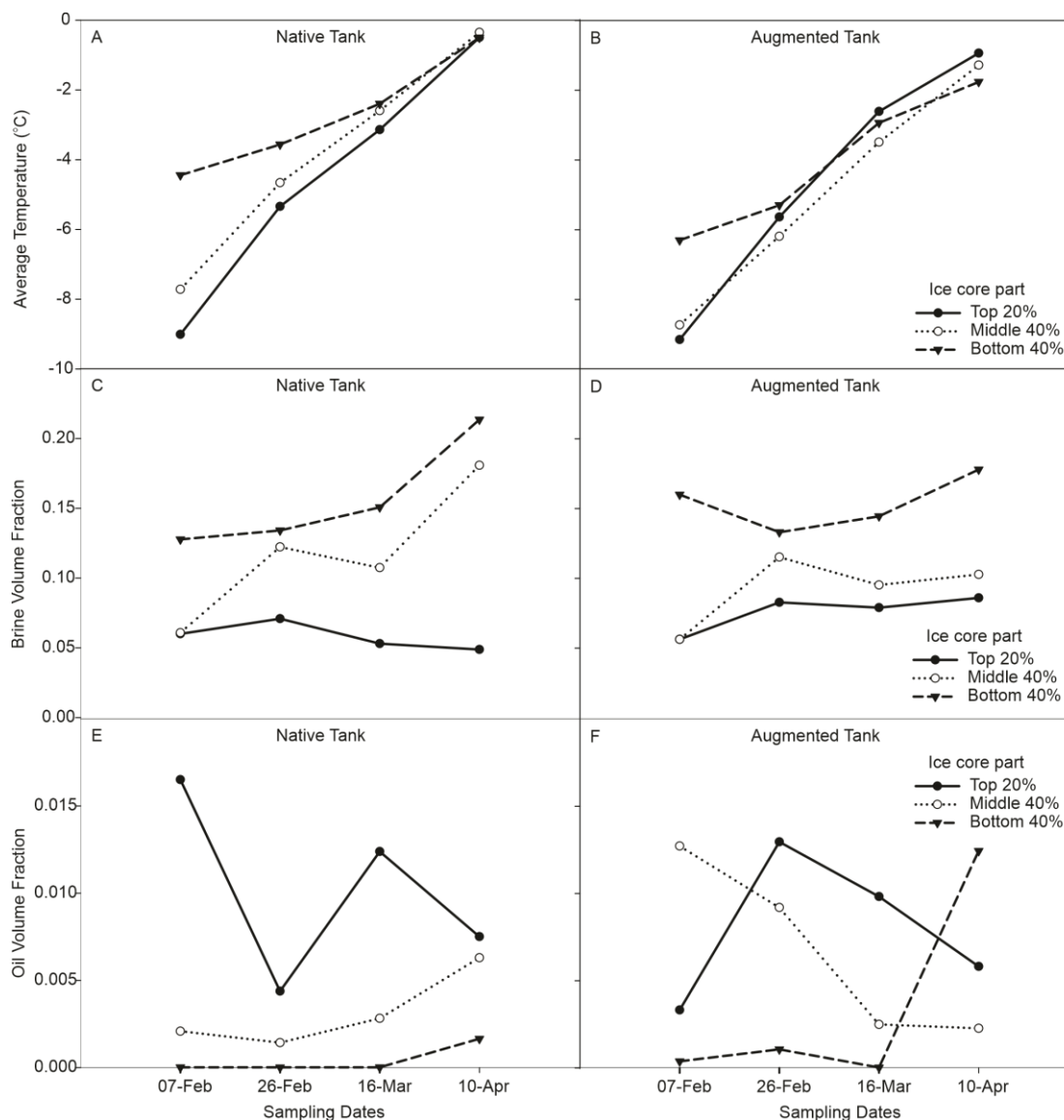


Fig. 4.4 Measured temperatures of top, middle, and bottom sectioned ice cores using a temperature probe for Native (A) and Augmented (B) tanks. Calculated brine volume fractions of top, middle, and bottom sectioned ice cores for Native (C) and Augmented (D) tanks using the measured temperatures and bulk salinities following (Frankenstein and Garner, 1967). Measured oil volume fractions (V_{OIL}/V_{ICE}) of top, middle, and bottom sectioned ice cores for Native (E) and Augmented (F) tanks following (Desmond et al., 2019a).

4.4.2 Microbial Populations Capable of Biodegradation

Analysis of the microbial community in the ice of the pools by 16S rRNA gene amplicon sequencing revealed a shift in both pools from a community dominated by Bacteroidia to a Gammaproteobacteria-dominated community (Fig. 4.5A). Although the ability to degrade hydrocarbons varies significantly among bacteria, members of the Gammaproteobacteria are commonly observed to respond following oil spills in sea water (Prince et al., 2010). Therefore, the increase in the relative abundance of Gammaproteobacteria is consistent with a shift to a microbial community that is better adapted for crude oil degradation.

Gammaproteobacteria were also an important component of the microbial community in the ground water used to prepare the two pools (Fig. 4.5, first bar), comprising about 20% of this initial community. Major groups in this community were *Marinobacter*, *Shewanella* and the Marine Methylophilic Group 3 (MMG3). Both *Marinobacter* and *Shewanella* include strains that have been reported to degrade hydrocarbons (Prince et al., 2010) and they have also been reported to respond to the addition of crude oil to sea ice (Brakstad et al., 2008; Gerdes et al., 2005). However, both genera are also metabolically flexible and commonly found in cold marine environments without the presence of oil (Deming, 2009). Increases in the relative abundance of Gammaproteobacteria over the course of the experiment featured mainly *Pseudomonas* in the Native pool and a combination of *Pseudomonas*, *Shewanella*, and *Idiomarina* in the Augmented pool (Fig. 4.5B). These results are similar to the observations of Gerdes et al. (2005) and Brakstad et al. (2008), who also observed shifts in sea ice microbial communities to include higher proportions of

Pseudomonas and *Shewanella*. While it is plausible that these results reflect the development of a hydrocarbon-degrading microbial community in the sea ice, it is noted that many of these groups are generalists capable of metabolising a wide array of compounds other than hydrocarbons; their presence does not necessarily confirm that crude oil biodegradation was taking place.

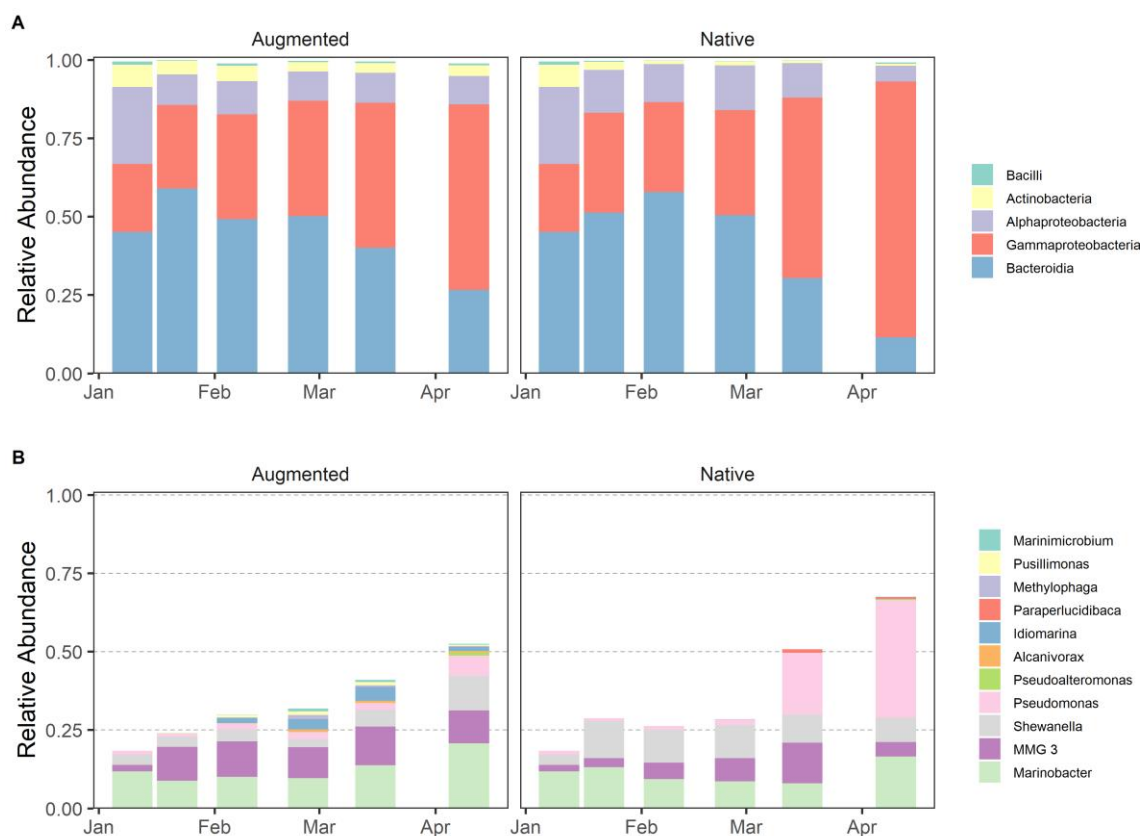


Fig. 4.5 Relative sequence abundance of bacterial lineages at the class level (A), and within the Gammaproteobacteria lineage at the genus level (B). The bars reflect the mean community composition across all ice samples collected on a given sampling date. Classes that never comprised >1% of the microbial community are not shown in (A). MMG3: Marine methylotrophic group 3.

In contrast to the microbial community found in the ice (Fig. 4.5) and depth water (Fig. S4.1 – Appendix Section 7.1), the microbial composition of the melt pond samples in April were quite distinct (Fig. 4.6). These samples were dominated by a single genus of Gammaproteobacteria, *Alcanivorax*. Unlike most of the other genera that were detected, this genus is commonly considered to be an ‘obligate’ hydrocarbon (in particular, n-alkanes) degrader, meaning that species from that genus are not considered to be able to grow using other sources of carbon. Furthermore, bacterial respiration from within the melt pond was visually observed during April in the form of bubbling on the surface water. Similar Arctic marine experiments have showed *Alcanivorax* to be associated with water but not with ice (Garneau et al., 2016).

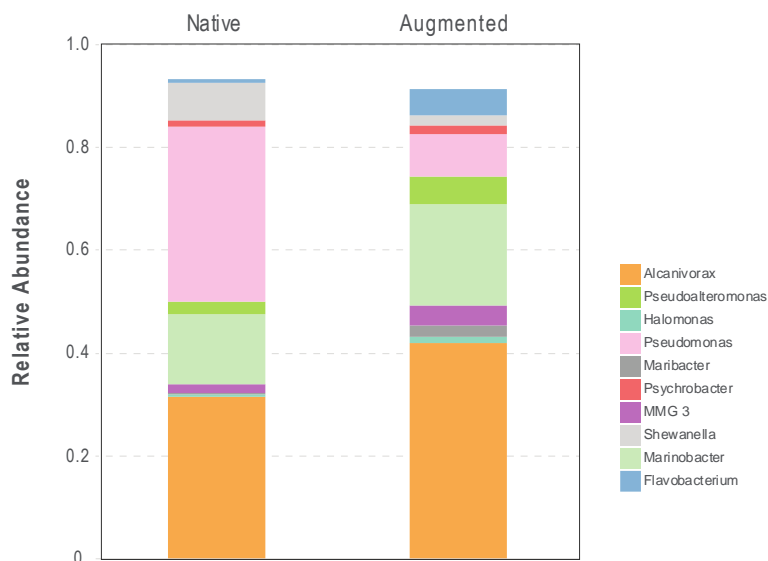


Fig. 4.6 Relative sequence abundance of bacterial lineages at the genus level for the melt pond samples on April 10. The bars reflect the mean community composition across all samples collected on that sampling date. Genera that never comprised >1% of the microbial community are not shown. MMG3: Marine methylotrophic group 3.

4.4.3 Extent of Oil Transformation

The dielectric constant of oil is one of the governing factors of active microwave measurements concerning oil-contaminated sea ice (Firoozy et al., 2018). Simply defined, the dielectric constant is a measure of resistance or lack of polarization of the Coulomb force between two-point charges in a dielectric material when applied to an electric field in a particular medium (Knight, 2013). The relative dielectric constant of a material is defined as a ratio relative to the permittivity of vacuum. In general, highly polarizable materials have larger dielectric constants relative to less polarizable materials (Knight, 2013). As crude oil is a complex mixture, it encompasses compounds which differ in their dielectric constant (e.g., Table 4.2). Therefore, as the composition of an oil mixture changes as a result of weathering or transformation processes, the effective dielectric constant will, in turn, reflect these changes (Desmond et al., 2019a, 2019b; Saltymakova et al., 2020a; Alvarez et al., 2021). Consequently, comparing the dielectric constant profiles of both pools can be used as an assessment of transformation (degradation) extent in the two pools. As biodegradation is known to degrade lower molecular weight alkanes and PAHs to produce products which contain elements such as oxygen (Vergeynst et al., 2019; Prince and Walters, 2016), a quantifiable increase in the dielectric constant should be observed in both pools, given a transformation takes place (Table 4.2). Similarly, photooxidation would result in an increase in the dielectric constant due to a transformation of aromatics to include elements such as oxygen and/or sulfur (Saltymakova et al., 2020a; Albaigés et al., 2016; Fresco-Rivera et al., 2007; Sydnese et al., 1985). The dielectric constant of 1,8-dimethyl naphthalene is 2.449 and the dielectric constant of its products after photooxidation are 2.511 and 2.889 for 1-methoxy-

8-methylnaphthalene-1-ketal and 1-methoxy-8-methylnaphthalene-1,4-diol (Sydnes et al., 1985), respectively (Table 4.2). It is worth pointing out that transformation products are less volatile and more soluble (Table 4.2) and are expected to end up in the water column.

Table 4.2 Modeled Physical Properties of Compounds found in Crude Oil using ADF2017/2018 COSMO-RS. Adapted from Saltymakova et al., 2020a and Desmond et al., 2019b.

Compounds	Density, g/mL	Dielectric constant	Solubility, -2.4°C, ng/L		Log K _{ow}	Vapor pressure
	25°C	25°C	Freshwater	35 g/g Salty water	-12°C	-12°C, µBar
Undecane	0.733	1.970	19250.00	9940.00	7.030	101.01
Pentadecane	0.756	2.011	48.41	20.24	9.506	0.30
Heptadecane	0.764	2.03	2.44	0.92	10.730	0.02
Pristane	0.789	2.07	1.12	0.41	11.207	0.01
Nonadecane	0.770	2.036	0.14	0.05	11.908	<10-2
Heptacosane	0.786	2.065	0.000001	0.0000002	16.719	<10-2
Octacosane	0.788	2.069	0.0000003	0.00000007	17.213	<10-2
Nonacosane	0.789	2.071	0.00000006	0.00000001	17.846	<10-2
Cyclopentane	0.790	2.072	262221040	190575390	3.003	194683.49
Cyclohexane	0.826	2.140	92444180	64548810	3.470	648.83
Naphthalene	1.003	2.507	168905100	121161900	3.330	101.42
1,8-Dimethylnaphthalene	0.977	2.449	31915480	21787150	3.825	661.27
Phenanthrene	1.065	2.651	16660260	11046620	4.373	0.40
Chrysene	1.103	2.744	1513010	926110	5.424	<10-2
Dibenzothiophene	1.147	2.857	24607790	16555580	4.242	0.45
Dibenzofuran	1.153	2.873	40771920	28085320	3.985	2.53
1-methoxy-8-methylnaphthalene-1-ketal *	1.005	2.511	791208230	541357520	2.777	8.55
1-methoxy-8-methylnaphthalene-1,4-diol *	1.159	2.889	6059508380	3986412890	1.994	<10-2

*- Based on structures from (Sydnes et al., 1985); Log K_{ow} – n-Octanol/Water Partition Coefficient

4.4.3.1 Photooxidation

From the analysis of light measurements taken with photodiodes above and below the sea ice of both pools, it was found that sunlight was able to interact sufficiently with the encapsulated oil over the first two weeks of the experiment (Fig. 4.7A), when the ice surface was relatively bare with no or little snow cover (Fig. 4.7B) and the ice thickness was ~40 cm (Table S4.2 – Appendix Section 7.1). Solar radiation can transmit through oil-contaminated sea ice due to dispersion of oil within sea ice (Saltymakova et al., 2020a), and it is reasonable to expect ~40% light transmittance through bare sea ice with a thickness of 40 cm (Taskjelle et al., 2016). Notably, more light transmitted through the ice of the augmented pool during the beginning of the experiment (Fig. 4.7A), owing to an initially thinner snow layer than the native pool (Fig. 4.7B). Proceeding this time (Feb. 7 - Mar. 16), the presence of snow cover was found to impede the potential for photo-oxidation significantly (Fig. 4.7B), despite the increase of daily sunlight with the transition of winter to spring (Fig. 4.3). Photooxidation in the presence of a snow layer (e.g., 2 cm thickness) is relatively negligible (Desmond et al., 2019a; Perovich, 2007).

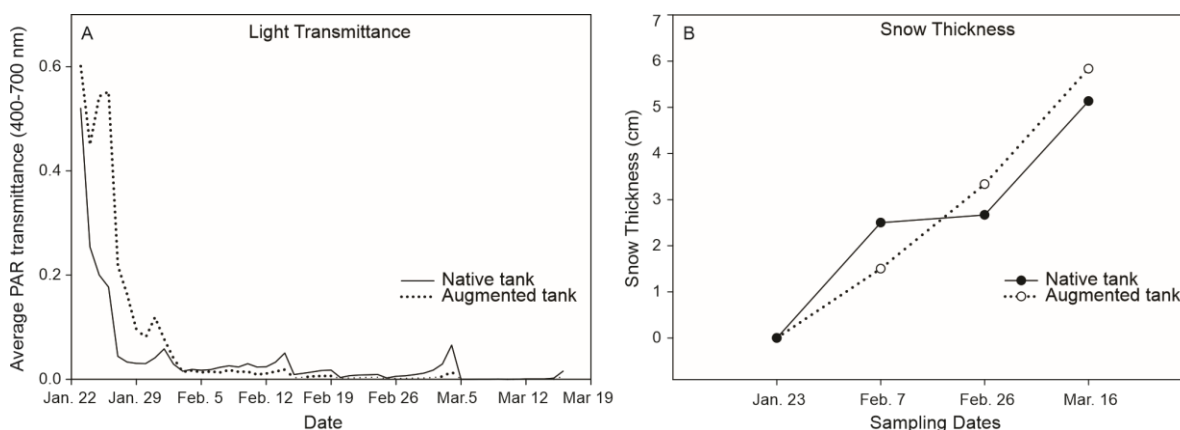


Fig. 4.7 A) PAR transmittance for Native tank and Augmented tank. Daily Average Sunlight Peak Hours (10 am to 3 pm); B) Average snow thickness accumulated on both Native and Augmented pools.

From Fig. 4.8, the dielectric constant measurements of both pools show very similar profiles from the date of oil injection (Jan. 23) through the sampling dates of Feb. 7, Feb. 26, Mar. 16, and Apr. 10. Note that the measurement technique required oil samples with volumes greater than 2 mL and as such many of the oil samples derived from bottom ice core sections could not be measured (refer to Section 4.3.3.5 for details). Based on both the light measurement analyses as well as the ATR-IR analysis below, the initial rise in the oil dielectric constant [1.8 GHz] from 2.26 to 2.80 (or higher) found for both pools on Feb. 7 was deemed to be attributed to photo-oxidation.

Attenuated total reflectance infrared spectroscopy was used as a means of assessing photo-oxidation (Albaigés et al., 2016; Fresco-Rivera, et al. 2007; Saltymakova et al., 2020a) (Table 4.1, Fig. 4.9). Significant photooxidation was observed on Feb. 7 with large increases seen by the C–O (ester) absorbance band (1250 cm^{-1}) and sulfoxide band (1030 cm^{-1}) indicating an increase in the transformation of aromatic ring structures to esters and

sulfoxides (Figs. 4.8C, D, and 4.9). Furthermore, an increase in the C-H aromatic ring peak 743 cm^{-1} absorbance band (Fig. 4.9) indicates a decrease of trisubstituted aromatics $[814/(864+814+743)]\text{cm}^{-1}$ ($R^2=0.83$) and a corresponding relative increase of mono and disubstituted aromatic rings $[743/(864+814+743)]\text{cm}^{-1}$ ($R^2=0.86$) (Table 4.1) (also seen in Saltymakova et al., 2020a), likely due to the higher susceptibility of higher branched compounds to photooxidation (Bobinger and Andersson, 2009; Garrett et al., 1998; Prince et al., 2003). A strong linear relationship ($R^2=0.99$) between the 1250 cm^{-1} and 743 cm^{-1} bands can be seen in Fig. S4.2 (Appendix Section 7.1) showcasing a systematic loss of highly conjugated aromatic species with greater additions of oxygen, indicative of photooxidation. As can be seen from Figs. 4.8C, D, and S4.3 (Appendix Section 7.1) there exists a strong positive correlation ($R^2=0.83$) between the IR C-O (1250 cm^{-1}) ether band trends and that of the oil dielectric constant trends, spatially and temporally within the ice. The close connection between these two methods of analysis provides good confirmation of the existence and extent of photooxidation during this experiment as well as the use of permittivity as a measure of polar compounds in the sample. Lastly, it is worth pointing out the larger extent of esters and sulfoxides measured by ATR-IR (Table 4.1, Figs. 4.8C, D, and 4.9) on Feb. 7 for the augmented pool compared to native, likely due to the augmented pool's thinner snow cover and larger light transmittance during the first week of the experiment (Fig. 4.7).

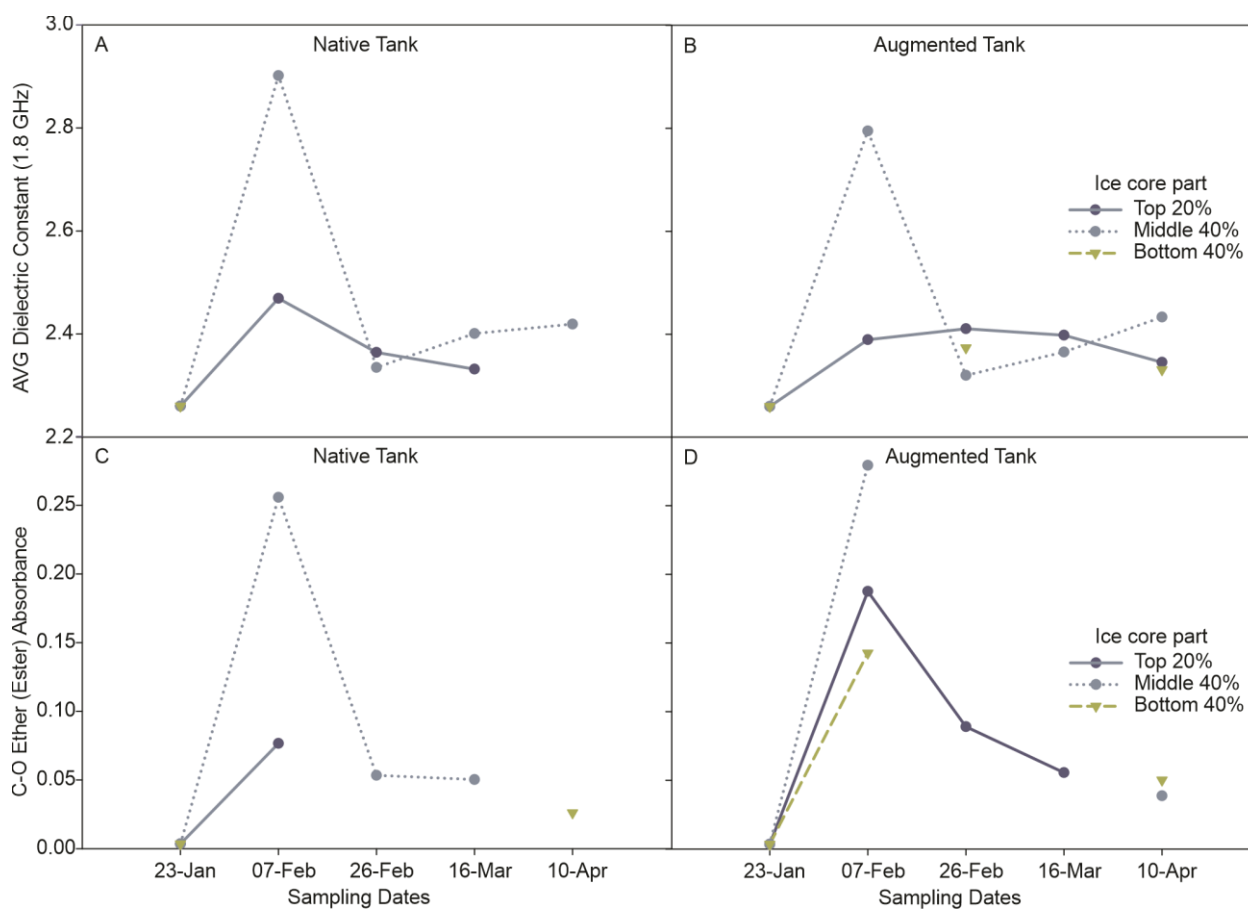


Fig. 4.8 The average dielectric constant of extracted oil taken from sampled sea ice core sections (i.e., top ice sections, middle and bottom ice sections) of Native (A) and Augmented (B) pools. All measurements were made at 1.8 GHz and 22.5 °C. Averaged ATR-IR absorbance of the C-O (1250 cm^{-1}) ether band associated with ester transformation products for Native (C) and Augmented (D) pools.

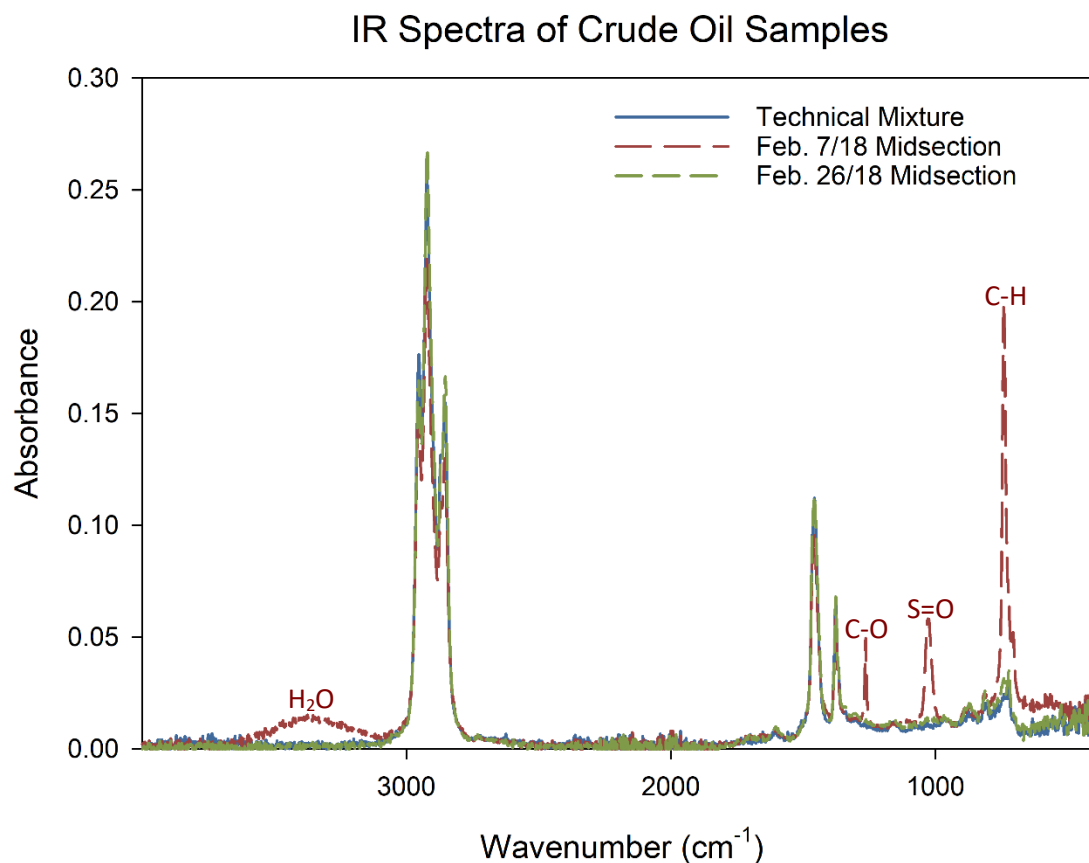


Fig. 4.9 ATR-IR Absorbance Spectrum of the technical mixture versus the extracted oil samples “Feb. 7 Augmented Site 3 Core 1 Middle Section” and “Feb. 26 Augmented Middle Section” (see Table 4.1).

4.4.3.2 Dissolution

The subsequent decrease in the dielectric constant and ATR-IR C–O absorbance band (1250 cm⁻¹) profiles found on Feb. 26 (Figs. 4.8 and 4.9) can be attributed to the loss of polar compounds into the water column due to their higher solubility (and lower volatility) (Table 4.2) and penchant for dissolution and migration from the surface to the water column (Desmond et al., 2019a; Saltmakova et al., 2020a; Payne et al., 1991) upon warmer ambient conditions (Fig. 4.3). This result is supported by the large increases in concentrations found

for heterocyclic compounds in the water column over time through our analysis with gas chromatography–mass spectrometry (Fig. 4.10). We observed differences in the concentration of polar compounds in the water between the native and augmented tanks for the first three sampling dates, owing to the differing degrees of their photooxidation, respectively (Section 4.4.3.1). The active melting process equalized the content of the compounds in the water by Apr. 10. Similar to the aromatics, a large increase in heptadecane relative to pristane (C_{17}/Pr) was observed in both pools on Feb. 26 (Fig. 4.11) presumably due to dissolution of lighter alkanes into the water column. Heptadecane is 2.2X more soluble than pristane (Table 4.2) and is expected to concentrate more readily in the water column.

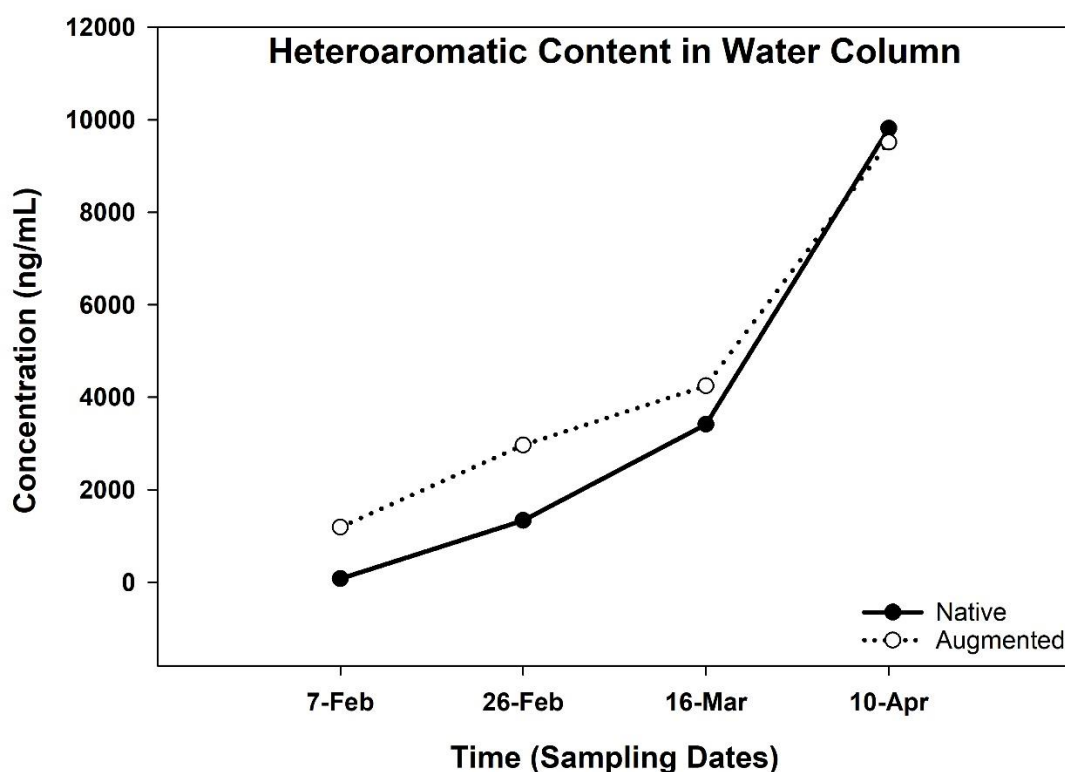


Fig. 4.10 Temporal concentrations of heterocyclic aromatics found in the water column by GC–MS.

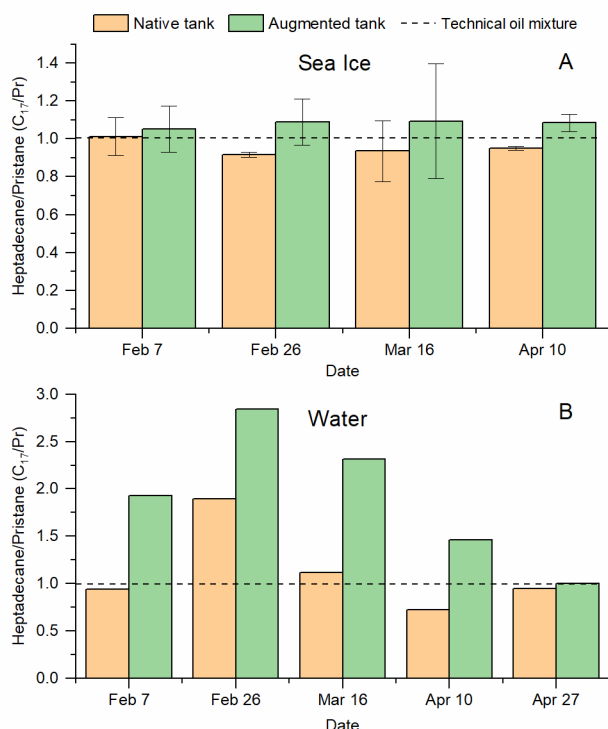


Fig. 4.11 C_{17}/Pr ratio measured per ice core (A) and depth water column (B). Error bars show standard deviation.

4.4.3.3 Biodegradation

From Feb. 26, the dielectric constant profiles of the oil-in-ice were observed to have plateaued showing little or no significant change (Fig. 4.8) for both tanks. However, a slight systematic increase was observed for the middle section of the ice in both pools, while their top sections display an overall decrease. The overall decrease observed for the top sections is postulated to be the result of downward dissolution of the aromatic fraction caused by warmer weather (Figs. 4.3, 4.10), as discussed previously (Section 4.4.3.2). The slight increase in the dielectric constant (~ 0.1) observed for the middle sections could be the result of biodegradation, owing in part to their larger brine content (Fig. 4.4), as brine is the medium in which sea ice microorganisms proliferate. However, we must bear in mind that the

uncertainty in the dielectric constant measurements is 0.03-0.04. Furthermore, other types of processes (e.g., partitioning within sea ice) could influence the effective dielectric constant values (Desmond et al., 2019a; Saltymakova et al., 2020a). For instance, the slight increase in the dielectric constant (~ 0.1) observed for the middle sections could also be due to the downward movement/dissolution of polar compounds from their respective top sections. To better assess if biodegradation took place within the ice, C_{17}/Pr ratio (Kristensen and others, 2015) was calculated for each ice core (Fig. 4.11A). From Fig. 4.11A, each C_{17}/Pr ratio stays within 20% of the initial value and does not show a significant decrease over time indicating a lack of biodegradation of oil in the ice.

Given that the presence of putative oil-degrading microbial populations in the sea ice was observed for both tanks throughout the experiment (Section 4.4.2), explanations as to why biodegradation was not very prevalent is provided in the following. The bulk of the oil was found to be typically encapsulated in the mid- or upper layers of the sea ice (Fig. 4.4E and F), while the bulk of the brine content was found towards the bottom of the sea ice (Fig. 4.4C and D). Moreover, μ -CT analysis (Fig. 4.12) provides strong evidence of the tendency of oil to remain separate from brine. Overall, oil-contact was limited to less than 2 and 3% for oil-contaminated sea ice taken from a Feb. 7 middle ice section and Mar. 16 top section, respectively. Although the oil-brine contact within sea ice can increase with growing brine/oil volumes (Fig. 4.12), biodegradation's greatest potential would lie with a high brine and low oil content. Consequently, it is not likely that biodegradation would have contributed significantly (or at all) to the increases of oil polarity seen in Fig. 4.8 (Jan. 23 – April 10), but may have become more prevalent with the formation of a melt pond in April. As brine or

sea water is the phase in which sea ice microorganisms proliferate and contain the necessary nutrients for metabolic functioning, including oil biodegradation (Vergeynst et al., 2019; Boetius et al., 2015; Prince and Walters, 2016; Stevenson et al., 2015), only under such conditions in which the bulk of the oil is in direct contact with the brine or sea water can significant biodegradation ensue. However, small amounts of hydrocarbons in the brine or seawater may still have an appreciable effect on the microbial community composition, by promoting proliferation of oil-degrading bacteria, even when overall biodegradation in the system is minimal.

The lighter compounds more effectively dissolve in brine due to their higher solubilities in comparison to heavier compounds (Table 4.2) and are flushed down towards the water column (Fig. 4.10) (Saltymakova et al., 2020a; Desmond et al., 2019a; Payne et al., 1991) where they can be potentially degraded by the presence of crude oil-degrading bacteria (Brakstad et al., 2008; Delille et al., 1997). Fig. 4.11B shows a steady decrease in the C_{17}/Pr ratio in the water column after Feb. 26, indicating gradual biodegradation of dissolved oil constituents. This evidence of biodegradation is likely underestimated due to heptadecanes' greater solubility relative to pristane (Table 4.2).

Furthermore, air temperature above 0 °C in April (Fig. 4.3) facilitated the presence of a melt pond in both Native and Augmented tanks. There is also potential for significant biodegradation of oil in a melt pond scenario due to the media's direct contact with oil compounds. As the melt pond period entailed a single sampling instance, we could not directly evaluate the occurrence of biodegradation in the melt ponds; however, the melt pond samples were dominated by a single genus of Gammaproteobacteria, *Alcanivorax* (Fig. 4.6).

Unlike most of the other genera that we detected, this genus is commonly considered to be an ‘obligate’ hydrocarbon (in particular, alkane) degrader (Berry and Gutierrez, 2017), pointing to the likelihood that its high relative abundance in the melt ponds in both tanks was due to growth coupled to crude oil metabolism.

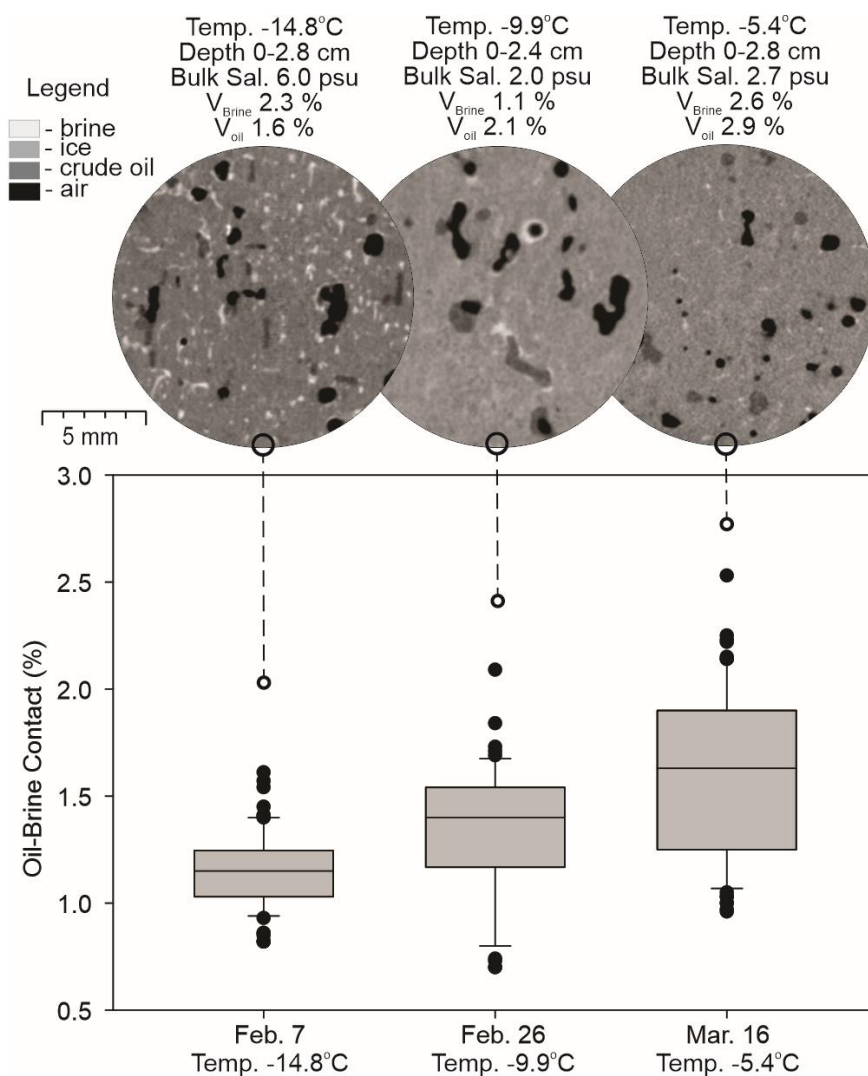


Fig. 4.12 μ -CT Tomographic grayscale images of coronal (X-Z) view vertical slices of three oil-contaminated samples showcasing the oil, and brine inclusion distribution. In these images, air is shown in black, brine is shown in white, ice is shown in light grey, and oil is shown in dark grey. Box plots showing the percentage of oil and brine interface connection for the two μ -CT oil-contaminated sea ice samples.

Further analyses entailing a more in-depth investigation into the paraffinic (GC-MS) and hetero-aromatic fractions (liquid chromatography-mass spectrometry) of oil samples (light-heavy concentrations) are currently being conducted and will be linked spatially and temporally with the microbial community data (Snyder et al., 2019; Saltymakova et al., 2019).

4.5 Conclusion

To better understand the fate of oil spilled in the Arctic marine environment, a mesoscale study was carried out at the University of Manitoba as a part of the Microbial Genomics for Oil Spill Preparedness in Canada's Arctic Marine Environment GENICE project. This study involved two large (7m³ and 12m³) outdoor, above-ground pools filled with artificial seawater mixed with nutrients. The larger pool was inoculated with indigenous bacteria collected from Cambridge Bay during the R/V *Martin Bergmann* 2017 summer field season. Light crude oil was released under the ice in both pools after 20cm of ice was grown under natural ambient temperature. Ice cores were taken from both pools every three weeks, and extraction of crude oil was followed by various analyses including the measurement of the oil's dielectric constant (permittivity) spatially and temporally for both Augmented and Native pools. As oil permittivity is affected by compositional changes, it was used as a means of assessing the extent of biodegradation and photooxidation for the bulk crude oil content found within the sea ice. Our analyses found that photooxidation increased the oil permittivity, when there was little or no snow cover, while dissolution within the sea ice acted to decrease the oil permittivity. Through μ -CT X-ray analysis, it was found that the bulk oil

content in the ice remained separate from the brine and that the potential biodegradation extent of the concentrated oil was minimal.

Herein, our investigation focused on the potential for biodegradation of the bulk encapsulated oil found towards the upper regions of sea ice. We observed that the dielectrics of the bulk oil content plateaued after its initial photooxidation and dissolution, and remained frozen in the ice with minimal subsequent weathering and transformation processes. Based on this result, we expect that the bulk encapsulated oil will be better preserved in the sea ice with less extensive weathering compared to open water, and potentially subject to biodegradation upon the melt season, when the oil is released back into the ocean.

4.6 Acknowledgements

This research was funded by GENICE, Genome Canada, Research Manitoba. The authors thank Canada Research Chair (CRC) programs, Natural Sciences and Engineering Research Council (NSERC) of Canada, the Canada Foundation for Innovation (CFI) and the University of Manitoba. We also thank Dave Binne (SERF Technician, CEOS), Jake Ritchie (Technician, CEOS), Gregory Bridges (Advanced RF Systems Lab, Dept. of Elec. & Comp. Eng.), Horace Luong (Dept. of Chem.), Lesa Cafferty (Cafferty's Scientific Glassblowing), Thomas Neusitzer (CEOS), Michael Stone (DNA extraction, UCalgary), Emily Ellefson (DNA extraction, UCalgary), as well as the Manitoba Chemical Analysis Laboratory (MCAL) and Manitoba Institute for Materials (MIM). This work was made possible by the facilities of the Shared Hierarchical Academic Research Computing Network (SHARCNET:www.sharcnet.ca) and Compute/Calcul Canada as well as Software for Chemistry & Materials (SCM).

4.7 References

Abdulkadir, I., Uba, S., Salihu A., A., Almustapha, M.N., 2016. “A Rapid Method of Crude Oil Analysis Using FT-IR Spectroscopy.” *Nigerian Journal of Basic and Applied Science* 24(1): 47-55.

Albaigés, J., Bayona, J.M., Radovic', J.R., 2016. “Photochemical effects on oil spill fingerprinting”, in *Standard Handbook Oil Spill Environmental Forensics: Fingerprinting and Source Identification*, Chap. 20, S. Stout and Z. Wang (2nd ed.), Elsevier/Academic Press.

Alvarez, J.O., Jacobi, D., Althaus, S., Elias, S., 2021. “Dielectric characterization of geochemical properties of liquid hydrocarbons from 25°C to 125 °C.” *Fuel* 288: 119679.

AMAP, 2010. AMAP Assessment 2007: oil and gas activities in the arctic — effects and potential effects. Arctic Monitoring & Assessment Programme, Oslo, vols. 1 and 2.

Barber, D.G., Meier, W.N, Gerland, S., Mundy, C.J., Holland, M., Kern, S., Li, Z., Michel, C., Perovich, D.K., Tamura, T., 2017. Arctic sea ice. In: Snow, Water, Ice and Permafrost in the Arctic (SWIPA) 2017. pp. 119-127. Arctic Monitoring and Assessment Programme (AMAP), Oslo, Norway.

BBC News (2020), Arctic Circle oil spill prompts Putin to declare state of emergency. Retrieved from <https://www.bbc.com/news/amp/world-europe-52915807>.

Berry, D., Gutierrez, T., 2017. “Evaluating the Detection of Hydrocarbon-Degrading Bacteria in 16S rRNA Gene Sequencing Surveys.” *Front. Microbiol.* 8:896.

Bobinger, S., Andersson, J.T., 2009. “Photooxidation products of polycyclic aromatic compounds containing sulfur.” *Environ. Sci. Technol.* 43:8119–8125.

Boccardo, C., Krolicka, A., Receveur, J., Aeppli, C., Le Floch, S., 2018. “Microbial community response and migration of petroleum compounds during a sea-ice oil spill experiment in Svalbard.” *Marine Environmental Research* 142:214-233.

Boetius, A., Anesio, A.M., Deming, J.W., Mikucki, J.A., Rapp, J.Z., 2015. “Microbial ecology of the crosphere: sea ice glacial habitats.” *Nature Reviews Microbiology* 13:677-690.

Brakstad, O.G., Nonstad, I., Faksness, L.-G., Brandvik, P.J., 2008. “Responses of Microbial Communities in Arctic Sea Ice After Contamination by Crude Petroleum Oil.” *Microb Ecol* 55:540–552.

Chen, L.F., Ong, C.K., Neo, C.P., Varadan, V.V., Varadan, V.K., 2004. “Resonant-perturbation Methods”, in *Microwave electronics: measurement and materials characterization*, Chap. 6, John Wiley & Sons.

Crabeck, O., Galley, R., Delille, B., Else, B., Geilfus, N.-X., Lemes, M., Des Roches, M., Francus, P., Tison, J.-L., Rysgaard, S., 2016. "Imaging air volume fraction in sea ice using non-destructive X-ray tomography", *The Cryosphere* 10:1125–1145.

Dawson, J., Pizzolato, L., Howell, S.E.L., Copland, L., Johnston, M., 2018. "Temporal and spatial patterns of ship traffic in the Canadian Arctic from 1990 to 2015." *Arctic* 71(1):15–26.

Delille, D., Bassères, A., Dessommes, A., 1997. "Seasonal variation of bacteria in sea ice contaminated by diesel fuel and dispersed crude oil." *Microb. Ecol.* 33:97–105.

Deming, J.W., "Sea Ice Bacteria and Viruses", in *Sea Ice*, D.N. Thomas, and G.S. Dieckmann, eds. (Oxford, UK: Wiley-Blackwell), pp. 247–282, 2009.

Desmond, D.S., Crabeck, O., Lemes, M., Polcwiartek, K., Neusitzer, T.D., Saltymakova, D., Synder, N., Rysgaard, S., Barber, D.G., Stern, G.A., 2018. "Investigation into the Geometry and Distribution of Oil Inclusions in Sea Ice using non-destructive X-ray Tomography", in *Proceedings of the 2018 ArcticNet Annual Scientific Meeting*, Ottawa, ON, CA.

Desmond, D.S., Neusitzer, T.D., Lemes, M., Isleifson, D., Saltymakova, D., Mansoori, A., Barber, D.G., Stern, G.A., 2019b. "Examining the Physical Interactions of Corn Oil (Medium Crude Oil Surrogate) in Sea Ice and its Potential for Chemical Partitioning within an Arctic Environment", in *Proceedings of the Forty-second AMOP Technical Seminar*, Environment and Climate Change Canada, Ottawa, ON, Canada, pp. 66-95.

Desmond, D.S., Saltymakova, D., Neusitzer, T.D., Firoozy, N., Isleifson, D., Barber, D.G., Stern, G.A., 2019a "Oil Behavior in Sea Ice: Changes in Chemical Composition and Resultant Effect on Sea Ice Dielectrics." *Marine Pollution Bulletin* 142:216-233.

Dong, X., Kleiner, M., Sharp, C.E., Thorson, E., Li, C., Liu, D., Strous, M., 2017. "Fast and Simple Analysis of MiSeq Amplicon Sequencing Data with MetaAmp." *Front. Microbiol.* 8.

Eicken, A., "From the microscopic to the macroscopic to the regional scale: Growth, microstructure and properties of sea ice", in Contribution to Thomas D. & G. S. Dieckmann (eds.): *SEA ICE – AN INTRODUCTION TO ITS PHYSICS, BIOLOGY, CHEMISTRY AND GEOLOGY*, Blackwell Science, London, 2003, pp. 22-81, 2003

Firoozy, N., Neusitzer, T., Chirkova, D., Desmond, D., Lemes, M., Landy, J., Mojabi, P., Rysgaard, S., Stern, G., Barber, D.G., 2018. "A Controlled Experiment on Oil Release Beneath Thin Sea Ice and its Electromagnetic Detection." *IEEE Transactions on Geoscience and Remote Sensing* 56(8):4406-4419.

Frankenstein, G., Garner, R., 1967. "Equations for determining the brine volume of sea ice from -0.5 to -22.9°C." *J. Glaciology* 6.48:943-944.

Fresco-Rivera, P., Fernández-Varela, R., Gómez-Carracedo, M.P., Ramírez-Villalobos, F., Prada, D., Muniategui, S., Andrade, J.M., 2007. "Development of a fast analytical tool to identify oil spillages employing infrared spectral indexes and pattern recognition techniques." *Talanta* 74:163–175.

Friisø, T., Schildberg, Y., Rambeau, O., Tjomsland, T., Førde, H., Sjøblom, J., 1998. "Complex permittivity of crude oils and solutions of heavy crude oil fractions." *J. Dispersion Sci. Technol.* 19:93–126.

Gaden, A. (2019), GENICE-Microbial Genomics for Oil Spill Preparedness in Canada's Arctic Marine Environment. Retrieved from <http://umanitoba.ca/faculties/environment/departments/ceos/research/GENICE.html>.

Garneau, M.-E., Michel, C., Meisterhans, G., Fortin, N., King, T.L., Greer, C.W., Lee, K., 2016. "Hydrocarbon biodegradation by Arctic sea-ice and sub-ice microbial communities during microcosm experiments, Northwest Passage (Nunavut, Canada)." *FEMS Microbiology Ecology* 92: fiw130.

Garrett, R.M., Pickering, I.J., Haith, C.E., Prince, R.C., 1998. "Photooxidation of crude oils", *Environ. Sci. Technol.* 32:3719–3723.

Gerdes, B., Brinkmeyer, R., Dieckmann, G., Helmke, E., 2005. "Influence of crude oil on changes of bacterial communities in Arctic sea-ice." *FEMS Microbiol Ecol* 53:129–139.

Knight, R.D., 2013. "Electricity and Magnetism" in *Physics For Scientists And Engineers: A Strategic Approach*, 3rd ed., vol. 4, Pearson Education.

Kristensen, M., Johnsen, A.R., Christensen, J.H., 2015. "Marine biodegradation of crude oil in temperate and Arctic water samples." *J. Hazard. Mater.* 300: 75–83.

Lewis, A., Prince, R., 2018. "Integrating Dispersants in Oil Spill Response in Arctic and Other Icy Environments." *Environmental Science & Technology* 52(11):6098–6112.

Martin, S., 1979. "A Field Study of Brine Drainage and Oil Entrainment in First-Year Sea Ice." *Journal of Glaciology* 22(88):473–502.

Maus, S., Becker, J., Schneebeli, M., Wiegmann, A., 2015. "Oil Saturation of the sea ice pore space", in *Proceedings of the 23rd International Conference on Port and Ocean Engineering under Arctic Conditions*.

McMurdie, P.J., Holmes, S., 2013. phyloseq: An R Package for Reproducible Interactive Analysis and Graphics of Microbiome Census Data. *PLOS ONE* 8, e61217.

Oggier, M., Eicken, H., Wilkinson, J., Petrich, C., O'Sadnick, M., 2019. "Crude oil migration in sea-ice: Laboratory studies of constraints on oil mobilization and seasonal evolution." *Cold Regions Science and Technology* 174: 102924.

Payne, J.R., Hachmeister, L.E., McNabb, G.D., Sharpe, H.E., Smith, G.S., Menen, C.A., 1991. "Brine-induced advection of dissolved aromatic hydrocarbons to Arctic bottom waters." *Environ. Sci. Technol.* 25:940–951.

Perovich, D.K., 2007. "Light reflection and transmission by a temperate snow cover." *Journal of Glaciology* 53(181):201-210.

Petrich, C., Eicken, H., 2010. "Growth, structure and properties of sea ice", in *Sea Ice*, Chap. 4, Second Edition, Wiley-Blackwell, United Kingdom.

Petrich, C., Karlsson, J., Eicken, H., 2013. "Porosity of growing sea ice and potential for oil entrainment." *Cold Regions Science and Technology* 87:27-32.

Prince, R.C., Walters, C.C., 2016. "Biodegradation of oil hydrocarbons and its implications for source identification", in *Standard Handbook Oil Spill Environmental Forensics: Fingerprinting and Source Identification*, Chap. 19, S. Stout and Z. Wang (2nd ed.), Elsevier/Academic Press.

Prince, R.C., Garrett, R.M., Bare, R.E., Grossman, M.J., Townsend, T., Suflita, J.M., Lee, K., Owens, E.H., Sergy, G.A., Braddock, J.F., Lindstrom, J.E., Lessard, R.R., 2003. "The Roles of Photooxidation and Biodegradation in Long-term Weathering of Crude and Heavy Fuel Oils." *Spill Science & Technology Bulletin* 8(2): 145–156.

Prince, R.C., Gramain, A., McGenity, T.J., 2010. "Prokaryotic Hydrocarbon Degraders", in *Handbook of Hydrocarbon and Lipid Microbiology*, K.N. Timmis, ed. (Berlin, Heidelberg: Springer), pp. 1669–1692.

QIAGEN (2020), *DNeasy PowerWater Kit*. Retrieved from <https://www.qiagen.com/ca/products/discovery-and-translational-research/dna-rna-purification/dna-purification/microbial-dna/dneasy-powerwater-kit/#resources>

R Core Team, 2019. R: A Language and Environment for Statistical Computing. R Foundation for Statistical Computing, Vienna, Austria.

Salomon, M.L., Arntsen, M., Phuong, N.D., Maus, S., O' Sadnick, M., Petrich, C., Schneebeil, M., Wiese, M., 2017. "Experimental and Micro-CT study on the Oil Distribution in laboratory grown Sea Ice", in *Proceedings of the 24th International Conference on Port and Ocean Engineering under Arctic Conditions*, Busan, Korea, 1-13.

Saltymakova, D., Desmond, D.S., Isleifson, D., Firoozy, N., Neusitzer, T.D., Xu, Z., Lemes, M., Barber, D.G., Stern, G.A., 2020a "Effect of dissolution, evaporation, and photooxidation on crude oil chemical composition, dielectric properties and its radar signature in the Arctic environment." *Marine Pollution Bulletin* 151:110629.

Saltymakova, D., Desmond, D.S., Galley, R., Polcwiartek, K., Neusitzer, T.D., Firoozy, N., Barber, D.G., Stern, G.A., 2020b. "The influence of sea ice conditions on crude oil spill behavior." *Cold Regions Science and Technology*. Accepted pending major revisions on Jan. 31, 2023.

Saltymakova, D., Smith, A., Polcwiartek, K., Desmond, D., Snyder, N., Wolfe, T., Bautista, M.A., Stone, M., Ellefson, E., Hubert, C., Stern, G.A., 2019. "Enriched Arctic Bacteria potential for biodegradation of polycyclic aromatic hydrocarbons estimated from Crude Oil-in-ice Mesocosm Experiment", in *Proceedings of the Forty-second AMOP Technical Seminar*, Environment and Climate Change Canada, Ottawa, ON, Canada, pp. 66-95.

Snyder, N., Wang, F., Ritchie, J., Saltymakova, D., Polcwiartek, K., Desmond, D.S., Smith, A.F., Hubert, C., Stern, G.A., 2019. "Analysis of heteroatomic species in biodegraded crude oil using electrospray ionization ion mobility time-of-flight high-resolution mass spectrometry", in *Proceedings of the International Symposium on Sea Ice at the Interface*, International Glaciological Society, Winnipeg, MB, Canada.

Stevenson A., Cray, J.A., Williams, J.P., Santos, R., Sahay, R., Neuenkirchen, N., McClure, C.D., Grant, I.R., Houghton, J.D.R., Quinn, J.P., Timson, D.J., Patil, S.V., Singhal, R.S., Antón, J., Dijksterhuis, J., Hocking, A.D., Lievens, B., Rangel, D.E.N., Voytek, M.A., Gunde-Cimerman, N., Oren, A., Timmis, K.N., McGenity, T.J., Hallsworth, J.E., 2015. "Is there a common water-activity limit for the three domains of life?" *International Society for Microbial Ecology* 9:1333–1351.

Sydnese, L.K., Hansen, S.H., Burkow, I.C., 1985. "Factors affecting photooxidation of oil constituents in the marine environment. I. Photochemical transformations of dimethylnaphthalenes in an aqueous environment in the presence and absence of oil." *Chemosphere* 14:1043–1055.

Taskjelle, T., Hudson, S.R., Granskog, M.A., Nicolaus, M., Lei, R., Gerland, S., Stamnes, J.J., Hamre, B., 2016. "Spectral albedo and transmittance of thin young Arctic sea ice." *J. Geophys. Res. Oceans*, 121:540–553.

Vergeynst, L., Christensen, J.H., Kjeldsen, K.U., Meire, L., Boone, W., Malmquist, L.M.V., Rysgaard, S., 2019 "In situ biodegradation, photooxidation and dissolution of petroleum compounds in Arctic seawater and sea ice." *Water Research* 148:459-468.

Weeks, W., 1986. "The growth, structure, and properties of sea ice", in *The Geophysics of Sea Ice*, Springer US, Boston, MA, pp. 9–164.

Chapter 4 investigated aspects of oil behavior (i.e., migration tendencies, encapsulation potential, dissolution, photooxidation, biodegradation) and mitigation (i.e., bioremediation) in sea-ice environments. Specifically, this chapter aimed to test the following hypotheses:

1. Oil permittivity is affected by compositional changes.
2. Photooxidation will increase the oil permittivity.
3. Dissolution within sea ice will act to decrease the oil permittivity.
4. Surficial oil will remain separate from the brine.
5. Biodegradation extent on surficial oil-in-ice will be minimal, but apparent in water.

Each of these assumptions was found to be true based on the data presented in Chapter 4. However, further research is required to study the fate and behavior of oil under various sea ice conditions and different oil concentrations. A better understanding of the fate and behavior of oil-in-ice is necessary to establish both remote sensing and mitigation practices suitable for cold environments. To this end, Chapter 5 utilizes μ -CT to analyze sea ice samples taken from both the SERF 2017 (Chapter 2) and 2018 (Chapter 4) oil-in-ice mesocosm studies. Implications for remote sensing detection and bioremediation of oil-contaminated sea ice were made based on quantifying the geometry, size, orientation, and distribution of sea ice inclusions (oil, air, brine) from the analyzed samples.

5 Investigation into the Geometry and Distribution of Oil Inclusions in Sea Ice using non-destructive X-ray Microtomography and its Implications for Remote Sensing and Mitigation Potential

5.1 Abstract

As climate change brings reduced sea ice cover and longer ice-free summers to the Arctic, northern Canada is experiencing an increase in shipping and industrial activity in this sensitive region. Disappearing sea ice, therefore, makes the Arctic region susceptible to accidental releases of different types of oil and fuel pollution resulting in a pressing need for the development of appropriate scientific knowledge necessary to inform regulatory policy formulation.

In this study, we examine the microstructure of the surficial layers of sea ice exposed to oil using X-ray microtomography. Through analysis, 3D imaging of the spatial distribution of the ice's components (brine, air, and oil) was made. Additional quantitative information regarding the size, proximity, orientation, and geometry of oil inclusions was computed to ascertain discernable relationships between oil and the other components of the ice. Our results indicate implications for airborne remote sensing and bioremediation of the upper sea ice layers.

5.2 Introduction

Within the Arctic, anthropogenic global warming has led to continual decreases in sea-ice extent, thickness, and changes in ice type (IPCC, 2014; AMAP, 2017). Shipping and oil exploration are, therefore, becoming increasingly more feasible, thereby increasing the potential of crude oil or fuel being spilled into the marine environment (AMAP, 2010; Schenk, 2011; Smith and Stephenson, 2013; Harsem et al., 2011). This impending possibility has generated a need for the development of oil detection and mitigation techniques suitable for ice-covered waters (Fritt-Rasmussen et al., 2015; Brown and Fingas, 2003; Brekke et al., 2014; Wilkinson et al., 2015; Bradford et al., 2015; Firoozy et al., 2017; Hubert and Stern, GENICE).

Sea ice is a heterogeneous porous media consisting of an ice matrix that is embedded with liquid brine inclusions, solid salts, and air bubbles. The presence of brine networks and air inclusions strongly influences the electromagnetic properties of the ice, thus impacting incident electromagnetic responses used in remote sensing detection and characterization (Fingas and Brown, 2007). Notably, the brine inclusions are often sites of biological activity (Fritsen et al., 1994; Krembs et al., 2000; Vancoppenolle et al., 2013). The abundance, distribution, and structure of brine and air inclusions are strongly dependent on the temperature and salinity of the sea ice. Its thermodynamic history, as well as its surface features (e.g., snowfall, frost flowers, and surface roughness) also play a major role (Cox and Weeks, 1983; Weeks and Ackley, 1986; Galley et al., 2015). As sea ice has the potential for oil entrainment (Petrich et al., 2013; Maus et al., 2015; Oggier et al., 2019), the inclusion of oil inside the ice matrix will influence the temperature and salinity of the ice and therefore

the presence and morphology of the brine and air inclusions (e.g., Payne et al., 1991a; O'Sadnick et al., 2017).

Remote sensing of oil in and on sea ice based on dielectric difference is well established in the literature (e.g., Puestow et al., 2013; Brekke et al., 2014; Firoozy et al., 2017; Firoozy et al., 2018). From past work, it was concluded that it is possible to detect the bulk oil content embedded within the surface of sea ice, using active radar, through the reduction of sea ice salinity caused by brine displacement from upward oil migration through brine channels (Desmond et al., 2019a; Saltymakova et al., 2020). This reduction of salinity lowers the dielectrics and thus the radar signature of sea ice, allowing for a detectable change. Furthermore, physical simulations have been linked to remote sensing of oil-contaminated sea ice previously (e.g., Neusitzer et al., 2018a; Desmond et al., 2019a; Isleifson et al., 2020; Firoozy et al., 2018). In particular, modeling the Normalized Radar Cross-Section (NRCS) of sea ice has been a common practice. The physics of the energy interactions based on real or simulated dielectric differences of oil, brine, and sea ice apply similarly to microwave remote sensing and X-ray tomography.

A moderate amount of research on oil behavior in sea ice has been conducted over the last few decades (e.g., Fingas and Hollebone, 2003; Brandvik and Faksness, 2009; Ballesterio and Magdol, 2011; Faksness et al., 2011; Faksness and Brandvik, 2008; Fritt-Rasmussen et al., 2015; Maus et al., 2015; Petrich et al., 2013; Afenyo et al., 2016a; Afenyo et al., 2016b; Payne et al., 1991a; Payne et al., 1991b; Oggier et al., 2019). Much of this research has focused on bulk physical movement tendencies (macroscopic behavior) and less on microscopic behavior within the ice. In order to properly establish detection technologies

and mitigation potential (Firoozy et al., 2017; Neusitzer et al., 2018a; Firoozy et al., 2018; Hubert and Stern, GENICE), a better understanding of the movements and interactions of oil in a sea ice environment on a microscopic scale is required. To this end, we present a methodology employing enhanced computed microtomography X-ray imaging for analyzing the microstructure of oil-contaminated sea ice.

Micro-Computed Tomography (μ -CT) X-ray imaging is a non-destructive radiographic technique which examines materials by creating images of density contrast. As dense materials and higher atomic numbers result in greater X-ray attenuation, an image of the target of interest can be created (Duliu, 1999). The resultant image is represented in grayscale whereby darker tones indicate a material of lower density (e.g. air) and lighter tones indicate higher density materials or phases (e.g., brine). Since μ -CT is capable of high-resolution three-dimensional characterization of the internal features of porous media, it has been advantageous for examining the brine and air components of sea ice microstructure (e.g., Crabeck et al., 2016; Golden et al., 2007; Lieb-Lappen et al., 2017; Maus et al., 2013; Maus et al., 2015; Obbard et al., 2009; Pringle et al., 2009; Frantz et al., 2019). Little X-ray work, however, has been conducted on oil-contaminated sea ice (Courville et al., 2017; Bazilchuk, 2018; Salomon et al., 2017). Oil and ice have similar densities producing little contrast in the resultant μ -CT-image (Salomon et al., 2017). Furthermore, small volume fractions of oil relative to the ice can also hinder the distinction between the two phases. Herein we introduce a novel method for the enhanced imaging of oil in sea ice in which we evaluate its qualitative and quantitative capabilities for assessing the oil inclusions and its implications for both remote sensing and bioremediation of oil-contaminated sea ice.

This study builds on the past X-ray work noted above. In particular, Salomon et al. (2017) performed a general analysis on the distribution of oil in the porous space of columnar sea ice. These authors noted that the absorption contrast between oil and ice was insufficient for automatic segmentation. Segmentation was therefore performed manually by tracing each visible oil inclusion within each 2D-slice. This method of analyzing oil inclusions was deemed to be exceedingly time consuming and unrealistic for the investigation of numerous samples. Other works such as (Courville et al., 2017; Maus et al., 2013) have incorporated the use of μ -CT for the purpose of investigating the microstructure of sea ice (e.g., skeletal layer at the water-ice interface) to better understand oil migration through brine channels (i.e., oil infiltration, porosity and permeability). These works were used to improve the modeling of 1) oil entrainment in sea ice (Maus et al., 2015), 2) fluid flow in porous media (Oggier et al., 2019), and 3) waterborne sensor performance (e.g., sonar) in different oil in ice scenarios (Courville et al., 2017). Overall, these works have focused on the bulk migration of oil through columnar sea ice and the remote sensing detection from under and within ice.

In our study, we developed a methodology for the improved detection of oil by μ -CT, facilitating a faster image processing through automatic segmentation. Our focus lies on the frazil/inter-frazil ice layer of sea ice (upper regions) with an emphasis on oil distribution and proximity to air and brine, as well as the geometry of all inclusions. The implications of these results are discussed in the context of 1) airborne remote detection (e.g., radar) of oil-contaminated sea ice, which is influenced by the shape, volume, distribution, and orientation of sea inclusions (Ulaby and Long, 2014); and 2) bioremediation of oil-in-ice which is dependent on the proximity of oil and brine (Vergeynst et al., 2018). In the Northern Arctic,

an oil spill is more likely to occur during fall freeze-up with a heightened shipping or industrial activity than mid-winter (Martin, 1979; Oggier et al., 2019; BBC News, 2020). Therefore, the presence of oil in the top part of the sea ice profile is a likely scenario. The findings reported in this chapter will be useful for 1) the development of remote sensing algorithms required to detect oil within the surficial sea ice and 2) the development of scientific knowledge required for the planning and coordination of proper mitigation response efforts (e.g., bioremediation) suitable for ice covered waters.

5.3 Materials and Methods

5.3.1 Source of X-ray Samples

Three annual artificial oil-in-ice mesocosm experiments were conducted at the University of Manitoba (UofM) Sea-ice Environmental Research Facility (SERF) during 2016-2018. From these experiments, crude oil-contaminated ice cores were sampled as described in the following works: (Desmond et al., 2019b, 2021; Saltymakova et al., 2019, 2020; Neusitzer et al., 2018b).

Each of the three oil-in-ice mesocosm experiments, from which our samples are derived, exhibited conditions that closely resemble natural sea ice thermodynamic states indicative of Arctic marine waters; that is, the temperature increased towards the water column and the bulk salinity demonstrated a normal C-shape profile. Furthermore, most of the oil that was injected below the ice was found to have migrated towards the ice surface due to the warm ice temperatures (i.e., $\geq -5^{\circ}\text{C}$) (Eicken, 2003; Petrich and Eicken, 2010) and lower density of the oil (860 kg/m^3) relative to that of seawater/brine ($> 1020\text{ kg/m}^3$).

Due to variation in atmospheric temperature and snow precipitation during the different experiments (2016, 2017, 2018), the extent of sea ice growth varied for each experiment. The maximum ice thickness over the course of the three experiments was ~60 cm. A general ice stratigraphy analysis was conducted using cores extracted from the ice. Cores were examined visually and photographed to qualitatively determine ice layering and type (i.e., granular or columnar) and were later sliced into horizontal thick sections and vertical thick/thin sections. Crossed optical polarizers were used to analyze the ice microstructure of a relatively clean sample (no visible oil) taken from the SERF 2018 experiment (Desmond et al., 2021). Example photographs depicting the alternations of granular and columnar ice can be seen in Figs. 5.1 and S5.1 (Appendix Section 7.1). The influence of oil on sea ice and the potential for the growth of additional granular layers has previously been reported by (Martin, 1979). Most of the X-ray samples investigated herein were taken from locations which were saturated with oil and visually resembled granular or inter-granular ice. A further assessment of the ice type (granular/inter-granular or columnar) corresponding to the X-ray samples is discussed in Section 5.4.2.1 based on μ -CT computed inclusion orientations.

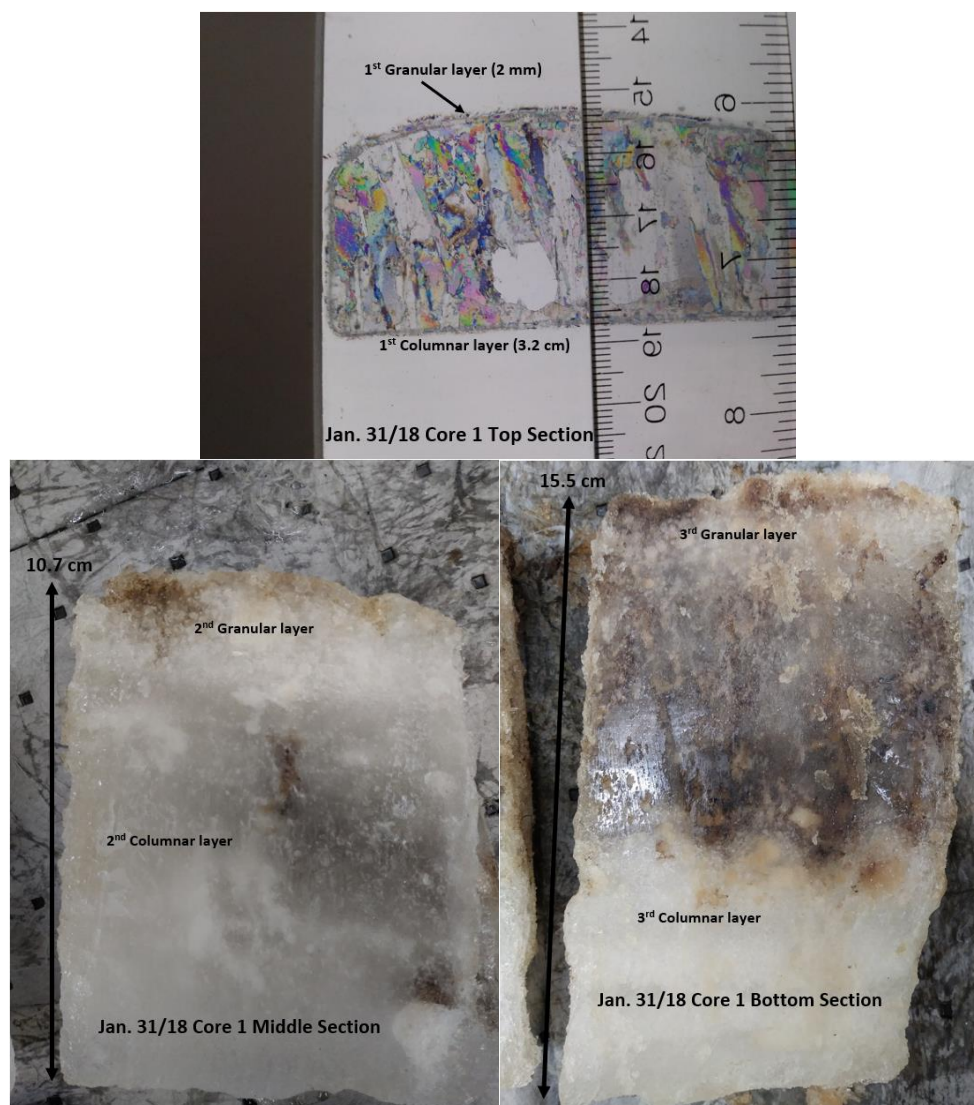


Fig. 5.1 Example photos of thick sections and a thin section of sea ice from an oil-in-ice mesocosm depicting alternating granular and columnar layers (Desmond et al., 2021).

5.3.2 Preparation of the X-ray Samples Before Scanning

X-ray samples were carefully cut with a boning saw into either cylindrical or rectangular prism sections, with 3 cm diameters/widths and 2-3 cm heights, from the top and middle sections of 10 separate oil-contaminated ice cores from the 2016-2018 experiments. These subsections were then stored in a freezer at -20°C until ready for $\mu\text{-CT}$ analysis. A list

of the investigated X-ray samples, their correspondent ice core depth, and their physical properties (see Sections 5.3.3 and 5.3.4.3) is provided in Table 5.1.

The μ -CT scanning of the samples took place at different cold room temperatures (-15°C , -10°C , -6°C , -5°C , and -4.8°C , see Table 5.1). Prior to X-ray analysis, each sample previously stored at -20°C was left inside a temperature controlled cold room for 24-hours at the intended scanning temperature (Table 5.1). In order to mimic the natural heat flux from the ocean to the atmosphere, allowing brine inclusions to expand along the vertical direction (z-axis), each X-ray sample (enclosed in a polypropylene tube) was placed on a metal plate with their sides encased in Styrofoam (Fig. 5.2). After 24 hours equilibration in the temperature-controlled room, the entire sample reached the targeted scanning temperature.

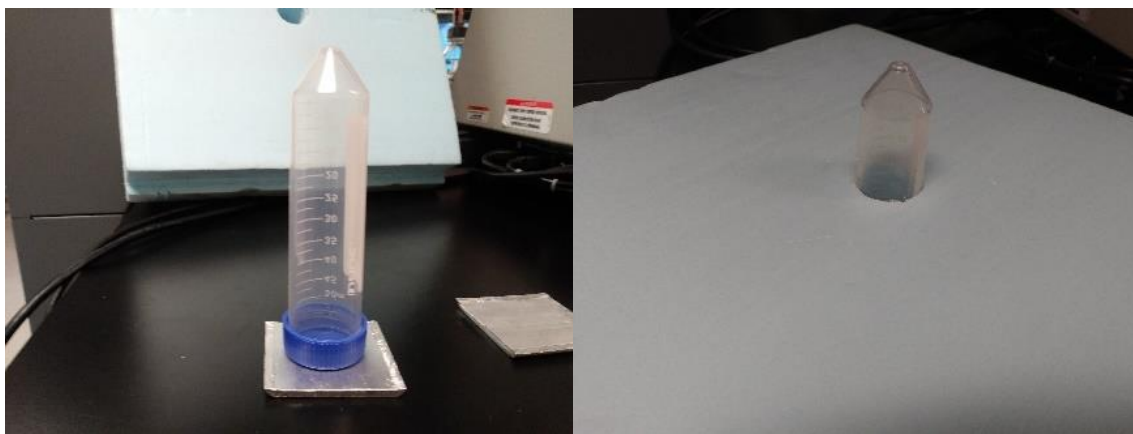


Fig. 5.2 Example of how X-ray samples were placed on a metal plate and encased in styrofoam prior to placement inside the μ -CT chamber for scanning.

Table 5.1 In Situ μ -CT Sea Ice Characteristics pertaining to a subset of the X-ray Samples

Ice Core ID	Inferred Ice Type	Ice Core Section Ice Depth (cm)	Chamber Temperature (°C)	Bulk Salinity (psu)	% Brine Volume*	Oil Volume (mL)**
Mar. 1/16 Core 8 Top	Frazil (transitional)	0 to 2.3	-14.8	7.4	2.8	<0.01
Mar. 1/16 Core 10 Middle	Frazil (transitional)	5 to 7	-14.8	5.7	2.2	0.30
Feb. 10/17 Core 9 Top	Frazil (transitional)	0 to 2.9	-14.8	12.4	4.8	0.07
Feb. 10/17 Core 9 Mid	Frazil (transitional)	5 to 7.8	-14.8	10.6	4.1	0.30
Mar. 14/17 Core 16	Pancake (transitional)	0 to 3	-14.8	18.0	6.9	0.03
Feb. 7/18 Top Site 3 Core 1	Frazil (transitional)	0 to 2.8	-14.8	5.96	2.3	0.15
Feb. 7/18 Middle Site 3 Core 1	Frazil (transitional)	7.6 to 10.6	-14.8	8.6	3.3	0.25
Feb. 7/18 Middle Site 3 Core 2	Frazil (transitional)	8.8 to 11.3	-14.8	12.6	4.9	<0.01
Feb. 26/18 Top Site 3 Core 3	Frazil (transitional)	0 to 2.4	-14.8	2.0	0.8	0.15
Feb. 26/18 Top Site 3 Core 3	Frazil (transitional)	0 to 2.4	-9.9	2.0	1.1	0.15
Mar. 16/18 Top Site 3 Core 2	Frazil (transitional)	0 to 2.8	-14.8	2.7	1.0	0.25
Mar. 16/18 Top Site 3 Core 2	Frazil (transitional)	0 to 2.8	-9.8	2.7	1.5	0.25
Mar. 16/18 Top Site 3 Core 2	Frazil (transitional)	0 to 2.8	-5.4	2.7	2.6	0.25
Mar. 16/18 Middle Site 3 Core 2	Frazil (transitional)	10.4 to 13.2	-4.7	1.8	2.0	0.30

*%Brine Volume derived from Frankenstein and Garner, 1967

**Oil Volume experimentally determined according to Section 5.3.3

5.3.3 Experimentally Determined Volume Fractions

After μ -CT analysis, each sub-sectioned X-ray sample was melted inside their respective polypropylene tube at room temperature. Each melted X-ray sample was then measured volumetrically using a graduated cylinder. The crude oil was then separated from the melted sea ice using a Vortex Mixer (VWR) and Hexanes (Fisher Scientific, Optima Grade) as solvent. The collected oil fractions were placed inside a new polypropylene tube and concentrated by fully reducing the solvent to dryness through natural room temperature evaporation. The volumes of the remaining oil samples were then measured by placing an empty polypropylene tube adjacent to the oil filled tube and filling it with known amounts of water, using 10-100 μ L pipettes, until both volumes were level with one another. The validity of this method was checked through a blind test using water, in a separate polypropylene tube, to measure known amounts of crude oil. The results of this blind test are shown in Table 5.2, in which all volumes were found to be accurately measured.

Table 5.2 Results of blind test assessing accuracy of method used to experimentally measure the oil volumes of the X-ray samples. Note ‘true volume’ pertains to known amounts of crude oil placed inside polypropylene tubes.

Trial #	True V (mL)	H₂O (mL)
V1	0.9	0.9
V2	0.5	0.5
V3	0.2	0.2
V4	0.09	0.08
V5	0.05	0.04
V6	0.02	0.02

5.3.4 Analysis by Micro-Computed Tomography (μ -CT) X-ray

5.3.4.1 *Scanning*

A Bruker SKYSCAN 1174 Compact Micro-CT system was placed inside a temperature controlled cold room (held at $-15/-10/-6/-5/-4.8$ °C according to Table 5.1) and used to analyze sea ice microstructure. Scanning at temperatures warmer than -4.5 °C resulted in degradation of the samples by surface melt. Thermocouples were placed inside the μ -CT sample chamber to record the in-situ ice temperature during scanning (Fig. 5.3) and typically read $+0.2$ °C relative to the ambient condition when the X-ray source was on. Samples were placed in polypropylene tubes (Fig. S5.2 – Appendix Section 7.1), mounted on a rotating stage in the μ -CT (Fig. 5.3), and rotated a full 180° , in 0.4° increments, averaging frames of 4, with the μ -CT running at 50 kV and 800 μ A. An aluminum filter (0.50 mm) was placed in front of the X-ray source during the scan. Individual scans took approximately 3 hours. The final image contained 1304×1024 pixels with a pixel size and slice thickness of 29 μ m. After the scan, the projected radiograph was reconstructed into two-dimensional grayscale slices stacked in the z-direction (corresponding to the vertical direction of the original ice core) using Bruker software (NRecon). During the reconstruction step, each voxel was assigned a grayscale value between 0 and 255 corresponding to a CT value. A CT value is expressed in Hounsfield Units (HU), representing the degree of X-Ray attenuation, whereby denser materials and higher atomic numbers result in greater X-ray attenuation (Duliu, 1999). Data reconstruction also included the removal of ring-artifacts, beam-hardening, post-alignment and Gaussian smoothing to reduce the noise (i.e., Ketcham and Carlson, 2001).

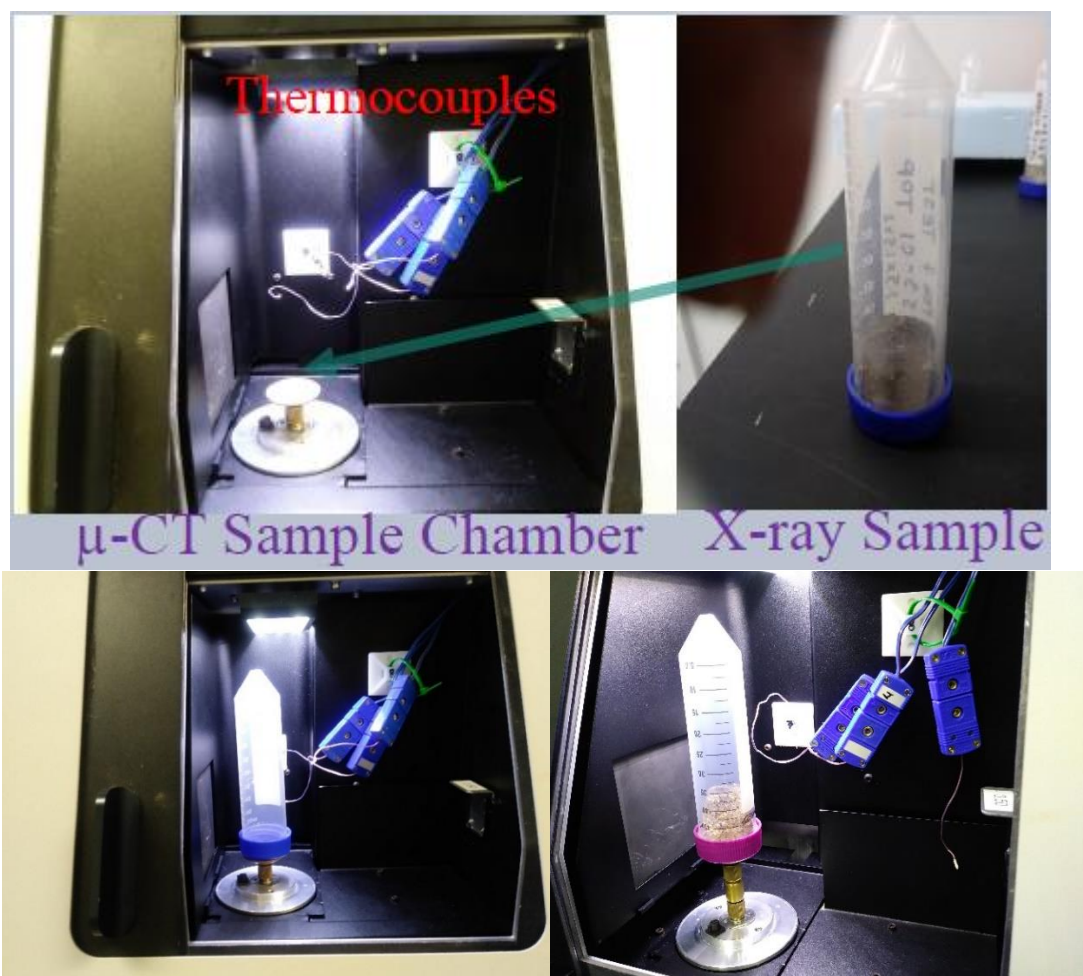


Fig. 5.3 Sub-sectioned X-ray sample placed inside a polypropylene Falcon tube and subsequently mounted on a rotating sample stage within the μ -CT chamber with installed thermocouples.

5.3.4.2 Image Processing

For any quantitative or qualitative result derived from a binary image, the most crucial step in the imaging technique is the proper segmentation of the grayscale image into individual windows or phases (e.g., oil, air, brine). In this study, the segmentation process consists of finding the CT-Value, a digital number between 0 and 255, for the ice matrix, the brine, air, and oil inclusions. Optimal thresholds can be determined by eye or automatically

based on information contained in the image histogram (Iassonov et al., 2009, Sezgin and Sankur, 2004).

Since air, brine and ice are mediums with different densities, they are easily distinguished by CT X-ray. To distinguish the air and brine from the ice matrix we used the histogram-based method called CL-Otsu (Crabeck et al., 2016, Iassonov et al., 2009) which separated the background (i.e. ice) and foreground voxels (i.e. air/brine) by approximating the histogram with a combination of two or more statistical distributions. The results of each segmentation method were visually evaluated by comparing the raw and segmented images. Finally, the volume fractions of the ice, brine, and air were quantified based on the selected thresholds.

5.3.4.2.1 Enhanced Imaging of Oil

Ice and oil have similar CT-values due to their similar density, rendering oil inclusions hardly detectable by the human visual system. Both manual and automated histogram-based threshold selections fail to differentiate these two phases from one another. To identify the CT- oil signature in sea ice, we analyzed two test samples (Fig. 5.4A and B) with a known volume of crude oil and corn oil in pure ice (i.e., ice formed from distilled water) with the CT. For the first test sample (Fig. 5.4A), a vertically downward hole (3.75 mm diameter) was drilled in a cylindrical section of pure ice (2.3 cm height X 2.1 cm diameter) and 120 μL of Tundra crude oil was injected into the hole with a micropipette. Similarly, for the second test sample (Fig. 5.4B), two vertically downward holes were drilled in a cylindrical section of pure ice in which 100 μL of Mazola corn oil was injected into the right cavity and 50 μL of Tundra crude oil was injected into the left cavity. The spiked

samples were then analyzed inside the μ -CT chamber with the use of a polypropylene tube (Falcon, Corning).

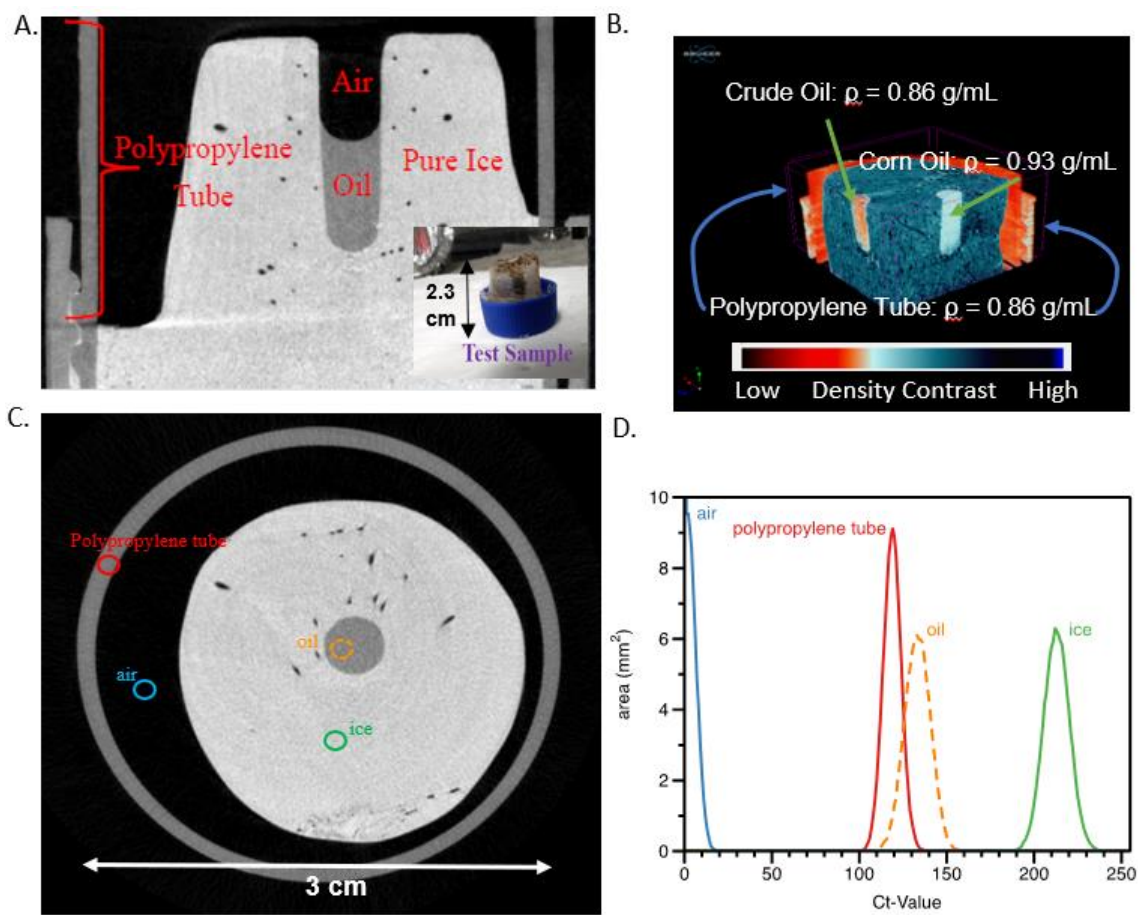


Fig. 5.4 Panel A shows a raw transversal in the XZ direction of a test sample contained in a polypropylene tube in which crude oil was injected. Panel B shows a second test sample contained in a polypropylene tube in which both crude and corn oil was injected. The density contrast of the different medium (ice, crude oil, corn oil and polypropylene tube) are shown in the color bar. Panel C shows a transversal slice of the test sample in panel A. Panel D shows a CT histogram of the medium highlighted in panel C. The histogram combined the data over a stack of 147 slices.

As shown in Fig. 5.4A and B, we can visually distinguish the oil from the other components (i.e., air and ice). Furthermore, the CT-value of the crude oil was observed to be very similar to the polypropylene tube used to hold the sample. The density of polypropylene

is known to be 860 kg/m^3 and the crude oil used in our experiments had an initial density of $855(8) \text{ kg/m}^3$ (Desmond et al., 2019c). Fig. 5.4D shows the CT-values between the crude oil and the polypropylene tube over the index range of 120-150 and 106-136, respectively. While their respective CT-values are similar to one another, the crude oil CT-values are 10% to 15% higher.

A sea ice sample (Feb. 7 Mid S3C1) (Table 5.1), taken during the 2018 oil-in-ice mesocosm experiment, was sub-sectioned for analysis by μ -CT and placed in a polypropylene tube (Fig. 5.5A). Observation of the constructed histogram (Fig. 5.5B) shows that it is difficult to detect dispersed oil due to the overwhelming ice volume fraction. The polypropylene tube was used as a “benchmark” for the oil index location, keeping in mind that the Tundra crude oil has a slightly higher CT-value (Fig. 5.4D); that is, the CT-signature of the polypropylene tube was used as a segmentation threshold allowing for an enhanced detection of oil in sea ice. This allowed for an easier assignment of the proper CT-value signature of the ice matrix and oil inclusions. It is important to note that the ranges of CT-value for the different media are not constant from sample to sample (e.g., Figs. 5.4D, 5.5B, Table 5.3). Consequently, great care must be taken in choosing appropriate thresholds for each respective sample. The human visual system was also used to verify the selection of accurate thresholds (CT-values) (e.g., Fig. 5.5C) by inspecting a variety of oil inclusions in different sample slices.

From these results, we can infer that it is possible to detect a dispersed amount of oil. Encasing the ice with a material possessing a similar density to that of the oil of interest

allows for a magnified imaging of the oil inclusions within the sea ice microstructure and the selection of a proper segmentation threshold.

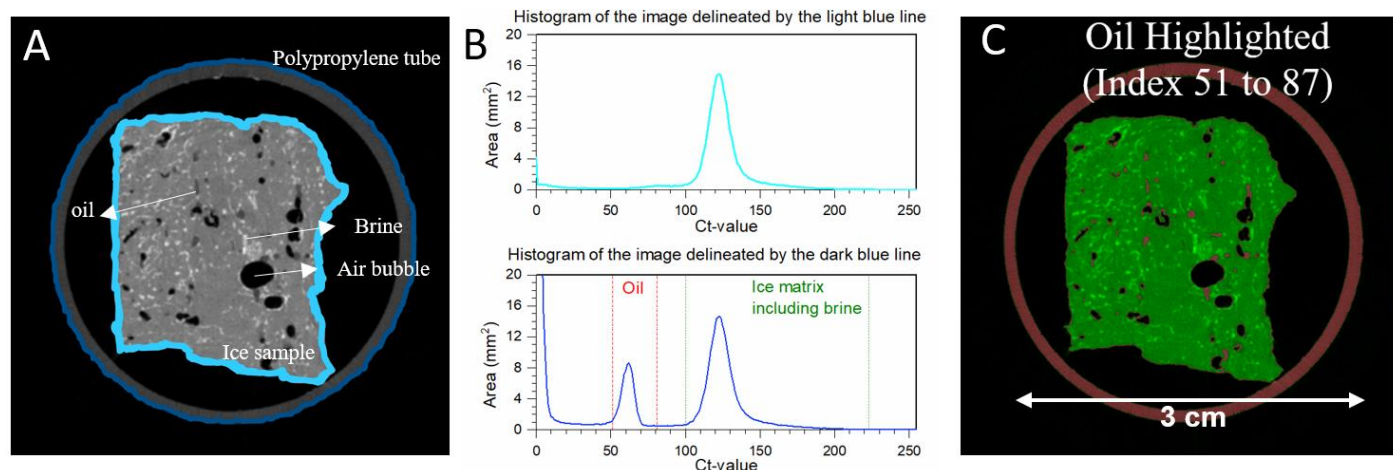


Fig. 5.5 Panel (A) shows a raw transversal slice of an oil-contaminated ice sample (Feb. 7/18 Middle S3C1) contained in a polypropylene tube. In this image, brine appears in white and very light grey, air bubbles appear in black, and oil inclusions appear in dark grey. Panel (B) shows histograms delineating the light blue and dark blue lines shown in the panel A image. Panel (C) shows the ice matrix in green, and the oil and polypropylene tube pixels in red, selected using the Ct-value of oil from the panel B histogram.

Table 5.3 Averaged (STDEV) 3D Individual Object Analysis of Sphericity and Structure Model Index (SMI) for a Subset of 2015-2018 X-ray Samples

Sample (Ambient T)	Media (CT thresholds)	Sphericity	SMI
Mar. 1/16 C10 Mid (-15°C)	Oil (80-120)	0.75(15)	2.74(62)
	Air (0-57)	0.75(12)	2.86(35)
	Brine (178-255)	0.78(10)	2.93(25)
Feb. 10/17 C9 5- 7.5 cm (-15°C)	Oil (60-94)	0.71(17)	2.57(63)
	Air (0-27)	0.74(13)	2.78(37)
	Brine (182-255)	0.74(11)	2.81(25)
Feb. 7/18 Top S3C1 (-15°C)	Oil (121-148)	0.69(16)	2.50(40)
	Air (0-74)	0.72(14)	2.68(40)
	Brine (242-255)	0.77(11)	3.00(25)
Feb. 7/18 Mid S3C1 (-15°C)	Oil (62-87)	0.71(17)	2.52(56)
	Air (0-41)	0.72(15)	2.63(41)
	Brine (167-255)	0.79(11)	3.09(28)
Feb. 7/18 Mid S3C2 (-15°C)	Air (0-35)	0.68(46)	2.87(47)
	Brine (170-255)	0.77(11)	2.97(28)
Feb. 26/18 Top S3C3 (-15°C)	Oil (81-107)	0.70(17)	2.49(56)
	Air (0-48)	0.72(15)	2.60(40)
	Brine (167-255)	0.79(09)	2.95(25)
Feb. 26/18 Top S3C3 (-10°C)	Oil (86-119)	0.72(18)	2.55(70)
	Air (0-48)	0.71(15)	2.58(41)
	Brine (175-255)	0.79(09)	2.96(24)
Feb. 26/18 Top2 S3C3 (-5°C)	Air (0-53)	0.72(14)	2.63(42)
	Brine (189-255)	0.78(10)	2.87(25)
Mar. 16/18 Top S3C2 (-15°C)	Oil (67-107)	0.74(17)	2.66(69)
	Air (0-43)	0.73(15)	2.72(46)
	Brine (166-255)	0.78(10)	2.93(24)
Mar. 16/18 Top S3C2 (-10°C)	Oil (71-107)	0.68(22)	2.37(96)
	Air (0-47)	0.75(14)	2.76(42)
	Brine (171-255)	0.78(10)	2.96(24)
Mar. 16/18 Top S3C2 (-6°C)	Oil (76-110)	0.77(13)	2.80(55)
	Air (0-49)	0.73(14)	2.67(41)
	Brine (155-255)	0.73(14)	2.95(25)
Mar. 16/18 Mid S3C2 (-4.8°C)	Oil (87-114)	0.70(17)	2.49(59)
	Air (0-43)	0.74(15)	2.75(50)
	Brine (189-255)	0.77(11)	2.93(25)
Total Average	Oil	0.72(17)	2.57(63)
	Air	0.73(17)	2.71(42)
	Brine	0.77(11)	2.95(25)

5.3.4.3 *Threshold Optimization*

A source of error that exists while processing a CT X-ray image occurs during the selection of thresholds due to a lack of knowledge of the optimal segmentation result. To verify the validity of the thresholds for brine, CT-derived brine volumes were compared to brine volumes computed using the state equations of Frankenstein and Garner (1967). Frankenstein and Garner (1967) state equations use in-situ temperature (here CT-chamber temperature) and bulk ice salinity to compute the brine and ice volume fractions. Bulk ice salinities of each X-ray sample were measured with a conductivity meter (Orion Star A212 – Thermo Scientific) on the collected saltwater fractions, previously obtained by separation from the oil. The accuracy of CT-derived fractions (air, brine) and their agreement with values derived from state equations have previously been investigated (Crabeck et al., 2016; Salomon et al., 2017). In case of a mismatch between CT-derived and state equation derived brine and ice volume fractions, the thresholds were adjusted to reach agreement (Table 5.4). Similarly, the CT-derived oil volume was compared to the experimentally measured oil volume. The threshold was finely adjusted to reach agreement if the CT-derived oil volume mismatched the experimental oil volume (Table 5.4).

A second source of error is linked to the resolution of the CT-image which is always insufficient to resolve every object and its boundary. When an inclusion is smaller than the spatial resolution of the image, it appears as a mixed pixel. In this study, the major source of mixed pixels is at the boundary of ice and air (e.g., in air pockets) resulting in an averaged CT-value similar to that of the Tundra crude oil, which can lead to a false positive of oil volume. This source of error is minimized while X-ray samples contain appreciable volumes

of oil. In this study, we focused our analyses on samples which contained $\geq 150 \mu\text{L}$ oil or 2.14% oil/ice vol (Table 5.1), which reduced the impact of false positives on the CT-derived volume. The human visual system was also used to verify the selection of accurate thresholds (CT-values) by inspecting and comparing several individual inclusions and their boundaries on raw and segmented images.

Table 5.4 Comparison of CT-derived and experimentally determined volumes for the media of brine, pure ice, and crude oil for sea ice sample “Feb. 7/18 Middle S3C1” (see Table 5.1 and Fig. 5.5)

Media	CT-derived Volume (mL)	Experimental Volume (mL)
Brine (Index 167-223)	0.264	0.265
Pure Ice (Index 100-167)	7.539	7.400
Crude Oil (Index 62-87)	0.198	0.200

5.3.5 Proximity of Oil and Brine Inclusions Analysis

To quantify the extent of boundary overlap or interface connection between the oil and brine inclusions, the segmented brine and oil components for each respective horizontal slice (XY-plane) of three representative X-ray samples were exported as individual PNG images. Images were processed in MATLAB 2020a to determine the pairwise pixel overlap and fraction of interface connection between horizontal slice pairs of oil and brine. A percentage of boundary overlap between the oil and brine was calculated based on the overlap of pixels from the oil and brine inclusions from each image set. The overlap percentages obtained for each horizontal slice of the representative X-ray samples were then displayed as box plots for oil-brine overlap. Interface connection was determined using a function to check pixels bordering a pixel of interest in both lateral and diagonal directions, calculated as a percentage over the calculated perimeter of the feature being checked against. For example,

the interface percent between brine and oil was calculated by determining the total oil pixels bordering all brine pixels, and dividing the resulting value by the total perimeter or border of all brine features. These results were used to help assess the potential for bioremediation of oil in sea ice.

5.3.6 Individual Object Analysis of Sea Ice Inclusions

The geometry, orientation, and size of the sea ice inclusions (i.e., oil, air, and brine) were determined from quantitative analysis of the X-ray microtomography scans. Averaged (standard deviation) 3D Individual Object Analyses (IOA) of sphericity (Ψ), structure model index (SMI), orientation (theta), and major diameter were conducted for a subset of the 2015-2018 X-ray samples. *Sphericity* (Ψ) is a measure of how spherical a 3D object is, with an index ranging from 0 to 1 (perfect sphere). This parameter is defined by (Wadell, 1935). SMI indicates the relative prevalence of rods and plates in a 3D structure and involves a measurement of surface convex curvature (Hildebrand and Rüegsegger, 1997). An ideal plate, cylinder and sphere have SMI values of 0, 3 and 4, respectively. A structure between the ideal state of a plate and cylinder will have a SMI value between 0 and 3. *Orientation* (theta) is defined as the angle of an individual 3D object oriented between 0° (horizontal XY-plane) and 90° (vertical Z-plane). For instance, an ellipsoid with an angle theta equal to 90 degrees would have its major axis along the vertical z-direction, and an angle theta equal to 0 degrees would correspond to an ellipsoid with its major axis within the XY-Plane. *Major diameter* is the distance between the two most distant pixels in a 3D object. The calculated parameters of sphericity (Ψ), SMI, orientation (theta), and major diameter are tabulated for a subset of the investigated X-ray samples (Table 5.3). Inclusions with a size similar to the spatial

resolution of the image were excluded from the statistical analyses provided in Table 5.3. When the inclusion has the size of a pixel, it means that the inclusion is smaller than the pixel and that the spatial resolution of the CT-image is insufficient to characterize its geometry.

Specifically, the calculated orientations were used to assess the randomness or degree of vertical alignment of oriented inclusions as a means of assessing sea ice type (granular, columnar). Major diameters of each inclusion type were calculated to determine the size of their features. Sphericity (Ψ) and SMI were used to infer the geometry of inclusions in conjunction with Eqs. (4.1)–(4.2) (Li et al., 2012).

$$4.1 \quad \Psi_{cylinder} = \frac{(1.5w)^{\frac{2}{3}}}{w+0.5}$$

$$4.2 \quad \Psi_{spheroid} = \frac{\pi(w)^{\frac{2}{3}}}{2 \int_0^{\pi/2} \int_0^{\pi/2} w \cos \varphi \sqrt{\sin^2 \varphi + \cos^2 \theta \cos^2 \varphi + \left(\frac{1}{w^2}\right) \sin^2 \theta \cos^2 \varphi} d\varphi d\theta}$$

where Ψ – sphericity (as defined above); w – aspect ratio of the height (z-direction) divided by the major axial length (XY-plane).

5.3.7 Remote Sensing Modeling: Application of Inclusion Geometry Analysis

To demonstrate the use of the inferred inclusion geometry to a remote sensing application, we incorporated our results in a modeling study on the Normalized Radar Cross-Section (NRCS) of sea ice based on physical measurements (Desmond et al., 2019b) and compared to experimentally determined NRCS (Neusitzer et al., 2018a; Firoozy et al., 2018). Wave scattering and consequently the electromagnetic footprint of the profiles measured by satellite or on-site radar systems are related to the incidence angle, surface roughness, volume fractions of all the components of sea ice (ice, brine, air, oil), and permittivity (dielectric)

profile including real and imaginary parts (Ulaby and Long, 2014). Generally speaking, the brine volume fraction has the greatest impact on the NRCS of the sea ice, assuming the incidence angle remains constant. The equivalent permittivity of a complex material such as sea ice is related to the complex permittivity (dielectrics) of the individual substances, their volume fractions, their spatial distributions, and their orientations relative to the direction of the incident electric-field vector. The substance with the highest volume fraction is regarded as the host material, or continuous medium, and the other substances are regarded as inclusions (Ulaby and Long, 2014). Popular dielectric mixture formulas for heterogeneous materials include the Tinga-Voss-Blossey (TVB) (Ulaby and Long, 2014; Tinga et al., 1973) and Polder–van Santen/de Loor (PVS) (Ulaby and Long, 2014; Polder and van Santen, 1946; De Loor, 1968) models. These models consider the inclusions to be ellipsoidal particles of identical shape and size, randomly oriented with respect to the direction of the electric field of the incident wave. Variations of ellipsoidal particles include 1) prolate spheroid with $x=y$ (symmetric about the z -axis) and $z>x$; 2) sphere with $x=y=z$; 3) oblate spheroid with $x=y$ and $z<x$; 4) circular disk inclusions for thin circular disks with $x=y$ and $z\ll x$; and 5) needle inclusions for long, narrow needles with $x=y$ and $z\gg x$. Herein, we model and compare the sea ice inclusions as circular disks (based on the results of our inclusion geometry analysis).

5.3.7.1 *Modeling Approach*

The Normalized Radar Cross-Section (NRCS) of the sea ice was simulated from the complex permittivity profiles of the physical samples collected throughout the experiment (Desmond et al., 2019b) (Table 5.5). The permittivity profiles of the ice were modeled at 5.5 GHz using the quasi two-phase Tinga-Voss-Blossey (TVB) and Polder–van Santen/de Loor

(PVS) mixture models following (Neusitzer et al., 2018a; Firoozy et al., 2018). The PVS and TVB model assumes that the mixture is comprised of randomly oriented inclusions (e.g., oil, air, brine) surrounded by the host material (i.e., pure ice). In this formulation, the inclusions are considered to be separate within the host material. The Integral Equation Model (I^2EM) (Fung et al., 2002; Ulaby and Long, 2014) was utilized to simulate the monostatic NRCS of the sea ice from the modeled dielectric profiles. As the I^2EM assumes a half-space with a rough interface, the permittivity profiles were reduced to an effective permittivity as a half-space by taking the first 2.5 cm of the modeled dielectric depth profiles based on their calculated NRCS penetration depth (Ulaby and Long, 2014) (Tables 5.6 and 5.7). Simulations were run at the same frequencies and incidence angles as the experimental conditions seen in (Neusitzer et al., 2018; Firoozy et al., 2017). Relevant root-mean-square (RMS) heights and correlation lengths from Table 5.8 were used for the roughness parameters of the NRCS simulation. Surface roughness is an integral parameter concerning microwave scattering from sea ice.

Table 5.5 Comparisons between modeled and experimental NRCS (dB) for various sampling times (Desmond et al., 2019a; Neusitzer et al., 2018).

Table 5.6 Calculated NRCS penetration depths (cm) of the circular disk dielectric mixture model of sea ice for various sampling times (Desmond et al., 2019a; Neusitzer et al., 2018a)

Sampling Dates	TVB/Circdisc	PVS/Circdisc
Jan. 18/16, 12:00 PM	0.5857	0.5653
Jan. 19/16, 12:00 PM	0.8442	0.8439
Jan. 20/16, 9:00 AM	0.7077	0.6881
Feb. 12/16, 1:15 PM	0.6806	0.6034

Table 5.7 Calculated effective permittivities “seen” by the I²EM NRCS model of the circular disk dielectric mixture model of sea ice for various sampling times (Desmond et al., 2019a; Neusitzer et al., 2018a)

Sampling Dates	TVB/Circdisc	PVS/Circdisc
Jan. 18/16, 12:00 PM	7.1584 - 4.1153i	7.3169 - 4.3180i
Jan. 19/16, 12:00 PM	5.4315 - 2.4542i	5.4230 - 2.4534i
Jan. 20/16, 9:00 AM	6.2074 - 3.1475i	6.2991 - 3.2650i
Feb. 12/16, 1:15 PM	7.3223 - 3.5459i	7.7769 - 4.1435i

Table 5.8 RMS heights and correlation lengths (L) of relatively smooth and rough ice obtained using LiDAR

	Observed Ice Characteristics	RMS Height (cm)	STDEV (cm)	L (cm)
Firoozy et al., 2018	Smooth ice, no accumulation	0.261	0.001	0.307
Firoozy et al., 2017	Frost flowers, small snow grains	0.39	0.088	0.965

*STDEV is the standard deviation of RMS height.

5.4 Results and Discussion

5.4.1 Qualitative Analysis

5.4.1.1 *Oil Behavior and Movement Tendencies in Sea Ice: Oil Distribution and Location*

Horizontal/vertical cross-sections of the samples were obtained through X-ray imaging and are shown in Figs. 5.5A, 5.6, and S5.3–S5.4 (Appendix Section 7.1). These cross-sections illustrate oil distribution within the ice, indicating that the oil included within the ice was quite dispersed and tended to surround the perimeter of air inclusions. Many exclusive pockets of oil were also observed. Further observation of these figures shows that the brine was separate from the oil within the ice, with minimal interface contact. This result is likely due to the natural separation of oil and water owing to differences in density and hydrophobic character; that is, the oil percolated through brine channels progressively pushing out and replacing the brine, and subsequently the oil became encapsulated within the ice (Petrich et al., 2013; Maus et al., 2015; Desmond et al., 2019a; Saltymakova et al., 2020). From Figs. 5.6 and S5.4 (Appendix Section 7.1), most oil accumulation is observed towards the top of each X-ray sample, respectively. In these areas of high oil concentration, less brine is present in contrast to the bottom of each sample which is richer in brine. This separation of brine is further demonstrated by Fig. 5.7, in which the average interface contact percentage between the brine and oil for the investigated X-ray samples was calculated to be less than 0.13%. It is worth noting that the samples investigated in Fig. 5.7 were analyzed by μ -CT at $-15\text{ }^{\circ}\text{C}$. It is expected that oil-brine contact would increase at warm temperatures approaching $0\text{ }^{\circ}\text{C}$. However, due to the resolution limitations of the μ -CT instrument at warm

temperatures and the possibility of sample melt during scanning, we were unable to extensively investigate samples at warmer temperatures.

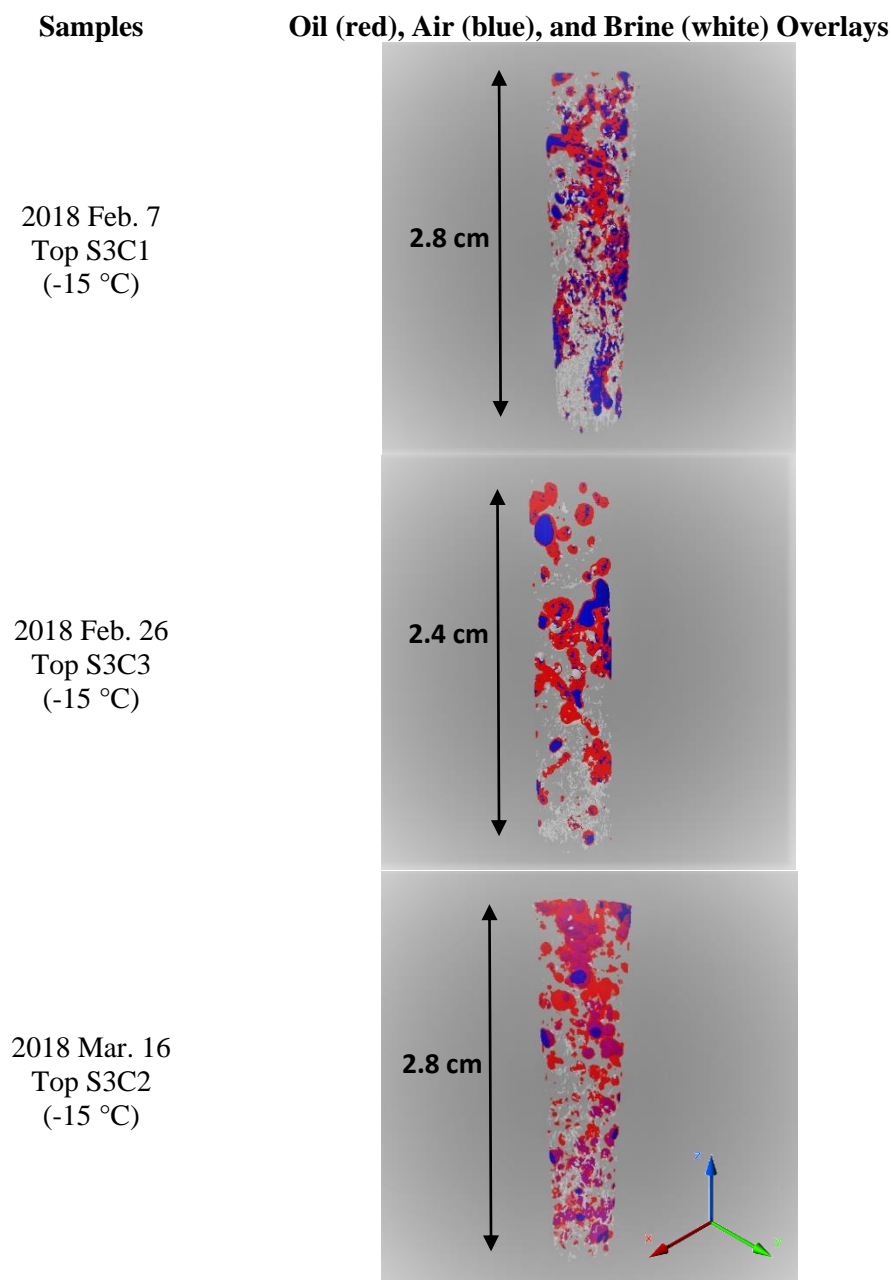


Fig. 5.6 The 3D decomposition of top sections of sea ice cores from SERF 2018 in which oil, air, and brine are represented in red, blue, and white respectively.

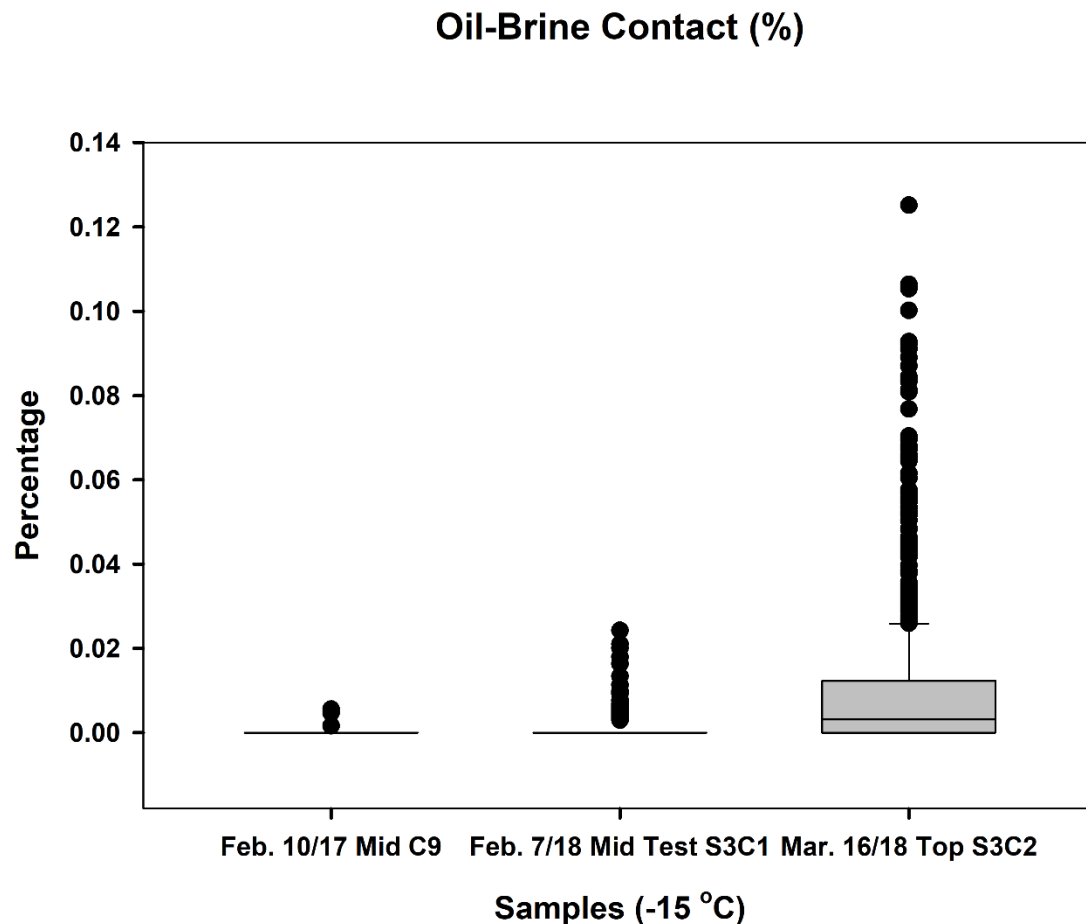


Fig. 5.7 Percentage of oil and brine boundary overlap (interface connection) for a subset of X-ray samples presented as box plots.

5.4.1.2 Mitigation Potential

Based on the aforementioned 2015-2018 oil-in-ice mesocosm experiments, the bulk of the oil was found to be encapsulated in the upper layers of the sea ice (Desmond et al., 2019a, 2019b, 2019c, 2021; Saltymakova et al., 2020), separate from the brine (Figs. 5.5A, 5.6–5.7, S5.3–S5.4 – Appendix Section 7.1). Brine and seawater are the media in which oil-degrading bacteria can thrive, containing the essential nutrients required to catalyze the biodegradation reaction (Vergeynst et al., 2018; Boetius et al., 2015; Prince and Walters, 2016). Significant biodegradation can only result when the bulk of the oil is in direct contact

with brine or sea water, such as at the base of the sea ice or in the presence of a melt pond (Vergeynst et al., 2018). The fact that oil remains separate from brine and attempts to concentrate towards the surface may act to decrease the likelihood of microbial bacteria interacting with the surfaced oil, as there is a larger bacterial population towards the sea ice base and within brine compared to vacant ice interstices (Boetius et al., 2015; Boccadoro et al., 2018). However, under warm ice temperatures (i.e., $\geq -5^{\circ}\text{C}$), there is greater potential for active brine to be in physical contact with or adjacent to oil surrounding ice interstices owing to the large increase and expansion of brine (Eicken, 2003; Petrich and Eicken, 2010); this may allow for a partial degradation of the bulk oil encapsulated within surficial ice.

Dissolution of lighter oil concentrations in brine (Saltymakova et al., 2020; Desmond et al., 2019b; Payne et al., 1991b), containing oil-degrading bacteria (Brakstad et al., 2008; Delille et al., 1997), may show greater potential for bioremediation of crude oil in the Arctic. The lighter fractions of crude oil are known to be toxic to marine life (Anderson et al., 1974), and the success of their bioremediation will be crucial in the case of an oil spill. We expect that bioremediation will effectively grow with a decrease in the concentration of crude oil in the ice as the dissolution efficiency increases (Saltymakova et al., 2020; Desmond et al., 2019b). We also expect the bulk oil encapsulated in the ice to be less weathered in comparison to open water (Saltymakova et al., 2020; Desmond et al., 2021), and will be prone to biodegradation during the spring-summer season, when the oil can come into direct contact with the ocean (Martin, 1979).

5.4.2 Quantitative Analysis

5.4.2.1 *Orientation, Size, and Geometry of Inclusions*

Based on the 3D IOA, all inclusions were found to be somewhat randomly oriented within the samples with orientation angles θ ranging from 0-90° (Fig. 5.8C). Air bubbles and oil inclusions show two modes (0 and 90°), while brine shows a very slight 90° mode and is more pronouncedly defined by random orientation (typical of granular ice) (Eicken, 2003; Galley et al., 2015).

Based on the calculated major diameters of all inclusion types, feature sizes for all three of the artificial oil-in-ice mesocosm experiments (Section 5.3.1) were less than 1 mm (Fig. 5.8A and B). The majority of brine inclusions analysed have a major diameter ranging from 0.1 to 0.3 mm. Similarly, Lieblappen et al. (2018) reported brine structure thicknesses of less than 0.2 mm. Air inclusions have a larger range of diameter with 75% of the air bubbles having diameters smaller than 0.4 mm. Fig. 5.8B shows the distribution of CT-derived major diameters of oil inclusions for various samples. From this figure we see that 1) the size of the oil inclusions was similar during the different experiments (2016, 2017, 2018), 2) sea ice temperature did not impact the size of the oil inclusions, 3) the inclusion size of oil does not vary with depth (top and middle sections are the same), and 4) more than 25% of the oil inclusions were smaller than 0.1 mm, and only 25% were larger than 0.2 mm.

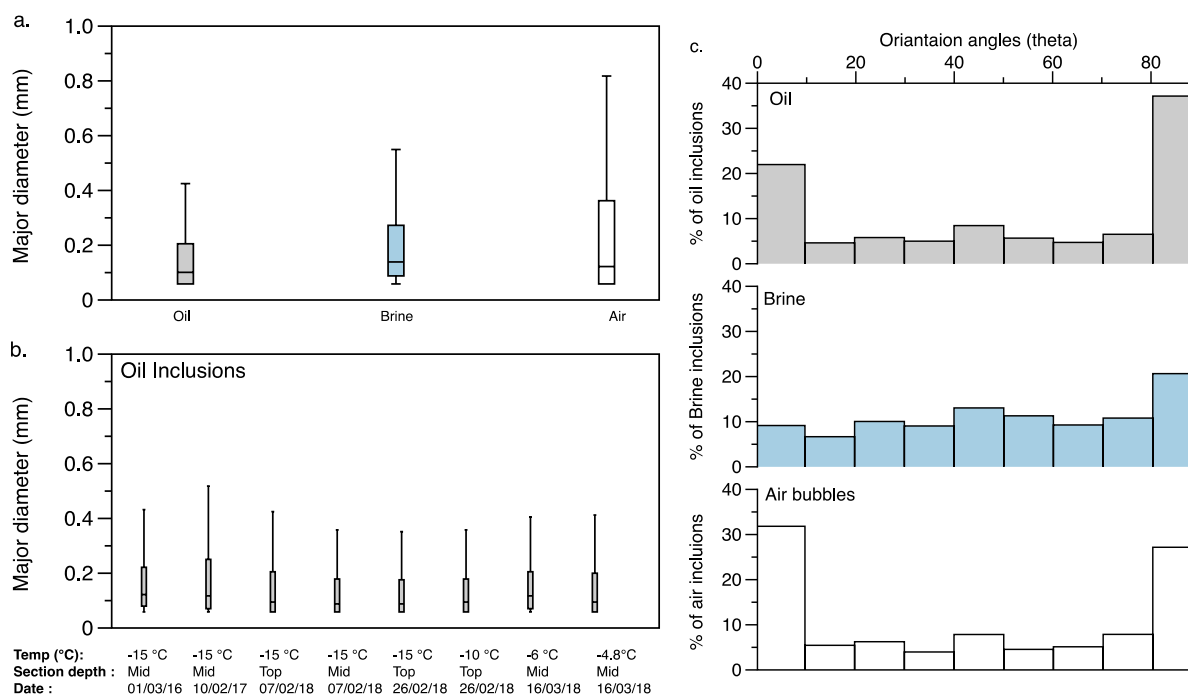


Fig. 5.8 The panel (a) shows IQR box plot for the distribution of CT-derived major diameter of all oil, brine and air inclusions analyzed. The panel (b) shows IQR box plot for the distribution of CT-derived major diameter of oil inclusions for various samples from the different experiment (2016, 2017, 2018). The box is defined by the first and third quartiles of the distribution, the line in the box is the median. The panel (c) shows the histogram of the orientation angles (theta) for all the oil, brine and air inclusions analyzed.

The CT-derived sphericities of the oil, air, and brine inclusions were 0.72(17), 0.73(16), and 0.77(10) on average(stdev), respectively (Table 5.3). Their typical SMI values were on average(stdev) 2.57(63), 2.72(42), and 2.94(25), respectively (Table 5.3). Our SMI results for brine are similar to those reported in Lieblappen et al. (2018), who also observed SMI values slightly below 3 for brine pockets. Based on the calculated SMI values, we know that the average inclusion best resembles ideal cylinders, rather than ideal plates or spheres, and that the inclusions are less than ideal (i.e., $\text{SMI} < 3$). Based on the calculated sphericity values ($\Psi=0.72, 0.73, 0.77$) we can infer that the inclusions resemble a cylinder of height (h)

/ diameter (d) = (0.3, 0.3, 0.4) (w) (Eq. (1) (herein); Fig. 1, Li et al., 2012). By definition, a cylinder with $h/d < 1$ (ideal) is considered a disk.

If we instead consider the average geometry of inclusions to be an oblong ellipsoid (or an oblate spheroid for simplicity), as they appear visually in Figs. 5.5A, 5.6, and S5.3–S5.4 (Appendix Section 7.1), and in other literature such as (Galley et al., 2015), results in $w=h/d=0.3$ using $\Psi=0.75$ (Eq. (2) (herein); Fig. 19, Li et al., 2012).

In either case, whether we consider the average inclusions as a cylinder or more realistically as an oblate ellipsoid, based on the computed sphericity and SMI values, we can conclude that the average inclusion most closely resembles a disk or oblate spheroid of marginal thickness with $h/d = 0.3-0.4$.

As a means of demonstration, we modeled the dielectrics of the 2016 SERF sea ice (Desmond et al., 2019b) with circular disk inclusions, and subsequently simulated the resultant Normalized Radar Cross-Section (NRCS) from the sea ice dielectrics. The modeled NRCS was then compared with experimental NRCS (see Sections 5.3.7 and 5.4.2.2 for more details).

5.4.2.2 *Remote Sensing Potential*

Table 5.5 compares experimental and simulated NRCS, whereby the simulated results correspond to sea ice inclusions modeled as randomly oriented circular disks (Section 5.4.2.1). All simulated results show a lower NRCS compared to experimental. Ice conditions with no accumulation show the best agreement with less than 1 dB difference. There is comparatively lesser agreement (~2 dB) between experimental and simulated NRCS for ice cover with accumulation; in particular, the presence of fully developed frost flowers. Reasons

for this include 1) the fact that frost flowers have not been studied extensively and are not fully understood (Isleifson et al., 2014), and 2) that brine expulsion during frost flower formation may not have been properly accounted for in the dielectric modeling, as surface ice scrapings were not taken for surface salinity measurements. Instead, the bulk salinity from the first 2.5 cm of each ice core was measured, which may have resulted in a slight systematic decrease in simulated NRCS compared to experimental.

The calculated penetration depth for the circular disk inclusions were found to be surficial and within the 1st cm of the upper sea ice layer (Table 5.6), which is fitting as the NRCS (I²EM) model used assumes surface scattering. Furthermore, in a naturally grown sea ice environment such as in the Northern Arctic, significantly thicker layers of granular ice are observed on the surface of sea ice (>5 cm) compared to artificially grown sea ice in microcosm/mesocosm tanks (Galley et al., 2015; Ehn et al., 2007; Isleifson et al., 2010). Consequently, modeling sea ice inclusions as randomly oriented ellipsoidal particles is quite applicable for airborne sensors which probe the sea ice surface (composed of randomly oriented crystals). Overall, these results suggest that the inclusions of surficial sea ice (granular/inter-granular) can be modeled by the profile of disks.

To confirm our findings, future work should include 1) the measurement of surficial sea ice dielectrics with the use of a dielectric probe for direct comparison with modeled dielectrics; and 2) a more thorough comparison between modeled and experimental NRCS at various incidence angles, incorporating LiDAR measurements corresponding to each physical sampling date. We also note that future studies should involve the modeling of oblate spheroid inclusions. It is important to establish which dielectric model(s) best describe

sea ice as it has implications for remotely inferring both the oil type (light, medium, heavy) and magnitude of spilled oil through the use of an inversion algorithm (e.g., Firoozy et al., 2017; Firoozy et al., 2018), allowing for swifter planning of an appropriate mitigation response.

Lastly, based on Section 5.4.1.1, we know that oil has the tendency to displace and remain separate from brine within surficial sea ice as well as in its depth profile (Figs. 5.5A, 5.6–5.7, S5.3–S5.4) (Desmond et al., 2019a; Saltymakova et al., 2020a). The lowering of sea ice salinity caused by the oil's presence can result in a reduction of the NRCS and may be eminently detectable in the case of a real-world oil spill (Firoozy et al., 2017; Firoozy et al., 2018).

5.5 Conclusion

X-ray computed microtomography was used to assess the qualitative and quantitative capabilities for examining oil-contaminated sea ice (granular/inter-granular). Use of polypropylene tubes were found to enhance the capacity for imaging crude oil-in-ice, as they possess a similar density to the crude oil used in this study ($\sim 860 \text{ kg/m}^3$). We postulate that polyethylene tubes (960 kg/m^3) would enhance the imaging of heavier crude oils-in-ice. It is worth noting the limitation of our proposed method which requires large quantities of oil in sea ice (e.g., $>2.1\%$ oil/ice vol.) to alleviate false positives arising from mixed pixels. Future X-ray work should improve and build on this work.

Through our investigations, oil was found to distribute throughout the ice to an extent and tended to occupy the perimeter of large vacant pockets or completely occupy smaller

void pockets and remained separate from the brine. Based on the oil distribution and proximity relative to brine within the upper layers of sea ice, the success of bioremediation is expected to be insignificant for the bulk oil but would likely be most significant for the lighter and potentially more toxic water soluble oil constituents which dissolved in the brine and became subsequently driven into the water column upon warm conditions. The bulk oil may be preserved within the upper layers of the ice until spring thaw, where it could be potentially biodegraded.

Based on the CT-derived sphericities and SMI values of the sea ice constituents, it was determined that the oil, air, and brine inclusions closely resemble the geometry of an elliptic disk or oblate spheroid. Based on this discovery, standard remote sensing modeling techniques were used to simulate the NRCS of sea ice representing inclusions as circular disks. These simulations were then compared to experimental NRCS, demonstrating the applicability of our modeling approach.

5.6 Acknowledgements

Canada Research Chair (CRC) programs, Natural Sciences and Engineering Research Council (NSERC) of Canada, the Canada Foundation for Innovation (CFI) and the University of Manitoba (UofM). This work was supported by and is a contribution to the ArcticNet Networks of Centres of Excellence and the Arctic Science Partnership (ASP), as well as Microbial Genomics for Oil Spill Preparedness in Canada's Arctic Marine Environment (GENICE). We would also like to thank Ryan Galley, Thomas D. Neusitzer, Nariman Firoozy, Katarzyna Polcwiartek, Nolan Snyder, and Dr. Nicolas-Xavier Geilfus (CEOS).

5.7 References

- AMAP, 2010. AMAP Assessment 2007: oil and gas activities in the arctic — effects and potential effects. *Arctic Monitoring & Assessment Programme*, Oslo, vols. 1 and 2.
- AMAP, 2017. Snow, Water, Ice and Permafrost in the Arctic (SWIPA) 2017. Arctic Monitoring and Assessment Programme (AMAP), Oslo, Norway. xiv + 269 pp.
- Afenyo, M., Khan, F., Veitch, B., Yang, M., 2016a. Modeling oil weathering and transport in sea ice. *Mar. Pollut. Bull.* 107: 206–215.
- Afenyo, M., Veitch, B., Khan, F., 2016b. A state-of-the-art review of fate and transport of oil spills in open and ice-covered water. *Ocean Eng.* 119: 233–248.
- Anderson, J.W., Neff, J.M., Cox, B.A., Tatem, H.E., Hightower, G.M., 1974. Characteristics of dispersions and water-soluble extracts of crude and refined oils and their toxicity to estuarine crustaceans and fish. *Mar. Biol.* 27: 75–88.
- Boccadoro, C., Krolicka, A., Receveur, J., Aeppli, C., Le Floch, S., 2018. “Microbial community response and migration of petroleum compounds during a sea-ice oil spill experiment in Svalbard.” *Marine Environmental Research* 142: 214–233.
- Ballesterio, H., Magdol, Z., 2011. “Biodegradation of Polycyclic Aromatic Hydrocarbons in Simulated Arctic Sea Ice Brine Channels and Protistan Predation.” *International Oil Spill Conference Proceedings*, vol. 2011, no. 1, doi:10.7901/2169-3358-2011-1-272.
- Bazilchuk, N., 2018. “Predicting the fate of oil spills in a frozen world.” *Gemini Research News from NTNU and SINTEF*, 15 Feb., geminiresearchnews.com/2018/02/predicting-fate-oil-spills-frozen-world/.
- BBC News (2020), Arctic Circle oil spill prompts Putin to declare state of emergency. Retrieved from <https://www.bbc.com/news/amp/world-europe-52915807>.
- Boetius, A., Anesio, A.M., Deming, J.W., Mikucki, J.A., and Rapp, J.Z., 2015. “Microbial ecology of the cryosphere: sea ice glacial habitats.” *Nature Reviews Microbiology* 13: 677–690
- Bradford, J.H., Babcock, E.L., Marshall, H.-P., Dickins, D.F., 2015. “Targeted reflection-waveform inversion of experimental ground-penetrating radar data for quantification of oil spills under sea ice.” *Geophysics* 81.1: WA59–WA70.
- Brakstad, O.G., Nonstad, I., Faksness, L.-G., Brandvik, P.J., 2008. Responses of Microbial Communities in Arctic Sea Ice After Contamination by Crude Petroleum Oil. *Microb. Ecol.* 55, 540–552.

Brandvik, P.J. and Faksness, L.-G., 2009. "Weathering processes in Arctic oil spills: Meso-Scale experiments with different ice conditions." *Cold Regions Science and Technology* 55(1): 160–166. doi:10.1016/j.coldregions.2008.06.006.

Brekke, C., Holt, B., Jones, C., Skrunes, S., 2014. "Discrimination of oil spills from newly formed sea ice by synthetic aperture radar." *Remote Sensing of Environment* 145: 1–14.

Brown, C.E., Fingas, M.F., 2003. "Review of the development of laser fluorosensors for oil spill application." *Marine Pollution Bulletin* 47.9-12: 477-84.

Courville, Z.R., Lieb-Lappen, R., Claffey, K., Elder, B., 2017. "Investigations of skeletal layer microstructure in the context of remote sensing of oil in sea ice." *Proceedings of the International Oil Spill Conference: Vol. 2017, No. 1*, pp. 2237-2255. <https://doi.org/10.7901/2169-3358-2017.1.2237>.

Cox, G., Weeks, W., 1983. Equations for determining the gas and brine volumes in sea-ice samples. *J. Glaciol.* 29 (102): 306–316.

Crabeck, O., Galley, R., Dellile, B., Else, B., Geilfus, N.-X., Lemes, M., Roches, M.D., Francus, P., Tison, J.-L., Rysgaard, S., 2016. "Imaging air volume fraction in sea ice using non-destructive X-ray tomography." *The Cryosphere* 10: 1125-1145.

Delille, D., Bassères, A., Dessommes, A., 1997. Seasonal Variation of Bacteria in Sea Ice Contaminated by Diesel Fuel and Dispersed Crude Oil. *Microb. Ecol.* 33: 97–105.

De Loor, G.P., 1968. Dielectric properties of heterogeneous mixtures containing water. *J. Microwave Power* 3(2): 67–73.

Desmond, D.S., Neusitzer, T.D., Firoozy, N., Isleifson, D., Barber, D.G., Stern, G.A., 2019a. "Examining the Physical Processes of Corn Oil (Medium Crude Oil Surrogate) in Sea Ice and its Resultant Effect on Complex Permittivity and Normalized Radar Cross-Section." *Marine Pollution Bulletin* 142: 484-493.

Desmond, D.S., Neusitzer, T.D., Lemes, M., Barber, D.G., Stern, G.A., 2019c. "Examining the Physical Interactions of Corn Oil (Medium Crude Oil Surrogate) in Sea Ice and its Potential for Chemical Partitioning within an Arctic Environment." *Proceedings of the Forty-second AMOP Technical Seminar, Environment and Climate Change Canada, Ottawa, ON, Canada*, pp. 66-95.

Desmond, D.S., Saltymakova, D., Neusitzer, T.D., Firoozy, N., Isleifson, D., Barber, D.G., Stern, G.A., 2019b. "Oil Behavior in Sea Ice: Changes in Chemical Composition and Resultant Effect on Sea Ice Dielectrics." *Marine Pollution Bulletin* 142: 216-233.

Desmond, D.S., Saltymakova, D., Smith, A., Wolfe, T., Snyder, N., Polcwiartek, Bautista, M., Lemes, M., Hubert, C.R.J., Barber, D.G., Isleifson, D., Stern, G.A., 2021.

“Photooxidation and biodegradation potential of a light crude oil in first-year sea ice” *Marine Pollution Bulletin* 165: 112154.

Duliu, O.G., 1999. “Computer axial tomography in geosciences: An overview.” *Earth-Sci. Rev.* 48: 265–281.

Eicken, A., 2003. “From the microscopic to the macroscopic to the regional scale: Growth, microstructure and properties of sea ice.” Contribution to Thomas D. & G. S. Dieckmann (eds.): *SEA ICE – AN INTRODUCTION TO ITS PHYSICS, BIOLOGY, CHEMISTRY AND GEOLOGY*, Blackwell Science, London, 2003, pp. 22-81.

Ehn, J.K., Hwang, B.J., Galley, R.J., Barber, D.G., 2007. “Investigations of newly formed sea ice in the Cape Bathurst polynya: 1. Structural, physical, and optical properties.” *J. Geophys. Res.*, vol. 112, no. C5, p. C05 003.

Faksness, L.-G. and Brandvik, P.J., 2008. “Distribution of water soluble components from Arctic marine oil spills — A combined laboratory and field study.” *Cold Regions Science and Technology* 54(2): 97–105. doi:10.1016/j.coldregions.2008.03.005.

Faksness, L.-G., Brandvik, P.J., Daae, R.L., Leirvik, F., Børseth, J.F., 2011. “Large-Scale oil-in-Ice experiment in the Barents Sea: Monitoring of oil in water and MetOcean interactions.” *Marine Pollution Bulletin* 62(5): 976–984. doi:10.1016/j.marpolbul.2011.02.039.

Fingas, M., Brown, C.E., 2007. “Oil spill remote sensing: a forensic approach.” *Oil Spill Environmental Forensics. Fingerprinting and Source Identification*.

Fingas, M.F., Hollebone, B.P., 2003. “Review of behaviour of oil in freezing environments.” *Marine Pollution Bulletin* 47.9: 333-340.

Firoozy, N., Neusitzer, T., Chirkova, D., Desmond, D., Lemes, M., Landy, J., Mojabi, P., Rysgaard, S., Stern, G., Barber, D.G., 2018. “A Controlled Experiment on Oil Release Beneath Thin Sea Ice and its Electromagnetic Detection.” *IEEE Transactions on Geoscience and Remote Sensing* 56(8): 4406-4419.

Firoozy, N., Neusitzer, T., Desmond, D.S., Tiede, T., Lemes, M., Landy, J., Mojabi, P., Rysgaard, S., Stern, G., Barber, D.G., 2017. “An Electromagnetic Detection Case Study on Crude Oil Injection in a Young Sea Ice Environment.” *IEEE Transactions on Geoscience and Remote Sensing* 55(8): 4465-4475.

Frankenstein, G., Garner, R., 1967. “Equations for determining the brine volume of sea ice from -0.5 to -22.9°C.” *J. Glaciology* 6.48: 943-944.

Frantz, C.M., Light, B., Farley, S.M., Carpenter, S., Lieblappen, R., Courville, Z., Orellana, M.V., Junge, K., 2019. “Physical and optical characteristics of heavily melted “rotten” Arctic sea ice.” *The Cryosphere* 13: 775–793.

Fritsen, C.H., Lytle, V.I., Ackley, S.F., Sullivan, C.W., 1994. “Autumn bloom of Antarctic pack-ice algae.” *Science* 266: 782–784.

Fritt-Rasmussen, J., Wegeberg, S., Gustavson, K., 2015. "Review on Burn Residues from In Situ Burning of Oil Spills in Relation to Arctic Waters." *Water, Air, & Soil Pollution* 226.10: 329.

Fung, A.K., Liu, W.Y., Chen, K.S., Tsay, M.K., 2002. "An Improved Iem Model for Bistatic Scattering From Rough Surfaces." *J. Electromagn. Waves Appl.* 16: 689–702.

Galley, R.J., Else, B.G.T., Geilfus, N.-X., Hare, A.A., Isleifson, D., Barber, D.G., Rysgaard, S., 2015. Imaged brine inclusions in young sea ice - Shape, distribution and formation timing." *Cold Regions Science and Technology* 111: 39-48. doi: 10.1016/j.coldregions.2014.12.011.

Golden, K.M., Eicken, H., Heaton, A.L., Miner, J., Pringle, D.J., Zhu, J., 2007. "Thermal evolution of permeability and microstructure in sea ice." *Geophys. Res. Lett.* 34: L16501. doi:10.1029/2007GL030447.

Harsem, Ø., Eide, A., Heen, K., 2011. "Factors influencing future oil and gas prospects in the Arctic." *Energy policy* 39.12: 8037-8045.

Hildebrand, T. Rügsegger, P., 1997. "Quantification of Bone Microarchitecture with the Structure Model Index." *Computer Methods in Biomechanics and Bio Medical Engineering* 1(1): 15-23.

Hubert, C., Stern, G., 2016-2017. "GENICE: Microbial Genomics for Oil Spill Preparedness in Canada's Arctic Marine Environment." *Genome Canada*, www.genomecanada.ca/en/genice-microbial-genomics-oil-spill-preparedness-canadas-arctic-marine-environment.

Iassonov, P., Gebrenegus, T., and Tuller, M., 2009. "Segmentation of X-ray computed tomography images of porous materials: A crucial step for characterization and quantitative analysis of pore structures." *Water Resour. Res.* 45: W09415. doi:10.1029/2009WR008087.

IPCC, 2014: Climate Change 2014: Synthesis Report. Contribution of Working Groups I, II and III to the Fifth Assessment Report of the Intergovernmental Panel on Climate Change [Core Writing Team, R.K. Pachauri and L.A. Meyer (eds.)]. IPCC, Geneva, Switzerland, 151 pp.

Isleifson, D., Byongjun Hwang, Barber, D.G., Scharien, R.K., Shafai, L., 2010. "C-Band Polarimetric Backscattering Signatures of Newly Formed Sea Ice During Fall Freeze-Up." *IEEE Trans. Geosci. Remote Sens.* 48: 3256–3267.

Isleifson, D., Galley, R.J., Barber, D.G., Landy, J.C., Komarov, A.S., Shafai, L., 2014. A study on the C-band polarimetric scattering and physical characteristics of frost flowers on experimental sea ice. *IEEE Trans. Geosci. Remote Sens.* 52(3): 1787-1798.

Isleifson, D., Komarov, A., Desmond, D., Stern, G., Barber, D., 2020. "Modeling Backscattering from Oil-contaminated Sea Ice using a Multi-layered Scattering Method."

Proceedings of the 2020 IEEE International Geoscience and Remote Sensing Symposium, pp. 1-2.

Ketcham, R., Carlson, W.D., 2001. "Acquisition, optimization and interpretation of X-ray computed tomographic imagery: Applications to the geosciences." *Computers & Geosciences* 27(4): 381-400.

Krembs, C., Gradinger, R., Spindler, M., 2000. "Implications of brine channel geometry and surface area for the interaction of sympagic organisms in Arctic sea ice." *J. Exp. Mar. Biol. Ecol.* 243: 55–80.

Lieb-Lappen, R.M., Golden, E.J., Obbard, R.W., 2017. "Metrics for interpreting the microstructure of sea ice using X-ray micro-computed tomography." *Cold Regions Science and Technology* 138: 24-35.

Lieblappen, R. M., Kumar, D. D., Pauls, S. D., and Obbard, R. W., 2018. "A network model for characterizing brine channels in sea ice." *The Cryosphere* 12: 1013–1026, <https://doi.org/10.5194/tc-12-1013-2018>, 2018.

Li, T., Li, S., Zhao, J., Lu, P., Meng, L., 2012. "Sphericities of non-spherical objects." *Particuology* 10: 97-104.

Martin, S., 1979. "A Field Study of Brine Drainage and Oil Entrainment in First-Year Sea Ice." *J. Glaciol.* 22(88): 473–502.

Maus, S., Becker, J., Schneebeli, M., Wiegmann, A., 2015. "Oil Saturation of the sea ice pore space." *Proceedings of the 23rd International Conference on Port and Ocean Engineering under Arctic Conditions*.

Maus, S., Leisinger, S., Matzl, M., Schneebeli, M., Wiegmann, A., 2013. "Modelling oil entrapment in sea ice on the basis of 3d micro-tomographic images." *Proceedings of the International Conference on Port and Ocean Engineering under Arctic Conditions*.

Neusitzer, T.D., Firoozy, N., Chirkova, D., Polcwiartek, K., Tiede, T., Desmond, D., Snyder, N., Lemes, M., Rysgaard, S., Wang, F., Smith, A., Hubert, C., Stern, G., Mojabi, P., Barber, D., 2018b. "Remote Sensing of Oil Spills in Freezing Environments at the University of Manitoba Sea-ice Environmental Research Facility", in Proceedings of the 18th International Symposium on Antenna Technology and Applied Electromagnetics (ANTEM), Waterloo, ON, CA, pp. 1-3.

Neusitzer, T.D., Firoozy, N., Tiede, T.M., Desmond, D.S., Lemes, M., Stern, G.A., Rysgaard, S., Mojabi, P., Barber, D.G., 2018a. "Examining the Impact of a Crude Oil Spill on the Permittivity Profile and Normalized Radar Cross-Section of Young Sea Ice." *IEEE Transactions on GEOSCIENCE and Remote Sensing* 56(2): 921-936, doi:10.1109/tgrs.2017.2756843.

Obbard, R., Troderman, G., Baker, I., 2009. "Imaging brine and air inclusions in sea ice using micro-X-ray computed tomography." *J. Glaciol.* 55: 1113–1115.

Oggier, M., Eicken, H., Wilkinson, J., Petrich, C., O'Sadnick, M., 2020. "Crude oil migration in sea-ice: Laboratory studies of constraints on oil mobilization and seasonal evolution." *Cold Regions Science and Technology* 174: 102924.
<https://doi.org/10.1016/j.coldregions.2019.102924>.

O'Sadnick, M.O., Petrich, C., Phuong, N.D., 2017. "The Entrainment and Migration of Crude Oil in Sea Ice, the Use of Vegetable Oil as a Substitute, and Other Lessons from Laboratory Experiments", in Proceedings of the 24th International Conference on Port and Ocean Engineering under Arctic Conditions, Busan, Korea.

Payne, J.R., Hachmeister, L.E., McNabb, G.D., Sharpe, H.E., Smith, G.S., Menen, C.A., 1991b. "Brine-induced advection of dissolved aromatic hydrocarbons to Arctic bottom waters." *Environ. Sci. Technol.* 25: 940–951.

Payne, J.R., McNabb Jr., G.D., Clayton Jr., J.R., 1991a. "Oil-weathering behavior in Arctic environments." *Polar Research* 10.2: 631-662.

Petrich, C., Eicken, H., 2010. "Growth, structure and properties of sea ice." *Sea Ice*, Second Edition. Wiley-Blackwell, United Kingdom. (Ch 2).

Petrich, C., Karlsson, J., Eicken, H., 2013. "Porosity of growing sea ice and potential for oil entrainment." *Cold Regions Science and Technology* 87: 27-32.

Polder, D., van Santen, J.H., 1946. The effective permeability of mixtures of solids. *Physica* 12(5), 257–271.

Prince, R.C. and Walters, C.C., 2016. "Biodegradation of oil hydrocarbons and its implications for source identification." *Standard Handbook Oil Spill Environmental Forensics: Fingerprinting and Source Identification*, 2nd. Ch 19.

Pringle, D.J., Miner, J.E., Eicken, H., Golden, K.M., 2009. "Pore space percolation in sea ice single crystals." *JOURNAL OF GEOPHYSICAL RESEARCH*, VOL. 114, C12017, doi:10.1029/2008JC005145.

Puestow, T., Parsons, L., Zakharov, I., Cater, N., Bobby, P., Fuglem, M., Parr, G., Jayasiri, A., Warren, S., Warbanski, G., 2013. "Oil Spill Detection and Mapping in Low Visibility and Ice: Surface Remote Sensing." *Arctic Response Technology Oil Spill Preparedness*, Final Report 5.1.

Salomon, M.L., Arntsen, M., Phuong, N.D., Maus, S., O'Sadnick, M., Petrich, C., Schneebeli, M., Wiese, M., 2017. "Experimental and Micro-CT study on the Oil Distribution in laboratory grown Sea Ice." Proceedings of the 24th International Conference on Port and Ocean Engineering under Arctic Conditions, Busan, Korea.

Saltymakova, Smith, A.F., Polcwiartek, K., Desmond, D., Snyder, N., Wolfe, T., Bautista, M.A., Stone, M., Ellefson, E., Hubert, C., Stern, G.A., 2019. "Enriched Arctic

Bacteria potential for biodegradation of polycyclic aromatic hydrocarbons estimated from Crude Oil-in-ice Mesocosm Experiment,” in the proceedings of the 42nd AMOP Technical Seminar on Environmental Contamination and Response, <https://www.researchgate.net/publication/334151994>.

Saltymakova, D., Desmond, D.S., Isleifson, D., Firoozy, N., Neusitzer, T.D., Xu, Z., Lemes, M., Barber, D.G., and Stern, G.A., 2020. “Effect of dissolution, evaporation, and photooxidation on crude oil chemical composition, dielectric properties and its radar signature in the Arctic environment.” *Marine Pollution Bulletin* 151: 110629.

Schenk, C.J., 2011. "Chapter 41 Geology and petroleum potential of the West Greenland-East Canada Province." *Geological Society, London, Memoirs* 35.1: 627-45.

Sezgin, M., Sankur, B., 2004. “Survey over image thresholding techniques and quantitative performance evaluation.” *J. Electron. Imaging* 13: 146–165. doi:10.1117/1.1631315.

Smith, L.C., Stephenson, S.R., 2013. "New Trans-Arctic shipping routes navigable by midcentury." *Proceedings of the National Academy of Sciences* 110.13: n. pag.

Tinga, W.R., Voss, W.A.G., Blossey, D.F., 1973. Generalized approach to multiphase dielectric mixture theory. *J. Appl. Phys.* 44(9): 3897–3902.

Ulaby, F.T., Long, D.G., 2014. “Microwave Radar and Radiometric Remote Sensing.” Ann Arbor, MI: University of Michigan Press.

Vancoppenolle, M., Meiners, K.M., Michel, C., Bopp, L., Brabant, F., Carnat, G., Delille, B., Lannuzel, D., Madec, G., Moreau, S., Tison, J.-L., van der Merwe, P., 2013. “Role of sea ice in global biogeochemical cycles: Emerging views and challenges.” *Quaternary Sci. Rev.* 79: 207–230. doi:10.1016/j.quascirev.2013.04.011, 2013.

Vergeynst, L., Kjeldsen, K.U., Lassen, P., Rysgaard, S., 2018. “Bacterial community succession and degradation patterns of hydrocarbons in seawater at low temperature.” *Journal of Hazardous Materials* 353: 127-134.

Wadell, H., 1935. “Volume, Shape, and Roundness of Quartz Particles.” *The Journal of Geology* 43(3): 250-280.

Weeks, W.F., Ackley, S.F.: The growth, structure and properties of sea ice, in: The geophysics of sea ice, edited by: Untersteiner, N., Plenum Press, New York, 9–164, 1986.

Wilkinson, J.P., Boyd, T., Hagen, B., Maksym, T., Pegau, S., Roman, C., Singh, H., Zabilansky, L., 2015. "Detection and quantification of oil under sea ice: The view from below." *Cold Regions Science and Technology* 109: 9-17.

Chapter 5 investigated aspects of oil behavior (i.e., migration tendencies, encapsulation potential), detection (i.e., radar), and mitigation (i.e., bioremediation) in sea-ice environments. Specifically, this chapter aimed to test the following hypotheses:

1. The use of a polypropylene tube can enhance the capacity for imaging oil-in-ice.
2. Oil will become incorporated in the sea ice matrix and will appear dispersed.
3. Oil will remain separate from the brine.
4. Oil inclusions will resemble the geometry of an oblate spheroid.

Each of these assumptions was found to be true based on the data presented in Chapter 5. However, the third hypothesis is based on having a high oil volume fraction. Therefore, further research is required to study the fate and biodegradation potential of low oil concentrations inside sea ice. Based on the fourth hypothesis, we demonstrated the applicability of modeling sea ice dielectrics with circular disk inclusions and subsequently simulating the NRCS based on the modeled dielectrics. However, further research should compare the applicability and accuracy of different sea ice dielectrics and NRCS models by comparing simulated and experimentally determined data.

Additional limitations and proposed future work will be discussed in the concluding chapter of this thesis.

6 Conclusion

6.1 Summary of Findings

An overarching hypothesis for the four projects (Chapters 2 to 5) was that crude oil would influence the physical properties of sea ice and would be chemically and, therefore, physically affected by the sea ice. Through the experiments conducted, we observed that crude oil influenced the temperature of sea ice through a change in sea ice albedo and thermal conductivity (Chapter 2). Similarly, crude oil affected sea ice salinity by a combination of brine displacement (through oil migration in brine channels) and brine drainage (through ice warming) (Chapters 2 and 5). Changes in these physical properties allowed for a detectable change in the dielectrics and normalized radar cross-section of the ice (Chapters 2 and 5).

In turn, the chemical composition of the oil was altered through its interaction with the sea ice environment. Lower molecular weight (MW) oil constituents were more readily dissolved in brine and transported similarly to solute salts, forming the characteristic c-shaped profile relative to higher MW compounds (Chapters 2 and 3). We also observed that the dissolved species for a particular compound group would distribute inside sea ice, whereby low MW compounds would concentrate towards the ice surface and high MW compounds would concentrate towards the ice subsurface and water column (Chapters 2 and 3). We speculate that the cause of this trend relates to differences in solubility, and therefore hydrophobicity, for low and high MW compounds. Brine salinity is lowest towards the sea ice base (and water column) and highest towards the sea ice surface. Therefore, high MW

compounds, which are less soluble and more hydrophobic, are believed to be more impacted by the salting-out effect innate to the upper ice layers, which are richer in salt content.

In connection with the observed changes in the oil's chemical state, we observed an inherent change in the oil's density, thermal conductivity, and dielectrics (Chapters 2 and 4). Changes in these physical properties were linked to oil partitioning within brine channels, dissolution, and evaporation (of the oil's water-soluble and volatile fraction) from the ice, as well as photooxidation (Chapters 2, 3, and 4). These observed weathering processes were found to be most pronounced for the lighter oil fractions. In comparison, heavier oil fractions were found to be better preserved through encapsulation in the air pockets and vacated brine channels of the ice (Chapters 4 and 5). However, as ice temperatures warmed, the more water-soluble (and potentially more toxic) oil fraction was observed to be prone to transport into the water column, where biodegradation was found to be most effective (Chapters 4 and 5).

6.2 Limitations and Future Work

Overarching limitation. A limitation inherent to each project is that each study used a single oil type (i.e., a light crude oil). Future experiments should incorporate diesel fuel, which is highly relevant to Arctic waters, as a large amount of diesel is shipped to northern communities – the same fuel is used for home heating, diesel vehicles, and electricity generation.

Chapter 2. First, this study demonstrated that oil-in-ice can positively be detected through the measurement of the normalized radar cross-section (NRCS). Moreover, a limit of detection in the oil volume fraction is ascertainable through its correlation with NRCS

(Fig. 2.3). However, the NRCS is also influenced by many other factors including ambient temperature which can impact brine volume, a major contributor to microwave scattering from the sea ice. Therefore, an additional metric that can be used for oil spill verification is an entropy/mean-alpha classification (Asihene et al., 2023). The scattering entropy of sea ice can be derived from the coherency matrix (which in turn is derived from the scattering matrix of a scatterometer) (Asihene et al., 2023; Ulaby and Long, 2014). Based on Asihene et al. (2024), oil-contaminated sea ice can be distinguished from oil-free sea ice if its mean alpha is above 18 and its entropy is above 0.3. However, false positive detections could arise from open water and snow accumulation, which also fall under the same classification as oil-contaminated sea ice (Asihene et al., 2024).

Second, a connection between the chemical state of oil and its physical properties (e.g., density and dielectrics) was established in this study. However, the physical properties were only measured at standard conditions. Given that a correlation is attainable between oil dielectrics (a property relevant to microwave remote sensing of oil-contaminated sea ice) and oil density (a property that can be related to the oil's chemical state – light, medium, or heavy), measuring these properties for various oils and fuels at a range of temperatures relevant to Arctic conditions could provide the framework for remotely inferring the chemical state of an Arctic oil spill through passive radiometer measurement or active radar inversion. Ascertaining the composition and whereabouts of an Arctic oil spill would potentially allow for an appropriate and swifter mitigation response.

Chapter 3. First, an inherent weakness to the modeling of physical properties of oil constituents at subzero temperatures is that we do not know how accurate the predictions are

at non-standard conditions. Future work should compare theoretical predictions with experimental literature (e.g., Desmond et al., 2022) in the hope of spreading awareness as to the need for measuring experimental properties at cold temperatures.

Second, the salting-out-effect was postulated to be a cause of oil constituent partitioning in sea ice brine channels, whereby compounds which are more hydrophobic concentrate in areas of lower salt concentration. However, this theory should be further established by conducting controlled experiments or simulations. Another factor that could potentially affect the partitioning of compounds within a brine channel–seawater network is temperature. Brine channels are colder toward the ice surface and increase in temperature toward the water column. Therefore, oil constituents would naturally be more soluble in the water column where it is warmer. The question is if hydrophobic compounds are more affected by temperature than less hydrophobic compounds and if this is a more significant factor than salinity. A simulation study could test the effect of temperature and assess if its effect on partitioning would be less or more significant than salt concentration.

Lastly, this study touched on the persistence and bioaccumulation of oil constituents in seawater as it relates to the octanol-water partition coefficient. Future work should continue to investigate the potential for persistence, bioaccumulation, and toxicity of crude oil and diesel fuel constituents in an Arctic setting and their potential availability to aquatic species. In particular, transformed products due to photo- and biodegradation should be explored and focused upon.

Chapter 4. While this study was conducted over a long enough period to assess both photooxidation and biodegradation processes occurring within the ice and water column,

degradation rates were not established. Therefore, future work should test degradation rates at different oil and nutrient level concentrations (low, moderate, and high), as this study focused only on high oil concentrations and high nutrient levels (relevant to summer conditions by the very productive ice edge). Second, this study compared the microbial and chemical analyses independently. Future work should include correlations/statistical analyses between the microbial and chemical composition for a more comprehensive investigation.

Third, this study used the C17/Pr ratio to assess if biodegradation occurred within the ice and water. Typically, hopane (191) has been used for normalization to assess the degree of biodegradation. However, based on Chapter 2, we chose not to use hopane for normalization as it was observed to have been flushed down to the water column, presumably due to the salting-out effect. Specifically, 17 α (H),21 β (H)-hopane was not used for data normalization because its concentration decreased in the ice as it migrated to the water column when the ice started to melt. Therefore, traditional methods for assessing biodegradation are not necessarily applicable in an Arctic setting due to the complex partitioning of oil in a sea ice environment. Future work should devise new normalization and statistical methods appropriate for Arctic conditions.

Lastly, the focus of this study was on bioremediation. However, another relevant mitigation procedure is in situ burning. Future work should develop methods for simulating in-situ burning of different oils (differing in composition) in various Arctic settings to better grasp which oil spill situations and states are optimal for in-situ burning mitigation. The modeling of in-situ burning of oil in open water and in various oil-in-ice scenarios can be

conducted using ReaxFF reactive force field for molecular dynamics simulations of hydrocarbon oxidation (van Duin et al., 2001; Chenoweth et al., 2008; ReaxFF 2010; ADF2010; ADF-GUI 2010). The theoretical results obtained (including burning efficiency, change in composition, relative losses, duration, formed by-products and their transition states and reactivity) should be compared to experimental results in the hope of validating, adapting, and improving theoretical methods.

Chapter 5. A limitation of this study is the oil density and volume fraction restrictions relevant to the proposed method, which allows the user to “see” oil-in-ice using X-ray microtomography. Future work should test the applicability of this method for analyzing the microstructure of diesel fuel-contaminated sea ice, which is highly relevant to the Arctic. A second limitation of this study is that the experimental NRCS was only compared to NRCS simulations incorporating circular disk inclusions. Future work should test the applicability of multiple sea ice dielectric and NRCS models by comparing experimental data to various simulations.

6.3 Proposed Arctic Oil Spill Strategy based on Conducted Research and Suggested Future Work

Arctic shipping activities peak throughout summer and early fall (Pizzolato et al., 2014). During this period of high activity, spilled oil originating from a vessel or drilling/extraction activity is likely to be found in open water or between ice floes. In the case an open water spill is not detected before fall freeze-up, the oil is likely to be incorporated in newly forming ice, where the oil may remain in the top portion of the sea ice profile throughout winter. In the marine Arctic environment, marine diesel and crude oil are the most

relevant oil products. These oils have the potential to be incorporated into the sea ice matrix, where they can potentially be detected by various airborne/spaceborne remote sensing technologies. Currently, radar (i.e., SAR), LiDAR, optical, and microwave (MW) radiometer systems are equipped on satellites that periodically monitor Arctic regions (Lillesand et al., 2015). These same remote sensing technologies can also be deployed by an aircraft or unmanned aerial vehicle (UAV) (e.g., drone). Both radar and optical remote sensors have the potential to detect and monitor spilled oil on open water or ice or within the surficial layers of sea ice. However, radar and MW radiometer systems are capable of detection under dark conditions and are suitable for most Arctic ambient weather. LiDAR is best used in conjunction with radar as surface roughness is a governing factor of radar remote sensing.

Logistically speaking, available spaceborne sensors (e.g., RADARSAT-2, ICESat-2, Landsat ETM, MODIS, AMSR2) should be used to monitor the Arctic for spilled oil. Usage of spaceborne sensors may be advantageous in tracking cross boundary oil spills (e.g., BBC News, 2020). However, their monitoring frequency is a day or longer. If there is a probable detection, airborne sensors via an aircraft or UAV (e.g., drone), employing a suite of appropriate sensors such as radar, LiDAR, and passive radiometer, could be used on a closer scale to positively find, monitor, and characterize spilled oil with increased monitoring frequency. In particular, flying a drone is far less expensive than the operational, repair, and pilot training fees associated with airplanes and helicopters and have gained popularity for remote sensing missions. If there is suspicion of an Arctic oil spill, a drone could be deployed off a ship or coastline for confirmation, further characterization, and monitoring. To this end, community-based monitoring (CBM) and response (CBR) in Arctic regions should be

established as response times from Coast Guards can be lengthy due to the remoteness of the Arctic. Ultimately, the positive detection of an oil spill (e.g., Chapters 2 and 5; Asihene et al., 2022), determination of its thickness and spatial location (above, within, or below ice, or on open water) (e.g., Asihene et al., 2024), and determination of its chemical classification (light, medium, heavy, extra-heavy) (Chapters 2 and 5) (ongoing research) will allow for fast response times to mitigate and minimize the extent of damage to Arctic waters and its local inhabitants. Furthermore, the capability of ascertaining the whereabouts and chemical state of the oil in a sea ice environment will provide guidance for an appropriate mitigation response, as the potential for various mitigation procedures (e.g., bioremediation, in-situ burning, and mechanical recovery) depend on the spatial location and composition of the oil (e.g., Chapters 1, 4 and 5).

Lastly, the ability to accurately simulate various oil spill scenarios using chemical (e.g., Chapter 3) and electromagnetic scattering (e.g., Chapters 2 and 5) models will allow one to perform various oil spill assessments in place of demanding and time intensive experimental procedures. Moreover, once a model is established, it can be implemented in existing detection, classification, and behavioral algorithms, or can be used in the creation of a new and viable method.

6.4 References

ADF2010, SCM, Theoretical Chemistry, Vrije Universiteit, Amsterdam, The Netherlands, <http://www.scm.com>

ADF-GUI 2010, SCM, Amsterdam, The Netherlands, <http://www.scm.com>

Asihene, E., Komarov, A.S., Stern, G., Gilmore, C., Isleifson, D., 2024. “Towards the Estimation of Oil Slick Thickness on Newly Formed Sea Ice using C-Band Radar Backscatter.” *IEEE Transaction Geoscience Remote Sensing* 62: 1-15.

Asihene, E., Stern, G., Barber, D.G., Gilmore, C., Isleifson, D., 2022. "Toward the Discrimination of Oil Spills in Newly Formed Sea Ice Using C-Band Radar Polarimetric Parameters." *IEEE transactions on geoscience and remote sensing* 61: 1-15.

BBC News (2020), Arctic circle oil spill prompts Putin to declare state of emergency. Retrieved from <https://www.bbc.com/news/amp/world-europe-52915807>.

Chenoweth, K., van Duin, A.C.T., Goddard, W.A., 2008. "ReaxFF reactive force field for molecular dynamics simulations of hydrocarbon oxidation." *Journal of Physical Chemistry A* 112: 1040-1053.

Desmond, D.S., Xidos, J., Schreckenbach, G., Barber, D.G., Isleifson, D., Stern, G.A., 2022. Estimation of the Temperature Dependence of the Octanol-Water Partition Coefficient for Select Chlorobenzenes Using Computational Chemistry, Proceedings of the Forty-fourth AMOP Technical Seminar, Environment and Climate Change Canada, Ottawa, ON, Canada, pp. 539-552, 2022.

Lillesand, T.M., Kiefer, R.W., Chipman, J.W., 2015. "Remote Sensing And Image Interpretation." WILEY, 7th Edition.

Pizzolato, L., Stephen E.L., Derksen, C., Dawson, J., Copland, L., 2014. "Changing sea ice conditions and marine transportation activity in Canadian Arctic waters between 1990 and 2012." *Climatic Change* 123: 161-173.

ReaxFF 2010, SCM, Theoretical Chemistry, Vrije Universiteit, Amsterdam, The

Ulaby, F.T., Long, D.G., 2014. Microwave Radar and Radiometric Remote Sensing. Ann Arbor, MI, U.S.A.: University of Michigan Press.

van Duin, A.C.T., Dasgupta, S., Lorant, F., and Goddard, W.A., 2001. "ReaxFF: A reactive force field for hydrocarbons." *Journal of Physical Chemistry A* 105: 9396-9409.

7 Appendix

7.1 Supplementary Tables and Figures

Table S2.1 Average Surrogate Recoveries

Compound	Average recovery, %
Deuterated Aromatic compounds	
D8 Naphthalene	12.65
D8 Acenaphthylene	19.89
D10 Acenaphthene	21.03
D10 Fluorene	25.06
D10 Phenanthrene	31.99
D10 Fluoranthene	41.89
D10 Pyrene	42.85
D12 Benz[a]anthracene	50.93
Deuterated Alkanes	
D26 Dodecane	13.81
D34 Hexadecane	23.56
D42 Eicosane	38.84
D50 Tetracosane	46.31
D58 Octacosane	46.86
D66 Dotriacontane	70.27
D72 Hexatriacontane	104.08

Table S2.2 Table of identified compounds in the crude oil composition, their quantifiers, and recovery standards

Compounds	Target Ion	Quantifier	# of comp.	Recovery std.
Saturated compounds				
Alkanes C ₁₁ – C ₃₆	71.0861	N-alkanes ¹	26	Closest d-alkane
2,6-dimethylundecane	71.0861	Undecane ¹	1	D ₂₆ Dodecane
2,6,10-trimethylundecane (nor-Farnesane)	71.0861	Dodecane ¹	1	D ₂₆ Dodecane
2,6,10-trimethyldodecane (Farnesane)	71.0861	Tridecane ¹	1	D ₂₆ Dodecane
2,6,10-trimethyltridecane	71.0861	Tetradecane ¹	1	D ₂₆ Dodecane
2,6,10-trimethylpentadecane (nor-Pristane)	71.0861	Heptadecane ¹	1	D ₃₄ Hexadecane
Pristane	71.0861	Octadecane ¹	1	D ₃₄ Hexadecane
Phytane	71.0861	Heptadecane ¹	1	D ₃₄ Hexadecane
Alkylcyclopentanes C ₁₃ - C ₂₅	68.0626	The closest cyclohexane ²	17	Closest d-alkane
Alkylcyclohexanes C ₁₁ - C ₂₃	82.0783	Cyclohexanes ²	13	Closest d-alkane
1,1; 1,2; 1,3; 1,4 - MethylAlkylcyclohexanes C ₁₃ - C ₂₀	97.1017	The closest cyclohexanes ²	32	Closest d-alkane
*Tricyclic Terpane C ₂₀ – C ₂₃	191.18	17a(H)-22,29,30 - Trisnorhopane ³	4	D ₄₂ Eicosane
*Tricyclic Terpane C ₂₄ – C ₂₆	191.18	17a(H)-22,29,30 - Trisnorhopane ³	4	D ₅₀ Tetracosane
*Tricyclic Terpane C ₂₈ – C ₃₁	191.18	17a(H)-22,29,30 - Trisnorhopane ³	8	D ₅₈ Octacosane
*Tetracyclic Terpane C ₂₄	191.18	17a(H)-22,29,30 - Trisnorhopane ³	1	D ₅₀ Tetracosane
*Hopanes C ₂₇ – C ₃₀	191.18	Hopanes ³	6	D ₅₈ Octacosane
*18a(H)-22,29,30 - Trisnorneohopane	191.18	17a(H)-22,29,30 - Trisnorhopane ³	1	D ₅₈ Octacosane
*17a(H),21(b)-23 S/R-Homohopane	191.18	17a(H),21(b)-22 S/R-Homohopane ³	2	D ₅₈ Octacosane
*Diasteranes C ₂₁ -C ₂₆	217.1956	ααα20S-Cholestane ³	6	D ₅₀ Tetracosane

¹ n-alkanes (mix of tree SPEX standards: C₁₁-C₁₈, odd C₁₅-C₃₅, even C₁₆-C₃₆);² alkylcycloalkane mixture 1 (Chiron, 9 mix)³ hopanes and steranes (chiron, 12 mix)

Table S2.2 Continued

Compounds	Target Ion	Quantifier	# of comp.	Recovery std.
Saturated compounds				
*Regular sterane C ₂₁	217.1956	ααα 20S-Cholestane ³	1	D ₅₀ Tetracosane
*Iso-steranes C ₂₁ -C ₂₃	217.1956	αββ 20S-Cholestane ³	5	D ₅₀ Tetracosane
*Diasteranes C ₂₇ -C ₂₉	217.1956	ααα 20S-Cholestane ³	9	D ₅₈ Octacosane
*Regular and iso-steranes C ₂₇ -C ₂₉	217.1956	The closest regular or iso-sterane from steranes std ³	9	D ₅₈ Octacosane
Aromatic compounds				
Alkylbenzenes C ₁₀ - C ₂₅	92.0626	Alkylbenzenes ⁴	16	Closest d-alkane
1-alkyl-3methylbenzenes C ₁₃ - C ₂₂	106.0783	The closest alkylbenzene ⁴	9	Closest d-alkane
Para-; Orto- Methylalkylbenzenes C ₁₃ - C ₂₂	105.0704	The closest alkylbenzene ⁴	20	Closest d-alkane
Trimethylalkylbenzenes C ₁₁ - C ₂₂	133.1017	The closest alkylbenzene ⁴	24	Closest d-alkane
Naphthalene	128.0626	Naphthalene ⁵	1	D ₈ Naphthalene
1; 2 -Methylnaphthalenes	142.0783	1-Methylnaphthalene ⁶	2	D ₈ Acenaphthylen e
Dimethylnaphthalenes	156.0939	1,6-Dimethylnaphthalene ⁶	8	D ₁₀ Acenaphthene
Trimethylnaphthalenes	170.1096	2,3,5-Trimethylnaphthalene ⁶	7	D ₁₀ Fluorene
Tetramethylnaphthalenes	184.1252	2,3,5-Trimethylnaphthalene ⁶	9	D ₁₀ Fluorene
Pentamethylnaphthalenes	198.1409	2,3,5-Trimethylnaphthalene ⁶	4	D ₁₀ Phenanthrene
Phenanthrene	178.0783	Phenanthrene ⁵	1	D ₁₀ Phenanthrene
1; 2; 3; 9 -Methylphenanthrenes	192.0939	2-Methylphenanthrene ⁶	4	D ₁₀ Phenanthrene
Dimethylphenanthrenes	206.1096	2,4-dimethylphenanthrene ⁶	12	D ₁₀ Fluoranthene
Biphenyl	154.0783	1-Methylnaphthalene ⁶	1	D ₈ Acenaphthylen e

⁴ alkylbenzene mixture (Chiron, 16 mix)⁵ PAHs mix (CV calibration mix # 5, Restek, 16 mix)⁶ PAH Dibenzothiophene (and alkylated homologues) mixture (Chiron, 20 mix)

Table S2.2 Continued

Compounds	Target Ion	Quantifier	# of comp.	Recovery std.
Aromatic compounds				
2; 3; 4 -Methylbiphenyl	168.0939	1,6-Dimethylnaphthalene ⁶	3	D ₈ Acenaphthylene
Diphenylmethane	168.0939	1,6-Dimethylnaphthalene ⁶	1	D ₈ Acenaphthylene
Dimethylbiphenyls	182.1096	2,3,5-Trimethylnaphthalene ⁶	12	D ₈ Acenaphthylene
Methyldiphenylmethane	182.1096	2,3,5-Trimethylnaphthalene ⁶	3	D ₈ Acenaphthylene
Heteroaromatic compounds				
Dibenzothiophene	184.0347	Dibenzothiophene ⁶	1	D ₁₀ Phenanthrene
4; 2; 3; 1 -Methyldibenzothiophene	198.0503	2-Methyldibenzothiophene ⁶	4	D ₁₀ Phenanthrene
Dimethyldibenzothiophenes	212.066	2,8-Dimethyldibenzothiophene ⁶	13	D ₁₀ Fluoranthene
Trimethyldibenzothiophenes	226.0816	2,4,7-Trimethyldibenxothiophene ⁶	12	D ₁₀ Fluoranthene
Dibenzofuran	168.0575	Dibenzofuran ⁷	1	D ₁₀ Acenaphthene
1; 2; 3; 4-Methyldibenzofuran	182.0732	Dibenzofuran ⁷	4	D ₁₀ Acenaphthene
Dimethyldibenzofuran	196.0888	Dibenzofuran ⁷	9	D ₁₀ Acenaphthene
Surrogate compounds				
Deuterated PAHs		D ₈ , D ₁₀ , D ₁₂ ⁸	16	d- PAHs
Deuterated Alkanes	66.1256	D ₂₆ , D ₃₄ , D ₄₂ , D ₅₀ , D ₅₈ , D ₆₆ , D ₇₂ ⁹	7	d-alkanes

*- analyzed on Triple Quadrupole GC-MS

⁷ Dibenzofuran (SPEX)⁸ Deuterated PAH (D₈, D₁₀, D₁₂, Wellington Laboratories, 8 mix)⁹ n-alkane (D₂₆ - D₇₂, Fisherbrand, 7 mix)

Table S2.3 Multiple reaction monitoring mass spectrometry method for steranes and terpanes

Compound name	Precursor	Product	Dwell	CE (eV)	Type
Regular and diastaranes	217	93	30	24	Qualifier
	217	121	30	12	<i>Quantifier</i>
	217	135	30	10	Qualifier
$\alpha\beta\beta$ Steranes	218	93	30	24	Qualifier
	218	161	30	14	Qualifier
	218	175	30	12	<i>Quantifier</i>
$\beta\alpha$ Steranes	259	95	30	20	Qualifier
Steranes C ₂₆	358	217	30	20	Qualifier
Steranes C ₂₇	372	217	30	20	Qualifier
Steranes C ₂₈	386	217	30	20	Qualifier
Steranes C ₂₉	400	217	30	20	Qualifier
Terpanes	191	107	30	16	Qualifier
	191	95	30	12	<i>Quantifier</i>
	177	93	30	20	Qualifier
	177	107	30	12	Qualifier
	177	121	30	10	Qualifier

Table S3.4 Table of identified compounds in the crude oil composition, their quantifiers, and recovery standards

Compounds	Target Ion	Quantifier	# of comp.	Recovery std.
Saturated compounds				
Alkanes C ₁₁ – C ₃₆	71.0861	N-alkanes ¹⁰	26	Closest d-alkane
*Tricyclic Terpane C ₂₀ – C ₂₃	191.18	17a(H)-22,29,30 - Trisnorhopane ¹¹	4	D ₄₂ Eicosane
*Tricyclic Terpane C ₂₄ – C ₂₆	191.18	17a(H)-22,29,30 – Trisnorhopan ¹¹	4	D ₅₀ Tetracosane
*Tricyclic Terpane C ²⁸ – C ₃₁	191.18	17a(H)-22,29,30 – Trisnorhopane ¹¹	8	D ₅₈ Octacosane
*Tetracyclic Terpane C ₂₄	191.18	17a(H)-22,29,30 – Trisnorhopane ¹¹	1	D ₅₀ Tetracosane
*Hopanes C ₂₇ – C ₃₀	191.18	Hopanes ¹¹	6	D ₅₈ Octacosane
*18a(H)-22,29,30 - Trisnorneohopane	191.18	17a(H)-22,29,30 – Trisnorhopane ¹¹	1	D ₅₈ Octacosane
*17a(H),21(b)-23 S/R-Homohopane	191.18	17a(H),21(b)-22 S/R-Homohopane ¹¹	2	D ₅₈ Octacosane
*Diasteranes C ₂₁ -C ₂₆	217.1956	ααα20S-Cholestane ¹¹	6	D ₅₀ Tetracosane
*Regular sterane C ₂₁	217.1956	ααα 20S-Cholestane ¹¹	1	D ₅₀ Tetracosane
*Iso-steranes C ₂₁ -C ₂₃	217.1956	αββ 20S-Cholestane ¹¹	5	D ₅₀ Tetracosane
*Diasteranes C ₂₇ -C ₂₉	217.1956	ααα 20S-Cholestane ¹¹	9	D ₅₈ Octacosane
*Regular and iso-steranes C ₂₇ -C ₂₉	217.1956	The closest regular or iso-sterane from steranes std ¹¹	9	D ₅₈ Octacosane
Aromatic compounds				
Naphthalene	128.0626	Naphthalene ¹²	1	D ₈ Napthalene
1; 2 -Methylnaphthalenes	142.0783	1-Methylnaphthalene ¹²	2	D ₈ Acenaphthylen e
Dimethylnaphthalenes	156.0939	1,6-Dimethylnaphthalene ¹²	8	D ₁₀ Acenaphthene
Trimethylnaphthalenes	170.1096	2,3,5-Trimethylnaphthalene ¹²	7	D ₁₀ Fluorene
Tetramethylnaphthalenes	184.1252	2,3,5-Trimethylnaphthalene ¹²	9	D ₁₀ Fluorene
Pentamethylnaphthalenes	198.1409	2,3,5-Trimethylnaphthalene ¹²	4	D ₁₀ Phenanthrene
Surrogate compounds				

¹⁰ n-alkanes (mix of tree SPEX standards: C₁₁-C₁₈, odd C₁₅-C₃₅, even C₁₆-C₃₆);¹¹ hopanes and steranes (chiron, 12 mix)¹² PAHs mix (CV calibration mix # 5, Restek, 16 mix)

Table S3.1 Continued

Compounds	Target Ion	Quantifier	# of comp.	Recovery std.
Deuterated PAHs		D ₈ , D ₁₀ , D ₁₂ ¹³	16	d- PAHs
Deuterated Alkanes	66.1256	D ₂₆ , D ₃₄ , D ₄₂ , D ₅₀ , D ₅₈ , D ₆₆ , D ₇₂ ¹⁴	7	d-alkanes

¹³ Deuterated PAH (D₈, D₁₀, D₁₂, Wellington Laboratories, 8 mix)

¹⁴ n-alkane (D₂₆ - D₇₂, Fisherbrand, 7 mix)

Table S3.5 Multiple reaction monitoring mass spectrometry method for steranes and terpanes

Compound name	Precursor	Product	Dwell	CE (eV)	Type
Regular and diastaranes	217	93	30	24	Qualifier
	217	121	30	12	<i>Quantifier</i>
	217	135	30	10	Qualifier
$\alpha\beta\beta$ Steranes	218	93	30	24	Qualifier
	218	161	30	14	Qualifier
	218	175	30	12	<i>Quantifier</i>
$\beta\alpha$ Steranes	259	95	30	20	Qualifier
Steranes C ₂₆	358	217	30	20	Qualifier
Steranes C ₂₇	372	217	30	20	Qualifier
Steranes C ₂₈	386	217	30	20	Qualifier
Steranes C ₂₉	400	217	30	20	Qualifier
Terpanes	191	107	30	16	Qualifier
	191	95	30	12	<i>Quantifier</i>
	177	93	30	20	Qualifier
	177	107	30	12	Qualifier
	177	121	30	10	Qualifier

Table S4.6 Indices and Formulae used in Calculating Indices

Calculated Indices	Formulae used
Esters Index	A_{1265}/A_T
Three Substituted Rings Index	$A_{814}/A_{(864+814+743)}$
Mono and Di Substituted Index	$A_{743}/A_{(864+814+743)}$

*A is area under the subscripted peak; Subscripts (e.g., 1265) represent the wave numbers at which the peaks occur; A_T is total sum of areas of absorption peaks for designated functional groups in the sample spectrum given by...

$$A_T = A(2950 + 2920 + 2860 + 1700 + 1600 + 1458 + 1377 + 1263 + 1155 + 1028 + 875 + 810 + 742 + 705)$$

Table S4.7 Measured Ice Thicknesses (cm) of Sampled Ice Cores

Native	AVG	STDEV	Min	Max
Feb. 7/18	37	2	35	40
Feb. 26/18	49	3	44	52
Mar. 16/18	51	1	51	53
Apr. 10/18	9	4	6	12
Augmented	AVG	STDEV	Min	Max
Feb. 7/18	42	4	37	47
Feb. 26/18	50	5	41	55
Mar. 16/18	55	6	47	65
Apr. 10/18	17	6	13	21

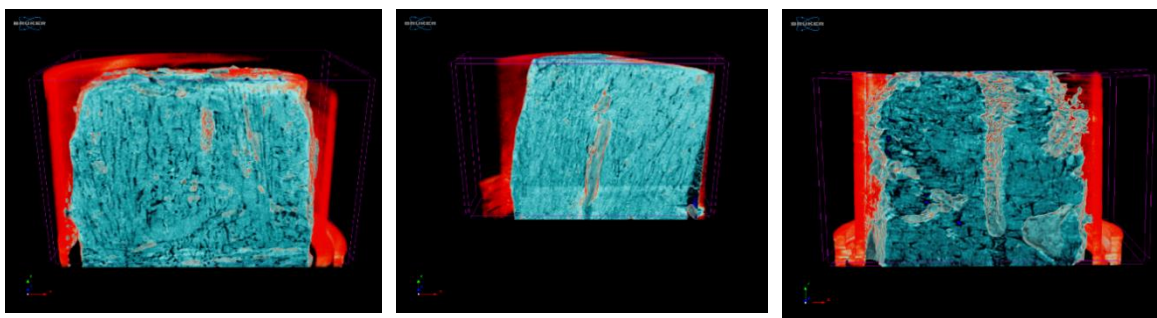


Fig. S2.1 Reconstructed images of core 9 0-2.5 cm (left), core 9 2.5-5 cm (middle), and core 16 0-4 cm (right) showing sliced ensembles in a 3D view. In these images, the air is shown in black, brine is shown in light blue/white, ice is shown in blue, and oil is shown in red. The polypropylene tubes are visible in each image in red, bounding the sample within.

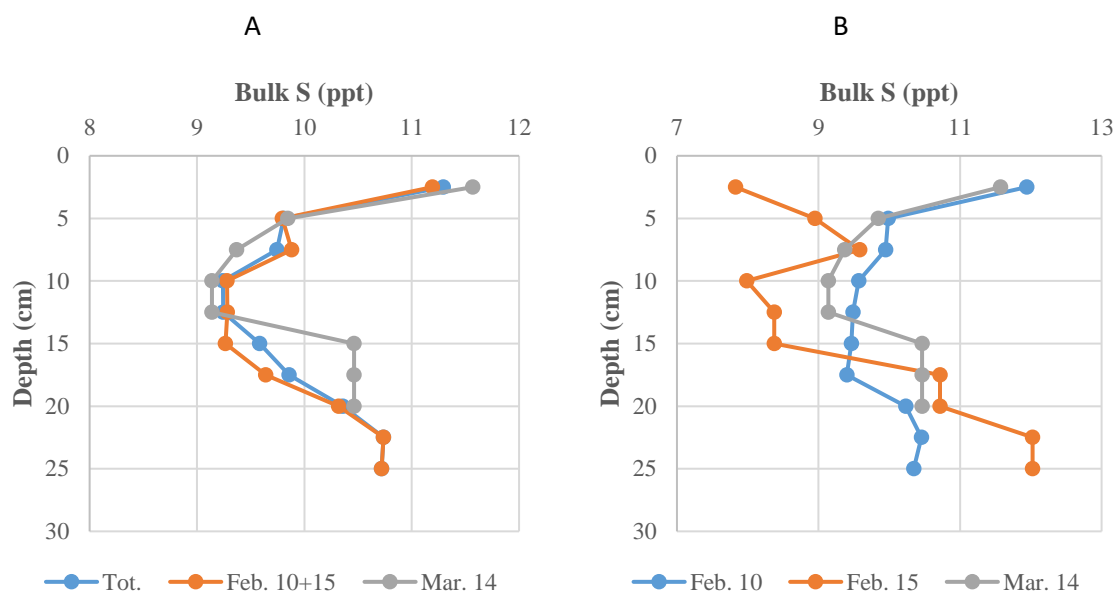


Fig. S2.2 A - Average bulk Salinity Profiles for all the ice cores (Tot.), Phases 1 (Feb. 10 + 15) and Phase 2 (Mar. 14); B - Average bulk Salinity Profiles for the three sampling dates on the right.

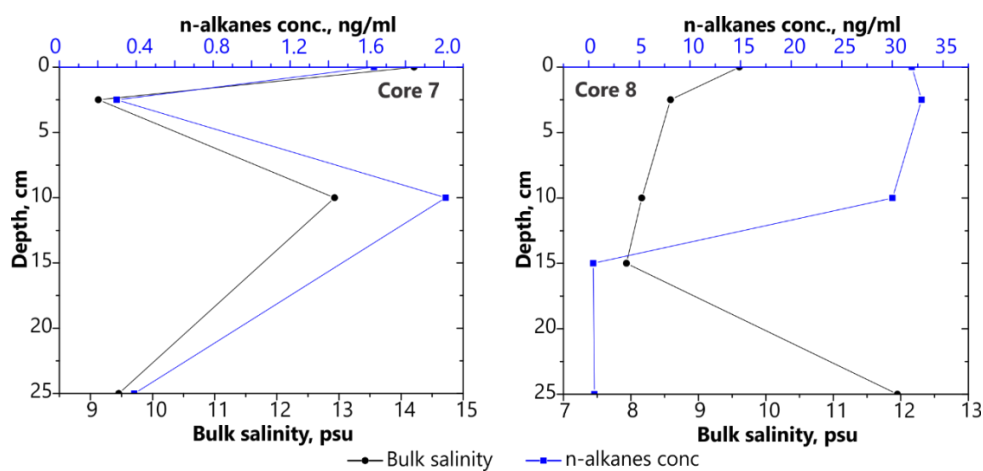


Fig. S2.3 Bulk salinity and n-alkanes concentration distribution profiles for cores #7 and 8. The n-alkanes constitute the majority of the relative oil composition based on GC-MS (Desmond et al., 2019a).

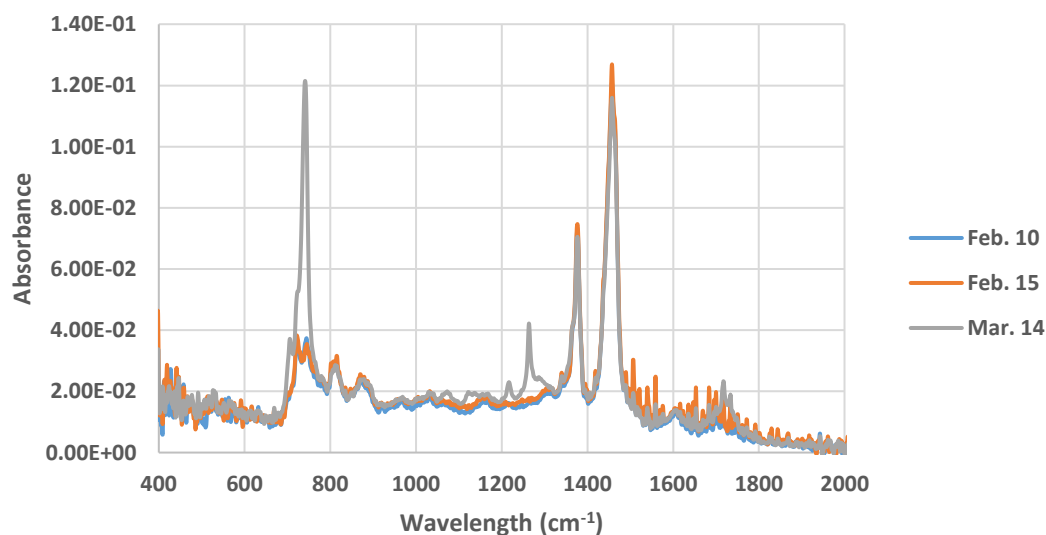


Fig. S2.4 Infrared spectra of a representative set of crude oil samples derived from top sections of sampled ice from the Feb. 10, Feb. 15, and Mar. 14/17 sampling dates.

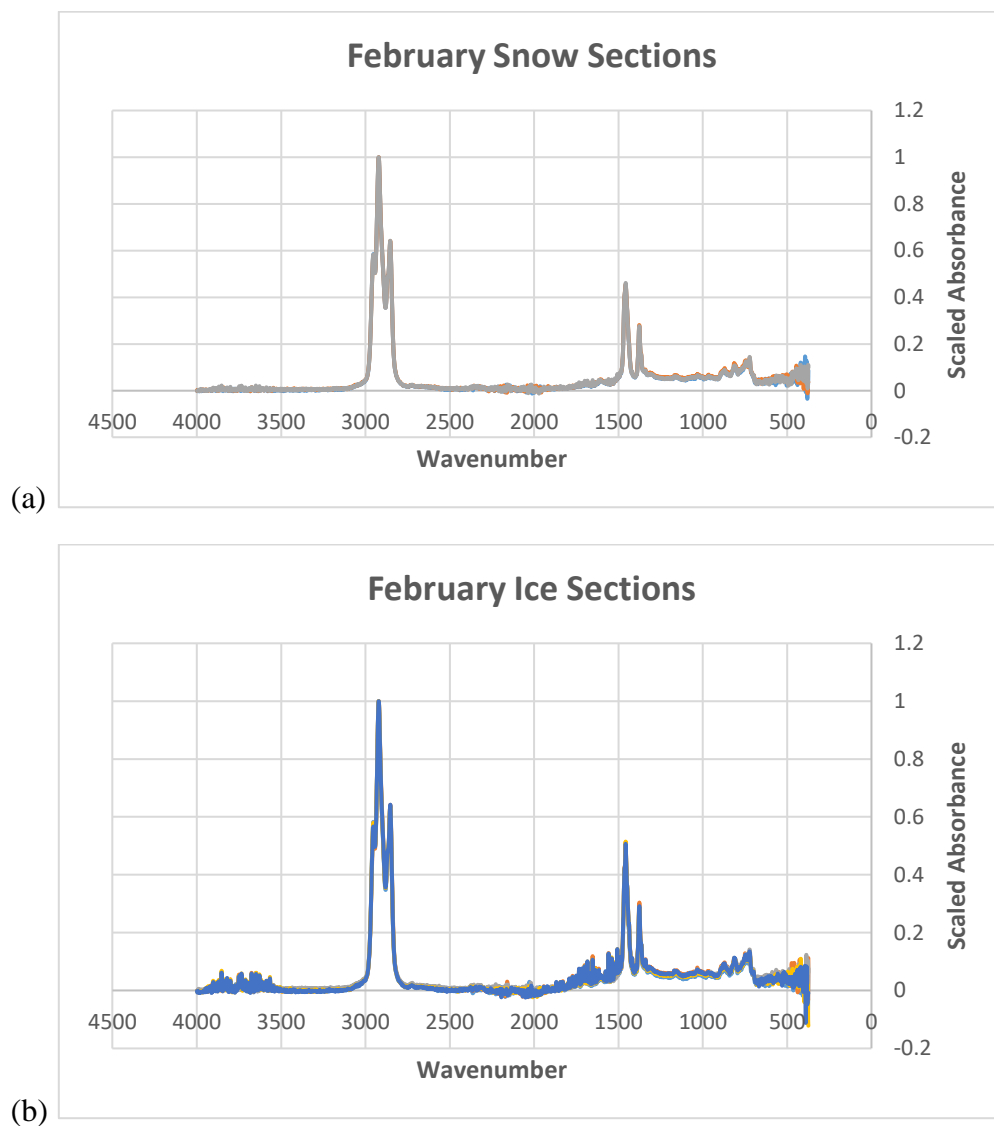


Fig. S3.1 ATR IR Spectra of February (a) snow section and (b) ice section oil Samples

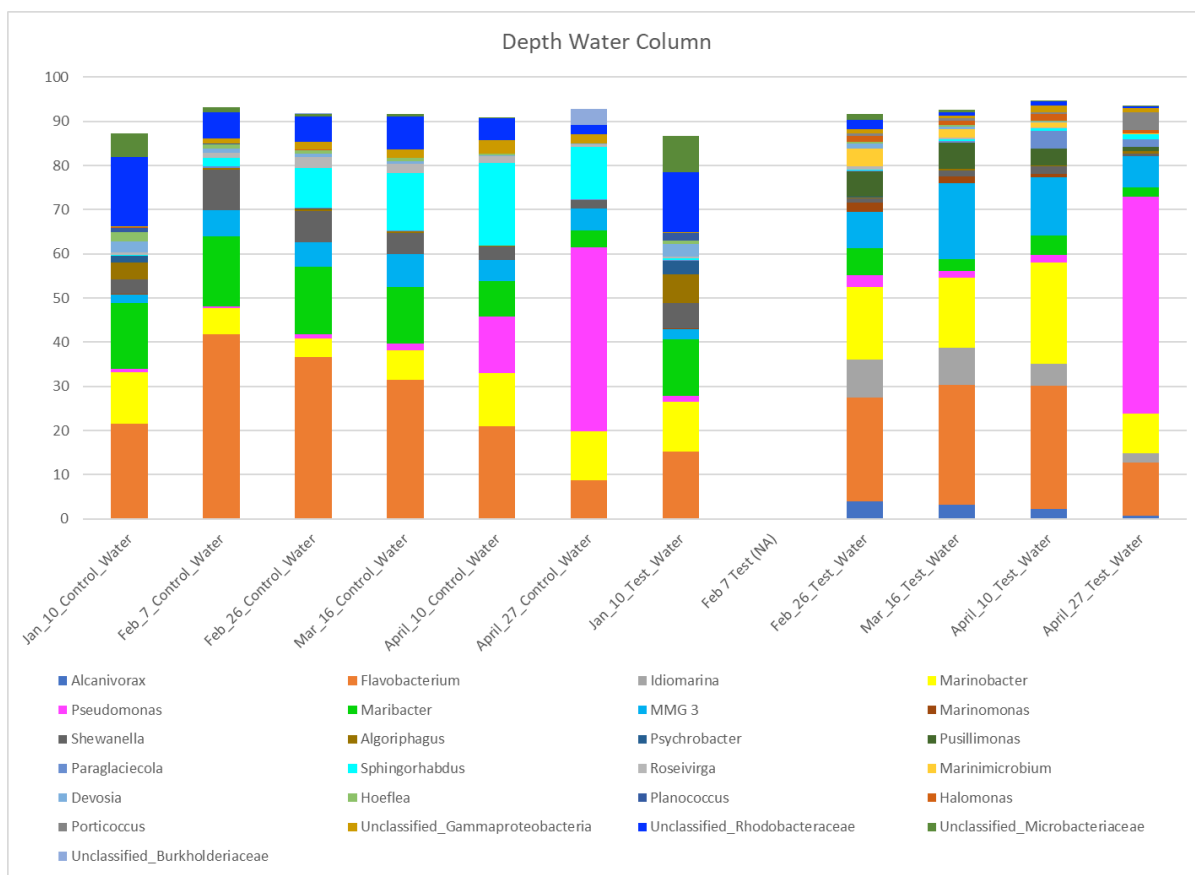


Fig. S4.5 Relative sequence abundance of bacterial lineages at the genus level for the depth water samples throughout the experiment duration. The bars reflect the mean community composition across all samples collected on that sampling date. Genera that never comprised >1% of the microbial community are not shown. MMG3: Marine methylotrophic group 3. In this figure, “Control” corresponds to the Native tank and “Test” corresponds to the Augmented tank.

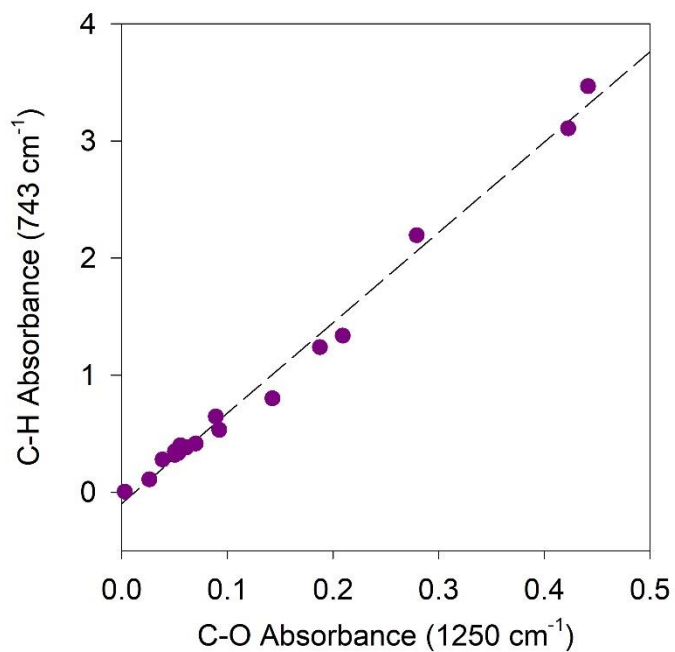


Fig. S4.6 Correlation of the C-H aromatic ring and C-O ether ATR-IR Absorbance bands showing loss of aromaticity due to inclusions of oxygen from photo-oxidation transformation.

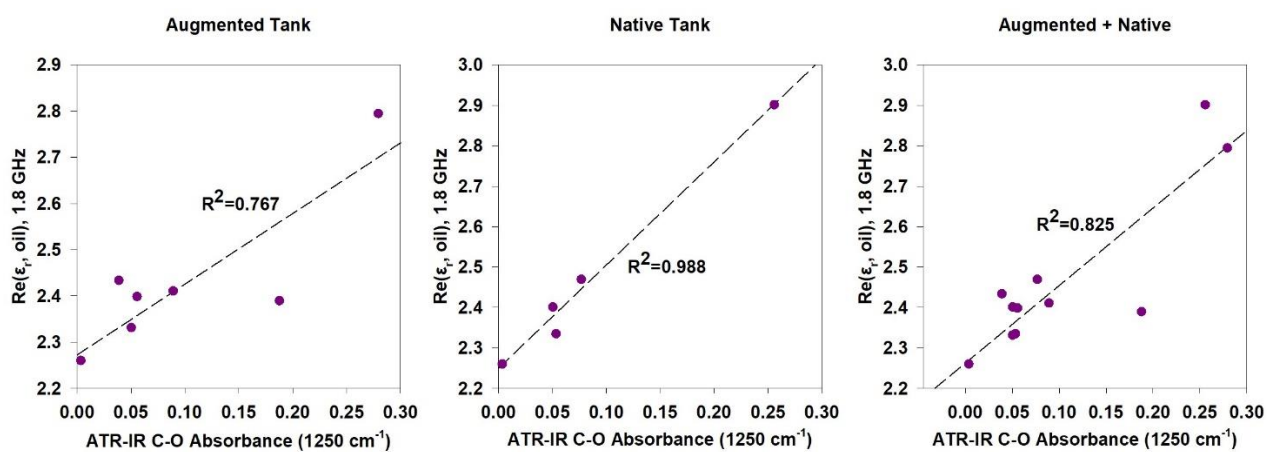


Fig. S4.7 Association between the measured oil dielectric constants (Fig. 4.8) and ATR-IR absorbance of the C-O (1250 cm⁻¹) ether band (Fig. 4.9) for Augmented (left), Native (middle), and combined (right) pools.

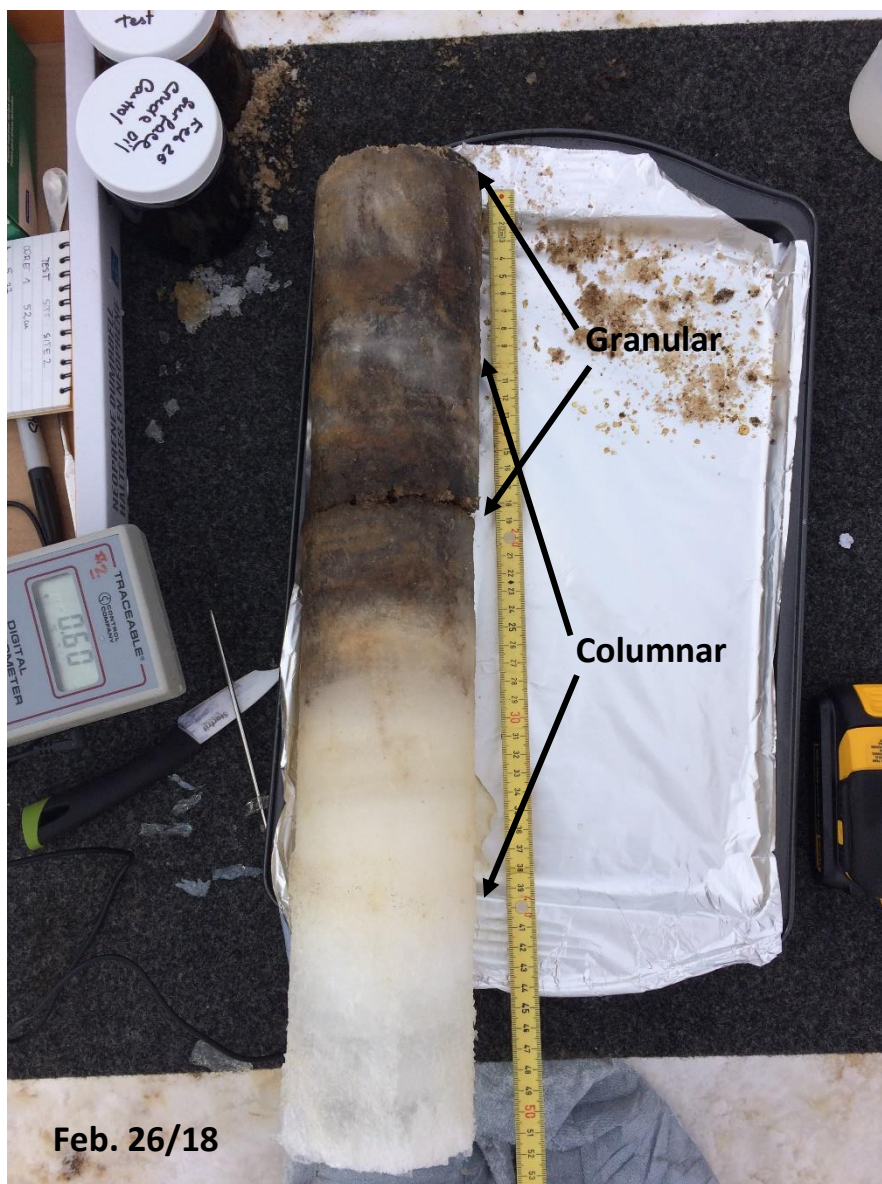


Fig. S5.8 Example photo of a vertical slab of sea ice from an oil-in-ice mesocosm depicting alternating granular and columnar layers (Desmond et al., 2021).

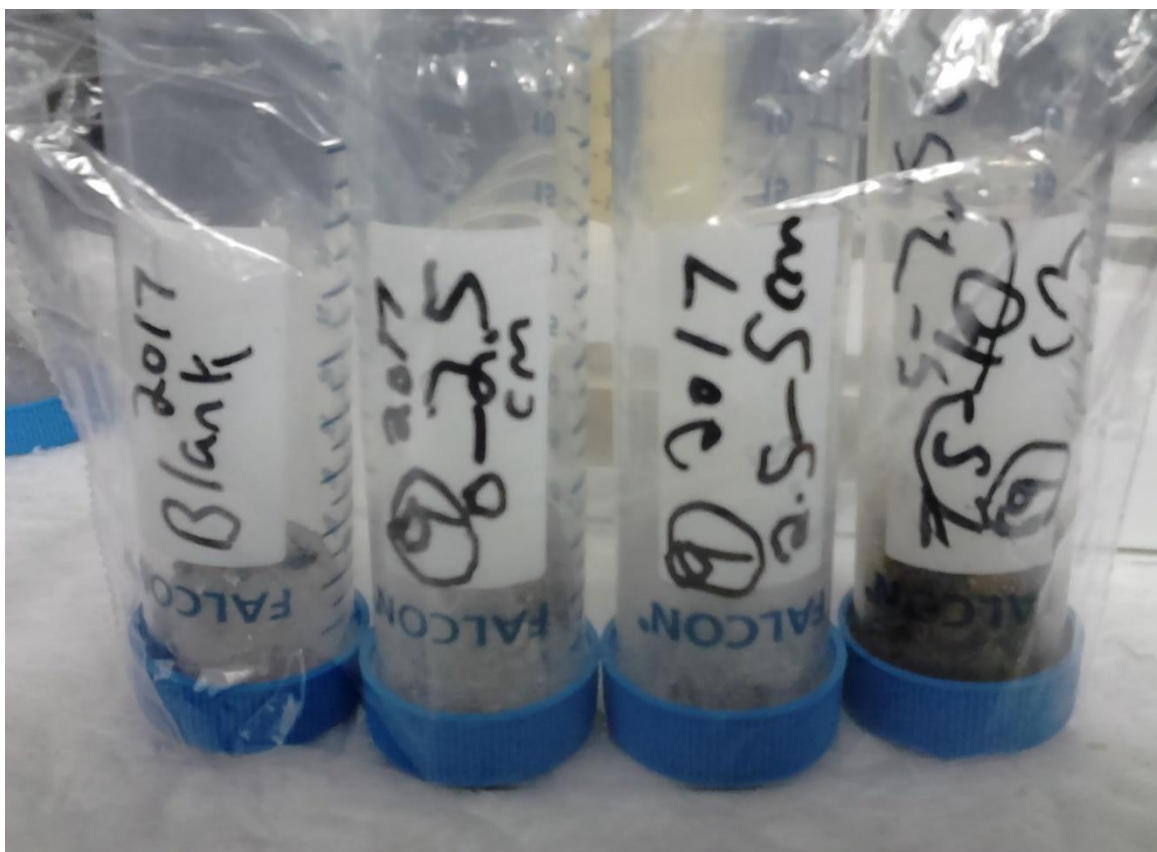
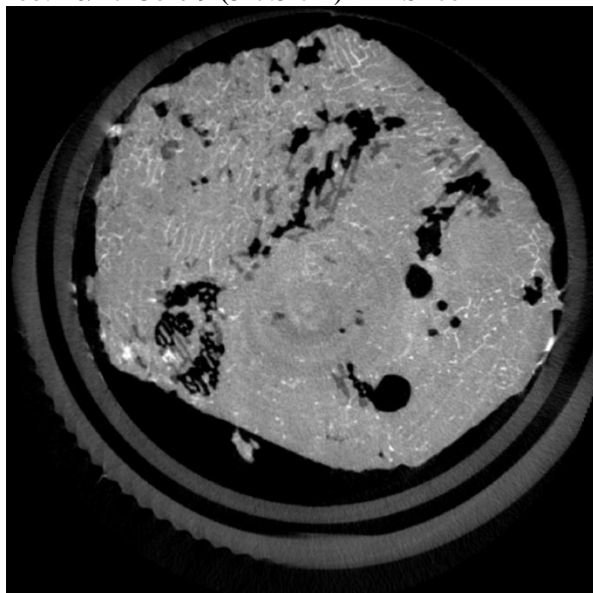


Fig. S5.9 Sub-sectioned X-ray samples placed inside polypropylene Falcon tubes.

Feb. 10/17 Core 9 (5-7.5 cm) XY-Slice 1



Feb. 10/17 Core 9 (5-7.5 cm) XY-Slice 2

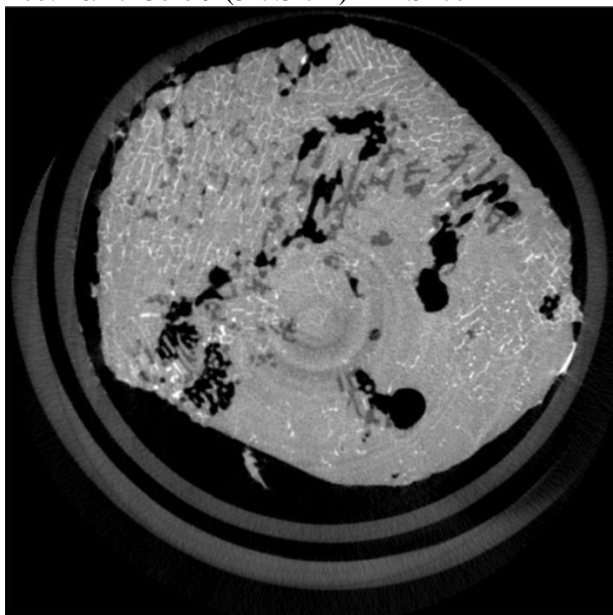
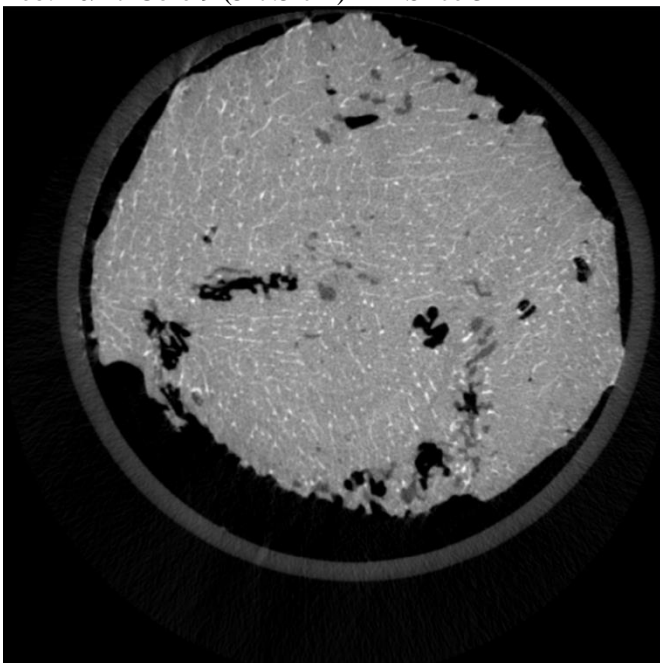


Fig. S5.10 Tomographic grayscale images of horizontal slices (XY-Plane) of a subset of sea ice samples showcasing the oil, air, and brine inclusion distribution. In these images, air is shown in black, brine is shown in white, ice is shown in light grey, and oil is shown in dark grey. The polypropylene tubes (~3 cm OD) are visible in each image in dark grey, bounding the sample within.

Feb. 10/17 Core 9 (5-7.5 cm) XY-Slice 3

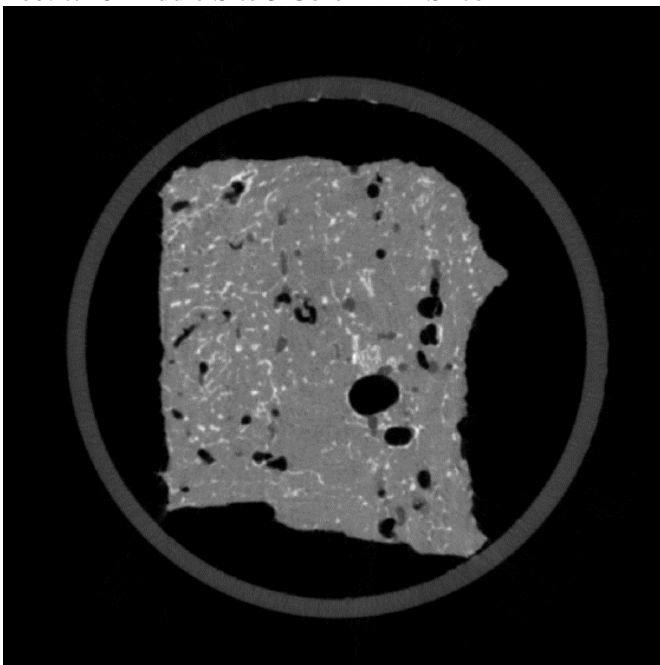


Feb. 7/18 Middle Site 3 Core 1 XY-Slice 1



Fig. S5.3 Continued

Feb. 7/18 Middle Site 3 Core 1 XY-Slice 2



Feb. 7/18 Middle Site 3 Core 1 XY-Slice 3

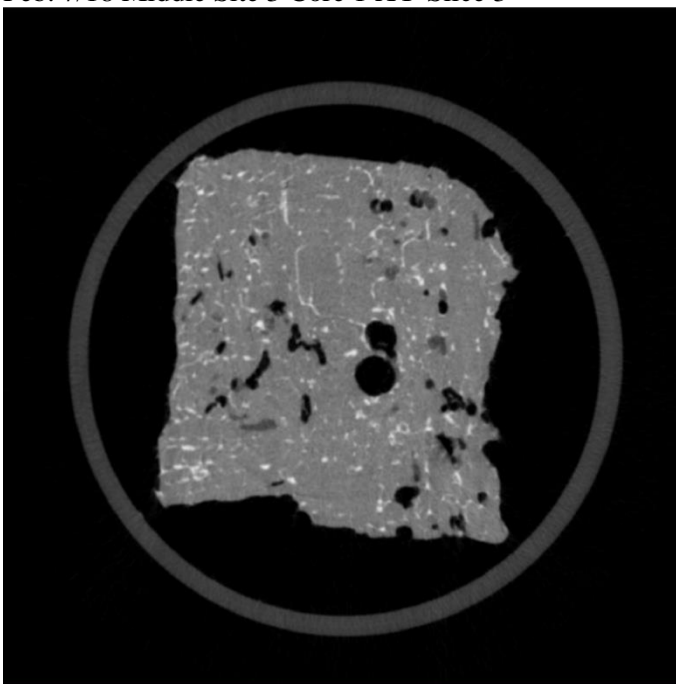
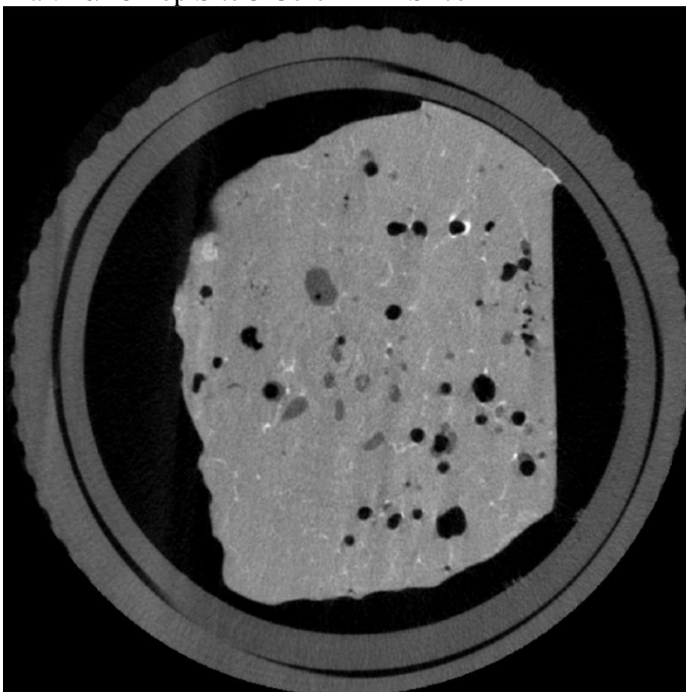


Fig. S5.3 Continued

Mar. 16/18 Top Site 3 Core 2 XY-Slice 1



Mar. 16/18 Top Site 3 Core 2 XY-Slice 2

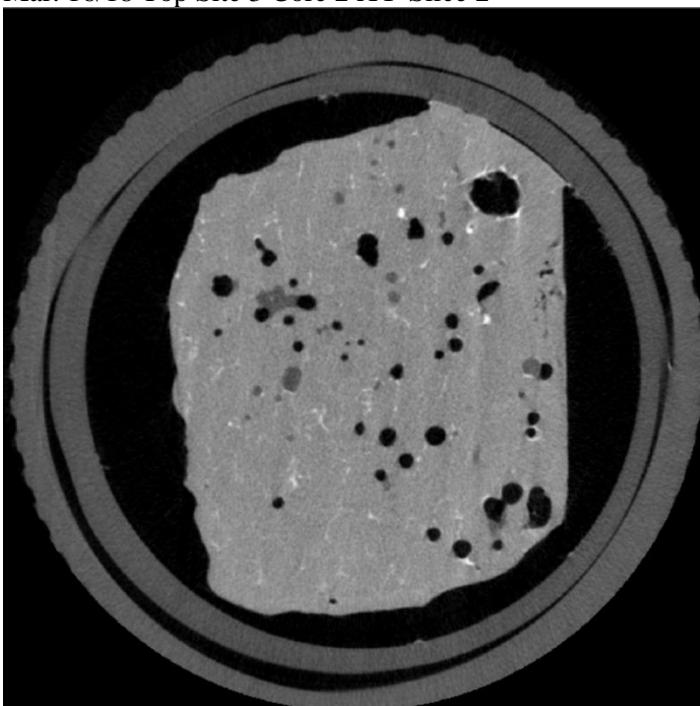


Fig. S5.3 Continued

Mar. 16/18 Top Site 3 Core 2 XY-Slice 3

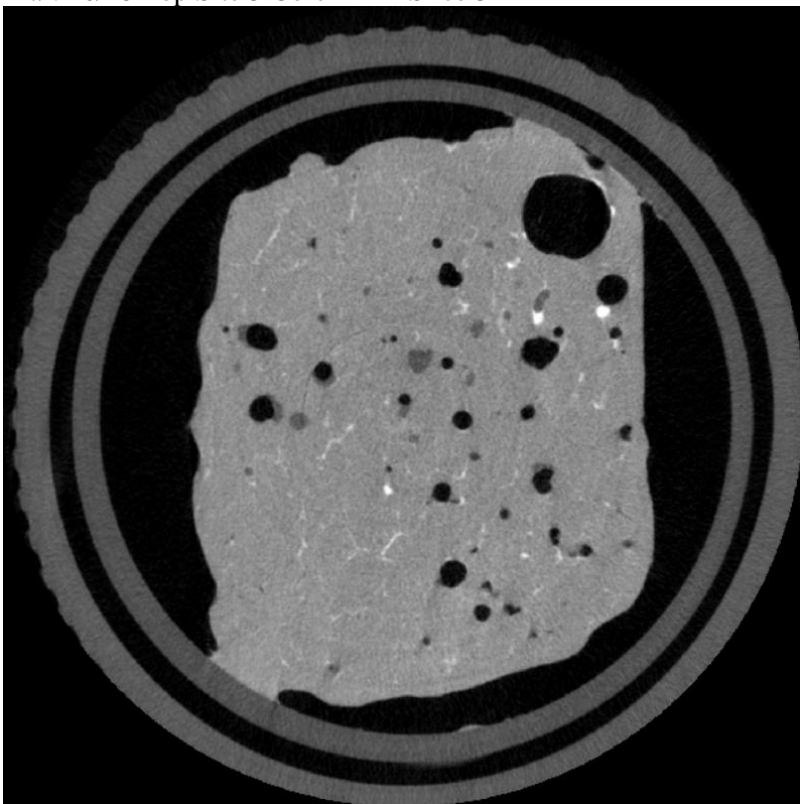


Fig. S5.3 Continued

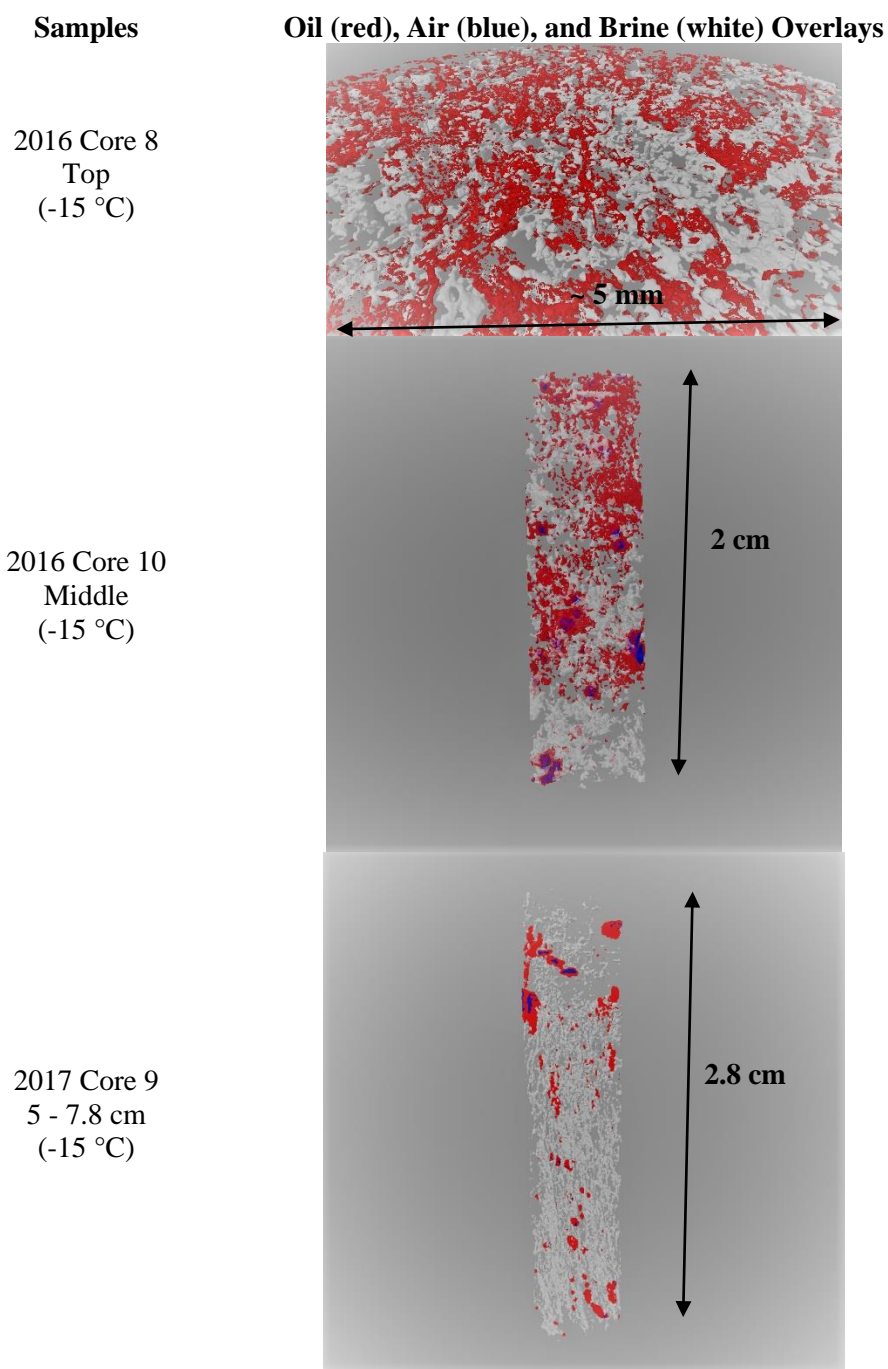
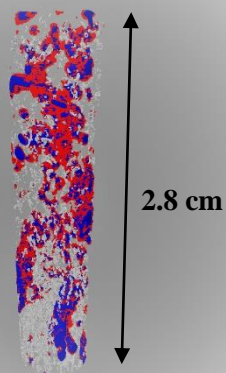
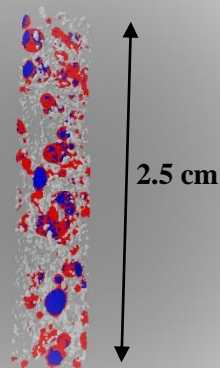


Fig. S5.11 The 3D decomposition of top and middle sections of sea ice cores from SERF 2016-2018 in which oil, air, and brine are represented in red, blue, and white respectively.

2018 Feb. 7
Top S3C1
(-15 °C)



2018 Feb. 7
Middle S3C2
(-15 °C)



2018 Feb. 26
Top S3C3
(-15 °C)

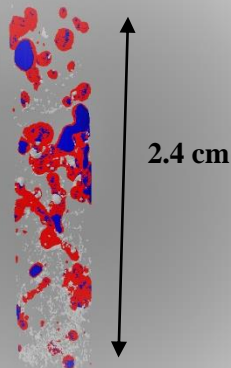
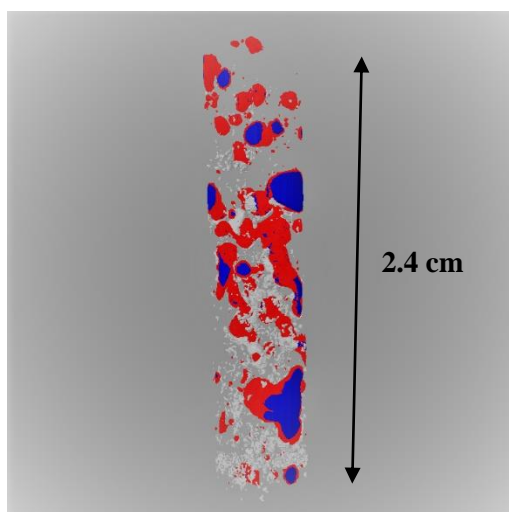
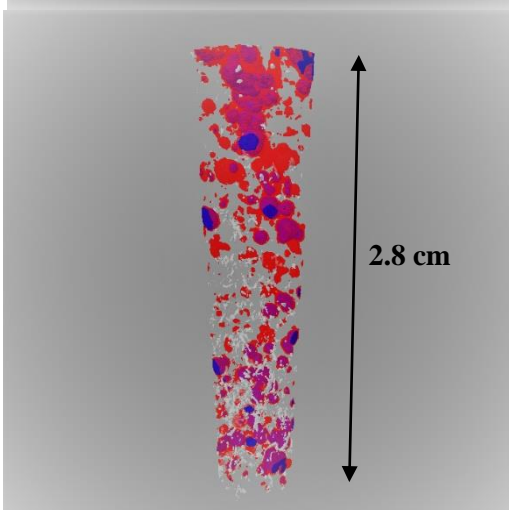


Fig. S4.4 Continued

2018 Feb. 26
Top S3C3
(-10 °C)



2018 Mar. 16
Top S3C2
(-15 °C)



2018 Mar. 16
Top S3C2
(-10 °C)

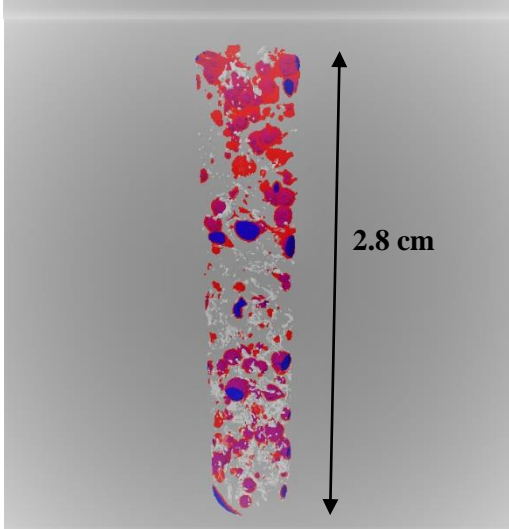
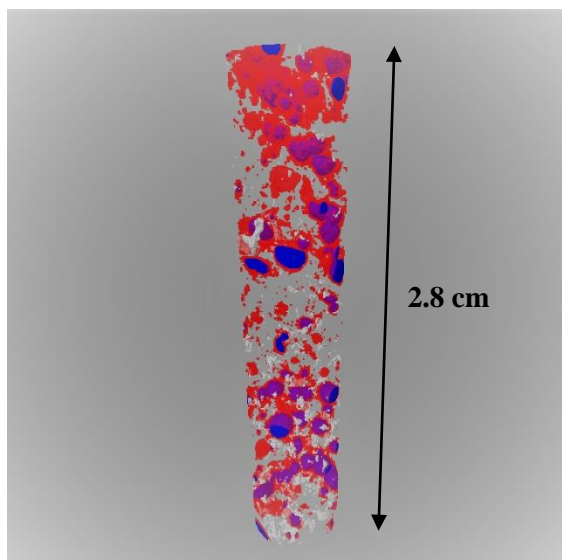


Fig. S4.4 Continued

2018 Mar. 16
Top S3C2
(-6 °C)



2018 Mar. 16
Mid S3C2
(-4.8 °C)

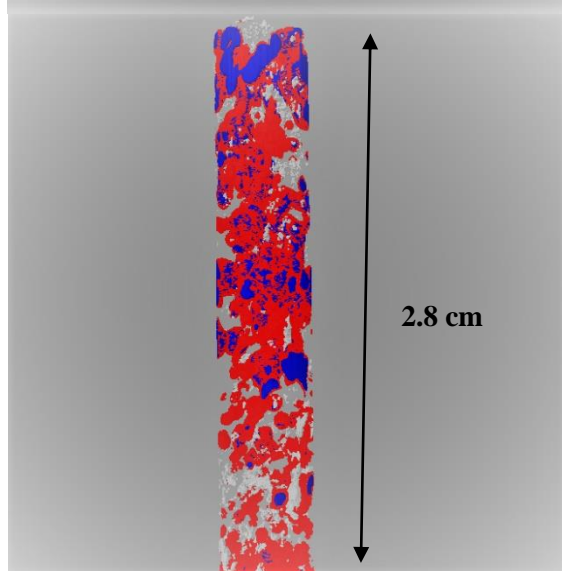


Fig. S4.4 Continued

2018 Mar. 16
Mid S3C2
(-4.8 °C) 2nd

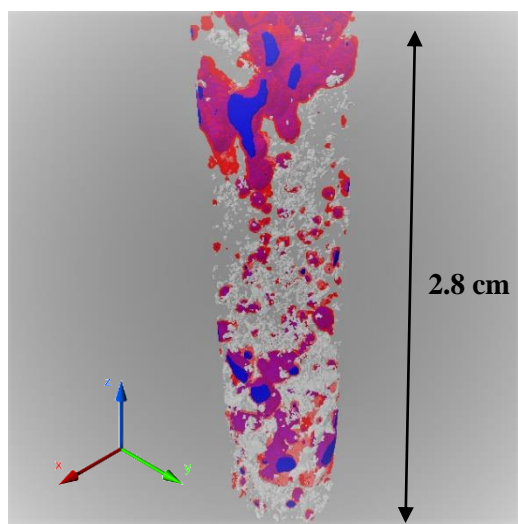


Fig. S4.4 Continued

7.2 Additional Contributions to the Literature

In addition to the manuscripts that comprise Chapters 2 through 5, several refereed journal and conference papers were published throughout the course of the research presented herein. These contributions to the literature are listed below.

Peer-reviewed journal articles:

3. Saltymakova, D., **Desmond, D.S.**, Galley, R., Polcwiartek, K., Neusitzer, T.D., Firoozy, N., Barber, D.G., and Stern, G.A. “The influence of sea-ice conditions on crude oil spill behavior.” *Cold Regions Science and Technology* 221: 104160.
2. Mayvan, M.Z., Asihene, E., **Desmond, D.**, Hicks, L., Polcwiartek, K., Stern, G.A., Isleifson, D., 2024. “Monitoring Diesel Spills in Freezing Seawater under Windy Conditions Using C-Band Polarimetric Radar.” *Remote Sensing* 16: 379.
1. Asihene, E., **Desmond, D.S.**, Harasyn, M.L., Landry, D., Veenaas, C., Mansoori, A., Fuller, M.C., Stern, G., Barber, D.G., Gilmore, C., and Isleifson, D., 2022. “Toward the Detection of Oil Spills in Newly-Formed Sea Ice using C-Band Multi-polarization Radar,” in *IEEE Transactions on Geoscience and Remote Sensing*, doi: 10.1109/TGRS.2021.3123908.

Peer-reviewed conference papers:

8. Saltymakova, D., Smith, A.F., **Desmond, D.S.**, Bautista, M.A., Polcwiartek, K., Snyder, N., Wolfe, T., Hubert, C., and Stern, G. “Biodegradation potential of Arctic microbes in connection with crude oil concentration in sea ice.” To be submitted to 2025 AMOP Technical Seminar.
7. Isleifson, D., Mead, J.B., Fuller, M.C., Hicks, L., **Desmond, D.S.**, Asihene, E., Stern, G.A., Barber, D.G. “A Multi-frequency Suite of Polarimetric Scatterometers for Arctic Remote Sensing.” *Proceedings of the URSI International Symposium on Electromagnetic Theory* 2023, pp, 1-4.
6. **Desmond, D.S.**, J. Xidos, G. Schreckenbach, D.G. Barber, D. Isleifson, and G.A. Stern, Estimation of the Temperature Dependence of the Octanol-Water Partition Coefficient for Select Chlorobenzenes Using Computational Chemistry, *Proceedings of the Forty-fourth AMOP Technical Seminar, Environment and Climate Change Canada, Ottawa, ON, Canada*, pp. 539-552, 2022.

5. Mansoori, A., **Desmond, D.**, Stern, G., Isleifson, D., 2021. "Modeling Normalized Radar Cross-Section of Oil-contaminated Sea Ice with Small Perturbation Method." Proceedings of 19th International Symposium on Antenna Technology and Applied Electromagnetics (ANTEM) & Canadian Radio Science Meeting, pp. 1-2. DOI: <https://doi.org/10.1109/ANTEM51107.2021>

4. Asihene, E., **Desmond, D.S.**, Mansoori, A., Fuller, M.C., Stern, G., Barber, D., Gilmore, C., Isleifson, D., 2021. "C-band Backscatter of Oil-polluted New Sea Ice in a Mesocosm." Proceedings of 19th International Symposium on Antenna Technology and Applied Electromagnetics (ANTEM) & Canadian Radio Science Meeting, pp. 1-2. DOI: <https://doi.org/10.1109/ANTEM51107.2021>

3. Isleifson, D., Komarov, A.S., **Desmond, D.**, Stern, G., Barber, D., 2020. "Modeling Backscatter from Oil-contaminated Sea Ice using a Multi-layered Scattering Method." Proceedings of the 2020 IEEE International Geoscience and Remote Sensing Symposium, pp. 1-2.

2. Mansoori, A., Isleifson, D., **Desmond, D.**, and Stern, G., 2020. "Development of Dielectric Measurement Techniques for Arctic Oil Spill Studies." Proceedings of the 2020 IEEE International Symposium on Antennas and Propagation and North American Radio Science Meeting pp. 1-2.

1. **Desmond, D.S.**, Neusitzer, T.D., Lemes, M., Isleifson, D., Saltymakova, D., Mansoori, A., Barber, D.G., and Stern, G.A., 2019. "Examining the Physical Interactions of Corn Oil (Medium Crude Oil Surrogate) in Sea Ice and its Potential for Chemical Partitioning within an Arctic Environment." Proceedings of the Forty-second AMOP Technical Seminar, Environment and Climate Change Canada, Ottawa, ON, Canada, pp. 66-95.

Peer-reviewed conference presentation abstracts:

9. **Desmond, D.S.**, Saltymakova, D., Smith, A., Wolfe, T., Snyder, N., Polcwiartek, K., Bautista, M., Lemes, M., Hubert, C.R.J., Barber, D.G., Isleifson, D., and Stern, G.A., 2022. Photooxidation and Biodegradation Potential of a Light Crude Oil in First-Year Sea Ice," in Proceedings of the 2022 International Oil Spill Science Conference, Halifax, Nova Scotia, Canada.

8. **Desmond, D.S.**, Saltymakova, D., Smith, A., Wolfe, T., Snyder, N., Polcwiartek, K., Bautista, M., Lemes, M., Hubert, C.R.J., Barber, D.G., Isleifson, D., and Stern, G.A., The potential of crude oil photooxidation and biodegradation in first-year sea ice, Proceedings of the Forty-fourth AMOP Technical Seminar, Environment and Climate Change Canada, Ottawa, ON, Canada.

7. **Desmond, D.S.**, Smith, A., Saltymakova, D., Wolfe, T., Snyder, N., Polcwiartek, K., Lemes, M., Hubert, C., Chavarriaga, M., Ellefson, E., Stone, M., Barber, D.G., Isleifson, D., and Stern, G.A. "Assessing the Potential for Photooxidation and Biodegradation of Crude Oil in Surficial Sea Ice and the Fate of Transformed Products," in Proceedings of the 2020 ArcticNet Annual Scientific Meeting, Online (Virtual).
6. **Desmond, D.S.**, Schreckenbach, G., Xidos, J.D., Saltymakova, D., Isleifson, D., Barber, D.G., and Stern, G.A., 2019. "Methods for Predicting Partitioning and Fate of Petroleum Hydrocarbons and Heterocyclic Compounds in a Sea Ice Environment." Proceedings of the International Symposium on Sea Ice at the Interface, International Glaciological Society, Winnipeg, MB, Canada.
5. Saltymakova, D., **Desmond, D.**, Neusitzer, T., Firoozy, N., Polcwiartek, K., Snyder, N., Barber, D., and Stern, G.A., 2019. "The influence of sea-ice conditions on crude-oil spill behavior." Proceedings of the International Symposium on Sea Ice at the Interface, International Glaciological Society, Winnipeg, MB, Canada.
4. Snyder, N., Wang, F., Ritchie, J., Saltymakova, D., Polcwiartek, K., **Desmond, D.S.**, Smith, A.F., Hubert, C., and Stern, G.A., 2019. "Analysis of heteroatomic species in biodegraded crude oil using electrospray ionization ion mobility time-of-flight high-resolution mass spectrometry." Proceedings of the International Symposium on Sea Ice at the Interface, International Glaciological Society, Winnipeg, MB, Canada.
3. Półcwiartek, K., Saltymakova, D., Snyder, N., **Desmond, D.**, Stern, G.A., and Wang, F., 2019. "Distribution of volatile hydrocarbons within sea ice: a mesocosm study." Proceedings of the International Symposium on Sea Ice at the Interface, International Glaciological Society, Winnipeg, MB, Canada.
2. **Desmond, D.S.**, Neusitzer, T.D., Isleifson, D., Saltymakova, D., Wolfe, T., Polcwiartek, K., Synder, N., Barber, D.G., and Stern, G.A., 2018. "Remote Sensing of Oil Spills in a Sea Ice Environment: Investigations on Oil Composition and Mitigation Potential," in Proceedings of the 2018 ArcticNet Annual Scientific Meeting, Ottawa, ON, CA.
1. **Desmond, D.S.**, Crabeck, O., Lemes, M., Polcwiartek, K., Neusitzer, T.D., Saltymakova, D., Synder, N., Rysgaard, S., Barber, D.G., and Stern, G.A., 2018. "Investigation into the Geometry and Distribution of Oil Inclusions in Sea Ice using non-destructive X-ray Tomography," in Proceedings of the 2018 ArcticNet Annual Scientific Meeting, Ottawa, ON, CA.

Technical reports:

1. Smith, A., Bakker, A., Lavoie, C., Hubert, C., Veenas, C., Greer, C., **Desmond, D.**, Stern, G., Hostetler, G., Schuster, J., Peterson, K., Jantunen, L., Ji, M., Carvalho, P., Cai,

Q., 2019. “R/V William Kennedy Leg 4 Cruise Report (Sep 1-15, 2019): Cruise along the Kivalliq transportation corridor (Hudson Bay),” pp. 1-49.

7.3 Sea Ice and Sea Ice Dielectrics

Sea ice exists in a variety of diverse forms; that is, new ice (frazil, nilas, and pancake), FYI, MYI, drifting pack ice, fast ice (floating and grounded), and icebergs. This diversity is dependent on various thermodynamic and dynamic forces that control the growth, evolution, and decay of sea ice. As a result of this diversity, a given sea ice environment can differ on scales of less than 1 m to 100’s of km’s (Wilkinson et al., 2013). Given the diversity of sea ice types and the heterogeneity of sea ice environments, it is expected that oil will behave and interact differently with each environment. In this section, I will provide a basic/general overview of sea ice formation with an emphasis on factors that can influence sea ice dielectrics.

Seawater with a salinity of 34 has a freezing point temperature of -1.86°C due to the freezing-point depression caused by the dissolved inorganic salts (Eicken, 2003). When seawater freezes, ice crystals form on the surface waters, forming platelets, needles, or spicules, which are intertwined into aggregates known as frazil ice. After further freezing facilitates the consolidation of the frazil ice layer, additional layers of ice termed congelation ice are added to the bottom of the ice sheet through quiescent growth. Vertical sections of grown sea ice consist of granular ice (randomly oriented ice crystals) at the surface (up to a few dm in the Arctic) followed by a frazil transitional layer (composed of ice crystals starting to orient in the vertical) which is underlain by columnar ice (composed

of vertically elongated crystals) that can grow several meters (Eicken, 2003). During the formation of sea ice, dissolved inorganic salts are excluded from the ice crystal lattice in which some of the salt is rejected to the surface of the ice, while the majority drips out the bottom. Because of this process, MYI, which has grown for a longer duration compared to FYI, is much less saline and contains more air pockets. Due to this brine expulsion of salt content to the surface and subsurface of the ice, the bulk salinity of FYI (in particular) resembles a C-shape. Furthermore, in FYI, concentrated salt form brine veins (liquid salty inclusions) within the ice interstices (Thomas and Dieckman, 2010). Given that sea ice temperature decreases towards the ice surface, these brine veins freeze and shrink towards the ice top, thereby increasing/concentrating brine salinity (formulated by Equation 7.1) (Cox and Weeks, 1983; Leppäranta and Manninen, 1988). The brine volume of sea ice is given by Equation 7.2 (Frankenstein and Garner, 1967) and is defined as the volume of liquid salted water present in a given sea ice section. Given that the bottom of sea ice is warmer and has a high bulk salinity, the brine volume (or porosity) is expected to be highest towards the subsurface (Equation 7.2). According to the “rules of fives” (Golden et al., 2007), when the ice temperature is $\geq -5^{\circ}\text{C}$, the bulk salinity is ≥ 5 , and the brine volume (porosity) is $\geq 5\%$, the sea ice is permeable and can exchange fluid thus allowing for the potential uptake and movement of entrained oil through interconnected brine veins (Petrich et al., 2013; Oggier et al., 2020).

$$7.1 \quad S_B = \frac{1}{1 - \left(\frac{54.11}{T}\right)} * 1000$$

$$7.2 \quad \frac{V_B}{V} = 10^{-3} * S * \left(-\frac{49.185}{T} + 0.532\right)$$

where S_B – brine salinity; V_B/V – brine volume fraction; T – temperature; S – bulk salinity.

The incorporation of oil into the sea ice matrix (ice, brine, air) can potentially influence the relative complex permittivity (i.e., dielectrics) of sea ice through both direct and indirect means. Sea ice dielectrics is an important parameter associated with the remote sensing of sea ice by remote sensing technologies such as radar. The term dielectrics is defined by Equation 7.3, comprising both real (ϵ'_r) and imaginary ($j\epsilon''_r$) parts, respectively. The imaginary part is associated with the loss in the system (Chen et al., 2005) and is also related to the conductivity of the material (Neusitzer, 2017). The real part is known as the dielectric constant. The dielectric constant is related to the degree of polarization of the Coulomb force between two-point charges in a dielectric material when applied to an electric field in a particular medium (Knight, 2013). More specifically, the dielectric constant is defined by Equation 7.4 and is the factor by which a dielectric weakens an electric field $E = E_0/\epsilon'_r$, in which E_0 is the external electric field and E is the net electric field due to the superposition of E_0 and E_{induced} . The relative dielectric constant of a particular material is the ratio relative to the dielectric constant of a vacuum. Given that the dielectric constant of a vacuum is 1 (i.e., $E_0=E$), the dielectric constant of a material is then $\epsilon'_r \geq 1$. Materials that are easily polarizable (e.g., water) have higher dielectric constants, whereas less polarizable materials (e.g., oil) have lower dielectric constants (Knight, 2013). Given that sea ice is a heterogeneous material, it consists of several components each with different dielectric constants (i.e., seawater: ~80, snow: ~1 to 2, MYI: ~3, FYI: 3 to 5) (Wang and Stout, 2007); albeit the exact values are frequency, temperature, and salinity dependent (Neusitzer, 2017).

Similarly, the imaginary component of dielectrics also differs for each component of sea ice (Neusitzer, 2017). Therefore, the inclusion of oil ($\epsilon'_r = \sim 2$ to 3) (Wang and Stout, 2007) into the sea ice matrix is expected to perturb the overall sea ice dielectrics (ϵ_{mix}) (Equation 7.5). Equation 7.5 provides a formulated mixture model describing oil-contaminated sea ice dielectrics as a mixture of individual components (air, ice, oil, brine) (Desmond, 2018; Ulaby and Long, 2014) where ϵ denotes the dielectrics of air/ice/oil/brine, and v_{brine} denotes the brine volume fraction defined by Equation 7.2. In simplicity, ϵ_{mix} is a composite of the respective volume fractions and dielectrics of air, ice, oil, and brine. When oil is added to the sea ice matrix, ϵ_{mix} will be changed directly by perturbing the overall average of the sea ice dielectrics, taken as a whole system. However, the extent of this change is relatively negligible considering 1) oil has similar dielectrics to ice and 2) the volume fraction of oil tends to be lowest compared to the other volume fractions (Desmond, 2018) and so does not carry much weight in the sea ice dielectric mixture model. More importantly, when oil is incorporated into the sea ice matrix, it has the potential to alter the brine volume fraction (v_{brine} , Equation 7.5; V_b/V , Equation 7.2) through a change in the temperature and salinity of the ice (Equation 7.2). Therefore, the oil's indirect influence on sea ice thermodynamics (i.e., salinity and temperature) (Payne et al., 1991; O'Sadnick et al., 2017) has more potential to affect the sea ice dielectrics.

$$7.3 \quad \epsilon_r = \epsilon'_r - j\epsilon''_r$$

$$7.4 \quad \epsilon'_r = \frac{E_0}{E}$$

$$7.5 \quad \epsilon_{mix} = \epsilon_{air,ice,oil} + \frac{3v_{brine}\epsilon_{air,ice,oil}(\epsilon_{brine} - \epsilon_{air,ice,oil})}{2\epsilon_{air,ice,oil} + \epsilon_{brine} - v_{brine}(\epsilon_{brine} - \epsilon_{air,ice,oil})}$$

References

- Chen, L.F., Ong, C.K., Neo, C.P., Varadan, V.V., Varada, V.K., 2005. Microwave Electronics: Measurement and Materials Characterization. N.p.: John Wiley & Sons. Ch 6.2 – Cavity Perturbation Method. Print.
- Cox, G., Weeks, W., 1983. “Equations for Determining the Gas and Brine Volumes in Sea-Ice Samples.” *J. Glaciol.* 29 (102): 306–316.
- Desmond, D.S., 2018. “Oil Behavior in Sea Ice: Changes in Chemical Composition and Resultant Effect on the Complex Permittivity (Dielectrics) and Radar Signature of Sea Ice.” University of Manitoba.
- Eicken, H., 2003. “From the microscopic to the macroscopic to the regional scale: Growth, microstructure and properties of sea ice.” Contribution to Thomas D. & G. S. Dieckmann (eds.): SEA ICE - AN INTRODUCTION TO ITS PHYSICS, BIOLOGY , CHEMISTRY AND GEOLOGY, Blackwell Science, London, 2003, pp. 22-81
- Frankenstein, G., Garner, R., 1967. “Equations for determining the brine volume of sea ice from -0.5 to -22.9°C.” *J. Glaciology* 6.48: 943-944.
- Golden, K.M., Eicken, H., Heaton, A.L., Miner, J., Pringle, D.J., Zhu, J., 2007. “Thermal Evolution of Permeability and Microstructure in Sea Ice.” *Geophys. Res. Lett.* 34, 1-13. DOI: 10.1029/2007GL030447
- Knight, R., 2013. “Electricity and Magnetism.” Physics For Scientists And Engineers: A Strategic Approach, 3rd ed., vol. 4, Pearson Education.
- Leppäranta, M., Manninen, T., 1988. “The Brine and Gas Content of Sea Ice With Attention to Low Salinities and High Temperatures.” *Finnish Institute of Marine Research*.
- Neusitzer, T.D, 2017. “On the Dielectric Properties and Normalized Radar Cross-Section of Crude Oil-Contaminated Sea Ice.” University of Manitoba.
- Oggier, M., Eicken, H., Wilkinson, J., Petrich, C., O’Sadnick, M., 2020. “Crude Oil Migration in Sea-Ice: Laboratory Studies of Constraints on Oil Mobilization and Seasonal Evolution.” *Cold Reg. Sci. Technol.* 174, 102924.
- O’Sadnick, M., Petrich, C., Phuong, N.D., 2017. “The Entrainment and Migration of Crude Oil in Sea Ice, the Use of Vegetable Oil as a Substitute, and Other Lessons from Laboratory Experiments.” Proceedings of the 24th International Conference on Port and Ocean Engineering under Arctic Conditions.
- Payne, J.R., McNabb Jr., G.D., Clayton Jr., J.R., 1991. “Oil-weathering behavior in Arctic environments.” *Polar Research* 10(2): 631-662.

Petrich, C., Karlsson, J., Eicken, H., 2013. “Porosity of Growing Sea Ice and Potential for Oil Entrainment.” *Cold Reg. Sci. Technol.* 87: 27-32.

Thomas, D.N.; Dieckmann, G.S. *Sea Ice: An Introduction to its Physics, Chemistry, Biology and Geology*, second edition, Blackwell, 2010.

Ulaby, F.T. and Long, D.G., 2014. *Microwave Radar and Radiometric Remote Sensing*. Ann Arbor, MI, U.S.A.: University of Michigan Press.

Wang, Z., Stout, S.A., 2007. “Oil Spill Remote Sensing: A Forensics Approach.” *Oil Spill Environmental Forensics: Fingerprinting and Source Identification*, Elsevier/Academic Press.

Wilkinson, J., Maksym, T., Hole, W., 2013. “Capabilities for detection of oil spills under sea ice from autonomous underwater vehicles.” *Arctic Response Technology Oil Spill Preparedness, Final Report 5.2*.

7.4 Sea Ice and Oil Interactions

Depending on the season (e.g., fall freeze up, spring/summer thaw), sea ice form (new, broken, old), spill scenario (shipping accident, pipeline breach, well blowout), and oil type/age (light, heavy), spilled oil can either be located on top of, under, or within sea ice (Wilkinson et al., 2013; Wilkinson et al., 2017; Dickins and Buist, 1999; Dickins, 2011). The many possible distributions of oil can complicate oil spill detection and mitigation practices as different remote sensing and mitigation technologies fair differently under different oil-in-ice scenarios (Brandvik et al., 2006; Dickens, 2017; Wilkinson et al., 2017; Wilkinson et al., 2013). In this section, I will provide an overview of oil spill behavior under various ice conditions to gauge when (i.e., season) and in which locations (i.e., on, within, below ice) oil spill detection and mitigation is feasible for a given spill scenario.

Given that the height of shipping activities in the Arctic takes place during summer (Wilkinson et al., 2013; Wilkinson et al., 2017) or early freeze-up (i.e., September) (Pizzolato et al., 2014), the presence of spilled oil from a vessel (e.g., tanker) is expected to be either in the top portion of the sea ice profile or floating on top of open water. That being said, oil drilling outside the traditional summer months has become more feasible owing to a longer open water season (AMAP, 2017), capable vessels, advanced marine technology, and active ice management (Dickins, 2011). Therefore, there is potential for a late-season blowout which can lead to large volumes of oil trapped under, within, or beside sea ice, where it could possibly remain throughout the winter.

In the summer, Arctic regions will experience variable ice cover that can consist of both MYI and FYI (Wilkinson et al., 2013; Wilkinson et al., 2017). Oil spilled from a vessel in these ‘broken ice’ conditions will behave differently depending on the sea ice concentration. Ice concentrations less than 30 or 40% will allow oil to spread as in open water conditions, whereas ice concentrations above 60 or 70% serve as a natural containment limiting the spread of oil (Dickins and Buist, 1999; Venkatesh et al., 1990). If an open water spill is not detected and cleaned-up before fall freeze-up, the oil may become incorporated in pre-existing ice or newly forming ice. One of the major factors which dictate the extent of oil incorporation in porous developing ice forms (frazil, grease, slush) is oil density (Dickins, 2011). A light oil ($<850 \text{ kg/m}^3$) ([Crude Oil Methodology | Alberta Energy Regulator \(aer.ca\)](https://www.aer.ca/en/energy/industry/crude-oil-methodology)) will readily surface through and insert itself within slush and brash ice. On the other hand, a heavy ($\geq 900 \text{ kg/m}^3$ and $< 925 \text{ kg/m}^3$) or ultra-heavy ($\geq 925 \text{ kg/m}^3$) fuel oil is more likely to be suspended within the thick accumulations of slush ice (during freeze-up conditions) and

may end up accumulating in leads (during winter) due to the convergence of pack ice (Dickins, 2011).

If oil is instead released in the water column (at depth), from a pipeline rupture, well blowout, or sunken vessel, the oil will rise (breaking down into small spherical droplets) through the water column (towards the surface) if its density is lower than the surrounding seawater ([Density of Seawater - The Physics Factbook \(hypertextbook.com\)](http://hypertextbook.com/facts/2003/031503.shtml)) (Wilkinson et al., 2013; 2017). If the occurrence of this oil release happens during the summer (near open water), then oil will spread out on the sea surface to the extent governed by the overall ice concentration. If instead, oil is released below ice cover (e.g., winter), the oil will coalesce to form an oil slick on the underside of the ice. While oil viscosity and release rate affect the rate at which oil spreads, the main factor that controls lateral oil movement under the ice is the ice subsurface roughness (Wilkinson et al., 2017). If oil accumulates in significant quantities underneath the ice, the oil will concentrate in areas of thinner ice (i.e., interconnected depressions) (Fingas and Hollebone, 2003; Wilkinson et al., 2013; 2017). Once oil has accumulated on the underside of the ice, it will attempt vertical migration into the sea ice. This migration is limited when the ice is cold ($< 5\text{ }^{\circ}\text{C}$) and is feasible when the ice is warm ($\geq 5\text{ }^{\circ}\text{C}$) and porous ($V_B \geq 5\%$) (Golden et al., 2007).

If oil is present below the ice during the ice growth season (e.g., late fall, mid-winter), then the ice may form a lip around the oil's perimeter before fully encapsulating the oil (NORCOR, 1975), inhibiting any further horizontal spreading (Wilkinson et al., 2013; 2017). This encapsulation process depends on the efficiency of subsurface ice growth, which in turn

depends on the ocean-atmosphere heat flux, and therefore the ice and snow thickness. Therefore, oil encapsulation is more efficient under thin ice, and may not occur at all under thick ice (Wilkinson et al., 2017). It has been reported that new ice will completely encapsulate an oil layer within 12 to 72 hours (NORCOR, 1975; Dickins and Buist, 1981). Come spring/summer, encapsulated oil (or oil located at the ice subsurface) will be able to migrate upward through the ice towards the surface. The rate of this vertical migration is dependent on oil pool thickness (affecting buoyancy), oil viscosity/density (i.e., lighter oil – faster versus heavier oil – slower), ambient air temperature and degree of brine drainage within the ice (a function of internal temperature) (Dickins and Buist, 1999). A competing process of the vertical migration of oil to the surface is the natural melt of the ice surface downwards (which acts to expose the encapsulated oil) (Lewis, 1976; Martin, 1979). However, for a concentrated oil slick underneath ice, vertical migration typically brings most of the oil to the ice surface before surface ablation/melt can expose the formerly encapsulated oil (Dickins and Buist, 1999). Once oil reaches the ice surface, it will either accumulate on the surface of a melt pond or on melting ice. If the ice is still intact, the accumulated oil will spread similarly to how oil spreads on snow or land. The rate of spreading of oil on an ice surface is akin to spreading on the ice's subsurface, and is dependent on the oil's density/viscosity, the rate of oil accumulation, and the surface roughness of the ice. Ultimately, oil spreading on ice is much slower than oil spreading on water, and therefore can accumulate thicker oil slicks (Dickins and Buist, 1999).

7.4.1 References

AMAP, 2017. Snow, Water, Ice and Permafrost in the Arctic (SWIPA) 2017. Arctic Monitoring and Assessment Programme (AMAP), Oslo, Norway. xiv + 269 pp.

Brandvik, P.J., Sørheim, K.R., Singsass, I., Reed, M., 2006. “Short state-of-the-art report on oil spills in ice-infested waters. Final” Report no.: 1. SINTEF Materials and Chemistry, Marine Environmental Technology.

Dickins, D., Buist, I., 1981. Oil and gas under sea ice. Prepared by Dome Petroleum Ltd for COOSRA, Report CV-1, Vols I and II.

Dickins, D.F., 2011. “Behavior of Oil Spills in Ice and Implications for Arctic Spill Response.” Offshore Technology Conference.

Dickins, D.F., 2017. “Arctic Oil Spill Response Technology Joint Industry Programme Synthesis Report.” Arctic Response Technology, Oil Spill Preparedness.

Dickins, D.F., Buist, I., 1999. “Countermeasures for ice covered waters.” *Pure Appl. Chem.* 71(1): 173-191.

Fingas, M.F., Hollebone, B.P., 2003. “Review of behaviour of oil in freezing environments.” *Marine Pollution Bulletin* 47(9-12): 333-340.

Lewis, E.L. 1976. OIL IN SEA ICE Institute of Ocean Sciences, Patricia Bay, 1976, 26 pp.

Martin, S., 1979. “A field study of brine drainage and oil entrainment in first-year sea ice.” *Journal of Glaciology* 22: 473–502.

NORCOR Engineering and Research Ltd. (1975), The interaction of crude oil with arctic sea ice. Beaufort Sea Technical Report, No. 27, Beaufort Sea Project, Department of the Environment, Victoria, BC, pp. 201.

Pizzolato, L., Stephen E.L., Derksen, C., Dawson, J., Copland, L., 2014. “Changing sea ice conditions and marine transportation activity in Canadian Arctic waters between 1990 and 2012.” *Climatic Change* 123: 161-173.

Venkatesh, S., El-Tahan, H., Comfort, G., Abdelnour, R., 1990. “Modelling the Behavior of Oil Spills in Ice- infested Water.” *Atmosphere-Ocean* 28(3): 303-329.

Wilkinson, J., Beegle-Krause, C.J., Evers, K.-U., Hughes, N., Lewis, A., Reed, M., Wadhams, P., 2017. “Oil spill response capabilities and technologies for ice-covered Arctic marine waters: A review of recent developments and established practices”. *Ambio* 46(Suppl. 3): S423–S441.

Wilkinson, J., Maksym, T., Hole, W., 2013. “Capabilities for detection of oil spills under sea ice from autonomous underwater vehicles.” Arctic Response Technology Oil Spill Preparedness, Final Report 5.2.

7.5 Sea Ice and Oil Weathering

In this section I will describe some of the oil weathering processes applicable to cold regions and will also discuss the resultant impacts made to the oil’s physical properties (density, dielectrics), which can influence oil behavior and remote sensing detection. For example, changes in oil density can influence the buoyancy of the oil and therefore influence the location of oil in a sea ice environment (e.g., surfaced or sunken), thus affecting applicable remote sensing technologies for detecting oil.

The extent of oil weathering is season dependent. Oil spilled during freeze-up conditions (i.e., fall) may accumulate amongst broken ice or become incorporated in the top portion of newly forming ice (Dickins, 2011). Under these two scenarios, oil can undergo evaporation, dissolution, emulsification (i.e., water-in-oil), natural dispersion, photooxidation, and biodegradation. However, the major weathering process that occurs at this time is evaporation (Dickins and Buist, 1999). Freezing temperatures imply low water and air temperatures which serve to lower the rate of evaporation, dissolution, and biodegradation (AMAP, 2010; Dickins, 2011). Furthermore, the presence of ice significantly dampens wave movement, reducing the rates of emulsification and natural dispersion. Lastly, the presence of snow on ice acts to further limit the evaporation of oil on or within the ice (Dickins, 2011).

As the season transitions from fall to winter, oil will be encased by the growing ice sheet with little to no opportunity for evaporation or natural weathering (Wilkinson et al., 2013; Dickins and Buist, 1999; Dickins and Buist, 1981). However, while the oil is encapsulated, there is the potential for water-soluble compounds to dissolve in the brine and be released into the ocean during ice growth (Wilkinson et al., 2017; Faksness and Brandvik, 2008). Given the “polar night” conditions of winter, photooxidation of the encapsulated oil would be negligible. Biodegradation of the bulk oil within the ice would also be limited as there is a smaller active microbial population in sea ice compared to seawater (Vergeynst et al., 2019). Moreover, biodegradation of the bulk oil-in-ice may not be feasible due to a low brine-oil contact inherent to ice, which would limit the ability for microbes to interact and degrade oil (Desmond et al., 2021). If the oil was instead spilled in the midst of winter, oil may not be encapsulated within ice, but may instead be trapped under ice or in leads. Oil below thick ice will not evaporate, and the absence of any significant wave action (or mixing energy) will hinder emulsification and dispersion. Dissolution of the oil’s water-soluble compounds would, however, be feasible as the oil would then be in direct contact with the water column. Similarly, biodegradation of oil would be feasible under ice due to the direct contact with the underlying seawater. Oil present in a lead will undergo evaporation, as the oil would then be exposed to the atmosphere; however, the rate of evaporation would be dependent on the ambient temperature and the degree of oil thickness (Dickins, 2011).

Come spring/summer melt, oil trapped within or under ice is exposed to the ice surface through either the ice’s brine channel system or melting of the ice’s surface downwards (Fingas and Hollebone, 2003; Wilkinson et al., 2013; Dickins and Buist, 1999). Due to the

reduced weathering that occurs during winter, oil tends to surface close to a “fresh” state (Dickins and Buist, 1999), at which time evaporation, dissolution, photooxidation, and biodegradation can all occur while the oil floats either on melt ponds or surfaces on top of intact ice. Given the warmer conditions and the direct exposure to the atmosphere, sunlight, and seawater, summer is the season in which weathering is most prevalent.

As oil weathers, its chemical composition, and therefore its physical properties (Desmond, 2018; Fingas, 2011), will be altered. The overall density of an oil mixture can be described by a weighted average of its individual constituents (API Technical Data Book, 2016). Therefore, as compounds are lost (by evaporation and dissolution) or transformed (by photooxidation and biodegradation), the overall density of the oil mixture will resultantly change. Evaporation and dissolution results in the loss of volatile and water-soluble compounds, respectively. Typically, these losses comprise of low molecular weight compounds of low carbon number; however, aromatics are more water-soluble (Nicodem et al., 1997) than paraffins (which are more volatile) for a given carbon number. Depending on what compounds are lost, the density may either increase or decrease. Aromatics as well as nitrogen, sulfur, and oxygen (NSO) species have higher densities than paraffins ([Hydrocarbons, Linear Alcohols and Acids - Densities \(engineeringtoolbox.com\)](https://www.engineeringtoolbox.com/hydrocarbons-linear-alcohols-acids-densities-d_1429.html)), and so losses of these more polar constituents can act to reduce the oil’s density. In contrast, losses of paraffins typically act to increase the oil’s density. Given that evaporation leads to more significant losses compared to dissolution (Stout and Wang, 2016), the overall density of oil typically increases. This is especially true of open water conditions (National Academies of Sciences, 2016). Similar to evaporation, the weathering processes of photooxidation and

biodegradation result in an overall increase in the oil's density through the conversion of compounds to oxidized products (Vergeynst et al., 2019; AMAP, 2010). Given that weathering of oil is most applicable to the spring/summer, an overall increase in density is expected over time as the oil ages. Depending on the weathering severity, some oil may sink warranting it undetectable by surface remote sensing technologies.

Similar to oil density, the dielectrics of oil (Equation 7.3) is related to the oil's chemical composition. In fact, the oil dielectric constant (ϵ'_r) is directly proportional to oil density (Panuganti et al., 2016). Specifically, the dielectric constant (real part of dielectrics) of oil is related to the density, age, and weathering of the oil, while the imaginary term (ϵ''_r) is related to the conductivity of the oil (and therefore its aromatic, metal, and asphaltene content) (Alvarez et al., 2021). While the dielectrics of oil is not directly measured with remote sensing technologies, it is a governing factor of active microwave measurements as regards oil-contaminated sea ice (Firoozy et al., 2018) through its dependence on sea ice dielectrics (Equation 5). However, a change in the dielectrics of oil by weathering is not expected to impact the dielectrics of sea ice appreciably given the similar dielectrics of oil to ice and the low volume fraction of oil (as discussed in Appendix Section 7.3). Therefore, a change in the oil's dielectrics may not make a substantial difference to oil detection in ice.

7.5.1 References

AMAP, 2010. AMAP Assessment 2007: oil and gas activities in the arctic — effects and potential effects. Arctic Monitoring & Assessment Programme, Oslo, vols. 1 and 2.

Alvarez, J.O., Jacobi, D., Althaus, S., Elias, S., 2021. "Dielectric characterization of geochemical properties of liquid hydrocarbons from 25 °C to 125 °C." *Fuel* 288: 119679.

API Technical Data Book, 2016. "Density", 10th ed., The American Petroleum Institute and EPCON International.

Desmond, D.S., 2018. "Oil Behavior in Sea Ice: Changes in Chemical Composition and Resultant Effect on the Complex Permittivity (Dielectrics) and Radar Signature of Sea Ice." University of Manitoba.

Desmond, D.S., Crabeck, O., Lemes, M., Harasyn, M.L., Mansoori, A., Saltymakova, D., Fuller, M.C., Rysgaard, S., Barber, D.G., Isleifson, D., Stern, G.A., 2021. "Investigation into the geometry and distribution of oil inclusions in sea ice using non-destructive X-ray microtomography and its implications for remote sensing and mitigation potential." *Marine Pollution Bulletin* 173: 112996. DOI: <https://doi.org/10.1016/j.marpolbul.2021.112996>

Dickins, D., Buist, I., 1981. Oil and gas under sea ice. Prepared by Dome Petroleum Ltd for COOSRA, Report CV-1, Vols I and II.

Dickins, D.F., 2011. "Behavior of Oil Spills in Ice and Implications for Arctic Spill Response." Offshore Technology Conference.

Dickins, D.F., Buist, I., 1999. "Countermeasures for ice covered waters." *Pure Appl. Chem.* 71(1): 173-191.

Faksness, L., Brandvik, P., 2008. "Distribution of water soluble compounds from Arctic marine oil spills A combined laboratory and field study." *Cold Regions Science and Technology* 54: 97–105.

Fingas, M., 2011. Introduction to Spill Modeling. In: Fingas, M. (Ed.), *Oil Spill Science and Technology*. Elsevier, New York, pp. 187-200.

Fingas, M.F. and Hollebone, B.P., 2003. "Review of behaviour of oil in freezing environments." *Marine Pollution Bulletin* 47(9-12): 333-340.

Firoozy, N., Neusitzer, T., Chirkova, D., Desmond, D., Lemes, M., Landy, J., Mojabi, P., Rysgaard, S., Stern, G., and Barber, D.G., 2018. "A Controlled Experiment on Oil Release Beneath Thin Sea Ice and its Electromagnetic Detection." *IEEE Transactions on Geoscience and Remote Sensing* 56(8): 4406-4419.

National Academies of Sciences, Engineering, and Medicine. 2016. *Spills of Diluted Bitumen from Pipelines: A Comparative Study of Environmental Fate, Effects, and Response*. Washington, DC: The National Academies Press.

Nicodem, D.E., Fernandes, M.C.X., Guedes, C.L.B., and Correa, R.J., 1997. "Photochemical processes and the environmental impact of petroleum spills." *Biogeochem.* 39: 121-138.

Panuganti, S.R., Wang, F., Chapman, W.G., Vargas, F.M., 2016. “A Simple Method for Estimation of Dielectric Constants and Polarizabilities of Nonpolar and Slightly Polar Hydrocarbons.” *Int. J. Thermophys.* 37: 75. <https://doi.org/10.1007/s10765-016-2075-8>

Stout, S.A., Wang, Z., 2016. “Chemical fingerprinting methods and factors affecting petroleum fingerprints in the environment”, in *Standard Handbook Oil Spill Environmental Forensics: Fingerprinting and Source Identification*, Chap. 3, S. Stout and Z. Wang (2nd ed.), Elsevier/Academic Press.

Vergeynst, L., Christensen, J.H., Kjeldsen, K.U., Meire, L., Boone, W., Malmquist, L.M.V., Rysgaard, S., 2019. “In situ biodegradation, photooxidation and dissolution of petroleum compounds in Arctic seawater and sea ice.” *Water Res.* 148: 459–468.

Wilkinson, J., Beegle-Krause, C.J., Evers, K.-U., Hughes, N., Lewis, A., Reed, M., Wadhams, P., 2017. “Oil spill response capabilities and technologies for ice-covered Arctic marine waters: A review of recent developments and established practices”. *Ambio* 46(Suppl. 3): S423–S441.

Wilkinson, J., Maksym, T., Hole, W., 2013. “Capabilities for detection of oil spills under sea ice from autonomous underwater vehicles.” *Arctic Response Technology Oil Spill Preparedness*, Final Report 5.2.

7.6 Radar

Radar systems actively transmit pulses of microwave energy (between 1 mm to 1 m) towards an object (or area of interest) and records the strength and origin of reflections (or scattering) within the system’s field of view (Lillesand and Kiefer, 2015). The transmitted and received pulses are typically linearly polarized, in which the radio frequency signals are rapidly switched between vertical (V) and horizontal (H) polarization ([Dual polarization radar - Radartutorial](#)). Depending on the orientation of the transmitted and received signal, possible (transmitted)(received) polarizations include HH, VV, VH, and HV. A radar system that is capable of all four polarizations is termed fully polarimetric ([RADARSAT-2 - eoPortal Directory - Satellite Missions](#)). The main advantage of radar

systems is that they are not prone to atmospheric scattering, and are capable of “seeing” at night and through clouds, fog, haze, light rain, snow, and smoke (Fingas, and Brown, 2016; Lillesand and Kiefer, 2015). Another unique feature of radar systems is that the inherent microwave reflections of earth materials do not resemble their counterpart reflections in the thermal (IR) and visible portions of the electromagnetic spectrum, thus providing a different “view” of the environment. For instance, surfaces that appear “rough” in the visible part of the spectrum may appear “smooth” by microwaves (Lillesand and Kiefer, 2015).

Radar systems can either be ground based (e.g., scatterometer on a ship), mounted on an aircraft or unmanned aerial vehicle (UAV), or spaceborne (e.g., RADARSAT-2) ([RADARSAT-2 - eoPortal Directory - Satellite Missions](#)). Furthermore, radar systems may produce either (or both) images (i.e., qualitative information) or/and quantitative information such as the normalized radar cross-section (NRCS) (discussed later in this section). For instance, RADARSAT-2 is a fully polarimetric synthetic aperture radar (SAR), capable of high resolution (3-100 m) through the synthesis of a “very long antenna”, and is capable of both imaging and the measurement of NRCS ([RADARSAT-2 - eoPortal Directory - Satellite Missions](#); Zhang et al., 2011). On the other hand, scatterometers are typically not capable of imaging. However, scatterometers are fully polarimetric and are capable of measuring not only the NRCS, but also the full scattering matrix, allowing calculation of the covariance matrix, coherency matrix, and muller matrix (Ulaby and Long, 2014; Asihene et al., submitted).

There are many factors that can affect the remote sensing signal of radar systems; three

of which are incidence angle, surface roughness, and frequency/wavelength. For instance, a downward-looking radar (such as an altimeter) receives a strong signal when the surface is relatively smooth. On the other hand, a “smooth” surface results in specular reflection for a monostatic side looking radar, causing no (or little) signal to be received by the sensor.

However, if the surface is instead “rough”, the transmitted signal from a side looking radar will create a diffuse scattering pattern, in which an increased amount of backscattered energy makes its way back to the monostatic radar. Therefore, a “smooth” surface is optimal for a radar altimeter, and a “rough” surface is optimal for a side looking monostatic radar (Berg et al., 2016). In the Arctic, sea ice features can vary on scales less than a meter (Wilkinson et al., 2013) causing variability in surface roughness. Consequently, a single optimal incidence angle does not exist and will be dependent on a particular setting.

Another property that can affect the degree of diffuse versus specular reflection for a given surface roughness is frequency (or wavelength) (Lillesand and Kiefer, 2015). For instance, higher frequency (or lower wavelength) radar systems can “sense” more fine details/features on the surface. Therefore, a surface can appear “rougher” to a X-band (7.0–11.2 GHz) radar system compared to a L-band (1-2 GHz) system. Other notable operational frequencies of radar systems include C-band (4 to 8 GHz) and Ku-band (12-18 GHz).

The NRCS is defined by Equations 7.6 and 7.7. Radar cross section (σ) is given by Equation 7.6 and is directly proportional to π – mathematical constant, r – observation distance from the target in meters, and S_r – scattered power density at the receiving site in W/m^2 . Conversely, σ is inversely proportional to S_t – power density of the transmitter at the

radar target in W/m^2 ([Radar Cross-Section - Radartutorial](#)). The NRCS in dB is then given by Equation 7.7 in which σ is normalized by the radar's illumination area (A) (Berg et al., 2016). The NRCS of sea ice is dependent on many factors, including incidence angle, surface roughness, frequency/wavelength, sea ice dielectrics, and penetration depth (Fung et al., 2002; Ulaby and Long, 2014); of which the first three factors have been previously discussed. As discussed in Appendix Section 7.3 and 7.5, the dielectrics of oil-contaminated sea ice can exhibit a complicated dielectric behavior owing to its heterogeneous nature (oil, ice, air, salt and brine pockets). Most notably, the sea ice dielectrics (Equation 7.5) varies with changes in salinity and temperature (Equation 7.2). Additional factors that influence the sea ice dielectrics are the shape, size, and orientation of brine inclusions, as well as the frequency and polarization of the incident wave. In general, as the sea ice dielectrics decreases, so does the NRCS (Saltymakova et al., 2020; Ulaby and Long, 2014). A formulation of the penetration depth (δ_p) in meters for a given remote sensing signal is given by Equations 7.8 and 7.9 and assumes that $\epsilon''_r \ll \epsilon'_r$ (Ulaby and Long, 2014). The penetration depth of sea ice is dependent on the real and imaginary components of sea ice dielectrics (ϵ'_r and ϵ''_r), as well as k_0 – wave number in free space defined by Equation 10, in which λ_0 is the free-space wavelength in meters. Therefore, sea ice that is lossy (high ϵ''_r) will result in a lower penetration depth. For instance, a brine-wetted sea ice surface will dissipate much of the electromagnetic signal. Similarly, a remote sensing signal with a small wavelength (λ_0) (or high frequency) will also result in a lower penetration depth. For instance, Ku-band (~ 17 GHz) is better at surface detections of oil on the ice surface owing to its lower penetration depth and better discernment of surface

features. On the other hand, L-band (~1 GHz) is capable of detecting oil within and under newly formed ice (up to ~10 cm depending on brine content). C-band (~5.5 GHz) has the benefit of both extremes and may be suitable for detecting oil within 1-5 cm of newly formed sea ice (Firoozy et al., 2018; Asihene et al., 2022). Given the larger penetration depth of C- and L-band frequencies, these bands have the potential to ascertain the oil thickness of encapsulated oil or oil pooled underneath ice through inversion (Firoozy et al., 2018; Asihene et al., 2024).

$$7.6 \quad \sigma = (4 * \pi * r^2 * S_r) / S_t$$

$$7.7 \quad \sigma_0 = \sigma / A$$

$$7.8 \quad \delta_p = \frac{\sqrt{\epsilon'_r}}{k_0 \epsilon''_r}$$

$$7.9 \quad k_0 = \frac{2\pi}{\lambda_0}$$

7.6.1 References

Asihene, E., Desmond, D.S., Harasyn, M.L., Landry, D., Veenaas, C., Mansoori, A., Fuller, M.C., Stern, G., Barber, D.G., Gilmore, C., and Isleifson, D., 2022. "Toward the Detection of Oil Spills in Newly-Formed Sea Ice using C-Band Multi-polarization Radar," in *IEEE Transactions on Geoscience and Remote Sensing* 60: 1-15.

Asihene, E., Komarov, A.S., Stern, G., Gilmore, C., Isleifson, D., 2024. "Towards the Estimation of Oil Slick Thickness on Newly Formed Sea Ice using C-Band Radar Backscatter." *IEEE Transaction Geoscience Remote Sensing* 62: 1-15.

Berg, A., Carvajal, G., Eriksson, L., Haas, R., and Hobiger, T., 2016. "Sensing Planet Earth - Water and Ice (edX)." Chalmers University of Technology, Web.

Fingas, M., Brown, C.E., 2016. "Oil spill remote sensing: a forensics approach "Standard Handbook Oil Spill Environmental Forensics Fingerprinting and Source Identification." Ottawa, Ontario. Print. Ch 21.

Firoozy, N., Neusitzer, T., Chirkova, D., Desmond, D., Lemes, M., Landy, J., Mojabi, P., Rysgaard, S., Stern, G., Barber, D.G., 2018. "A Controlled Experiment on Oil

Release Beneath Thin Sea Ice and its Electromagnetic Detection." *IEEE Transactions on Geoscience and Remote Sensing* 56(8): 4406-4419.

Fung, A.K., Liu, W.Y., Chen, K.S., Tsay, M.K., 2002. "An Improved Iem Model for Bistatic Scattering From Rough Surfaces." *J. Electromagn. Waves Appl.* 16: 689–702.

Lillesand, T.M., Kiefer, R.W., Chipman, J.W., 2015. "Remote Sensing And Image Interpretation." WILEY, 7th Edition.

Saltymakova, D., Desmond, D.S., Isleifson, D., Firoozy, N., Neusitzer, T.D., Xu, Z., Lemes, M., Barber, D.G., and Stern, G.A., 2020. "Effect of dissolution, evaporation, and photooxidation on crude oil chemical composition, dielectric properties and its radar signature in the Arctic environment." *Marine Pollution Bulletin* 151: 110629.

Ulaby, F.T. and Long, D.G., 2014. Microwave Radar and Radiometric Remote Sensing. Ann Arbor, MI, U.S.A.: University of Michigan Press.

Wilkinson, J., Maksym, T., Hole, W., 2013. "Capabilities for detection of oil spills under sea ice from autonomous underwater vehicles." Arctic Response Technology Oil Spill Preparedness, Final Report 5.2.

Zhang, B., Perrie, W., He, Y., 2011. "Wind speed retrieval from RADARSAT-2 quad-polarization images using a new polarization ratio model." *Journal of Geophysical Research Oceans* 116, C08008, doi:10.1029/2010JC006522, 2011C080081of13

7.7 Instrumentation for Oil Analysis

There are many devices or types of instrumentation (e.g., chromatography, spectrometry, spectroscopy, cavity perturbation) that can probe information on the chemical composition and the physical properties (e.g., dielectrics) of an oil sample under investigation. Advantages and disadvantages exist for each technique in terms of what specific information can be obtained and what cannot be, due to limitations. For example, gas chromatography is suitable for characterizing the composition of thermally labile constituents of a sample (i.e., non-polar compounds), while the chromatographic technique of liquid chromatography is suited to analyze polar constituents that are not readily volatile. Chromatographic techniques

are limited in their ability to analyze only a fraction of a complex mixture such as oil, while infrared spectroscopy can investigate the bulk composition of a complex mixture but cannot necessarily identify individual compounds as a chromatographic technique is capable of doing. Hence, to complement each individual technique and to provide a more thorough analysis, various instruments can be utilized in conjunction with one another. Furthermore, the coupling of instruments in tandem can offer favourable advantages such as high-resolution separations. In the following, a brief description of gas chromatography, mass spectrometry, infrared spectroscopy, X-ray microtomography, and cavity-perturbation is provided.

7.7.1 Gas Chromatography

Gas-liquid chromatography (GC) is a column chromatography separation method in which a sample under investigation is dissolved in a mobile gaseous phase that is forced under pressure through a liquid stationary phase, fixed in place inside a column. The components of a sample are first vaporized and injected into the head of the column where an inert mobile phase transports the analyte through the column. The sample components partition and distribute themselves inside the column based on affinity with the stationary phase. Sample components that are strongly retained by the stationary phase move more slowly through the column and elute through the end of the column to a detector later than components that interact weakly with the stationary phase. Based on the separation of the sample components, and their migration rates to the detector, discrete bands are formed which can be analyzed qualitatively or quantitatively (Skoog et al., 2007a). Each band may

represent an individual sample component (compound) or a combination of compounds in the case of coelution.

For complex mixtures such as oil, which contain 1000s of compounds, considerable coelution is likely, due to the great chemical diversity of oil and the lack of resolving power of a one-dimensional chromatographic method. Multidimensional separation can be achieved through the coupling of two gas chromatograms (GC X GC). The use of two chromatographic columns with different selectivity coupled by a modulator allows for increased separation. The modulator collects the eluent from the first GC column and periodically injects the collected eluent into the second GC column (Nelson et al., 2016). Even further separation can be achieved through the additional coupling of a mass spectrometer.

7.7.2 Mass Spectrometry

A mass spectrometer provides information on the elemental composition and the molecular structures contained within an organic sample (Skoog et al., 2007b). In short, a compound is ionized using an ionization method. The ionized molecules are then separated by their mass/charge (m/z) ratio using an ion separation method. Each respective m/z ratio is tallied, and a m/z histogram is created (Silverstein et al., 2005a). In what follows, a short description on the ionization method “electron-impact” and the ion separation methods “quadrupole mass spectrometer” and “time-of-flight mass spectrometer” will be provided.

7.7.2.1 *Electron-Impact Ionization*

Electron impact (EI) ionization is a gas-phase ionization method which requires thermally stable compounds with boiling points less than ~ 500 °C and a minimum vapor pressure of ca. 10^{-6} Torr. EI is a hard ionization technique in which the sample is raised to a

temperature sufficient to produce vapor phase molecules which are then bombarded with a beam of high-energy electrons (typically 70 eV), emitted from either a tungsten or rhenium filament. The collision between analyte molecules and the high-energy electrons results in electron ejection of the analyte molecules, producing radical cations, also known as molecular ions. Because the ionization potential of most organic molecules is less than 15 eV, the resultant molecular ions are left with excess energy (≥ 50 eV) from the electron bombardment, leaving them in a highly excited energy state. The molecular ions then relax through the rupturing of covalent bonds, which contain bond strengths between 3 and 10 eV. The created fragment ions possess m/z ratios less than the molecular ion (Skoog et al., 2007b; Silverstein et al., 2005a).

7.7.2.2 *Mass Analyzers*

The purpose of a mass analyzer is to separate ions, with different m/z ratios, created during the ionization of analyte molecules. A mass analyzer should be able to distinguish between small mass differences so that an accurate m/z spectrum is produced. There are many different types of mass analyzers, but only a general overview on the function of the quadrupole mass spectrometer and time-of-flight mass spectrometer will be given in the following.

7.7.2.2.1 *Quadrupole Mass Spectrometer*

A quadrupole mass spectrometer is composed of four cylindrical rods, each of length 100-200 mm. Each rod is mounted parallel to one another in a square-like fashion, located at the corners of what would be a square, forming a “tunnel” for ions to pass through. Ions enter the center of the “square” or “tunnel” at one end of the rods and are then filtered through the

tuning of the quadrupole. The quadrupole acts as a tunable mass filter through the application of a constant DC voltage, modified by a radio frequency voltage. Different combinations of the DC voltage and modified voltage are applied to the rods at appropriate frequencies. Ions with a specific m/z ratio pass all the way through the quadrupole to the detector, while all other ions travel unstable trajectories either colliding with one of the rods or falling outside the quadrupole. This filtering is applied to the entire mass range in less than 1 second to produce an entire m/z spectrum (Silverstein et al., 2005a).

7.7.2.2.2 *Time-of-Flight Mass Spectrometer*

The concept of time-of-flight (TOF) is as follows. Ions are accelerated through a TOF drift tube to a detector by an electric field potential of 10^3 to 10^4 V. Ions are separated by mass during their travel through the drift tube. Under the assumption that all ions entering the drift tube have the same kinetic energy ($zeV = mv^2/2$), ions differing in mass will have a velocity given by $v = (\frac{2zeV}{m})^{1/2}$, where z – atomic charge, eV – electron volt, m – mass, and v – velocity. Given the drift tube length L , the TOF for an ion is defined by $t = \sqrt{L^2m/2ZeV}$, whereby heavier ions arrive at the detector later than lighter ones (Skoog et al., 2007b; Silverstein et al., 2005a).

7.7.3 Infrared Spectroscopy

The electromagnetic spectrum's infrared (IR) region lies between the visible and microwave regions, ranging from $10,000$ to 100 cm^{-1} . In particular, the IR region between 4000 and 400 cm^{-1} has the most practical value to the typical organic chemist. When an organic molecule absorbs IR radiation, it is converted into energy in the form of molecular

vibrations. In an IR spectrum, this absorption appears in the form of bands (and not lines), despite being quantized, as rotational bands accompany each vibrational energy change. Along the x-axis of an IR spectrum, vibrational band positions are represented by wavenumbers (cm^{-1}) given by $\bar{\nu} (\text{cm}^{-1}) = \frac{1}{\lambda(\mu\text{m})} * 10^4 \left(\frac{\mu\text{m}}{\text{cm}} \right) = \frac{\nu(\text{Hz})}{c \left(\frac{\text{cm}}{\text{s}} \right)}$, where λ is wavelength, ν is frequency, and c is the speed of light in vacuum. Along the y-axis, band intensities can either be expressed as transmittance (T) or absorbance (A). Transmittance is defined as the transmitted radiant power through a given sample divided by the incident radiant power. Absorbance is related to transmittance by $A = \log_{10} \left(\frac{1}{T} \right)$. An infrared spectrum for a sample can be obtained by the process of Fourier Transform, as explained in the following (Silverstein et al., 2005b).

7.7.3.1 *Fourier Transform Infrared Spectrometer (Interferometer)*

A Fourier Transform Infrared (FTIR) Spectrometer splits the incoming IR source radiation into two beams. One beam is maintained at a fixed length with the use of a fixed mirror and the second beam is of variable length by use of a movable mirror. By adjusting the position of the movable mirror in a smooth and continuous fashion, an interferogram is created through the varied path lengths of the two beams. Fourier transform converts each resultant interference pattern at successive points from the time domain to the frequency domain. The complete IR spectrum is created through the successive variation of the movable mirror, and subsequent Fourier transform of each respective interference pattern (Silverstein et al., 2005b).

7.7.4 X-ray Microtomography

X-rays are high frequency (or short wavelength) electromagnetic radiation within the wavelength range of 10^{-5} and 100 \AA (Skoog et al., 2007c). An X-ray microtomography (μ -CT) instrument uses X-rays to create a series of two-dimensional (2D) slices of a sample which are then used to reconstruct a three-dimensional (3D) representation of the sample. In short, μ -CT is a non-destructive radiographic imaging technique capable of characterizing the microstructure of a sample at high resolution (micrometer resolution as its name implies). The sample is rotated about a single axis during an X-ray scan while the X-ray source and detector remain stationary. While the sample rotates, 2D cross-sectional images are recorded and used to create a 3D digital image. Based on the relationship between X-ray absorption and material density, a sample's internal structure can be observed (Landis and Keane, 2010). For instance, for a heterogeneous sample such as oil-contaminated sea ice, X-ray μ -CT can differentiate between oil, air, and brine inclusions and that of the sample's ice background.

7.7.5 Dielectrics

An insulating material becomes polarized within an external electric field, producing an excess positive charge on one surface and an excess negative charge on the other. In the case of an insulator, this polarization is due to a slight charge separation in the atoms creating induced dipoles. The term *dielectric* stems from the creation of *two* sheets of induced *electric* charge. Hence the prefix *di*, meaning two. The dielectric constant is defined as the factor by which a dielectric weakens an electric field under vacuum, given by $k = \frac{E_0}{E} \geq 1$, where E_0 and E are the electric fields under vacuum and with dielectric, respectively (Knight, 2013). Materials that are more easily polarized have larger dielectric constants compared to less

easily polarized materials (Knight, 2013). There are various methods for calculating the dielectrics of a material (Chen et al., 2004a). Resonant-perturbation is one such technique.

7.7.5.1 *Resonant-perturbation: Cavity-perturbation Method*

Cavity-perturbation (or material-perturbation) is a resonant-perturbation technique commonly used to infer the electromagnetic properties of dielectrics (i.e., complex permittivity) of low-loss materials (e.g., oil). Compared to non-resonant methods, the cavity-perturbation technique is known to possess a higher accuracy and sensitivity. The cavity-perturbation method works as follows. A sample under investigation is inserted into the electric or magnetic field inside a cavity resonator, thus perturbing the cavity's resonant frequency and quality factor. The dielectrics of the sample can then be calculated from this change of resonant frequency and quality factor (Chen et al., 2004b). Notable requirements for this technique include 1) that a small volume of material (<1 mL) be used in the study, and 2) that the size of material inserted into the cavity must be small enough so as not to disturb the formation of the standing wave inside the cavity (Mansoori et al., 2020).

7.7.6 References

Chen, L.F., Ong, C.K., Neo, C.P., Varadan, V.V., Varadan, V.K., 2004a. Microwave Theory and Techniques for Materials Characterization. *Microwave Electronics: Measurement and Materials Characterization* (pp. 37–139). Chapter, John Wiley & Sons, Ltd.

Chen, L.F., Ong, C.K., Neo, C.P., Varadan, V.V., Varadan, V.K., 2004b. Resonant-perturbation Methods. *Microwave Electronics: Measurement and Materials Characterization* (pp. 250–287). Chapter, John Wiley & Sons, Ltd.

Landis, E.N., Keane, D.T., 2010. “X-ray microtomography.” *Materials Characterization* 61: 1305-1316

Mansoori, A., Isleifson, D., Desmond, D., Stern, G., 2020. "Development of Dielectric Measurement Techniques for Arctic Oil Spill Studies." *Proceedings of the 2020 IEEE International Symposium on Antennas and Propagation and North American Radio Science Meeting* pp. 1-2.

Nelson, R.K., Aeppli, C., Samuel, J., Chen, H., de Oliveira, A.H.B., Eiserbeck, C., Frysinger, G.S., Gaines, R.B., Grice, K., Gros, J., Hall, G.J., Koolen, H.H.F., Lemkau, K.L., McKenna, A.M., Reddy, C.M., Rodgers, R.P., Swarthout, R.F., Valentine, D.L., White, H.K., Stout, S.A., and Wang, Z., 2016. Applications of comprehensive two dimensional gas chromatography (GC X GC) in studying the source, transport, and fate of petroleum hydrocarbons in the environment. *Standard Handbook Oil Spill Environmental Forensics: Fingerprinting and Source Identification* (Second, pp. 398–448). Chapter, Academic Press.

Knight, R., 2013. "Electricity and Magnetism." *Physics For Scientists And Engineers: A Strategic Approach*, 3rd ed., vol. 4, Pearson Education.

Silverstein, R.M., Webster, F.X., Kiemle, D.J., 2005a. Mass Spectrometry. *Spectrometric Identification of Organic Compounds* (7th ed., pp. 1-71). Chapter, John Wiley & Sons, Inc.

Silverstein, R.M., Webster, F.X., Kiemle, D.J., 2005b. Infrared Spectrometry. *Spectrometric Identification of Organic Compounds* (7th ed., pp. 72-126). Chapter, John Wiley & Sons, Inc.

Skoog, D.A., Holler, F.J., Crouch, S.R., 2007a. Gas Chromatography. *Principles of Instrumental Analysis* (6th ed., pp. 788-815). Chapter, BROOKS/COLE CENGAGE Learning.

Skoog, D.A., Holler, F.J., Crouch, S.R., 2007b. Molecular Mass Spectrometry. *Principles of Instrumental Analysis* (6th ed., pp. 550–588). Chapter, BROOKS/COLE CENGAGE Learning.

Skoog, D.A., Holler, F.J., Crouch, S.R., 2007c. Atomic X-ray Spectrometry. *Principles of Instrumental Analysis* (6th ed., pp. 303–333). Chapter, BROOKS/COLE CENGAGE Learning.

7.8 Optical Measurements (Supplementary Information of Chapter 2)

The incident, reflected, and transmitted sunlight (390-700 nm) was measured periodically throughout the aforementioned experiments to assess the interaction and impedance of the light and oil in a sea-ice environment. A single optical channel spectrum instrument (ASD FieldSpec Handheld 2), connected to irradiance detectors through a fiber, was used to measure the albedo and transmittance of the oil and oil-contaminated sea ice. The Irradiance detector is a polytetrafluorethylene cosine collector, which samples irradiance from all angles of a hemisphere (π sr) according to the cosine of the incident angle. Two irradiance detectors were used to measure the albedo and transmittance in this study and were calibrated by setting the detectors in the same location to measure the sunlight.

Surface albedo $\alpha(\lambda)$ and transmittance $T(\lambda)$ are given by

$$\alpha(\lambda) = E_u(\lambda) / E_d(\lambda, 0)$$

$$T(\lambda, h) = E_d(\lambda, h) / E_d(\lambda, 0)$$

where $E_u(\lambda)$ is the reflected irradiance from the surface of the sea ice, $E_d(\lambda, 0)$ is the spectral incident irradiance, and $E_d(\lambda, h)$ is the downwelling irradiance beneath the sea ice layer, oil layer, and seawater layer. To measure albedo, an irradiance detector was set to look upwards, to record downwelling irradiance, and downwards, about 50 cm above the ice, to record upwelling irradiance reflected from the ice surface. To measure transmittance, a waterproof irradiance detector was mounted on a long arm with an elbow joint, and adjusted to be perpendicular to the bottom center of the oil tank, looking upwards at a 0° zenith angle to record downwelling irradiance. The incident, reflected, and transmitted light were

measured individually at separate times. In order to alleviate error associated with changing sky conditions, full sets of measurements were conducted in no more than four minutes. Note, an air-surface (ice) interface correction and a sun glint correction were not applied to the measured albedos. However, as the downwelling irradiance was measured at a 0° elevation angle with a modest height of 50 cm from the ice surface, the resultant albedos would not be significantly overestimated.

7.9 Dielectric Measurement: Resonance Perturbation Method (Quality Assurance/Control) (Supplementary Information of Chapter 2)

The dimensions of the custom cavity (Gregory Bridges, Advanced RF Systems Lab) and samples used in the setup are (W=86mm, H=43 mm, L=262mm) and (O/D=2mm, I/D=1mm, H=43mm), respectively.

Precise measurements of the cavity and sample volume are required to calculate accurate permittivity values based on Eq. (2.10). Pyrex glass tubing was used for oil sample containment inside the resonant cavity. For situations in which samples are liquid and require a container such as a glass tube to keep the sample in place within the cavity, perturbing the cavity with an identical but empty container for the “empty” cavity measurements allows the effect of the container on the measurement to be calibrated out.

As manufactured tubing, drawn from molten glass, is not precise and varies in wall thickness, its inner and outer diameters can fluctuate over a 1-meter span. Furthermore, minute changes in the glass wall thickness (e.g., 0.1 mm) can affect the degree of losses associated with measurement in the resonant cavity. To avoid inaccuracy in results due to

inconsistency in glassware dimensions, each glass tube was measured twice, with and without its oil sample, assuring an exact response from the resonant cavity.

Furthermore, manual measurements of the inner diameters of the glass tubes were taken with an inverted light microscope (Leica DMIL LED) equipped with an ocular ruler with 0.01 mm spacing. The measured inner diameters of the glass tubes ranged from 0.95 to 1.05 mm. An assigned uncertainty of 0.02 mm in the ability to read the ocular ruler results in an uncertainty in the hundredths place of calculated relative permittivities.

7.10 NRCS Modeling (Supplementary Information of Chapter 2)

- a) $\sigma_{vv} = 10 \log_{10}(\sigma_{vv})$;
- b) $\sigma_{vv} = g (\cos(\theta))^3 / \sqrt{p} * (\gamma_v + \gamma_h)$;
- c) $g = 0.70 (1 - e^{-0.65 ks^{1.8}})$;
- d) $p = (1 - (2 \theta / \pi)^{1/(3 * \gamma_0)} e^{-ks})^2$;
- e) $ks = s (2 \pi f / 0.3)$;
- f) $\gamma_v = \left| \frac{\rho_{ov}}{\rho_{oh}} \right|^2$;
- g) $\gamma_h = \left| \frac{\rho_{oh}}{\rho_{ov}} \right|^2$;
- h) $\rho_{ov} = -(n_2 \cos(\theta_1) - n_1 \cos(\theta_2)) / (n_2 \cos(\theta_1) + n_1 \cos(\theta_2))$;
- i) $\rho_{oh} = (n_1 \cos(\theta_1) - n_2 \cos(\theta_2)) / (n_1 \cos(\theta_1) + n_2 \cos(\theta_2))$;
- j) $n_1 = \sqrt{\epsilon_1}$;
- k) $n_2 = \sqrt{\epsilon_2}$;
- l) $\cos \theta_2 = \sqrt{1 - (n_1 \sin(\theta_1) / n_2)^2}$;
- m) $\gamma_0 = \left(\left| \frac{1 - \sqrt{\epsilon}}{1 + \sqrt{\epsilon}} \right| \right)^2$;
- n) $\theta_2 = \theta_1 (\pi / 180.0)$;

where:

θ_1 - incidence angle (degrees);

θ_2 - incidence angle (radian);

s - rms height (m);

f - frequency (GHz);

σ_{vv} - backscattering of sea ice profile (dB);

γ_0 - Fresnel reflectivity at normal incidence;

$\epsilon = \epsilon' - j \epsilon''$ - complex dielectric constant of the scattering;

ks - calculate roughness parameter;

γ_v - Fresnel reflectivities of v polarization at given set of incidence angles;

γ_h - Fresnel reflectivities of h polarization at given set of incidence angles;
 ρ_v - calculates the v reflection coefficient of a plane dielectric surface;
 ρ_h - calculates the h reflection coefficient of a plane dielectric surface.